<SCUOLA DI DOTTORATO
UNIVERSITÀ DEGLI STUDI DI MILANO-BICOCCA

Department of
Materials Science

PhD program Materials Science and Nanotechnology
Cycle XXXII

Ab initio study of ground and excited state properties of dopamine-functionalized TiO_2: from flat surfaces to realistic spherical nanoparticles

Surname: RONCHI Name: Costanza

Registration number: 736779

Supervisor: Professor Cristiana DI VALENTIN

Coordinator: Professor Marco BERNASCONI

ACADEMIC YEAR 2018/2019

Nella pietà che non cede al rancore

Madre ho imparato l'amore

Abstract

Bioinorganic hybrid nanocomposites, built by connecting inorganic nanostructures, such as TiO_2 nanoparticles (NPs), to bioactive molecules (e.g. drugs, proteins, DNA fragments), have been recently used for several biomedical applications, due to their biocompatibility and the possibility of targeting specific cells or of drug delivery.[1]

The aim of my project is to study, through density functional theory (DFT) calculations, the interplay between TiO_2 surfaces and a bifunctional linker (dopamine, DA), which can efficiently anchor the metal oxide surface but also attach biomolecules.

During the first year of PhD, we simulated the adsorption of DA on the flat anatase (101) TiO_2 surface, which is a simplified model for faceted NPs, using hybrid DFT calculations. We investigated several adsorption modes and increasing coverage regimes to explore the process of self-assembling both under kinetic and thermodynamic conditions. We found out that the DA ethyl-amino functional group plays a crucial role, interacting with the surface at low coverage and ruling the organization of the self-assembled monolayer at high coverage, when unexpected proton transfers between the protonated TiO_2 surface and the DA molecules are observed.

During the second year, we investigated the behavior of DA on a more complex, but more realistic, model of TiO_2, i.e. the curved surface of a spherical NP. First, we studied the possible adsorption configurations of an isolated DA molecule. For the most stable, we investigated the effect of light irradiation, considering the formation of excitons, the separation of photoexcited holes and electrons, their trapping or recombination. Then, we built a high-coverage model, adsorbing a gradually increasing number of DA and, finally, considering temperature effects through molecular dynamics density functional tight-binding (MD-DFTB). We clarified the effect of the number of adsorbed molecules on the binding energy and on the electronic structure of the system. To this aim, we assessed the validity of a single point DFT calculation on the DFTB geometry to correctly reproduce electronic properties at an acceptable computational cost.

In the third year, we studied, through real-time time dependent DFT (TDDFT), the optical properties of DA adsorbed on the flat anatase TiO_2 surface. First, we compared the optical spectrum of a DA molecule in vacuum and of bulk TiO_2 anatase with previous experimental data.[2,3] Then, from the electronic absorption spectrum of different adsorption

configurations of DA on the anatase surfaces, at both low and full coverage regimes, we could determine the detailed mechanism of the charge transfer between the molecule and TiO_2.

Overall, the performed study clarifies various aspects of the interface between DA and the flat or curved TiO_2 surfaces, and on its response to light, which will be the basis for future studies where the linkers tether biomolecules.

Contents

1 Introduction

Cancer is the second leading cause of death at a global level and is responsible for estimated 9.6 million deaths in 2018.[4] Cancer, often also referred as malignant tumours and neoplasms, consists on the rapid creation of abnormal cells that grow beyond their usual boundaries, then invade adjoining parts of the body and, in case of metastasizing, spread to other organs.

Although conventional therapies, such as surgery, radiation, hormone therapy, and chemotherapy, have improved patients' survival, they also have several limitations. In conventional cancer chemotherapy, the therapeutic agents can cause several adverse side effects since they distribute non-specifically in the human body, thus affecting both cancerous and normal cells, limiting the therapeutic dose and causing excess toxicity to normal cells, tissues and organs.[5].The kinetics of tumour's diffusion implies the existence of a threshold for clinical detection, from which it is possible to start with the treatment supposed to trigger the process of remission and to diminish the number of cancer cells. [6] The treatment needs to be continued over a long period of time, because if the number of insane cells does not get to zero, the tumour is destined to grow again.

The issue with traditional medicine is that it is not specific for tumour cells. Moreover, it does not allow for any detection when the number of cancer cells is close to zero. In order to avoid the tumour to grow again after the treatment, there is a need for a diagnostic tool with a sensitivity of one single cell and a necessity of a therapeutic agent as specific as possible for cancer cells.

Nanomedicine (**Figure 1.1**), the medical application of nanotechnology, emerged as an innovative approach in cancer treatment, in alternative to traditional cancer therapy (**Section 1.1**). A variety of different materials could be used for nanomedicine, including nano-emulsions, colloidal particulate systems constituted by solid spheres with an amorphous and lipophilic surface with a negative charge, polymeric nanoparticles, solid-lipid nanoparticles, quantum dots, colloidal gold nanoparticles, nanodiamonds, dendrimers, which are repetitively

branched molecules, metal or metal-oxide nanocrystals, liposomes and nanotubes.[7] Among the several kinds of nanostructures, semiconducting oxide nanoparticles, e.g. magnetite (Fe_3O_4) and titanium dioxide (TiO_2), have promising properties, which make them responsive to an external *stimulus*, allowing the remote controlling of their action.

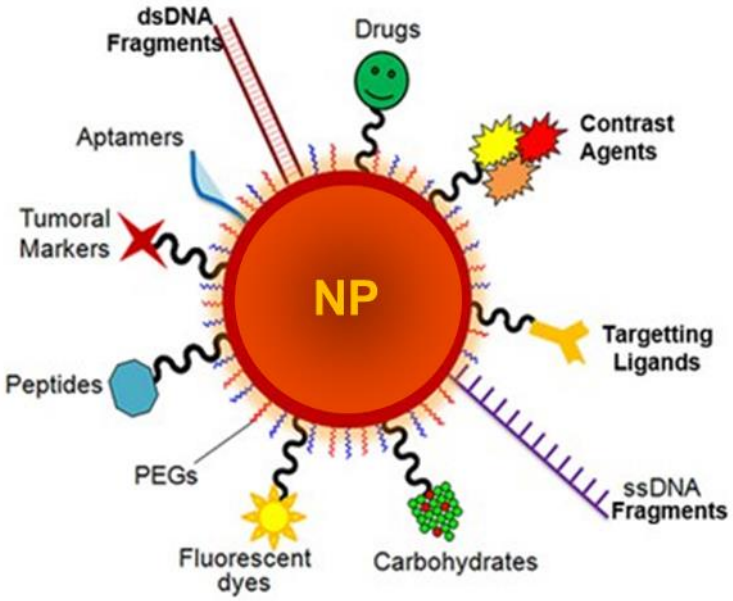

Figure 1.1 Schematic representation of the possible applications of functionalized nanoparticles.

In this work of thesis, we focus on TiO_2 (**Section 1.2**), which we contextualize not only for advanced nanomedicine applications, but also for solar light-based conversion processes like photocatalysis and photovoltaics. We discuss firstly the different crystalline phases of TiO_2, the absorption properties of this material and, finally, its nanostructuring.

Functionalization of TiO_2 nanoparticles (**Section 1.3**) could make them appropriate for several applications in nanomedicine, on one side red-shifting the range of absorption from the ultraviolet to lower photon energies, on the other side providing them with a hook, which could be used for the linking of bioactive molecules (**Figure 1.1**), i.e. for bioconjugation.

1.1. Nanomedicine for cancer therapy

Nanomedicine seeks to deliver a valuable set of molecular tools and clinically useful devices in the near future, derived from the molecular knowledge of the human body, which could be the key to revolutionize the approach to cancer therapy. The concept of nanomedicine was anticipated over 50 years ago by Albert R. Hibbs, as mentioned by Richard Feynman in his famous talk "There's plenty of rooms at the bottom".[8] Hibbs suggested a very interesting possibility, which is still valuable nowadays and provides us the rationale of nanomedicine:"…although it is a very wild idea, it would be very interesting in surgery if you could swallow the surgeon".

In the frame of nanomedicine, the role of the surgeon is played by nanoparticles or, more generically, by nanosize materials.

Nanoparticles (NPs) have been of significant interest over the last decade as they offer great benefits for drug delivery to overcome limitations of conventional chemotherapy. When the nano-size regime is reached, so the dimension of the material ranges approximately between 1-100 nm,[9] new features, which are strongly dependent on the size and shape of the particles, arise. NPs can be made using a variety of materials including polymers (e.g. biodegradable polymeric nanoparticles, dendrimers), lipids (e.g. solid-lipid nanoparticles, liposomes), inorganic materials (e.g. metal nanoparticles, quantum dots), and biological materials (e.g. viral nanoparticles, albumin nanoparticles). [10]

Despite the many advantages of employing nanoparticles, deriving mainly to the enhanced surface-to-bulk ratio, these nano-sized objects have also some drawbacks including the lack of surface properties and the incurring of possible undesired interaction with the cellular environment.[11] In addition, NPs can undergo undesired interactions with the host medium, substrates and/or other individual species such as molecules and other particles, all of which could limit their use in specific applications.

Therefore, in order to be employed for biomedical application, the NPs should be modified to make them soluble in physiological media, biocompatible, non-toxic, "stealth" by the immune system and selective for the target.

Functionalization with organic or inorganic molecules could, on one hand, reduce the toxicity and, on the other hand, give site-specificity properties to the nanoparticles, i.e. the NPs can react only with specific molecules or compounds according to their chemistry. In fact, when a NP is modified by covalent linking, the undercoordinated reactive sites at the surface are saturated by the adsorbed molecules, reducing the a-specific interaction with the biological environment and, therefore, the toxicity. In addition, it is possible to bind molecules with

specific functional groups (or antibodies), which would be responsible for the triggering of chemical reaction only with specific biomolecules, according to the active targeting mechanism already discussed in **Section 1.2**.

The modified NPs (**Figure 1.1**) could then be suitable for targeted drug delivery,[12,13] for biocompatibility,[14], [15]sensing of biomolecules[16,17] and cells,[18,19] for imaging of specific cells[20] and, eventually, for photodynamic therapy (PDT).[21,22]

Polymer coatings provide an alternative to small molecule ligands, imparting the properties of macromolecular systems to the particle surface.[23]

1.1.1. Targeting of nanoparticles towards cancer cells

In the previous section, we mentioned that nanoparticles should be selective for the targeted cells. We would like now to look further into the targeting mechanism.

The targeting of the tumour can be carried out in two main ways: passive and active targeting. The former one exploits the enhanced permeability and retention effect (EPR), according to which nano-sized molecules or systems should accumulate at the tumour's site much more than what they do in normal tissues.[25,24] Such effect is exists even for bare nanoparticles and it should take them automatically in the tumour, because the tumoural tissues produce a higher amount of blood vessels in order to allow the malignant cells to grow quickly. Coating NPs with polymers such as polyethylene glycol (PEG) has been shown to facilitate passive targeting of tumour tissues through EPR effect.[25,26]

The active targeting mechanism involves the incorporation of targeting modules such as ligands or antibodies, which are specific to certain types of cells around the body, on the surface of the nanoparticles. Active targeting sensibly improves the specificity of the action of the NP. Next generation NPs privilege active targeting, which means that the inorganic substrate should be functionalized to be able to link proteins (mainly antibodies and their fragments), peptides, nucleic acids (aptamers), small molecules, or other possible targeting moieties (vitamins or carbohydrates).[27]

1.1.2. S*timuli*-responsive nanoparticles

Another method, which could be used in order to avoid the side effects of the antitumoural treatment and to enhance therapeutic efficiency at the same time, is to employ nanoparticles based on *stimuli*-responsive materials.

The concept of stimuli-responsive drug delivery was first suggested in the late 1970s with the use of thermosensitive liposomes for the local release of drugs through hyperthermia.[28] *Stimuli*-responsive materials present a peculiar ability to change one or more of their properties under a defined *stimulus*, which could be either exogenous (variations in temperature, magnetic field, ultrasound intensity, light or electric pulses) or endogenous (changes in pH, enzyme concentration or redox gradients). The idea is that the toxic NPs should be activated only locally, where their action is needed, starting the process of cell death in a remotely controlled way.

These *stimuli*-responsive NPs are able to cause cell death through different mechanisms, depending on the properties of the material. For example, iron oxide (Fe_3O_4) NPs are magnetic and, after being exposed to an external magnetic field, they are able to generate hyperthermia, causing the death of the cells in the targeted area.

Other nanoparticles, based on semiconducting materials, such as silica or titanium dioxide NPs, respond to a light *stimulus*, and can be used for photodynamic therapy (PDT), a light based therapy used to ablate tumors (**Figure 1.2**).

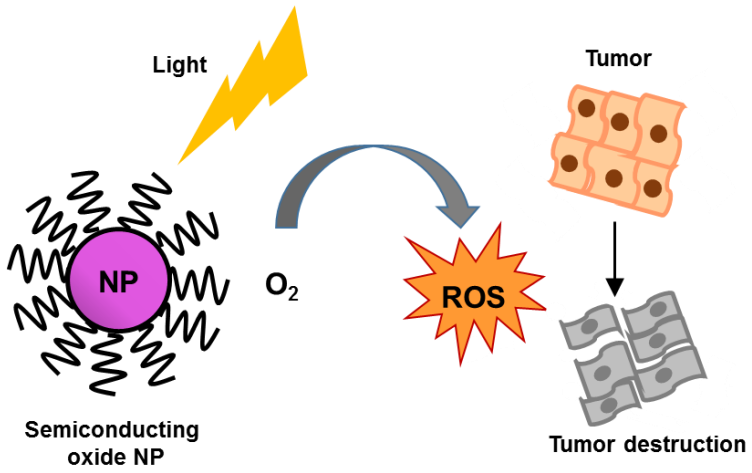

Figure 1.2 Schematic mechanism of photodynamic therapy exploiting functionalized semiconducting oxide nanoparticles.

The mechanism of PDT involves administration of a photosensitizing agent, which could also be a semiconducting oxide NP, followed by irradiation at a wavelength corresponding to the absorbance band of the sensitizer. In the presence of molecular oxygen, a series of events leads to direct tumour cells death. The functionalization of the NPs could play a crucial role also for PDT applications, giving the possibility of tuning the optical absorption range with respect to the bare material (see **Section 1.4.**).

In addition, *stimuli*-responsive materials can be used in drug delivery (**Section 1.1.2**). The controlled local release of an antitumoural drug, such as, for example, deoxorubicin (DOX),

could be obtained as the response to an external stimulus.[29] Drug loading on the nanocarrier can be improved by functionalized NPs.

1.1.3. Hybrid materials for bioconjugation

In the wide family of hybrid materials, we are interested in composites consisting on an intimate mixture of inorganic and organic components. Several examples of hybrid nanocomposites are present in nature, such as crustacean carapaces or mollusk shells and bone tissues in vertebrates. More sophisticated hybrid nanocomposites have been developed by humans to be used as dyes or for the creation of porcelain. [30] More precisely, the term hybrid does not only refer to the summing of two dissimilar components to make a single entity, but it also includes the emergence of enhanced or completely new properties.[31] Higher flexibility and mechanical strength, greater temperature range of usability, increased durability, improved electrical, magnetic or redox properties and the creation of multifunctional domains are some of the possible properties arising by the synthesis of the nanohybrids.[32]

Functional hybrids can be obtained through two different approaches: either the two well-defined building blocks *lego*-like maintain their original integrity, or the structural units are formed *in situ* by a precursor, which transforms into a new structure.

In the former approach, the separate building blocks are still recognizable in the final structure. Inorganic NPs with attached reactive organic groups are representative examples of such well-defined building blocks. Since in this kind of nanosized building blocks there are not significant structural changes during the matrix formation, better structure–property predictions are possible and, therefore, also a better design of the single component in order to suite the needed purpose. In particular, nanotechnology focuses on a bottom-up approach in which complex structures are hierarchically formed by these small building blocks.

Alternatively, the formation of the hybrid is based on the chemical transformation of the precursors used throughout materials' preparation. In order to create hybrid materials, reactions that are employed to form the inorganic component *in situ* should have the character of classical covalent bond formation in solutions, through the so-called soft chemistry, which takes place at room temperature and does not destroy the organic moiety. An example of this *in situ* formation of the hybrid materials is the application of the sol–gel process to produce the inorganic component. The sol-gel process requires the synthesis of colloidal solutions (sol), which act like precursors for the formation of a gel (an inorganic continuous net containing an interconnected liquid phase), by means of hydrolysis and condensations reactions. The final

material is determined by the composition of the precursors but also by the reaction conditions. Hence, the final performance of the derived materials is strongly dependent on their processing and its optimization. Low temperature processes often lead to kinetic rather than thermodynamic products, which means that derived inorganic materials are often amorphous or crystallinity is only observed on a very small length scale.

Hybrid nanomaterials, which exploit the properties of the inorganic and the organic component at the same time, are promising candidates to be used in nanomedicine for bioconjugation. For example, inorganic NPs can be functionalized with an inorganic linker to tether bioactive molecules, like DNA fragments, proteins, drugs, etc. (**Figure 1.3**).

The inorganic component could be represented by a semiconducting oxide nanoparticle, while oxygen-containing molecules with double functionalities, i.e. catechol derivatives, could act as suitable linkers and, eventually, give rise to further reactivity.

In this work of thesis, we investigated titanium dioxide as the inorganic nanomaterial (see **Section 1.2**) and the dopamine molecule as possible linker (**Section 1.3)**, investigating structural, electronic and optical properties.

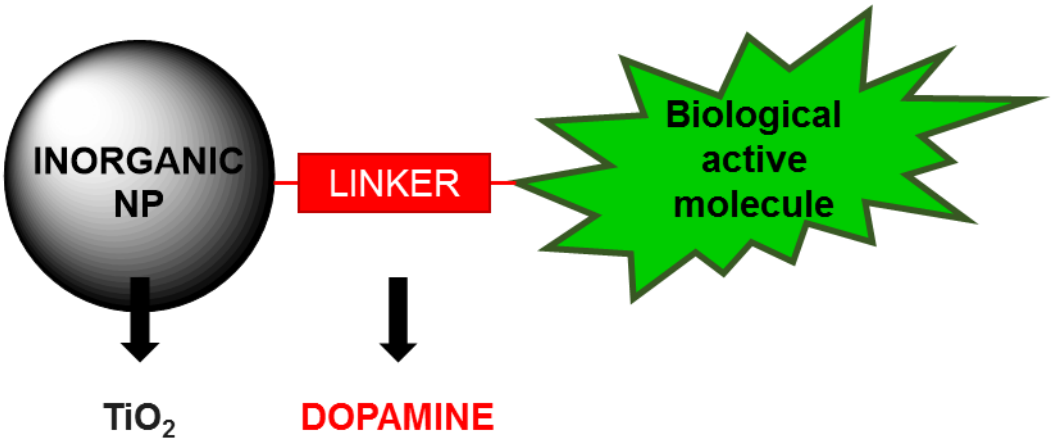

Figure 1.3 Scheme of a bioinorganic nanohybrid, composed of an inorganic nanoparticle (e.g. TiO_2 NP), a linker molecule (e.g. dopamine) and a biological active molecule

1.2. Titanium dioxide as the inorganic nanomaterial

Titanium dioxide (TiO_2), the natural occurring oxide of titanium, is a low-cost and chemically inert semiconductive oxide with a large refractive index, high photostability and strong ultraviolet (UV) light filtering. TiO_2 is the most investigated material for photon energy conversion applications, whose mechanism is explained in the following section.

1.2.1. Applications photocatalysis and photovoltaics

Upon irradiation of any semiconducting material, a portion of light energy is transferred to it and converted into another form of energy. The best-suited materials for photon energy conversion are semiconductors, which are defined by a band gap (E_g) between 1 and 4 eV. According to band energy theory, the discontinuous band structure of semiconductors is composed of low energy valence bands filled with electrons, high-energy conduction bands, and band gaps. [33] When the incident light has an energy equal or higher than the band gap of the semiconducting material, an electron (e^-) is excited into the conduction band (CB), leaving an electron hole (h^+) in the valence band (VB).

The photogenerated charges could be used to promote chemical reactions in photocatalytic applications. The photoexcited charges can migrate to the surface of the semiconductor and trigger a series of redox processes, as reported on the right of **Figure 1.5** for a general electron donor (D/D^+) and acceptor (A/A^-) couple. For example, semiconductors are used to catalyze fundamental redox processes, such as water splitting for and CO_2 reduction.[34]

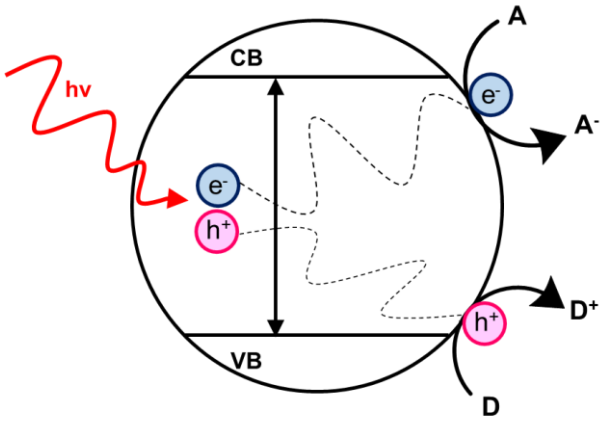

Figure 1.5 Scheme of a generic process of conversion of photon energy into chemical energy, promoting the reaction between an electron donor (D) and an electron acceptor (A) inside the semiconductor.

In competition with charge transfer to adsorbed species, there is the electron and hole recombination process. Recombination of the separated electron and hole, which can occur in

the volume of the semiconductor particle or at the surface with the release of heat, is detrimental to the efficiency of a semiconductor photocatalyst.

Modifications of semiconductive surfaces, such as the addition of dopants, the combination with other semiconductors or the adsorption of organic ligands, are beneficial in decreasing the electron and hole recombination rate and, thereby, increasing the quantum yield of the photocatalytic process.

Clearly, the occurrence of redox events will depend on the reduction and oxidation electrochemical potential of the adsorbate, as well as on the relative position of the CB and VB edges. This means that the conduction band minimum (CBM) needs to be higher in energy than the reduction potential of the catalyzed reaction and the valence band maximum (VBM) lower than the oxidation potential. In the case of the photoelectrolysis of water, therefore, the lower limit is 0 eV vs NHE (Normal Hydrogen Electrode) for the cathodic semireaction ($H_2O \rightarrow H_2$), while the upper limit is 1.23 eV according to the anodic semireaction ($H_2O \rightarrow O_2$). Actually, many semiconductors meet this requirement (**Figure 1.6**).

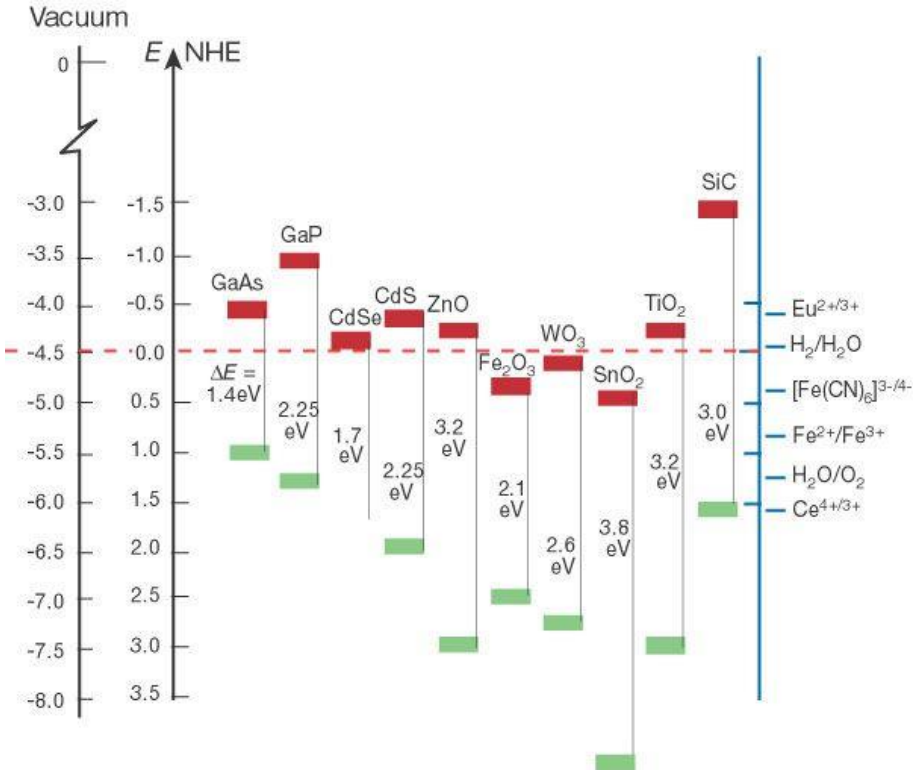

Figure 1.6 Band positions of several semiconductors in contact with aqueous electrolyte at pH 1. The lower edge of the conduction band (red color) and upper edge of the valence band (green color) are presented along with the band gap in electron volts. The energy scale is indicated in electron volts using either the normal hydrogen electrode (NHE) or the vacuum level as a reference. On the right, several redox potentials of the redox couples are fiven against the NHE potential.

Nevertheless, most of them cannot be used for photocatalysis because either the electron-hole recombination is too fast, or because the semiconductor is not stable with respect

to light (CdS) or aqueous environment (ZnO). Among the available semiconductors, TiO_2 shows the highest performances in photocatalysis, thanks to is stability to light and water, with a relatively long life-time of the electron-hole pair, demonstrated in 1972 by the pioneering work of Honda and Fusjishima about light-induced water splitting.[35]

Alternatively, the photogenerated charges could be employed to produce an electric current in photovoltaic devices, which range from the classical silicon or inorganic semiconductor based solar cells, limited by the high production cost and the low diffuse light absorption, to the more advanced hybrid organic-inorganic dye-sensitized solar cells (DSSCs), which will be better discussed in **Section 1.2.7**. In a photovoltaic cell, the electrons generated a result of the excitation, flow from the CB through an external circuit, generating electrical current towards the counterelectrode, where they are collected by a redox couple solvated in the electrolyte, usually triiodide ions, which regenerate the oxidized dye.

1.2.2. Applications in nanomedicine: photodynamic therapy and drug delivery

Among the several ways of taking advantage of the photocatalytic properties of TiO_2, there is the possibility to employ this material as a light harvester in photodynamic therapy. The photoinduced electrons and holes generated after the illumination of TiO_2 NPs are able to reach the surface and to give birth to light-induced redox chemistry. Then, the holes can react with surface adsorbed H_2O to produce hydroxyl radicals (OH•). Meanwhile, the electrons are usually scavenged by O_2 to yield superoxide radical anions (O_2^-•). These species in solution can further react to give other cytotoxic reactive oxygen species (ROS), such as hydroperoxyl (HO_2•) and hydrogen peroxide (H_2O_2), which are harmful to cells.[36] The major reactions that results in the formation of ROS are:

$$TiO_2 + h\nu \rightarrow h^+ + e^- \quad (1.1)$$

$$H_2O + h^+ \rightarrow {}^{\bullet}OH + H^+ \quad (1\,2)$$

$$O_2 + e^- \rightarrow O_2^{\bullet -} \quad (1.3)$$

$$O_2^{\bullet -} + H^+ \rightarrow HO_2^{\bullet} \quad (1.4)$$

$$2HO_2^{\bullet} \rightarrow H_2O_2 + O_2 \quad (1.5)$$

$$H_2O_2 + O_2^{\bullet -} \rightarrow {}^{\bullet}OH + OH^- + O_2 \quad (1.6)$$

The fact that the TiO_2 NPs are cytotoxic only once they are light-activated is crucial for the purpose of selectively kill only the targeted sick cells, limiting the side effects on the rest of the body, and making such nanoparticles good candidates for treatment of cancer.[37]

TiO2 nanoparticles could also be used for the photoinduced release of drugs.
Premature drug release and insufficient drug release at target sites are major limitations of drug delivery. Moreover, when the therapeutic compounds are systematically administrated and they are distributed in the whole body through blood circulation, their activity is limited due to hydrolysis, enzymatic degredation and rapid excretion through the urinary system.
The controlled local release of an antitumoural drug, such as, for example, deoxorubicin (DOX), could be obtained as the response to an external light-stimulus.[29] Drug loading on the nanocarrier can be improved by functionalized NPs.

1.2.3. The best photoconverting phase of TiO_2: anatase

There are four fundamental crystal forms of TiO_2: anatase (tetragonal), rutile (tetragonal), brookite (orthorhombic)and TiO_2(B) (monoclinic), which does not commonly exist in minerals (**Figure 1.7**).

All of these polymorphs are composed by TiO_6 octahedral units, where each Ti^{4+} is coordinated by six O^{2-}, and they differ in terms of distorsion. Differences in the lattice structure are responsible for different electronic structures. Therefore, the photocatalytic activities of these different forms of TiO_2 are quite different. Nonetheless, the different phases of TiO_2 have some general features in the electronic structure: the *2p* orbitals of the oxygen atoms contribute to the filled VB, while *3d*, *4s*, *4p* orbitals of the titanium atom contribute to the unoccupied CB; the lower part of the CB being dominated by Ti *3d* orbitals.

The two most stable and widespread polymorphs are rutile and anatase. More precisely, rutile is the most stable phase at ambient pressure and temperature in macroscopic sizes, while anatase is more stable in nanoscopic sizes.[38-40]

With respect to rutile, anatase is 9% less dense, which means that in rutile there is major covalent mixing between the O *2p* and Ti *3d*, while anatase exhibits a valence and a conduction band with more pronounced O *2p* and Ti *3d* characters.

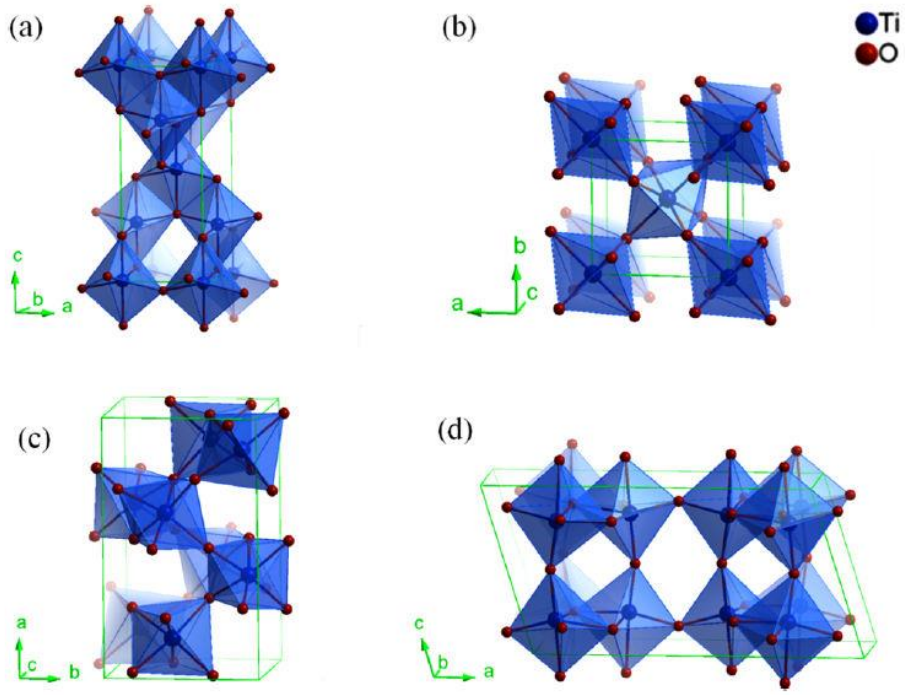

Figure 1.7 Crystalline structure of titanium dioxide in four different phases: a) anatase b) rutile c) brookite d) TiO_2 (B). Oxygen atoms are shown in red, Ti atoms are blue and the TiO6 octahedra are represented by blue polyhedra.

TiO_2 anatase and rutile are mostly used for research purposes as a solar energy conversion material. Absorption of light with an energy greater than the band gap (for anatase: 3.20 eV at environmental temperature,[41] 3.03 eV for rutile)[42] promotes electrons from VB to the CB of the semiconductor, leaving electronic vacancies (positively charged holes) in the VB.

Photogenerated electrons and holes in TiO_2 have been probed by electron paramagnetic resonance (EPR) spectroscopy,[43,44]photoluminescence[45,46]and O_2 photodesorption.[47] These charge carriers are transported to the surface to react with redox couples in solution.[48]

Due to the proven photocatalytic properties and since it is cheap, stable, nontoxic, environmentally friendly, titanium dioxide is widely used for catalyzing several processes, such as environmental purification, self-cleaning, organic synthesis, solar cells and CO_2 reduction.[49]

Recently, TiO_2 nanoparticles have been proposed to be used also for biomedical applications, for example for photoinduced therapy and, for light-driven drug release,[50] due to its high photocatalytic efficiency, low toxicity and excellent photostability.[1]

Among the different TiO_2 phases, anatase is usually considered to be more suitable for photocatalytic and photovoltaic applications with respect to rutile due to the fact that, depending on the shape of the nanostructure, it can reach a higher surface area at the nanoscale, leading to enhanced adsorption capability and to the generation of much more active sites (e.g. oxygen vacancies). In addition, due to the fact that it has got an indirect band gap (see Figure 1.8 in

Section 1.2.3.1), the recombination of the photogenerated charge carriers is significantly slower.[42] In fact, photoconductance measurements have shown that the lifetimes of photoexcited carriers are longer in anatase than in rutile, which is a direct semiconductor.[51]

Because of these photocatalytic features and aware of the major stability of the anatase phase at the nanoscale, from now on we will refer exclusively to TiO_2 anatase.

1.2.3.1. Bulk anatase

Bulk anatase is characterized by a tetragonal lattice ($P4_2/mnm$, D_{d2} point symmetry) with four TiO_2 units per unit cell, forming chains of slightly elongated TiO_6 octahedra, resulting in a D_{2d} axial symmetry. The cell parameters of bulk anatase are a=b=3.782 Å, c=9.502 Å.[52] The Ti–O bonding is largely ionic with some covalent contribution.[53] In bulk anatase, all the Ti atoms are six-fold-coordinated (Ti_{6c}^{3+}), while all O atoms are three-fold coordinated (O_{3c}^{-}) (**Figure 1.8a**).

For semiconducting oxides, the band gap is one of the most crucial quantities to predict. From the electronic structure of bulk anatase, calculated according to DFT (GGA/PBE) calculations (**Figure 1.8b**), anatase is correctly predicted to be an indirect semiconductor, with the top of the valence band placed close to the X *k*-point and the bottom of the conduction band Γ at the point. However, as it is well known in literature, the band gap calculated by standard DFT is significantly underestimated with respect to the experimental value of 3.4 eV measured at the liquid helium temperature,[54] due to the self-interaction error. The matching with the experimental value could be improved by using hybrid DFT methods (see **Chapter 2**) that, by introducing a component of Hartree-Fock exact exchange in the expression of the density functional, partially correct the self-interaction error. The band gap calculated by hybrid DFT are tipically overestimated by 0.4-0.5 eV.[55]

Another possibility to obtain a better description of the band gap of semiconducting oxides is to exploit methods deriving from the Many Body Perturbation Theory (MBPT), such as the Bethe-Salpeter equation or the GW approximation. Since the bulk TiO_2 cell is quite small (six atoms), it is feasible to perform computationally heavy GW calculations. When standard DFT is used as a starting point, the resulting band gap is overestimated by GW calculations, as shown in the yellow points in **Figure 1.8b**.

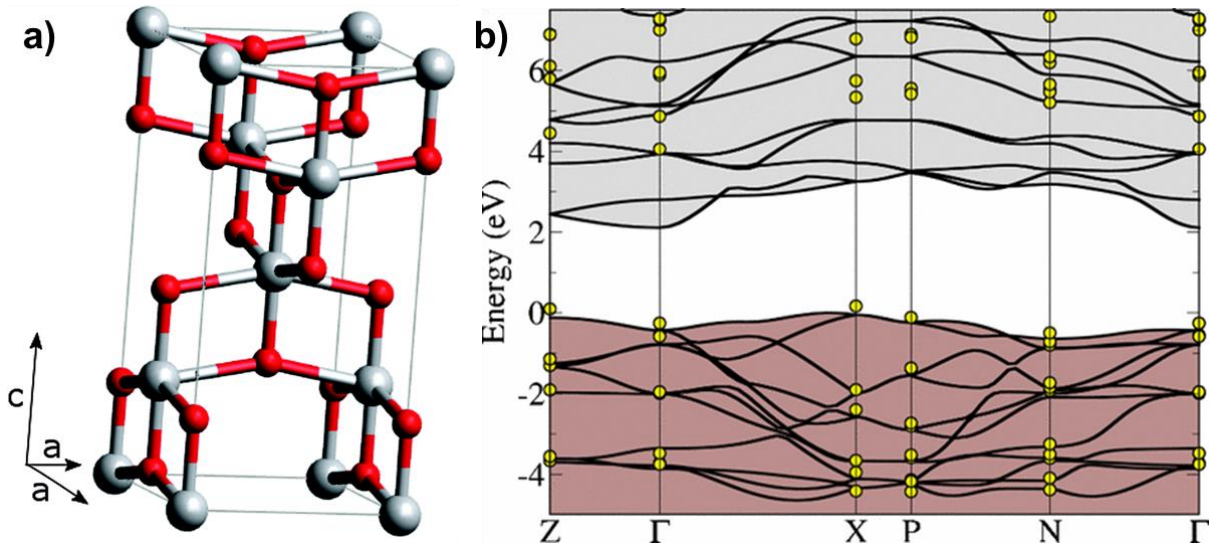

Figure 1.8 a) Bulk anatase unit cell **b)** Band structure of bulk anatase along with the high symmetry directions of the first Brillouin zone. Black lines indicate the GGA/PBE calculations, yellow dots indicate the values obtained after G_0W_0 corrections.[56]

Di Valentin and Selloni demonstrated by atomic relaxation of the triplet exciton by B3LYP that charge carriers produced by UV photoexcitation of TiO_2 form localized polaronic states at low temperature, i.e. charge induced distortions.[48] This means that the photogenerated charges do not behave like free electrons and hole, but they couple with the lattice to form polarons. According to this work, the triplet exciton is highly localized on next-neighboring Ti_{6c}^{3+} and O_{3c}^{-} sites, inducing a structural reorganization with an energy gain of 0.6 eV. The computed photoluminescence (PL) of 2.6 eV satisfactorily agrees with the experimental one.

In order to describe the polaronic nature of extra electrons and holes in bulk anatase, it is necessary to use hybrid functionals[48] or DFT+U,[57,58] even if the size of the polaron cannot be easily established, being dependent on the method employed. According to hybrid DFT calculations, 76% of the electron is localized on a single Ti site and most of the remaining is confined within a sphere with a radius of 6 Å.[48] The electron trapping energy is calculated to be 0.23 eV, suggesting that the electron is weakly bound to the bulk anatase lattice. The energy barrier associated to the electron hopping between the lattice sites is quite low, in particular it is evaluated to be ~0.3 eV according to DFT+U.[57]

Concerning the hole, according to B3LYP the charge is highly localized on an O_{3c} (85%) and its midgap state is deeper with respect to the one of the electron, therefore it is more stabilized. The trapping energy for the hole is calculated to be 0.74 eV,[48] in agreement with experimental values for EPR hyperfine coupling.[59] The estimated hopping barriers for the hole transport are between 0.5 and 0.6 eV, according to DFT+U.[57]

1.2.4. Red-shift of TiO_2 absorption energy

The major drawback of TiO_2 is its wide band gap, triggering light absorption in the ultraviolet region.

This prevents TiO_2 to be extensively used in photovoltaic and photocatalytic applications, since the ultraviolet light represents only 5% of the solar light spectrum. Even more so, for nanomedicine applications, the range absorption should be moved towards longer wavelengths, in order to fit the optical therapeutic window where photoactive species can be efficiently activated for photodynamic therapy, which is in the range of 600-1000 nm (visible and near-IR).

The absorption of incident light and redox potential of TiO_2 mainly depends on its energy band configuration. Hence, to utilize solar energy more effectively, it is necessary to develop long-wavelength-light-sensitive TiO_2 photocatalysts with excellent performance on the basis of energy band engineering.[60]

Several approaches are possible in order to move the edge of absorption of a material: doping the semiconductor with other elements (cationic or anionic), interfacing TiO_2 to other semiconductors, or modifying the surface with organic or organometallic molecules. These surface modifiers could be distinguished in light-harvesters, i.e. visible light active materials, or with molecules which do not absorb visible-light when they are isolated, but that are able to create colorful charge transfer complexes, when coupled with semiconducting materials.
In addition to light sensitization, nanostructuring is crucial to improve the performances of the material for advanced applications, since the increase of the surface-to-bulk ratio, leads to an increasing of the surface area and, consequently, of the surface active sites, which could coordinate organic molecules (see **Section 1.2.5.2.**).

1.2.5. TiO_2 nanostructuring

The unique properties of TiO_2 strongly depend on the physical characteristics of the material including crystallization, grain size, morphology, specific surface area, surface state and porosity. Various physical forms of TiO_2 can be synthesized, such as nanoparticles, nanowires, nanorods, nanotubes and nanofibers. Every time one of these structure is synthetized, the bulk material is limited in space and separated by the environment through the creation of a surface.

When a faceted crystalline micro- or nano-structure is synthetized, the stable surfaces of the anatase TiO_2 crystal are exposed in different proportions depending on the shape of the object. The reactivity at the TiO_2 surfaces can be studied through theoretical methods, either by

modeling periodic bi-dimensional flat surfaces (**Section 1.2.5.1**), or by building zero-dimensional nanocrystals through cluster models, which better describe edges and corners of the real structure (**Section 1.2.5.2.**).

When instead a curved nano-object is synthetized (e.g. nanospheres or nanotubes), periodic bi-dimensional models are not anymore sufficient to account for the peculiar reactivity of the undercoordinated sites at the surface and the use of a zero-dimensional cluster model is mandatory (**Section 1.2.5.2.)**.

TiO_2 nanoparticles are fundamental building blocks in many technological applications,[61] especially in all those involving the photon energy conversion, comprehending also the biomedical field.[1]

Typically, TiO_2 NPs are grown via hydrothermal or sol-gel synthesis (see **Section 1.2.7.1.**).[62] The shape and size of TiO_2 NPs can be efficiently and successfully tailored by controlling the conditions of preparation and by using apposite surface chemistry and it allows for control of their electronic and chemical properties. Moreover, the coordination and structure of Ti surface atoms and thus the nature of surface defects is expected to depend on the shape and size of the nanostructure, hence opening the route towards more efficient site-selective chemistry.

1.2.5.1. Faceted TiO_2 *nanoparticles*

Bernard et al. predicted that the minimum energy shape for TiO_2-NPs below 10 nm of dimension is a decahedral shape in which the two lowest energy surfaces, (101) and (001), are exposed.[63] Faceted TiO_2 nanoparticles have been extensively investigated, experimentally[64,65,66,67] and theoretically through first-principles studies.[63,68,69,70,53,71] The formation rate and the shape of anatase nanoparticles in aqueous solution are dependent on the pH value.[72] It has been found that the introduction of titanium (IV) fluoride (TiF_4) to the synthesis of faceted TiO_2 NPs resulted in the preferential exposure of the 001 facets of anatase, while control of a surface modifier binding group (amino vs OH group, i.e. dopamine) lead to the exposure of the 101 facets.[73] Another growth determining factor is the particle density during synthesis: an excessive dilution may cause a partial dissolution of titania nanocrystals leading to the formation of spherical nanoparticles (**Section 1.2.5.2.**).[1]

Faceted nanoparticles are characterized by a major crystallinity with respect to curved NPs. This makes the recombination of the photogenerated hole and electron more difficult with respect to the defective curve NPs, where the defects can act as recombination centers. For this reason, faceted NPs are generally considered to be more suitable for photocatalytic applications.

At a computational level, the surfaces of faceted nanoparticles can be successfully described through two-dimensional periodic surfaces.

Surfaces have a prominent role in nanomaterials, where a large fraction of atoms is at surface sites, and are essential for understanding the material's reactivity. Usually, they are modeled as few layers slabs with periodic boundary conditions in the plane of the surface.

Surface energies are obtained from the total energy difference between the slab and an equal number of bulk TiO_2 units, normalized for the surface area. Aware of the surface energies, through Wulff construction, it is possible to obtain the equilibrium crystal shape of anatase, which closely resembles the shape of naturally occurring anatase mineral specimens (**Figure 1.9a**).[39]

The (101), and, to a lesser extent, (001) surfaces are the crystal faces that are most frequently exposed by anatase (nano)crystals, including natural anatase samples. Consequently, they are also the surfaces for which the larger amount of theoretical studies is available. In particular, the (101) surface (**Figure 1.9b**) is the most stable one, according both to experimental data[74] and calculations.[75,76]

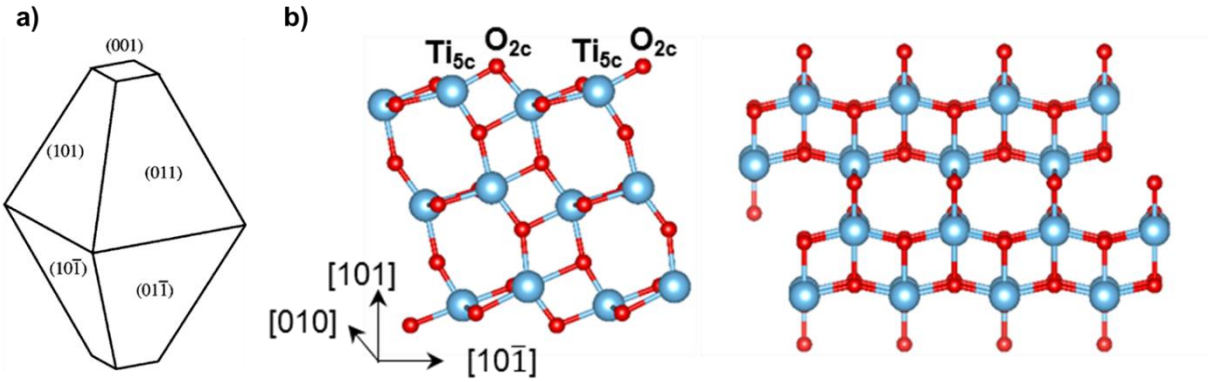

Figure 1.9 a) Equilibrium shape of the anatase crystal;[39] b) side and top view of atomic structure of the majority (101) surface. Blue and red spheres are for Ti and O, respectively.

After cutting the anatase TiO_2 (101) surface from bulk, two kinds of undercoordinated sites can be found on the surface: the fivefold coordinated titanium atoms (Ti_{5c}) and twofold coordinated oxygen atoms (O_{2c}). On the surface there are also species in a bulk-like coordination, i.e. threefold coordinated O ions (O_{3c}) and six-fold coordinated Ti ions (Ti_{6c}), which do not influence significantly the surface reactivity.

Generally, structural relaxation, following the cutting of a surface, plays an important role in surface energy, [75,39,77] reducing the surface energy up to ~50%. Upon the (101) surface relaxation, a significant displacement of surface atoms is observed from bulk-like positions is

observed. [39,63,77,77,78] In particular, Ti-O bonds between Ti and O_{2c} atoms are ~5-10 % shorter than in bulk.

In a semiconductor in contact with the vacuum, surface states may be formed with drastic consequences on the electronic structure, but this is not the case for stoichiometric TiO_2, since flat bands have been observed.[79]

Nevertheless, if the surface contains defects or if it is functionalized with adsorbed molecules, an upward or downward bending of the valence and conduction bands can be induced, according to the amount of defects or to the electronegativity of the adsorbates.[74]

Similarly to bulk anatase, the formation of photoexcited charge carriers were investigated by means of the hybrid functional B3LYP by Di Valentin and Selloni.[48]
When the anatase TiO_2 (101) surface is irradiated, an extra CB electron becomes trapped at a five-fold coordinated Ti_{5c}^{3+} site with a localization of 90% and a trapping energy of 0.62 eV, while, for an extra hole in the VB, 94 % of the density is trapped at an O_{2c} with an energy gain of 1.45 eV. According to these calculation, therefore, the undercoordinated Ti_{5c} and O_{2c} sites are better traps for photoexcited charge carriers than the bulk lattice sites. In fact, the trapping energies for the hole and the electron are found to be lower for the bare anatase (101) surface with respect to the bulk, suggesting the importance of limiting the dimensions of the system. Thus, modeling two-dimensional surface systems or zero-dimensional nanoparticles is paramount for the correct description of photoexcitation.[48]

1.2.5.2. Spherical TiO_2 nanoparticles

Spherical NPs, together with nanotubes and nanorods, are characterized by a high curvature profile, which results in higher binding properties. In fact, these large curvature nanoparticles adjust their coordination environment to form under-coordinated sites, which are the source of novel enhanced and selective reactivity of nanoparticles toward oxygen-containing ligand ligands.[80]

Therefore, spherical TiO_2 NPs are more suitable to be used for further reactivity, hence, to be used as inorganic component in the building of bioinorganic nanohybrids. In fact, the undercoordinated sites are reactive towards oxygen-containing linkers, which could then be used to tether biomolecules.

Surface-to-bulk aspect ratios intimately depend on the shape and dimension of the nanoparticle: they are larger for nanospheres than for nanocrystals, and of course, they decrease

with increasing size.[81] This is due to the higher density of undercoordinated sites present in nanospheres compared to nanocrystals, which leads to a higher surface area.

Even if the major crystallinity of faceted NPs leads to better photocatalytic activity (see **Section 1.2.5.1**), once the spherical TiO_2 NPs are functionalized, the defect sites are saturated and the efficiency of the separation of the charge carriers could be improved, decreasing the recombination rate. Therefore, functionalized spherical NPs are good candidates to be employed as photosensitizers for photocatalytic therapy.[1]

Differently from faceted nanoparticles, spherical NPs have only been studied by means of force field approaches,[82] except for the works by Di Valentin & Co.,[81,83,84,85] that studied by by hybrid DFT diameter sizes up to 4.4 nm .[86]

1.2.5.3. DFT-optimized realistic spherical and faceted TiO_2 nanoparticles

A spherical and a faceted decahedral TiO_2 NPs were built by Fazio and other members of our research group (**Figure 1.10**), following two different approaches. The faceted NP have been built according to the minimum energy shape predicted by Barnard et al.,[63] while the spherical NP was carved by cutting a sphere with the desired radius from bulk anatase.

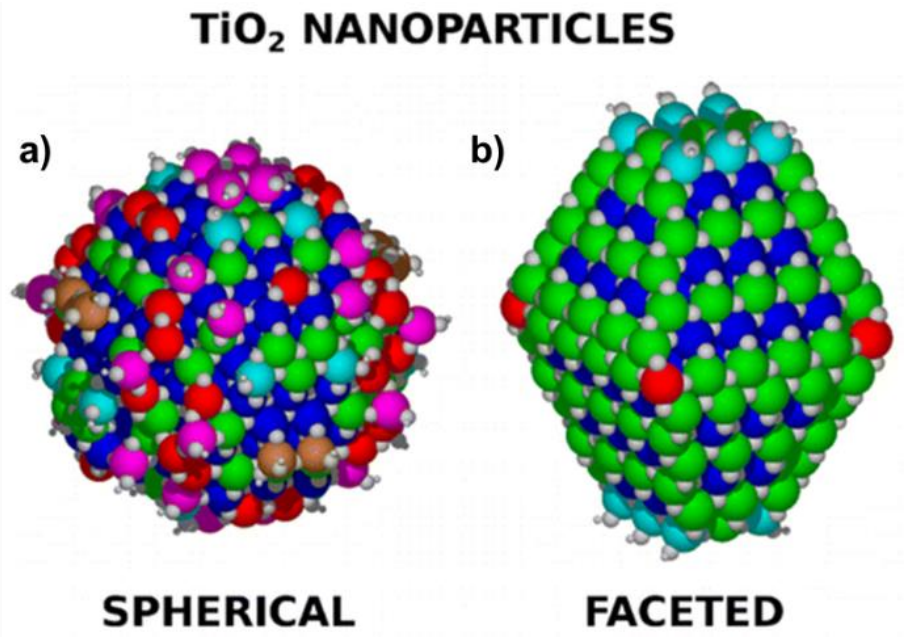

Figure 1.10 Space filling representation of a a) faceted and b) spherical anatase nanoparticles.

Unlike faceted anatase TiO_2 nanoparticles, which have a well-defined structure according to the Wulff shape construction, spherical NPs are more structurally complex. In fact, since they present many undercoordinated surface atoms, intrinsic water is necessary to keep the chemical stability. Moreover, the structural rearrangement of the surface is likely to happen. A detailed

description of the spherical NP model and its evolution is reported in **Chapter 2**, **Section 2.6.2** (Computational Details) and in **Chapter 4**, **Section 4.2**.

Concerning the size of TiO_2 NPs, their dimension can be tailored from hundreds down to 2 nm,[87,129] with the ones of 4-5 nm in diameter commonly investigated for practical applications.[1,132,135]

In fact, undercoordinated reactive sites are particularly important for NPs smaller than 20 nm since the fraction of surface atoms becomes comparable to that of bulk atoms. Therefore, small NPs (<10 nm) exhibit an enhanced reactivity.

1.3. TiO_2 functionalization

Surface functionalization of titanium dioxide nanoparticles or surfaces have attracted the scientific community over the last 50 years, due to the variety of photon energy conversion applications of this material, limited by the wide band gap, which triggers light absorption in the ultraviolet range (see **Section 1.2.1**, **Section 1.2.2**).

We already mentioned the most famous technology exploiting the surface modification of semiconductors with organic or metalorganic molecules, i.e. dye sensitized solar cells (DSSC). In DSSCs, originally developed by Grätzel et al. in 1991,[88] light harvesting dye molecules are adsorbed on a layer of sintered semiconductive nanoparticles, typically titanium dioxide (TiO_2) NPs. Photoexcited electrons are injected into the semiconductor CB, either directly or indirectly from the LUMO of the adsorbed dye (see **Chapter 5**), leaving the dye molecule in the oxidized state.

Surface modification of TiO_2 has also found application in nanomedicine. In particular, TiO_2 nanoparticles (NPs) are functionalized in order to build novel bioinorganic hybrid nanoconjugates (**Section 1.1.3**). These systems can be prepared by interfacing TiO_2 NPs to bioactive molecules (e.g., polymers, proteins, DNA fragments, drugs), by means of a linker with double functionalities. Once the surface of TiO_2 is modified, the hybrid systems could accomplish several biomedical tasks, including biocompatibility, site-specificity, multimodal imaging, and targeting of specific cells. On one hand, the surface modifiers could reduce the non-specific "dark" toxicity of pristine TiO_2 nanoparticles, [89–91] saturating the undercoordinated reactive sites on the surface by ligand molecules and, hence, minimizing the reactivity of the NPs with cellular proteins.[92] On the other hand, also in nanomedicine applications, surface modification is helpful to shrink the band gap, as anticipated in **Section 1.4.5**. To be used for light-responsive biomedical aims, the TiO_2-modified systems should match the therapeutic window of biological tissues (600-1000 nm). Hence, the systems could be suitable for applications *in vivo* for photodynamic therapy and light-controlled drug release.

In the following sections, we illustrate the state-of-the-art of the computational studies about TiO_2 modification, with some reference to experimental data, focusing in particular on functionalization by organic molecules.

1.3.1. State-of-the-art of the computational description of functionalized TiO_2

The binding of surface modifiers on TiO_2 surfaces is based on the high reactivity of the undercoordinated sites at the flat or curve surface of TiO_2, making the synthesis of such hybrid compounds quite trivial (see **Section 1.2.6.**). The majority of the theoretical investigations about surface modified TiO_2 are based on density functional theory (DFT), which is able to describe structural and electronic properties of medium size systems (~100 atoms) with a good balance between accuracy and computational cost.

Due to the importance of light conversion applications of functionalized TiO_2, there is a widespread interest in the optical properties of these systems. These excited state properties are not correctly predicted by standard DFT, which is a ground state theory. Therefore, theoretical studies on TiO_2 often rely on *time-dependent* DFT, which describes the response to an external stimulus (see **Chapter 2, Section 2.5.1**).

In order to study the reactivity at the TiO_2 surface, there are two main computational approaches. On one hand, it is possible to perform two dimensional periodic calculations on a slab model composed of few layers of the bulk material. Alternately, the anatase TiO_2 surfaces can be modeled by a cluster zero-dimensional structure, which could either simulate a flat surface or it could represent nanoparticles of different shapes.
Concerning the surfaces, the (101), followed by the (001), is the most investigated one, because it is the majority surface of the anatase crystal (**Section 1.2.5.1.**).

TiO_2 surfaces are typically photosensitized by metalorganic or organic dyes.
Between the formers, the ruthenium complexes are the most famous,[93,94,95,96,100] yielding solar-to-electric power conversion efficiencies of about 9−11%. Metal-free organic molecules could minimize the costs of production of these hybrid materials. These dyes are characterized by the presence of chromophore groups, such as C≡C, C=C, C=N, C=O, C=S, N=N, N=O, and they absorb light when they are in the isolated form or simply dissolved in solution. Some dyes having redox properties and visible light sensitivity can be used in solar cells as well as photocatalytic systems.[97,98,99]

Theoretical studies about these metalorganic and metal-free organic dyes usually exploit TDDFT, which is computationally expensive and requires massively parallelized quantum codes. Therefore, they are all quite recent.

The excitation of the hybrid systems of dye adsorbed on TiO_2, leads to a charge transfer from the molecules to the CB of the semiconductor, which is the reason for the observed tuning of the light absorption from the ultraviolet towards the visible range. Charge transfer at the

interface between anatase TiO_2 and several dye molecules, including Ru dyes, [96,100] $[Fe(CN)_6]^{4-}$, [101] and perylene[102] was extensively used by De Angelis and Co. by means of a big $(TiO_2)_{38}$ cluster. Zhao et al., instead, studied the adsorption of a metal-free C217 dye.[103] De Angelis et al. also managed to simulate the absorption spectrum of squaraine molecules adsorbed on the anatase TiO_2 surface through periodic model systems.[104,105,106]

Alternately to the mentioned photosensitizers, the surface sensitization could be carried out by molecules that do not absorb in the visible range when they are isolated, but are able to create charge-tranfer complexes if coupled with suitable semiconductors (see **Chapter 5**, **Section 5.1.3**).

The latter case is less studied, but these "transparent" organic molecules, usually benzene derivatives (such as catechol or carboxylic acids), are usually cheaper and would allow the large-scale production of TiO_2-based hybrid materials.

Moreover, bifunctional catechol-derivatives could be used as linkers providing an interesting and ductile bioconjugation approach (see **Section 1.1.3.1**)

1.3.2. Functionalization of TiO_2 with catechol derivatives

Adsorption of oxygen-rich ligands on the surface of TiO_2 was proven to repair undercoordinated Ti surface atoms.[80,107,108,127] Among organic molecules, catechol derivatives bind extremely strong to the TiO_2 surface and show a high stabilization through the bidentate anchoring.[107,108] These molecules can self-assemble on various inorganic and organic materials, including noble metals, metals, metal oxides, mica, silica, ceramics and even polymers.[109] Most of these molecules do not absorb visible light when they are isolated, but by coupling with TiO_2, they redshift the range of absorption of the bare material.

The functionalization of the anatase (101) TiO_2 surface with catechol, the archetype of 1,2-dihydroxybenzene ligands, was extensively studied both experimentally[110–117] and theoretically, with periodic surface and cluster models[118–123]. It was demonstrated that surface modification by catechol improves the absorption of the solar spectrum, refining the performances of the material in photoactivated devices.[124–127] Moreover, the mechanism of charge transfer between the catechol molecule and a small cluster of TiO_2 have been studied by means of TDDFT and compared to other the one exploited with other molecules with different amounts of π rings.[128]

In particular, Selloni & Co. studied the adsorption configurations on the anatase (101) TiO_2 periodic surface and the dynamics of a full monolayer of molecules, comparing DFT data to STM images.[110] They found out that catechol is adsorbed preferentially in a bidentate

configuration, in agreement with other quantum mechanical[114] and experimental studies,[112] and they unraveled the mechanism of self-assembling of the molecules along preferential directions.

Derivates of catechol, also known as "enediols", characterized by two hydroxyl groups in ortho position on the benzene ring and by the presence of an additional spare functionality, have been study experimentally mainly by Rajh & Co. as suitable linkers for the building of TiO_2-base nanoconjugates. [107,108,129,130–136] Due to the hybrid character of the modified NPs, light irradiation of these systems was found to enable excitation form the catechol-like ligand to the conduction band of TiO_2, moving the absorption towards the visible range (**Figure 1.11**).[107]

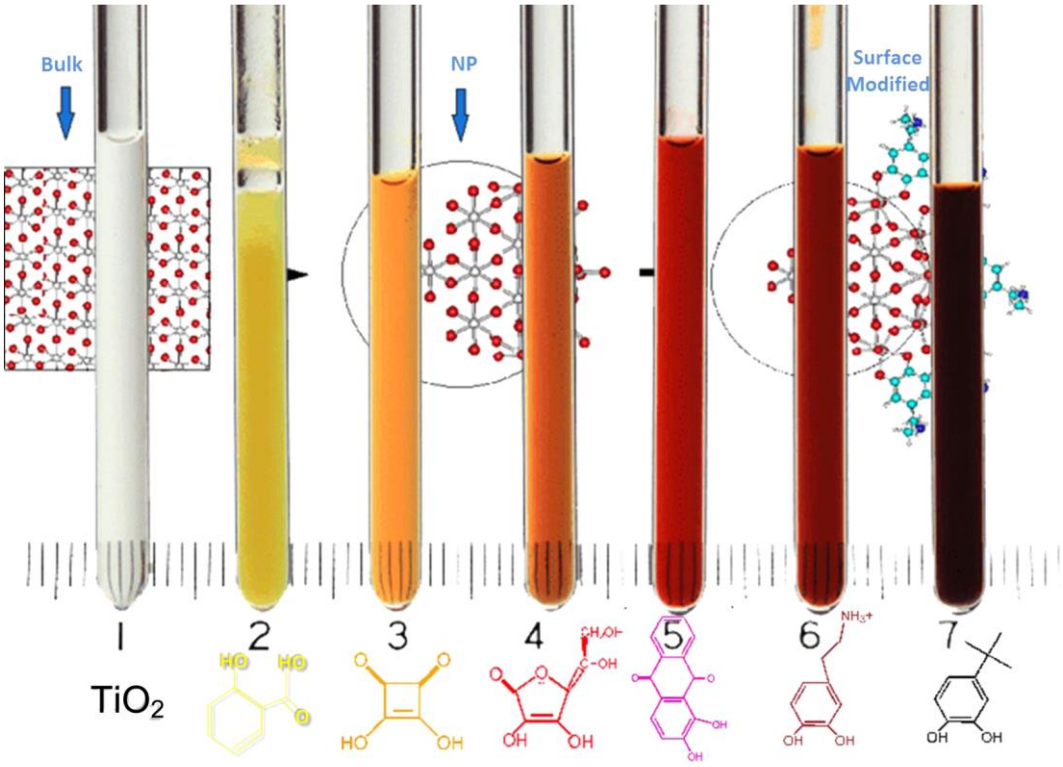

Figure 1.11 45 Å TiO_2 nanoparticles modified with different bidentate ligands: (1) bare TiO_2, (2) salicylic acid, (3) squaric acid, (4) ascorbic acid, (5) alizarin, (6) dopamine, and (7) tert-butyl catechol. Molecule structures of the ligands used for surface modification are shown below the corresponding tube. The binding of catechol-like ligands is enhanced because of the stability gained from adsorption-induced restructuring of the NP surface.[107]**Errore. Il segnalibro non è definito.**

Catechol-like ligands, like dopamine or dopac, used for surface modification also provide points of attachment for covalent linking of biologically active molecules through the spare functional groups of a surface modifying ligand. Binding of biological molecules through covalent bonding enables robust composites that can be used for targeted drug delivery or *in vivo* applications.[1]

1.3.3. Functionalization of TiO_2 with dopamine

In the variety of the catecholates, dopamine (DA) has been extensively studied as a possible functional linker in the building of nanoconjugates.[137-145] Dopamine (3,4-dihydroxyphenethylamine) is a molecule belonging to the catecholamine and phenethylamine families (**Figure 1.12**).

Dopamine (DA) is present in the human body where it performs several biological functions. First, DA is a neurotransmitter, playing a vital role in controlling our brain's functions associated with movement, emotion, pleasure and pain as well as drug addiction through specific receptors of G protein-coupled receptor family. Moreover, DA influences emotion and personality traits; thus, it has been proposed that personality traits and emotions may affect the risk of cancer development or growth by modulating dopamine release. In fact, dopamine is present at lower concentrations in tumor tissues than in benign tissues, and increasing dopamine levels via dopamine treatments seems to inhibit tumor cell proliferation. Moreover, Moreno-Smith et al. confirmed that dopamine reduces chronic stress-mediated angiogenesis and thus attenuates tumor growth.

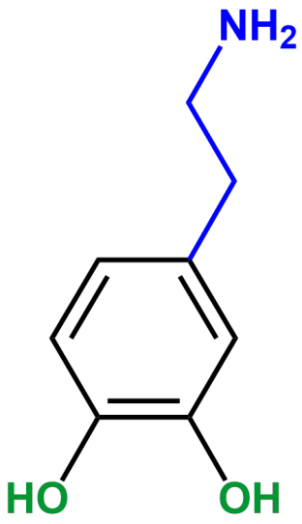

Figure 1.12 The structure of dopamine (4- (2-aminoethyl)benzene-1,2-diol), with the enediol group in red and the ethylamino in blue.

Dopamine exhibits a diolic group (two OH) in the catechol-like portion and one ethyl-amino functional group ($-CH_2CH_2NH_2$).

Since dopamine contains both the functional catechol group and amine group, it is a mimic of specialized mussel adhesive protein. Therefore, DA has become an important surface modifier, which can react with materials containing functional groups, such as thiol, amine and quinone, by the Michael addition or the Schiff base reaction to form covalently grafted functional layers, thereby further enhancing the interfacial adhesion.

These adhesive properties of dopamine could also be exploited at the aim of building bioinorganic nanohybrids.

1.3.3.1. Synthesis of dopamine functionalized TiO_2 nanoparticles

Dopamine functionalized TiO_2 nanoparticles are synthetized though a building block approach, in which the two components, i.e. the NP and the molecule, are firstly produced separately and connected in a second moment through the formation of covalent chemical bonds.

The several available methods for synthetizing TiO_2 NPs can be divided in two main groups: physical and chemical methods. In the former ones, small structures are producted from larger ones through a top-down approach, while chemical methods rely on a bottom-up approach, starting from molecular precursors. These methods are generally more precise and indicated to synthetize small structures (<100 nm).[62]

In particular, solution-phase approaches, i.e. hydrothermal or sol-gel synthesis, are best suited to obtain the finest control on the size and shape of the nanostructures. These methods usually employ organic or inorganic titanium precursors, such as titanium alcoxides[140] or halides ($TiCl_4$ and TiF_4),[141] which are hydrolyzed in contact with water, leading to the formation of $Ti(OH)_4$ and its subsequent condensation to give Ti-O-Ti chains. Usually, the condensation process is pH-dependent and, for enough concentrated solutions, it leads to the spontaneous nucleation and growth of the nanoparticles. However, small NPs (<50 nm) are not stable in solution. Hence, the use of surfactants or capping ligands, e.g. carboxylic acids, alcohols, phosphonic acids and amines, including dopamine,[142] is necessary to avoid agglomeration and it can be critical in determining the morphology of the final NP, since they can favor the growth with respect to others, as already mentioned in **Section 1.2.5**.

In order to functionalize the surface of TiO_2 nanoparticles by dopamine, a simple one-step method can be used. Usually, a dopamine solution, prepared by dissolving dopamine, is slowly added to TiO_2 NPs. The self-assembling of dopamine to TiO_2, for example in an ethanol solution, happens spontaneously under controlled pressure (**Figure 1.13**).[111]

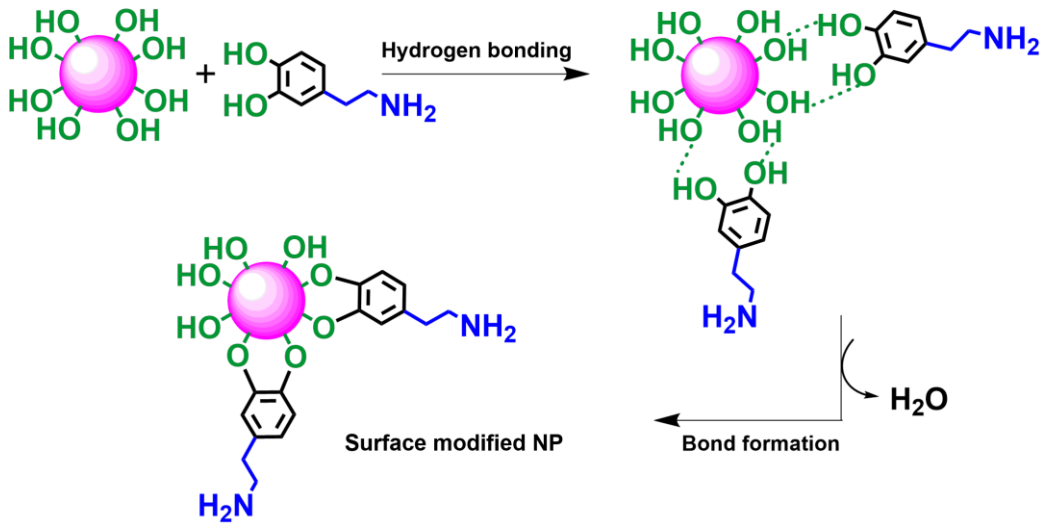

Figure 1.13 Schematic illustration for the preparation process of dopamine functionalize TiO_2 nanoparticles in ethanol solution.

The remaining ethyl-amino functionality could be used for binding further molecules, forming for example covalent bonds by reacting, with the carboxylic functional group of an oligonucleotide of DNA (amide bond) [87,107,129,] or through weak interactions, like hydrogen bonds, with anticancer drugs as doxorubicin (DOX).[143]

1.3.3.2. Dopamine as a linker for bioconjugates

In the frame of the synthesis of bionanoconjugates, the diolic group of the molecule can be used for surface anchoring and the ethyl-amino group for the bioactive molecule tethering. Moreover, this molecule has been shown to facilitate the charge transfer between the inorganic and biological component.[144]

Dopamine-modified TiO_2 NPs were used to detect and repair DNA mutations or to activate specific oxidation processes, in analogy to endonucleases activity.[107] Rajh and coworkers also developed a method to control charge transfer from DNA to TiO_2/dopamine, exploiting the sequence dependent charge separation.[137] Similarly-built systems were used to specifically bind proteins, altering cell metabolism and inducing cell death. [135,137,139] Moreover, Thurn et al. synthetized TiO_2/dopamine/DNA nanoconjugates to be used as gene knockout devices and tumor imaging agents at the same time.[145] Dopamine functionalized TiO_2 NPs can also bind proteins or peptides to build up electrochemical biosensors, relevant for drug discovery, diagnostics, environmental applications, as well as for food safety.[146,147] More simply, dopamine is also bound to TiO_2 nanostructures in order to improve the dispersion of nanoparticles.[148]

Differently from catechol, very little is known about dopamine adsorption on the anatase (101) TiO_2 surface, especially regarding the possible configurations. Most of the works assume that dopamine adsorbs on the TiO_2 surface in a bidentate configuration similar to catechol,[149] while the possible role of the ethyl-amino functionality in the binding to the surface is not investigated.[150,151,152] The adsorption of one single molecule of dopamine was studied theoretically by Vega-Arrojo et al. with a TiO_2 cluster model, who stated that the bidissociated bidentate adsorption mode is favored with respect to the monodentate or molecular ones.[150,151] Urdaneta et al. investigated the adsorption of dopamine in a low coverage regime, by considering uniquely a bidentate configuration on different low index anatase surfaces.[152]

Moving to the excited state properties, theoretical works are completely lacking. To our knowledge, there are not TDDFT studies about the optical properties of dopamine adsorbed on any TiO_2 surface or cluster, but the experimental spectrum of the molecule on commercial nanoparticles have been recorded and a redshift of light absorption with respect to the bare material is observed. [153,154]

1.4. Outline of the thesis

Within the context given in this introduction, in this work of thesis, we study ground state and excited state properties of dopamine-functionalized flat and curved TiO_2 surfaces by means of quantum mechanics calculations. We used both a periodic and finite models. On the one hand, the flat anatase (101) periodic surface is a reliable model to represent faceted nanoparticles.On the other hand, a spherical nanoparticle (NP) model is required to properly describe the reactivity at the more complex curved surface. We employ a realistic NP having a diameter of 2.2 nm, previously developed in our research group. [83]

We tackle geometrical and electronic properties through simulations based on hybrid density functional theory (DFT), which is able to describe the electronic structure of the ground state of the system. In addition, we use self-consistent charge density-functional tight-binding (SCC-DFTB), an approximate DFT method, which sets between DFT and molecular mechanics methodologies in terms of applicability and predictivity, allowing for accurate calculations of thousands atoms and molecular dynamics simulations in the order of hundreds of picoseconds. The optical properties of the functionalized TiO_2 systems, instead, are treated by means of time-dependent DFT (TDDFT).

The combined use of these three different approaches provides an all-around description of realistic dopamine-TiO_2 systems.

Given the large size of these systems, massively parallelized codes are required in order to keep the computational time acceptable. An overview of the theoretical methods and codes used in this work of thesis is given in **Chapter 2**.

In **Chapter 3**, I will present the first part of this work, devoted to the adsorption of dopamine on the flat anatase TiO_2 (101) surface, which is a model for faceted nanoparticles. We analyze different coverages investigating the process of self-assembling both under kinetic and thermodynamic conditions. Preliminarily, we show results for the adsorption of catechol molecule on the anatase (101) TiO_2 surface, which is the skeleton of dopamine without the additional functional group and allows, therefore, to focus only on the anchoring by the two hydroxyl groups. For the dopamine molecule, the additional ethyl-amino functional group plays a crucial role, interacting with the surface at low coverage, and ruling the organization of the self-assembled monolayer at high coverage.

In **Chapter 4**, we present the results for one or more dopamine molecules adsorbed to a more complex and realistic model for TiO_2, i.e. the curved surface of a spherical nanoparticle. In this second part, we studied firstly the different possible configurations at low coverage, both by DFT and DFTB calculations. For the most stable low coverage configuration of dopamine,

we investigated the effect of light irradiation of the system. We used the method developed by Di Valentin and Selloni[48] to investigate the destiny of the formed charge carriers, considering the formation of an exciton, the eventual recombination and separation of the hole and the electron on different atoms. Then, we built a high coverage model gradually adsorbing dopamine molecules respecting the symmetry of the spherical nanoparticle model and finally heating it through molecular dynamics DFTB in order to reach the global minimum structure. We used the high coverage model and the intermediate coverages to clarify the relation between the number of adsorbed molecules and the adsorption energy per molecule. Through the same model, we also investigated the effect of the coverage on the electronic structure of the system. At this aim, we developed a hybrid DFT/DFTB method, which allowed us to reproduce the delicate structure of the semiconducting oxide at a reasonable computational cost.

Finally, in **Chapter 5** we describe the optical properties of dopamine adsorbed on the flat anatase (101) TiO_2 surface, obtained through real-time TDDFT. We compare the optical spectra of a dopamine molecule in vacuum and of bulk TiO_2 anatase with experimental and computational data available in literature,[2,3] and then we analyze the electronic absorption spectrum for different geometrical configurations of dopamine adsorbed on anatase TiO_2 (101) surface at low and full coverage regimes, assessing the charge transfer between the molecule and the semiconductor with constant reference to the DFT electronic structure.

2 Theoretical Background

In this Chapter, we provide the theoretical background of the approaches used for the modeling and the description of the properties of dopamine adsorption on flat and curved surfaces of TiO_2. A detailed review of the approximated methods used throughout this work is essential to understand which information is left behind and to assess the validity of the results.

Throughout this work we performed both calculations on a periodic surface model and on a finite large nanosystem. The first-principles modeling of semiconducting oxides is a complex and computationally demanding task, especially when complex systems with many degrees of freedom, such as realistic nanoparticles, and the interaction with light are involved. The main issue is that it is not possible to obtain a highly accurate description, without paying a huge computational price. Indeed, inexpensive molecular mechanics approaches cannot provide any information on the electronic structure and the excited states, which are fundamental for the study of a photocatalitically active material, such as titanium dioxide.
In order to achieve a good compromise between accuracy and computational effort, it is necessary to apply smart approaches, i.e. efficient approximations of the fundamental equations of quantum physics.

In the next sections, we are going first to give an introduction of the fundamental tools in quantum chemistry used in this work (**Section 2.1.**). After a brief recall of the main features of the Hartree-Fock theory (**Section 2.2.**), we discuss the principles of the three theories employed in this computational study: we review the main ideas at the basis of density functional theory (DFT) (**Section 2.3.**), then we sum up the approximation within the density functional tight-binding method (DFTB) (**Section 2.4.**) and we review the fundamental theories and concepts behind time-dependent density functional theory (TDDFT), i.e. the extension of DFT to excited states (**Section 2.5.**) . Finally, we present the two atomic models of TiO_2 utilized in this work of thesis (**Section 2.6.**).

2.1. Fundaments of Quantum Mechanics

In the following section, we assess the Bloch functions used for the calculation of periodic systems (**Section 2.1.2.**). We also give an overview of both the localized Gaussian Type Orbital basis set (**Section 2.1.3.**) and the plane waves method (**Section 2.1.4.**)

2.1.1. Periodic Systems

A solid state systems is subjected to an electrostatic periodic potential due to the nuclei, which has the same periodicity of the direct crystal lattice. The Hamiltonian operator of the electrons in a periodic potential is periodic itself, since it has to obey to the periodicity of the lattice:

$$V(\boldsymbol{r} + N_j \boldsymbol{a_j}) = V(\boldsymbol{r}) \; with \; j = 1,2,3 \tag{2.1}$$

where a_j are the direct lattice vectors defining the unit cell ($\boldsymbol{R} = n_1\boldsymbol{a_1} + n_2\boldsymbol{a_2} + n_3\boldsymbol{a_3}$).

Given the lattice vectors in the direct space, the corresponding *reciprocal lattice vectors* in the reciprocal space, $\boldsymbol{b_1}$, $\boldsymbol{b_2}$, and $\boldsymbol{b_3}$, are obtained by applying the orthonormality condition, $\boldsymbol{a_j b_j} = 2\pi\delta_{ij}$, where δ_{ij} is the Kronecker delta. The equivalent of the unit cell in the reciprocal space is the (first) *Brillouin zone*.

The mono-electronic wave-functions, at the basis of the Kohn-Sham approach, have to respect the Bloch theorem, which states that the solutions to the mono-electron Schrödinger equation can be written as a modulated plane wave, called *Bloch functions*:

$$\psi_k(\boldsymbol{r_i}) = u_k(\boldsymbol{r_i}) e^{i\boldsymbol{k}\boldsymbol{r}} \tag{2.2}$$

where $\boldsymbol{k}$ is the reciprocal space vectror, corresponding to the direct space vector $\boldsymbol{r}$, and $u_k(\boldsymbol{r}) = u_k(\boldsymbol{r} + \boldsymbol{R})$ is the *modulation function* with the same periodicity of the direct lattice.

The Bloch orbitals can be expanded either into atom-centered Gaussian basis functions (χ^{GTO}), see **Section 2.1.2.**, or, more commonly, into a basis set of plane wave functions (χ^{PW}), see **Section 2.1.3**.

The electronic structure problem has been simplified, because now we need to consider only the electrons within the unit cell. However, the eingenvalue problem (see **Section 2.2.1**) will now also depend on the $\boldsymbol{k}$ vector within the first Brillouin zone (BZ):

$$\boldsymbol{F^k C^k} = \boldsymbol{S^k C^k} \epsilon^{\boldsymbol{k}} \tag{2.3}$$

where $\boldsymbol{S^k}$ is the overlap operator between wave functions and $\boldsymbol{F^k}$ are the elements of the Fock matrix, gathering the elements of the HF equations (see **Section 2.2**, equation (2.8)).

The resulting eigenfuntions are continuous functions of $\boldsymbol{k}$, varying in a range of energy called *bands*. The total energy of the system is given by the integration of the occupied bands, i.e. the bands below the Fermi level (E_F), over all the $\boldsymbol{k}$ space. Nevertheless, for non metallic systems, the integration can be done numerically with few $\boldsymbol{k}$ points. Moreover, when the unit cell of the system is large enough (thus the BZ is small), the total energy can be already converged at the origin of the $\boldsymbol{k}$ -space (i.e. the Γ point). For the periodic calculations in this work, the Brillouin zone has been sampled using a uniform grid of $\boldsymbol{k}$ points, generated via the Monkhorst-Pack algorithm.[155]

2.1.2. Gaussian Type Orbitals

For convenience, the one-electron wavefunctions ϕ_i can be expanded in a *linear combination* of functions $\{\chi_i\}$, called basis set functions, whose analytical form is known. In the computational practice, the summation is truncated to a certain number M of basis function:

$$\phi_i(\boldsymbol{r}) = \sum_{v=1}^{M} c_{iv}\,\chi_i(\boldsymbol{r}) \tag{2.4}$$

The number M must be at least equal to the number of electrons N. Adding new functions to the basis set increases the quality of the ϕ_i and lowers the total energy, due to the variational principle, until the complete basis set limit ($M \longrightarrow \infty$), also known as the Hartree-Fock limit, is reached. In practical calculations, the number M is determined as a balance between accuracy and computational cost.

The choice of the basis function depends on the physics of the problem and on the computational convenience. The natural choice for the functional form could seem to be the exponential one (*Slater Type Orbitals*, STOs), since it correctly describes both the behavior for $r = 0$ and the decay at large distances. However, Gaussian functions (*Gaussian Type Orbitals*, GTOs) are much easier for calculating multi-center integrals, which have to be solved self-consistently to get the solution of the many-electron problem, resulting in an overall computational efficiency higher than with STO. The radial part of a GTO is defined as:

$$\chi_n^{GTO} = r^{2(n-1)} exp(-\alpha r^2) \tag{2.5}$$

where α controls how compact (large α) or diffuse (small α) is the basis function.

In order to better reproduce the correct behavior of the wavefunction, a contracted Gaussian function, composed by a linear combination of k GTOs:

$$\chi_n = \sum_k a_n\,\chi_k^{GTO} \tag{2.6}$$

Since the atomic behavior is mostly determined by valence electrons, split-valence basis sets are generally employed, where the core orbitals are described by only one contracted Gaussian function and the valence shell is instead represented by two or more set of contracted GTOs. A split-valence basis set is indicated with the string N-KLG, where N are the GTOs used to describe each atomic orbital of the core, then the valence part is represented by two functions, one contracted and one diffused one, composed of K and L GTOs, respectively. Moreover, polarized functions (symbolized by a *), i.e. orbitals characterized by a higher momentum, and diffused functions (symbolized by a +), with small α exponents in

$$\chi_n^{GTO} = r^{2(n-1)} exp(-\alpha\ r2) \tag{2.5}$$

, may be added to the basis set to improve its quality.

2.1.3. Plane waves pseudopotentials

Alternatively to the already discussed localized basis set (**Section 2.1.2**), it is possible to use a plane wave basis set to represent the orbitals, and pseudopotentials to represent the nuclei and core electrons. The periodic function $u_k(\boldsymbol{r_i})$ in equation (2.2), can be expanded in a set of basis functions constituted by plane waves.

$$\chi_{\boldsymbol{k}}^{PW}(\boldsymbol{r_i}) = e^{i\boldsymbol{kr}} \tag{2.7}$$

where $\boldsymbol{k}$ is the crystal wavevector. The wavevector can be thought as frequency factor, where high $\boldsymbol{k}$ values indicate a fast oscillation of the wave.

Planewaves constitue an orthonormal and complete basis set and they are solution of the free electron Schrödinger equation.

The use of plane waves presents several advantages with respect to localized basis sets, e.g. the number of the basis functions depends uniquely on the volume of the cell and on the "cut-off" on the kinetic energy, which is defined by a certain value of $\boldsymbol{k_{max}}$.

Moreover, these basis functions do not contain any parameter that needs to be optimized and they are not biased to any particular atom, avoiding this way the basis set superposition error, affecting the localized basis set calculations. On the other hand, several plane waves are needed to describe the wavefunction near the atomic nuclei due to its high oscillation frequency. This means that a high "cut-off" value has to be used in order to represent the wavefunction near the core, which requires a high computational effort.

To overcome this issue, it is a widespread practice to use a pseudopotential, which allows the description of the valence wave functions closer to the core of the atom, so that the calculated functions will match the real wave functions after a certain cut-off radius (**Figure 2.1**).

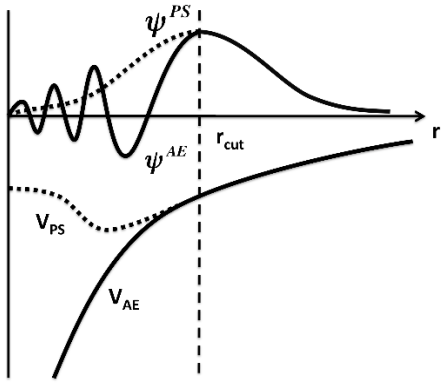

Figure 2.1 Comparison between the all-electron (AE) wavefunction in the Coulomb potential of the nuclei (ψ^{AE}) and the wavefunction in the pseudopotential (ψ^{PS}). The function and the real potential are equals over a certain value of r_{cut}.[156]

Some of the calculation of this work (see **Chapter 5**), have been carried out with the Octopus code, which is a real-space pseudopotentials-based code.[157] The calculations have been performed by a set of norm-conserving[158] Vanderbilt PBE pseudopotentials, the sg15 set.[159] Within this approximation, the charge density of the all-electron core is reproduced within the cut-off radius, which tends to be relatively short. The cut-off radius used for this work is 60 Ry.

2.2. Main features of Hartree-Fock

In the following section, we draft the main features of the Hartree-Fock approximation for the solution of the *time-independent* Schrödinger equation (**Section 2.1.1.**), focusing both on its goals and on its limits.

2.2.1. The Hartree-Fock Approximation

According to the *Hartree-Fock* (HF) approximation (*mono-determinant*), it is possible to approximate the many-electron wavefunction of the *time-independent* Schrödinger equation for an electrostatic non-relativistic many-electron system through the product of N one-electron wavefunctions, called *spin-orbitals*. The product is expressed in the form of a *Slater determinant*, so that the antisymmetry is respected. Therefore, the ground state of a system is described by means of only one electronic configuration, built starting from the n spin-orbitals with the lowest energy according to the *variational principle*.

The spin orbitals $\{\phi_u\}$ into the Slater determinant are varied until the minimum is reached and orthonormality constraints must be satisfied during the minimization, introducing the *Lagrangian multipliers* ε_u in the resulting equation, which are known as *Hartree-Fock (HF) equations*:

$$\hat{\boldsymbol{f}}\phi_u = \varepsilon_u\phi_u \text{ with } \hat{f} = \boldsymbol{h}(i) + \sum_v [2\boldsymbol{J}_v(i) - \boldsymbol{K}_v(i)] \tag{2.8}$$

In the N eigenvalue equations, the Lagangian multipliers ε_u and ϕ_u are the eigenvalues and eigenfunctions of the Fock operator $\hat{\boldsymbol{f}}$, respectively. The two operators $\boldsymbol{J}_v(i)$ and $\boldsymbol{K}_v(i)$, defined in equations (2.11) and (2.12) in the following, are the contributes to the potential energy of the i-th electron due to the interaction with the other (2n-1) electrons. The solution to the HF equations has to be found iteratively through *self-consistent field* (SCF) procedure: starting from a "guess" of the orbitals, the HF equations are solved obtaining a new set of orbitals; this set is used to define a new HF potential in the next iteration. The cycle is repeated until convergence, i.e. the energy and/or the spin-orbitals no longer change up to a defined threshold.

2.2.1.1. Hartree-Fock energy

The one-electron energy is given by:

$$\varepsilon_u = h_{uu} + \sum_{v=}^{n} (2J_{uv} - K_{uv}) \tag{2.9}$$

In particular,

$$h_{uu} = \int \phi_u^*(i) \left[-\frac{1}{2} \sum_i \nabla_i^2 - \sum_A \frac{Z_A}{r_{Ai}} \right] \phi_u(i) \tag{2.10}$$

is the mono-electronic *core* integral, including the kinetic energy of the core electrons, $-\frac{1}{2}\sum_i \nabla_i^2$, and the core potential nuclei-electron, $-\sum_A \frac{Z_A}{r_{Ai}}$.

$$J_{uv} = \int \int \phi_u^*(i) \phi_v^*(j) \frac{1}{r_{ij}} \phi_u(i) \phi_v(j) d\tau_i d\tau_j \tag{2.11}$$

is the bielectronic *Coulomb* integral, and

$$K_{uv} = \int \int \phi_u^*(i) \phi_v^*(j) \frac{1}{r_{ij}} \phi_v(i) \phi_u(j) d\tau_i d\tau_j \tag{2.12}$$

is the *exchange* integral.

These two last bi-electronic integrals embody the electronic interaction energy.

The fact that the Coulomb J_{uv} and the exchange K_{uv} contributions have the same expression, leads to an advantage in avoiding spurious effects, as we explain in the following.

Let us fix the index u, running on all the occupied orbitals, and let's consider the interaction of one of the two electrons in the orbital ϕ_u with the remaining $2n-1$ electrons. In a closed-shell system, the v index runs on all the doubly occupied orbitals.

For every value of $v \neq u$, the interaction energy between an electron in v_u and the two electrons in ϕ_v is:

$$\begin{aligned} 2J_{uv} - K_{uv} = 2 \left\langle \phi_u(i)\phi_v(j) \middle| \frac{1}{r_{ij}} \middle| \phi_u(i)\phi_v(j) \right\rangle \\ - \left\langle \phi_u(i)\phi_v(j) \middle| \frac{1}{r_{ij}} \middle| \phi_v(i)\phi_u(j) \right\rangle \end{aligned} \tag{2.13}$$

where the second term is the exchange term, generated by the antisymmetric nature of the wavefunction, appearing only once because the electron in v_u is in agreement with the spin of only one of the two electrons in v_v. It is evident how, for $v = u$, the integral K_{uu} becomes formally equal to J_{uu} and the expression of the electronic energy $2J_{uv} - K_{uv}$ is reduced to J_{uu}. This means that in the HF approximation there is no spurious interaction of the electron with itself. This exact HF exchange, is one of the most advantageous features of this wavefunction-based approximation, as will be better discuss in **Section 2.3**.

2.2.1.2. Electronic correlation in Hartree-Fock

The Hartree-Fock approximation is affected by two kind of errors. On the one hand, the accuracy of the self-consistent calculation is limited by the truncated basis used to describe the

orbitals (see **Section 2.1.3**). On the other hand, the correlation of the motion of the electrons, i.e. the *electronic correlation*, is not included in this approximation. This second error is intrinsic in the HF model, where the electrons are considered as independent particles. More precisely, the HF approximation accounts for the electronic correlation due to electrons having the same spin, while it does not include the effect of repulsion existing between the electrons independently from the spin, making the probability of finding one electron in a certain position lower if there are other electrons in the neighborhoods (*dynamic correlation*). Moreover, the mono-determinant approximation leads to another kind of mistake, due to the fact that there are some situations, e.g. the wavefunction of an *open-shell* system, which cannot be approximated through a unique electronic configuration (*static correlation*). Neglecting the electronic correlation has different consequences, for example in the calculation of the dissociation energy, of the excited states, of the dispersion forces, etc.[160]

The so-called post-HF methods aim to correct the correlation error either through a multi-determinant representation of the wavefunction (CI, CISD, CCSD, …) or through a perturbation of the wavefunction at the *n* order (MP2,MP3,…). Another method, recovering someway the electronic correlation, is Density Functional Theory, DFT (**Section 2.3**).

2.3. Density Functional Theory

The main issue of the HF approximation for a many-electron system is the dependence of the wavefunction ψ on 4N variable (three spatial and one spin coordinate for each of the N electrons). Thus, any wavefunction approach would be unmanageable for large quantum systems, such as the TiO_2 surfaces and nanoparticles under study in this PhD work.

Density functional theory is an approximation based on the electron density $\rho(\boldsymbol{r})$ of the many-electron system rather than the hard-to-compute wavefunction. The electron density is a non-negative function defined as the probability of finding an electron in the region of space $d\boldsymbol{r}$:

$$\rho(\boldsymbol{r}) = N \int \psi^* \psi ds_1 d\boldsymbol{x}_2 \dots d\boldsymbol{x}_N \tag{2.14}$$

This quantity is dependent only on the three spatial coordinates and on the spin. Differently from ψ, it is also a physical observable, measurable through X-ray diffraction.[161]

In the following, we summarize the Hohenberg-Kohn (**Section 2.3.1.**) and Kohn-Sham (**Section 2.3.2.**) theorems. Then, we give an overview of the exchange correlation functionals (**Section 2.2.3.**), focusing on hybrid functionals (**Section 2.3.4.**). Finally, we assess the problem of calculating electronic properties (**Section 2.3.5.**) and excited states (**Section 2.3.6.**), which are considered not accessible by standard-DFT.

2.3.1. The Hohenberg-Kohn theorems

Density functional theory (DFT) has been developed in 1964 by P. Hohenberg and W. Kohn at the aim of calculating the properties of many-electron systems. Given the two following theorems, all the properties of a many-electron system depend uniquely on its ground state electron density $\rho(\boldsymbol{r})$.[162]

Theorem 1 *The external potential (and hence the total energy) of a system is univocally determined, within a trivial additive constant, by the ground state electron density* $\rho(\boldsymbol{r})$.

The proof of the first Hohenberg-Kohn Theorem is based on the variational theorem, which states that the expectation value of the Hamiltonian operator from any well-behaved trial function ψ_{trial} will be an upper bound to the true energy of the ground state E_0. Therefore, the ground state of the system can be expressed as a *functional* of the ground state electron density.

$$E_0[\rho] = F[\rho] + \int d\boldsymbol{r} v(\boldsymbol{r}) \rho(\boldsymbol{r}) \tag{2.15}$$

where $F[\rho]$ is the *universal* functional, whose analytical expression is unknown but whose existence has been proven.[160]

Theorem 2 *Considering the relation* $\rho(\boldsymbol{r})_1 \Leftrightarrow v_1$ *from the first HK theorem, and assuming that there is a* $\rho(\boldsymbol{r})_2$*, such that* $\rho(\boldsymbol{r})_2 \geq 0 \; \forall \; \boldsymbol{r}$*, then:* $E_{v1} \leq E_{v2}$.

The second Hohenberg-Kohn Theorem has been proved again through the variational theorem, originally for non-degenerate ground states and later more generally.

To sum up, we can declare that the ground state energy of a many-electron system corresponds to the minimum value of $E[\rho]$ for all the possible electron density. However, this is true only when the exact universal F functional is used. In the common practice, the density functional is approximated, hence, DFT may not always be supported by the variational principle.

2.3.2. The Kohn-Sham equations

The main idea of Kohn and Sham is that the energy of a many-electron system can be expressed as the sum of the following contributes:

$$\mathrm{E}[\rho(\boldsymbol{r})] = T_s[\rho(\boldsymbol{r})] + E_H[\rho(\boldsymbol{r})] + E_{Ne} + E_{xc}[\rho(r)] \tag{2.16}$$

where $T_s[\rho(\boldsymbol{r})]$ is the kinetic energy of an non-interacting electron gas, $E_H[\boldsymbol{\rho}(r)]$ is Hartree energy, E_{Ne} is the potential energy describing the interaction between nuclei and electron, $E_{xc}[\rho(\boldsymbol{r})]$ is the exchange-correlation energy, which is the critical point for DFT calculations. Indeed, this last term must include not only the contribution of the exchange energy, E_x, and that of the correlation energy, E_c, but also the corrections the non-interacting in kinetic term and the self-interaction energy, which is the spurious interaction of each electron with itself in the $\boldsymbol{E_H}$ term. It is important to highlight how, differently from the HF theory, DFT is able to include the electronic correlation at a low computational cost.

Nevertheless, the exact analytic expression of $E_{xc}[\rho(\boldsymbol{r})]$ is unknown, which means that the introduced corrections are not exact. Therefore, in order to obtain the electron density of the ground state of the system, it is necessary to find a method to implement the variational principle. The formalism, developed by Kohn and Sham, is similar to the HF one for the solution of the many-electron problem. The system is considered as a set of non-interacting electrons moving in an effective potential, $V_{eff}(\boldsymbol{r})$, which is equal to the one of the real system. Since we considered the electrons as N non-interacting particles, we are able to describe them through a Slater determinant of one-electron eigenfunctions with the following expression:

$$-\frac{1}{2}\nabla^2\phi_{u,KS}(r) + V_{eff}(r)\phi_{u,KS}(r) = \varepsilon_u\phi_{u,KS}(r) \quad (2.17)$$

The eigenfunctions, $\phi_{u,KS}$, derived from the *N* equations are known as Kohn-Sham (KS) orbitals and they are connected to the electronic density, the core of DFT, through the following relation:

$$\rho(r) = \sum_{u=1}^{occ}\left|\phi_{u,KS}(r)\right|^2 \quad (2.18)$$

The term $V_{eff}(r)$ in (2.17), contains the coulombic interactions and the exchange correlation potential $V_{xc}(r)$:

$$V_{eff}(r) = -\sum_R \frac{Ze^2}{|r-R|} + \int dr' \frac{\rho(r')}{|r-r'|} + V_{xc}(r) \quad (2.19)$$

where Z is the nuclei charge, while **R** is the nuclei position.

The operator V_{xc}, contained in (2.19), depends on the employed DFT method and it is expressed as the functional derivative of $E_{xc}[\rho(r)]$ with respect to $\rho(r)$.

$$V_{xc}[\rho](r) = \frac{\delta E_{xc}[\rho(r)]}{\delta\rho(r)} \quad (2.20)$$

According to this definition, this effective potential V_{xc} is a function of the KS orbitals which we want to compute. Hence, this problem needs to be solved in a self-consistent way: starting from a trial electron density, it is possible to build the V_{eff} potential and to solve the *N* equations for occupied orbitals, obtaining *N* eigenfuntions, ϕ_i , which represent the new electron density. Then, through an iterative procedure, the eigenfunctions are cyclically calculated, till the variation of the ϕ_i (or of the energy, potential, forces…) is below a predefined threshold. Finally, the electron density, $\rho(r)$, is obtained from relation (2.18) and, consequently, the total energy and all the observable properties of the system.

As a concluding remark, it is important to mention that the KS eigenfunctions ϕ_i and the eigenvalues ε_i do not have a real physical meaning strictly speaking, since they are just mathematical devices used for the solution of the problem. Nevertheless, because of their similarity with the HF eigenfunctions and eigenvalues, they are often considered as mono-electronic orbitals and their related energies.

2.3.3. Exchange correlation functional

If the expression of $v_{xc}[\rho(\boldsymbol{r})]$ was known, the total energy calculated through a DFT method would match the exact (non-relativistic) energy of the system. On the other hand, the application of approximated functionals inevitably errors in the evaluation of the exchange-correlation energy and it could lead to an improper description of the self-interaction.

One of the first ideas to approximate $E_{xc}[\rho]$ is the *Local Density Approximation* (LDA), according to which $E_{xc}[\rho]$ depends uniquely on the local value of the electron density $\rho(\boldsymbol{r})$ in every point of the space.

$$\boldsymbol{E_{xc}^{LDA}} = \int \boldsymbol{\rho}(\boldsymbol{r}) \boldsymbol{e_{xc}^{HEG}}(\boldsymbol{\rho}(\boldsymbol{r}))\boldsymbol{dr} \tag{2.21}$$

where $\boldsymbol{e_{xc}^{HEG}}$ is the exchange-correlation energy of the homogenous electron gas (HEG). Thus, the quantity can be further divided into the individual contributions:

$$e_{xc}^{HEG}(\rho(\boldsymbol{r})) = e_{xc}^{HEG}(\rho(\boldsymbol{r})) + e_{xc}^{HEG}(\rho(\boldsymbol{r})) \tag{2.22}$$

The explicit form of $e_{xc}^{HEG}$for the homogeneous electron gas can be derived from the Hartree-Fock exchange.[163] No analytical form of the correlation part $e_{xc}^{HEG}$is known, but highly accurate expressions based on parametrization of quantum Monte-Carlo calculations are available,[164] as the one used by Vosko, Wilk and Nusair (VWN).[164,165]

This approximation derives from the uniform electron gas, i.e. a system of N electrons in a positive background of charge. Therefore, it is particularly suitable for metallic systems or for solids, but it does not work well for molecular systems, where the electron density is localized mainly on the atoms, having the clear tendency to overbind molecules (by ~ 1 eV). [166,167]

As a next step, it is possible to consider the value of the grandient $\nabla\rho(\boldsymbol{r})$ in every point, in addition to a $\rho(\boldsymbol{r})$, through the *generalized gradient approximation* (GGA).

$$\boldsymbol{E_{xc}^{GGA}} = \int \boldsymbol{f}(\boldsymbol{\rho}(\boldsymbol{r}), \boldsymbol{\nabla}(\boldsymbol{\rho}(\boldsymbol{r})))\boldsymbol{dr} \tag{2.23}$$

Thanks to the contribution of the gradient, the functional would better account for the inhomogeneity of the real electron density. Similarly to LDA, E_{xc}^{GGA} is generally split into two contributions, E_x^{GGA} and E_c^{GGA}. Prominent implementations are the Perdew, Burke and Ernzerhof (PBE) functional, [168] for both the exchange and correlation parts, and the widely used, Yang and Parr (LYP) correlation functional,[169] which is not based on the correlation energy of the electron gas, but on the exact one of the helium atom. The GGA functionals are largely employed in computational chemistry and material science for solids, since errors on the energies are usually lower than 0.3 eV, which is close to the chemical accuracy.[166,167]

2.3.4. Hybrid functionals

Both the LDA and the GGA functionals lead to satisfying results, until the electron density is homogeneous enough. When we move to systems in which the electrons are more localized, these approximations are not adequate anymore, since the electronic correlation becomes more important and the self-interaction error (of the electron density with itself) produces poorly accurate results. For the description of these systems, such as molecules or solids with d states, which have strongly irregular electron densities, *hybrid density functionals* are preferred.

According to the Hartree-Fock theory, the exchange energy can be computed exactly and when $i = j$ (the index identifies the same electron), the Coulomb integrals are equal to the exchange ones, solving completely the self-interaction issue. In order to exploit these features of HF, hybrid functionals replace a fraction of the GGA exchange with the HF exact exchange. The exchange-correlation functional is expressed as follows:

$$\boldsymbol{E_{xc}^{hyb} = E_{xc}^{GGA} + \lambda(E_x^{HF} - E_x^{GGA})} \tag{2.24}$$

where λ is the fraction of HF exchange calculated using the HF exchange operator and the KS orbitals $\{\phi_u\}$.

$$E_x^{HF} = -\frac{1}{2}\sum_{i,j,\sigma}^{occ}\int dr \int dr' \frac{\psi_{u\sigma}^*(r)\psi_{uj}^*(r')\psi_{u\sigma}^*(r')\psi_{uj}^*(r)}{|\boldsymbol{r} - \boldsymbol{r}'|} \tag{2.25}$$

The introduction of a portion of exact exchange λ improves the overall description of the exchange-correlation energy and the accuracy of the method.[166,167,160]

Moreover, it partially corrects the self-interaction error, giving more accurate results for band gaps and electron localization/delocalization. The most popular hybrid functional is B3LYP,[169,170] whose functional form is the following:

$$\boldsymbol{E_x^{B3LYP} = (1-\alpha)E_x^{LDA} + \alpha E_x^{HF} + b\Delta E_x^{B88} + (1-c)E_c^{LDA} + cE_c^{LYP}} \tag{2.26}$$

The exchange-correlation functional E_{xc} is composed of three exchange functionals E_x and two correlation functionals E_c. The three E_x are: an LDA exchange functional ($E_x^{LDA}[\rho(\boldsymbol{r})]$, a GGA exchange functional ($\Delta E_x^{B88}[\rho(\boldsymbol{r})]$) and the exact Hartree-Fock exchange ($E_x^{HF}[\{\phi_u\}]$), which depends on the KS orbitals and it is, therefore, the heaviest term to compute.

The energetic contribution related to the electron correlation is described by an LDA functional ($E_c^{LDA}[\rho(\boldsymbol{r})]$) and from the LYP functional ($E_c^{LYP}[\rho(\boldsymbol{r})]$).

These five terms are weighted by three parameters ($\alpha = 0.20, b = 0.72$ and $c = 0.81$), which have been determined through a fitting on thermodynamic data for a wide set of molecules.

Although this functional was initially developed to investigate the electronic structure of molecules, it showed surprisingly good performances in many other chemical applications, including transition-metal chemistry and condensed-phase systems. This functional has been widely used throughout this work, because the correction of the self-interaction, thought partial, is paramount for the description of the band gap and charge-carriers in TiO_2 systems.[171,172]

However, the introduction of a portion of exact exchange into the energy functional influences also the asymptotic behavior of the electron-electron repulsion, that is lower than it should ($-1/r$ for $r \longrightarrow \infty$). For this reason, range-separated hybrid functionals, where the Coulomb operator is split into a short- and a long-range part, have been developed. Through these functionals, the amount of exact HF exchange can be tuned as a function of the interelectronic distance, recovering the correct asymptotic limit.

In this work, we employed the screened hybrid functional Heyd-Scuseria-Ernzerhof functional (HSE06) for the DFT calculation of the adsorption of catechol and dopamine on the flat anatase (101) TiO_2 surface, since it was reported to predict the band gaps of semiconductors with errors as small as 0.2 eV.[173] This functional is essentially an improvement of the hybrid functional PBE0.[174] The correlation functional is analogous to PBE0, while the exchange part is range-dependent:

$$E_{xc}^{\omega PBEh} = aE_x^{HF,SR}(\omega) + (1-a)aE_x^{PBE,SR}(\omega) + E_x^{PBE,LR}(\omega) + E_c^{PBE} \qquad (2.27)$$

The first two terms, $E_x^{HF,SR}$ and $E_x^{PBE,SR}$ are the short-range constributions to the exchange energy, while $E_x^{PBE,LR}$ represents the long-range contributions. In the short range contributions, the HF exact exchange is included $E_x^{HF,SR}$ and weighed by the a coeeficient. The ω coefficient controls the differentiation between short- and long- range constributions. If $\omega = 0$, the exchange-correlation functional $E_{xc}^{\omega PBEh}$ reduces to the hybrid functional PBE0.

It is important to underline that hybrid functionals introduce a *non-local* in the total energy due to the exact exchange. This means that the energy functional in a specific point is not only dependent on the value of the density (and/or on its gradient) at that point as in *local* LDA and GGA approximation, but also on the Kohn-Sham orbitals, which are not local quantities, since they are delocalized in all the integration space.

2.3.5. Electronic properties

The energy gap, i.e. the HOMO-LUMO gap in molecules or the band gap in extended materials, is one of the most important properties defining the electronic structure of a system. Commonly, it is distinguished in fundamental and optical gap (**Figure 2.1**). The fundamental band gap, E_g, is defined as the energy difference between the first ionization potential (IP) and the first electron affinity (EA) and it can be measured by several techniques, for instance by photoemission spectroscopy. The optical gap, E_{opt}, instead, corresponds to the energy difference between the ground state and the first excited state of the system and it is usually determined by UV-vis spectroscopy. In a ground state theoretical framework, such as the one of DFT, it is common practice to approximate the fundamental band gap E_g to the Kohn-Sham gap E_{gKS}, since IP and EA are connected to the N-th and (N+1)-th Kohn-Sham orbital energies, i.e. ϵ_N and ϵ_{N+1} via the following equations (*Koopman's theorem*):[175]

$$\boldsymbol{IP(N) = -\epsilon_N(N-\delta)} \tag{2.28}$$

$$EA = -\epsilon_{N+1}(N-\delta) \tag{2.29}$$

where δ is an infinitesimal variation of the integer electron number. However, it is well-known that a standard Kohn-Sham DFT calculation is equivalent to approaching the integer electron number from below,[176] i.e. it provides $-\epsilon_{N+1}(N-\delta)$. However, the two values of ϵ_{N+1} approaching from below or from above are not equal and they differ by exactly the derivative discontinuity in E_{xc} (DD or Δ_{xc}).

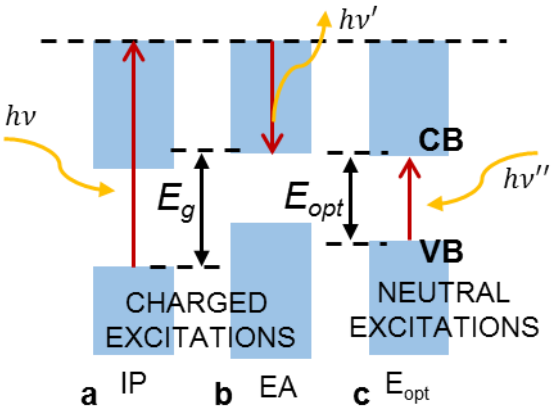

Figure 2.1 A representation of the band structure, showing the charged excitations occurring in **a**) the lowest IP in photoemission and **b**) the highest EA from inverse photoemission, the difference of which is the fundamental gap, $E_g = IP - EA$. The lowest neutral excitation is shown in **c**), whose excitation energy is defined as the optical band gap, E_{opt}. The difference between E_{opt} and E_g is the exciton binding energy. The band edge positions represent the final state energies after the excitation.[177]

Therefore, the fundamental gap can be expressed as follows:

$$E_g = IP - EA = -\epsilon_{N+1} - \epsilon_N + DD \tag{2.30}$$

Standard LDA or GGA functionals do not have a derivative discontinuity of the exchange-correlation energy. For this reason, the KS gaps obtained with these approaches are lower than the fundamental band gap.[178] On the contrary, for hybrid functionals, since they are orbital dependent potentials, the above derivative discontinuity argument does not apply. Therefore, hybrid functionals can yield more accurate predictions of the band gaps, although their performance depends on the choice of the functional.[179] Among them, B3LYP is able to predict the band gap of a wide range of solids with an error lower than 10%.[171]

2.4. Density Functional Tight-Binding

Despite the countless successes of DFT in the prediction of the properties of molecular and condensed phase, the system sizes and time scales accessible to this method are still limited to few hundreds atoms and few picoseconds. On the other hand, demanding calculations by classical or reactive force fields allow for very large-scale simulations, but the predictivity is limited and they cannot provide a quantum insight. Semi-empirical quantum-chemical methods (SE-QM) recover the quantum description at a lower cost than HF and DFT, even though they employ parameters with little physical meaning, limiting their application only to simple organic molecules.[180]

A good compromise for the investigation of systems in the nanoscale is the Density Functional Tight Binding (DFTB) method. The zeroth order approach of DFTB is equivalent to a common standard non-self-consistent (TB) scheme, while at second order a parameter-free, and readily calculable expression for generalized Hamiltonian matrix elements can be derived. These are modified by a self-consistent redistribution of Mulliken charges (SCC). In other terms, SCC-DFTB is a second-order expansion of the Kohn-Sham total energy in DFT with respect to charge density fluctuations. In **Section 2.4.1.**, we sum up the features of this approximation. This method sets in between DFT and molecular mechanics methodologies, allowing for accurate calculations of thousands of atoms and simulation time in the order of hundreds of picoseconds.

2.4.1. Self Consistent Charge Density Functional Tight Binding

The SCC-DFTB total energy can be defined as:

$$E_{tot}^{SCC-DFTB} = \sum_{i} \varepsilon_i + \frac{1}{2}\sum_{\alpha\beta} E_{rep,\alpha\beta}(R_{\alpha\beta}) + \frac{1}{2}\sum_{\alpha\beta} \gamma_{\alpha\beta}\Delta q_{\alpha}\Delta q_{\beta} \qquad (2.31)$$

where the first term is the attractive tight-binding energy, in which the one-electron energies ε_i results from the diagonalization of an approximated Hamiltonian matrix H^0, $E_{rep,\alpha\beta}(R_{\alpha\beta})$ is a pairwise distance-dependent repulsive potential for the pair of atoms α and β, which approximates the short-range repulsion term, Δq_α and Δq_β are the induced charges on the atoms α and β, respectively, and $\gamma_{\alpha\beta}$ is a Coulombic-like interaction potential, that accounts for the Hartree and exchange-correlation contributions.

One-electron molecular orbitals Ψ_i are expanded into a suitable set of localized atomic orbitals ϕ_v of Slater-type obtained from solving the atomic Kohn-Sham-DFT equations within the LDA or GGA approximation. The solutions to the eigenvalue problem are given by the following secular equation:

$$\sum_{v}^{M} c_{vi}\left(H^0_{\mu v} - \varepsilon_i S_{\mu v}\right) = 0 \qquad \forall \mu, i \tag{2.32}$$

$$H^0_{\mu v} = \langle \phi_u | \widehat{H_0} | \phi_v \rangle, \quad S_{\mu v} = \langle \phi_u | \widehat{H_0} | \phi_v \rangle, \quad \forall \mu \in \alpha, \ \forall \nu \in \beta \tag{2.33}$$

The Hamiltonian matrix elements $H^0_{\mu v}$ are computed using standard DFT-LDA or DFT-GGA potentials, according to the following rule:

$$H^0_{\mu v} = \begin{cases} \varepsilon_\mu^{neutral\ free\ atom} & if\ u = v \\ \left\langle \phi_u^\alpha \middle| \hat{T} + V_0^\alpha + V_0^\beta \middle| \phi_v^\beta \right\rangle + \frac{1}{2} S_{\mu v} \sum_K^N (\gamma_{\alpha K} + \gamma_{\beta K}) \Delta q_K & if\ \alpha \neq \beta \\ 0 & otherwise \end{cases} \tag{2.34}$$

The indexes α and β indicate the atoms on which the atomic orbitals ϕ_i, the effective potentials V_0 and the Coulombic-like potentials γ are centered. Therefore, the contributions are limited only to one-center and two-center integrals. The latter are corrected by a term, which is related to the induced charges Δq_K. Except this correcting term, which is determined self-consistently during the SCC, the integrals can be calculated and tabulated in advance as a function of the interatomic distance for each pair of atoms. This information is conventionally stored into the so-called Slater-Koster files (.skf).

The pairwise repulsive potential $E_{rep,\alpha\beta}$ is generally constructed taking the difference of the LDA or GGA cohesive and the corresponding tight-binding energy in a suitable reference structure for each couple of atoms 1 and j,

$$E_{rep,\alpha\beta}(R_{\alpha\beta}) = \left\{ E^{SCF}_{LDA/GGA}(R) - \sum_i^{occ} n_i \varepsilon_i(R) \right\}_{reference\ structure} . \tag{2.35}$$

Thus, it is clear that the pairwise repulsive potential, which is generally expressed by a polynomial function, will depend on the choice of the reference structures.

Besides the usual "band structure" and short-range repulsive terms the final approximate Kohn-Sham energy additionally includes a Coulomb interaction between charge fluctuations. At large distances this accounts for long-range electrostatic forces between two point charges and approximately includes self-interaction contributions of a given atom if the charges are located at one and the same atom. Due to the SCC extension, DFTB can be successfully applied to problems, where deficiencies within the non-SCC standard TB approach become obvious.

2.4.2. Molecular Dynamics-DFTB

Throughout this work, we studied the effect of the temperature on the dopamine-TiO2 interface through molecular dynamics (MD) density functional tight-binding (DFTB), both for the flat surface (**Chapter 3**) and the curved surface case (**Chapter 4**).

At a finite temperature, a molecular system will explore the part of the potential energy surface with energies lower than the kinetic energy $K_B T$. MD is one of the way of simulating this dynamical behavior, allowing the evolution of the system according to the relevant equations of motion.[160] Commonly, this technique is also used as a configurational space sampling tool, enabling the evaluation of macroscopic properties from the average of the microscopic configurations in the phase space.

A straightforward MD approach is the Born-Oppenheimer molecular dynamics (BO-MD), where the N nuclei of a molecular system are onsidered to behave, to a good approximation, as classical particles. Thus, their time evolution can be described integrating over time the Newton's second equation:

$$\boldsymbol{F_i} = -\frac{\boldsymbol{dV}}{\boldsymbol{dR_i}} = \boldsymbol{m_i}\frac{\boldsymbol{\delta^2 R_i}}{\boldsymbol{\delta t^2}}, \boldsymbol{i} = \boldsymbol{1}, \dots, \boldsymbol{N} \tag{2.36}$$

where m_i and $\boldsymbol{R_i}$ are mass and position of the i-th nucleus, respectively. On the left hand side, there is the negative of the first derivative of the potential energy V with respect to the atomic coordinates $\{\boldsymbol{R_i}\}$, also called forces F_i. Since the potential energy is generally known only for a given geometry, the Newton's equations are integrated numerically step by step.

The most used numerical methods are based on the *Verlet* algorithm.[181] First, the position of the nuclei after a small time step Δt are given by a Taylor expansion:

$$\boldsymbol{R}_{i+1=}\boldsymbol{R_i} + \frac{\delta \boldsymbol{R}}{\delta t}(\Delta t) + \frac{1}{2}\frac{\delta^2 \boldsymbol{R_i}}{\delta t^2}(\Delta t)^{\boldsymbol{2}} + \cdots \tag{2.37}$$

$$\boldsymbol{R}_{i+1} = \boldsymbol{R_i} + \boldsymbol{v_i}(\Delta t) + \frac{1}{2}\boldsymbol{a_i}(\Delta t)^{\boldsymbol{2}} + \cdots \tag{2.38}$$

Second, the positions a Δt earlier in time are obtained by substituing Δt with $-\Delta t$ in eq. (2.38):

$$\boldsymbol{R}_{i-1} = \boldsymbol{R_i} - \boldsymbol{v_i}(\Delta t) + \frac{1}{2}\boldsymbol{a_i}(\Delta t)^{\boldsymbol{2}} + \cdots \tag{2.39}$$

Combining equations (2.38) and (2.39), the position at the next time step $\boldsymbol{R}_{i+1}$ can be derived, given the current and the previous position and the current acceleration $\boldsymbol{a_i}$ from eq. (2.36):

$$\boldsymbol{R}_{i+1} = (2\boldsymbol{R}_i - \boldsymbol{R}_{i-1}) + \boldsymbol{a_i}(\Delta t)^2 + \cdots \tag{2.40}$$

At the first step, the previous positions are not known, but are estimated by a first-order approximation from the initial velocities, i.e. $\boldsymbol{R}_{-1} = \boldsymbol{R}_0 - \boldsymbol{v_0}(\Delta t)$.
Evaluating the first-derivatives of the energy and consequently the accelerator, the atomic positions can be propagated in time and generate a trajectory. The time step Δt is an important parameter for a MD simulation. In fact, the validity of the trajectory is higher when the time step is smaller. Nonetheless, a small time step would increase largely the computational effort.

The potential V in (2.36) can be computed with electronic structure methods, such as density functional theory, or using parametrized force fields. In the former case, a Born-Oppenheimer dynamics requires a very tight convergence of the wave function in each time step in order to satisfy the energy conservation over a long simulation time and avoid spurious electronic friction terms, making the procedure too computationally demanding in certain circumstances. [182]

An elegant solution to this issue has been formulated by Car Parrinello (CP-MD), introducing the evolution of the wave function coefficient simultaneously with the nuclear motion, so that it is not necessary anymore to fully converge the electronic structure. [183]

This can be achieved by assigning "fictive masses" in the order of few hundreds of a.u. to the electrons, i.e. the wave function orbital coefficients, and adding the kinetic energy of the orbitals to the total energy. Even thought in the "real" system there is no orbital kinetic energy, in this way the total energy is conserved and realistic results can be obtained keeping this energy contribution relatively small.

2.4.2.1. Non-natural ensembles

A molecular dynamics simulation will naturally generate a NVE ensemble, where the temperature and the pressure fluctuate and the number of atoms, the volume and energy are conserved. Nevertheless, it is possible to generate NVT or NPT ensembles by scaling at each time step the velocities or positions.

A robust methodology to perform this task is to couple the system with a *heat bath*, often called a *thermostat*, which gives or subtracts energy to the system with a certain time constant. The kinetic energy is of the system is then modified by scaling the velocities with an heat transfer rate depends on the coupling parameter τ.

$$v_{scale-factor} = \sqrt{1 + \frac{\Delta t}{\tau}\left(\frac{T_{desired}}{T_{actual}} - 1\right)} \tag{2.40}$$

Such a method will not reproduce a canonical ensemble and this means it will provide the correct average but incorrect fluctuations of the properties. In *Nosé-Hoover* thermostats,[184] fictitious dynamical variables, i.e. a degree of freedom s, a mass Q and a potential energy $(n+1)k_B T_{desired}\ln(s)$, are assigned to the energy reservoir. In this way, the heat flows and, consequently, the energy oscillations are regulated by the parameter Q. This thermostat may produce a non-ergodic ensemble and this property can be recovered using a series of *Nosé-Hoover chains*.[185] Similarly, the pressure can be held almost constant by coupling to a "pressure bath". In this case, the volume of the system is scaled periodically as follows:

$$R_{scale-factor} = \sqrt[3]{1 + k\frac{\Delta t}{\tau}\left(\frac{P_{desired}}{T_{actual}} - 1\right)} \tag{2.41}$$

where k is the system compressibility. Analogously to thermostats, this simple kind of *barostat* do not generate correct ensembles and the recourse to a Nosé-Hoover chain recovers the ergodicity.

2.5. Excited states

Density functional theory has been extensively used to study ground state properties of finite and periodic systems, such as total and binding energies, bond lengths and angles, lattice constants and also dipole moments and polarizabilities.

Nevertheless, especially when light-matter interaction is involved, one is interested in the excited state properties.

The response of a material to light absorption can be typically described by either charged excitations, which are related to the fundamental band gap E_g and, therefore, include the energy of the exciton, and neutral excitations, corresponding to the optical band gap E_{opt} (see **Figure 2.1**).

Neutral excitations could be studied through *time-dependent DFT*, an extension of DFT, at a reasonable computational cost (see **Section 2.3)**. Alternatively, neutral excitations could be accurately modeled through the Bethe Salpeter equation (BSE),[186] a Green's functions-based approximation deriving from the Many Body Perturbation Theory (MBPT), which introduces an electron–hole interaction between GW-derived quasiparticles.[177] The GW approach[187] is still a Green's functions-based approximation, which is suitable for the modeling of charged excitations, but it cannot model two-particles interactions, i.e. it does not describe excitonic effects. These approaches, in particular the Green's function-based ones, are computationally expensive and they become extremely demanding for systems with more than hundreds atoms.

Thought static DFT is a ground state theory, it is possible to use it to extrapolate some information about excited states. Through a ΔSCF-DFT method, it is possible to compute excited states energies and forces at the cost of a standard DFT calculation, employing *non-Aufbau* electronic configurations to converge the Kohn-Sham SCF equations to an excited state. In the case that the excited state is the lowest-energy state with that symmetry, the SCF is guaranteed to converge to the right solution, or otherwise it may collapse to lower -energy state. For example, a double radical single S_1 representing an excited state, would easily collapse to S_0. Instead, the triplet state T_1 is easily accessible, being a ground state for the triplet spin configuration. A focus on this DFT approach to excited states is proposed in **Chapter 4** (**Section 4.2.4.1**), where the method have been employed to study the interaction of light with TiO_2 realistic nanoparticles.

In the following, instead, we review the main theorems of *time-dependent* DFT, which we used in this thesis work to simulate the optical spectrum of dopamine-TiO_2 systems (see **Chapter 5**).

2.5.1. *Time-Dependent* Density Functional Theory

Density Functional Theory is a ground state theory. This implies that even if we knew the exact static ground-state functional, DFT could not be used to describe electronic excitations – for example, the optical response of a system. This limit is intrinsic in DFT: even if one could calculate the exact Kohn–Sham eigenvalues, their differences would not necessarily be close to measured excitation energies, nor they do represent optical (neutral) excitation energies. Such optical excitation represents the response of materials to visible light, which is simulated as a *time-dependent* vector potential.

The exact neutral excitation spectrum and optical gap can be, in principle, calculated within the framework of *time-dependent* DFT (TDDFT).[188-191] In this chapter, TD-DFT is introduced through an outline of the Runge–Gross theorem (**Section 2.5.1**) and of the time-dependent Kohn-Sham equations (**Section 2.5.2**). An equation for linear response within time-dependent density functional theory is derived (**Section 2.5.3**). Finally, we define the dielectric function and the strength function, giving an overview of how these quantities are calculated by the Octopus TDDFT code (**Section 2.5.4**).

2.5.2. The Runge-Gross theorem

Similarly to static DFT, which states that there is a one-to-one correspondence between densities and potentials, the *Runge and Gross Theorem* establishes a one-to-one mapping between the *time-dependent* densities and potentials.[188]

The time evolution of a (non-relativistic and spin unpolarized) system of N interacting electrons is governed by the time-dependent Schrödinger equation (atomic units are used everywhere):

$$i\frac{\partial}{\partial x}\phi(\boldsymbol{r}_1,\boldsymbol{r}_2\ldots\boldsymbol{r}_N,t)=\hat{H}(\{\boldsymbol{r}\},t)\phi(\boldsymbol{r}_1,\boldsymbol{r}_2\ldots\boldsymbol{r}_N,t)\quad\phi(t_0)\ given \tag{2.42}$$

where $\hat{H}(\{\boldsymbol{r}\},t)$ is the Hamiltonian operator which can be written as

$$\hat{H}(\{\boldsymbol{r}\},t)=\sum_{i=1}^{N}\left[-\frac{1}{2}\nabla_i^2+v_{ext}(\boldsymbol{r}_i,t)\right]+\frac{1}{2}\sum_{i\neq j}^{N}\frac{1}{|\boldsymbol{r}_i-\boldsymbol{r}_j|} \tag{2.43}$$

The first term on the right-hand-side is the one-particle kinetic energy and $v_{ext}(\boldsymbol{r}_i,t)$ is the *time-dependent* external potential.

The one electron density of this system is given by:

$$\rho(\boldsymbol{r},t) = N\int d^3r_2 \ldots \int d^3r_N |\psi(\boldsymbol{r},\boldsymbol{r_2},\ldots \boldsymbol{r_N},t)|^2 \tag{2.44}$$

Under the assumption that the density evolves from an initial state $|\phi(t_0)\rangle$ (which does not need to be the ground-state or an eigenstate of the initial external potential, $v_{ext}(\boldsymbol{r},t_0)$) and that the class of external potentials is restricted to those which can be Taylor expanded around the initial time, t_0, the Runge–Gross theorem states that if two time-dependent external potentials $v_{ext}(\boldsymbol{r},t)$ and $v'_{ext}(\boldsymbol{r},t)$ differ by more than a purely *time-dependent* function $c(t)$, then the associated time-dependent densities, $\rho(\boldsymbol{r},t)$ and $\varrho'(\boldsymbol{r},t)$, must be different.

In analogy with the first Hohenberg-Kohn theorem (**Section 2.2.1.**), we can assert that *the external time-dependent potential $v_{ext}(\boldsymbol{r},t)$ of a system is univocally determined, within a trivial additive constant, by the initial state of the system and its time-dependent electron density $\rho(\boldsymbol{r},t)$.*

2.5.3. *Time-dependent* Kohn-Sham equations

In order to evaluate the *time-dependent* density of the system, similarly to the static case, a fictitious Kohn-Sham scheme can be introduced by considering a system of non-interacting electrons subjected to an external potential $v_{KS}(\boldsymbol{r},t)$ that reproduces the exact time dependent density $\rho(\boldsymbol{r},t)$of the interacting system *for all the times*. The time-dependent density is obtained propagating a set of a Schrödinger-like equations, i.e. the *time-dependent* Kohn-Sham equations (TDKS), where all the many-body effects are included through a time-dependent exchange-correlation potential. This potential is unknown, and has to be approximated in any practical application of the theory. The TDKS equations can be written as:

$$i\frac{\partial}{\partial t}\phi_{u,KS}(\boldsymbol{r},t) = \left[-\frac{\nabla^2}{2} + v_{KS}[\rho](\boldsymbol{r},t)\right]\phi_{u,KS}(\boldsymbol{r},t) \tag{2.46}$$

The density of the interacting system can be obtained from the time-dependent Kohn-Sham orbitals:

$$\rho(\boldsymbol{r},t) = \sum_{\boldsymbol{i}=1}^{\boldsymbol{occ}} \left|\phi_{u,KS}(\boldsymbol{r},t)\right|^{\boldsymbol{2}} \tag{2.45}$$

The Kohn-Sham potential is conventionally separated in the following way:

$$v_{KS}(\boldsymbol{r},t) = v_{ext}(\boldsymbol{r},t) + v_H[\rho](\boldsymbol{r},t) + v_{xc}[\rho](\boldsymbol{r},t) \tag{2.46}$$

where $v_{ext}(\boldsymbol{r},t)$ is the (given) external potential that defines the problem that is to be solved, which tipically contains the Coulomb potential of the nuclei plus a laser field.

The Hartree potential has the form:

$$v_H[\rho](\boldsymbol{r},t) = \int d^3r' \frac{\rho(\mathbf{r}',\mathrm{t})}{|\boldsymbol{r}-\boldsymbol{r}'|} \tag{2.47}$$

and the exchange-correlation potential, v_{xc}, has a functional dependence on the density of the system at the current and at all previous times; hence it includes the information about the whole history of this time propagation. The exact xc potential accounts for all non-trivial many-body effects, as in the static case.

In parallel with static DFT, where the xc potentials is derived as a functional derivatives of the xc energy, in TDDFT the action functional $\tilde{\mathcal{A}}$ in the Keldish formalism is introduced:

$$v_{xc}[\rho](\boldsymbol{r},t) = \left.\frac{\delta\tilde{\mathcal{A}}_{xc}}{\delta\rho(\boldsymbol{r},\tau)}\right|_{\rho(\boldsymbol{r},t)} \tag{2.48}$$

where τ stands for the Keldish pseudo-time.[192]

As for static DFT, the knowledge of this functional would solve all time-dependent (externally driven) Coulomb problems; in practice, however, the xc potential is always approximated.

To conclude this section, the exchange-correlation kernel is reported:

$$f_{xc}(\boldsymbol{r},t,\cdot\ \boldsymbol{r}',t') = \left.\frac{\delta v_{xc}[\rho(\boldsymbol{r},t)]}{\delta\varrho(\boldsymbol{r}',t')}\right|_{dv_{ext}=0} \tag{2.49}$$

A more detailed description of this kernel is given in **Chapter 5**.

In contrast with static DFT, where very good xc potential exists, approximations to $v_{xc}(\boldsymbol{r},t)$ are less developed. Indeed, although formally exact, the predictions of optical absorption spectra from TDDFT are only as good as the approximation of the xc kernel. Also for the time-dependent problems, a *Local Density Approximation* (LDA) exists, which is local in time and, therefore, it is expected to work only in the case where the temporal dependence is small. Choosing the LDA for the time-dependent xc-potential leads to the *adiabatic LDA kernel* (ALDA kernel), which is local in space and local in time and hence does not contain any memory effects:

$$f_{xc}^{ALDA}(\boldsymbol{r},t,\cdot\ \boldsymbol{r}',t') = \delta(\boldsymbol{r}-\boldsymbol{r}')\delta(t-t')\left.\frac{df_{xc}^{HEG}(\boldsymbol{r},t)}{d\rho(\boldsymbol{r}',t')}\right|_{\rho=\rho(\boldsymbol{r},t)} \tag{2.50}$$

In particular, the ALDA misses the important $1 = q^2$ divergence, where q is a vector in the reciprocal space, that controls the optical absorption of extended systems with gap.

We used in this work the GGA/PBE functional[168] and adiabatic PBE approximation.

2.5.4. Linear response theorem

In the following, we show that the time-dependent Kohn–Sham equations can be used together with linear response to study electronic excitations efficiently. [193]. if the system is perturbated by some weak electric field.[194,195]

When the external perturbation, $v_{ext}(\boldsymbol{r},t) = v_{ext}^{0}(\boldsymbol{r}) + v_{ext}^{(1)}(\boldsymbol{r},t)$, is sufficiently small (such that it does not completely destroy the ground-state structure of the system), it is enough to calculate the linear-response of the system. The advantage of linear response is that the exact solution can be obtained using simple linear algebra operations. The first-order correction to the density, in terms of the perturbing external potential, ${v_{ext}}^{(1)}(\boldsymbol{r},t)$, is given by:

$$\rho^{(1)}(\boldsymbol{r},t) = \int_{-\infty}^{\infty} dt' \int d^3r' \chi(\boldsymbol{r},\boldsymbol{r}',t-t')\, v_{ext}^{(1)}(\boldsymbol{r}',t') \tag{2.51}$$

where χ is the linear density-density response function of the fully interacting system:

$$\chi(\boldsymbol{r},\boldsymbol{r}',t-t') = \left.\frac{\delta\varrho(\boldsymbol{r},t)}{\delta v_{ext}(\boldsymbol{r}',t')}\right|_{v_{ext}(\boldsymbol{r}',t')=v_{ext}^{(0)}(\boldsymbol{r}')} \tag{2.52}$$

and causality implies that $\chi(\boldsymbol{r},\boldsymbol{r}',t-t') = 0$ for $t < t'$.

After some elaborations, one gets a Dyson-like equation for the density-density linear response function of the fully interacting system. Notice that, for a time independent Hamiltonian the polarizability or the dielectric function (defined in **Section 2.5.4.1.** and **2.5.4.2.**, respectively) depends only on the time-differences. Therefore, a Fourier Transform in energy space can be easily performed.

$$\begin{aligned}\chi(\boldsymbol{r},\boldsymbol{r}',\omega) = \chi_{KS}(\boldsymbol{r},\boldsymbol{r}',\omega) \\ + \int d^3r'' \int d^3r''' \chi_{KS}(\boldsymbol{r},\boldsymbol{r}'',\omega)\left[\frac{1}{|\boldsymbol{r}''-\boldsymbol{r}'''|}\right. \\ \left. + f_{xc}(\boldsymbol{r}'',\boldsymbol{r}''',\omega)\right]\chi(\boldsymbol{r}''',\boldsymbol{r}',\omega)\end{aligned} \tag{2.53}$$

where f_{xc} is the exchange-correlation Kernel, defined as:

$$f_{xc}(\boldsymbol{r},\boldsymbol{r}',\omega) = \left.\frac{\delta v_{xc}[\rho(\boldsymbol{r},\omega)]}{\delta\rho(\boldsymbol{r}',\omega)}\right|_{dv_{ext}=0} \tag{2.54}$$

where χ_s is the Kohn-Sham response function, which can be calculated straightforwardly from *time-dependent* perturbation theory.

$$\chi_{KS}(\boldsymbol{r},\boldsymbol{r}',\omega)=\lim_{\eta\to 0}\sum_{i=1}^{\infty}\sum_{j=1}^{\infty}(n_i-n_j)\frac{\phi_i^*(\boldsymbol{r})\phi_j(\boldsymbol{r})\phi_i(\boldsymbol{r}')\phi_j^*(\boldsymbol{r}')}{\omega-\varepsilon_j+\varepsilon_i+i\eta} \tag{2.58}$$

From (2.58), it is possible to extract the excitation energies of the system, as these are simply the poles of the response function. So this equation allows to determine the exact excitation energies of the system once the Kohn-Sham KS and the xc kernel f_{xc} are known.

A full solution of (2.58) would require to include in the calculation, not only the KS orbitals, but also a big amount of unoccupied states.

2.5.4.1. Polarizability

The linear response of a molecule can be described via the dynamical polarizability tensor i.e.:

$$\delta\mu_i(\omega)=\sum_j \alpha_{ij}(\omega)E_j(\omega) \tag{2.59}$$

where $\delta\mu_i(\omega)=\int d\boldsymbol{r}x_i\delta\rho(\boldsymbol{r},\omega)$ is the induced dipole in the i direction and $E_j(\omega)$ is the external applied field. Assuming a dipolar perturbation, i.e.$\delta v(\boldsymbol{r},\omega)=-E(\omega)\cdot\boldsymbol{r}$, the dynamical polarizability tensor can be related to the response function by:

$$\alpha_{ij}(\omega)=-\int\int d\boldsymbol{r}d\boldsymbol{r}'\,x_i\chi(\boldsymbol{r},\boldsymbol{r}',\omega)x_j \tag{2.60}$$

The imaginary part of the dynamical polarizability is then related to the photo-absorption cross section $\sigma(\omega)$, which is the relevant magnitude measured in experiment:

$$\sigma_{ij}(\omega)=\delta_{ij}+\frac{4\pi}{V}\alpha_{ij}(\omega) \tag{2.61}$$

2.4.5.1. Dielectric function for extended systems

When an applied time-dependent external perturbation polarizes the system, the electrons screen the system from the applied perturbation. The total electrostatic potential felt by a test charge inserted into the medium is then given by

$$\begin{aligned} v_{tot}(\boldsymbol{r},t)&=v_{ext}(\boldsymbol{r},t)+v_{ind}(\boldsymbol{r},t)\\ &=\int_{-\infty}^{\infty}dt'\int d^3r''\int d^3r'\varepsilon^{-1}(\boldsymbol{r},\boldsymbol{r}',t-t')v_{ext}(\boldsymbol{r}',t') \end{aligned} \tag{2.62}$$

where the screened potential is expressed in terms of the inverse dielectric function ε, v_{ind} is the induced potential due to the polarization of the system, i.e., the potential generated by the induced density.

Hence, using $\rho^{(1)}(\boldsymbol{r},t) = \int_{-\infty}^{\infty} dt' \int d^3r' \chi(\boldsymbol{r},\boldsymbol{r}',t-t')\, v_{ext}^{(1)}(\boldsymbol{r}',t')$, the potential $v_{ind}(\boldsymbol{r},t)$ is related to the density–density response function as:

$$v_{ind}(\boldsymbol{r},t) = \int_{-\infty}^{\infty} dt' \int d^3r'' \int d^3r' \frac{\chi(\boldsymbol{r}'',\boldsymbol{r}',t-t')v_{ext}(\boldsymbol{r}',t')}{|\boldsymbol{r}-\boldsymbol{r}''|} \tag{2.63}$$

This, together with (2.61), leads to the following relation between the dielectric function and χ:

$$\varepsilon^{-1}\left(\boldsymbol{r},\boldsymbol{r}',t-t'\right) = \delta(\boldsymbol{r}-\boldsymbol{r}')\delta\left(t-t'\right) + \int d^3r'' \frac{\chi(\boldsymbol{r}'',\boldsymbol{r}',t-t')}{|\boldsymbol{r}-\boldsymbol{r}''|} \tag{2.64}$$

In a perfect crystal with translational symmetry, if the coordinates are shifted by a lattice vector $\boldsymbol{R}$, the dielectric function stays unchanged:

$$\varepsilon(\boldsymbol{r}+\boldsymbol{R},\boldsymbol{r}'+\boldsymbol{R},t-t') = \varepsilon(\boldsymbol{r},\boldsymbol{r}',t-t') \tag{2.65}$$

Therefore, it is convenient to perform a Fourier transform to reciprocal space, where the dielectric function is conventionally written as

$$\varepsilon(\boldsymbol{r},\boldsymbol{r}',t-t') = \frac{1}{\boldsymbol{\Omega}}\sum_{\boldsymbol{q}}\sum_{\boldsymbol{GG'}} e^{-i[(\boldsymbol{q}+\boldsymbol{G})\boldsymbol{r}-\omega(t-t')]}\varepsilon(\boldsymbol{q}+\boldsymbol{G},q+\boldsymbol{G}',\omega)e^{i[(\boldsymbol{q}+\boldsymbol{G})\boldsymbol{r}'-\omega(t-t')]} \tag{2.66}$$

where $\boldsymbol{q}$ is a vector within the first Brillouin zone, $\boldsymbol{G}$ and $\boldsymbol{G}'$ are reciprocal lattice vectors, and $\boldsymbol{\Omega}$ is the volume of the crystal. In reciprocal space, the three dimensional integral in (2.64) becomes a simple matrix multiplication resulting in:

$$\varepsilon^{-1}_{GG'}(\boldsymbol{q},\omega) = \delta(\boldsymbol{G}-\boldsymbol{G}') + \sum_{G''}\frac{4\pi\delta(\boldsymbol{G}-\boldsymbol{G}'')}{|(\boldsymbol{G}+\boldsymbol{q})(\boldsymbol{G}''+\boldsymbol{q})|}\chi_{G''G'}(\boldsymbol{q},\omega) \tag{2.67}$$

In reciprocal space, the Dyson equation (2.53) can be solved for the density–density response function χ yielding

$$\begin{aligned}\chi(\boldsymbol{G},\boldsymbol{G}',\boldsymbol{q},\omega) = \sum_{G''}\Bigg\{\Bigg[&\delta(\boldsymbol{G}_1+\boldsymbol{G}_2)\\ &-\sum_{\boldsymbol{G}_3}\chi_s(\boldsymbol{G}_1,\boldsymbol{G}_3,\boldsymbol{q},\omega)\\ &\times\left(\frac{4\pi\delta(\boldsymbol{G}_3-\boldsymbol{G}_2)}{|(\boldsymbol{G}_3+\boldsymbol{q})(\boldsymbol{G}_2+\boldsymbol{q})|}\right)\Bigg]^{-1}\Bigg\}_{G,G''}\chi_s(\boldsymbol{G}',\boldsymbol{G}'',\boldsymbol{q},\omega)\end{aligned} \tag{2.68}$$

The head of the dielectric tensor, also known as the macroscopic part, can be directly compared to experiments: $\varepsilon_M = [{}^{1}/_{\varepsilon^{-1}}(\boldsymbol{G},\boldsymbol{G}',\boldsymbol{q},\omega)]_{\boldsymbol{G}=\boldsymbol{G}'=0}$ corresponds to the absorption spectra[196,197] and $\varepsilon^{-1}(\boldsymbol{G}=\boldsymbol{G}'=0,\boldsymbol{q},\omega)$ to the electron energy loss spectra (EELS).[198]

2.5.5. Real time TD-DFT for the full solution of Kohn-Sham equations

In order to calculate the linear and non-linear response functions of finite systems, an alternative and very efficient method consists in the direct solution of the time dependent Kohn-Sham equations (2.46). This method has been used with success both for TD-DFT calculations of photo-absorption for clusters[199] and biomolecules.[200] More recently, the method has been extended also to periodic systems.[201] The starting point for the solution of the time dependent problem is the initial state of the electronic system, i.e. the Kohn-Sham ground state. Then, an external time-dependent field is applied and the time-dependent KS equations are propagated following a unitary scheme. In the particular case in which one is interested in obtaining the linear optical absorption, the system is instantaneously perturbed applying a small electric field $\delta v_{ext}(\boldsymbol{r},t) = -k_0 x_i \delta(t)$ where $x_i = x, y, z$. In this way, all the frequencies of the system are excited with equal weight, which it is equivalent to give a small momentum k_0 to all the electrons, so that at time 0^+ the perturbed wave functions are:

$$\psi_i(\boldsymbol{r}, t = 0^+) = e^{ik_0 x_i}\psi_i(\boldsymbol{r}, 0) \tag{2.69}$$

where $\psi_i(\boldsymbol{r}, 0)$ is the ground state of the system. Next, orbitals are propagated in time:

$$\psi_i(\boldsymbol{r}, t + \delta t) = \mathcal{T} exp\left\{-i \int_t^{t+\delta t} dt \hat{h}_{KS}(t)\right\}\psi_i(\boldsymbol{r}, t) \tag{2.70}$$

Then, the absorption spectrum for a finite system can be calculated by the equations (2.60) and (2.61).

Noticing that the perturbation (a delta-function in real time) is a constant function in the frequency domain, we can evaluate the polarizability as:

$$\alpha_{ii}(\omega) = -\frac{1}{k_0} \int d\boldsymbol{r} x_i \ \delta\varrho(\boldsymbol{r}, \omega) \tag{2.71}$$

where $\delta\varrho(\boldsymbol{r}, \omega)$ is the Fourier transform of $\varrho(\boldsymbol{r}, t) - \varrho(\boldsymbol{r}, 0)$. Of course according with (2.60), it is necessary to calculate the polarizability for each spatial direction.

As explained, this method has the great advantage of not requiring the explicit calculation of unoccupied states. Moreover, real-time TD-DFT can be extended to the study of non-linear phenomena and to perform nuclear dynamics, eventually driven by high intensity laser fields.[202]

2.6. TiO_2 Models

Throughout this work, the dopamine molecule has been adsorbed both on a flat and on a curved anatase TiO_2 surface. In the following, we give a brief overview of the two main models employed. Both were obtained originally from bulk anatase TiO_2, which is characterized by a tetragonal lattice ($P4_2/mnm$) with four TiO_2 units per unit cell, forming chains of slightly elongated TiO_6 octahedra, in a D_{2d} local symmetry. In bulk anatase, all the Ti atoms are six-fold-coordinated (Ti_{6c}^{4+}), while all O atoms are three-fold coordinated (O_{3c}^{2-}).

2.6.1. TiO_2 flat surface

Studying the adsorption of molecules on ordered and clean surfaces is fundamental not only for the aim of modeling an effectively flat surface, as for example the ones exposed by faceted nanocrystals, but also because it gives the opportunity to investigate complicated phenomena of organization and reciprocal interaction of layers of molecules on the surface, without the further complication of a defective surface. A surface can be created by cutting a crystal, which we simulate as an infinite object, through a crystalline plane. Two semi-infinite crystals are then generated in the direction orthogonal to the surface, where periodicity is lost. In order to simulate infinitive bi-dimensional surfaces, a slab model can be built. The slab model consists of a film formed by a few atomic layers parallel to the (*hkl*) crystalline plane of interest. The film, of finite thickness, is limited by two surface planes, possibly related by symmetry. For sufficiently thick slabs, this kind of model can provide a faithful description of the ideal surface. By using this slab approach, surfaces can be easily modeled with the quantum code CRYSTAL,[203] extensively employed throughout this work of thesis.

The (101) surface of TiO_2 anatase is the most stable one and, therefore, the most widespread in nature.

After the full optimization of bulk TiO_2 anatase was carried out on the primitive cell using a Monkhorst−Pack k-point mesh of 12 × 12 × 12, the 2D infinite system perpendicular to the (101) surface was cut out of the bulk structure. To model the (101) anatase surface, three triatomic layers of TiO_2 slab were considered. The bottom layer was kept fixed to the optimized bulk positions during the geometry optimization (no periodic boundary conditions were imposed in the direction perpendicular to the surface). To investigate binding energies and equilibrium geometries, we used principally a 1×4 supercell models (144 atoms, see **Figure 2.2.**), which has eight Ti_{5c} (5-fold-coordinated) adsorption sites and eight O_{2c} (2-fold-coordinated). On the surface there are also species in a bulk-like coordination, i.e. threefold

coordinated O ions (O_{3c}) and six-fold coordinated Ti ions (Ti_{6c}), which do not influence significantly the surface reactivity.

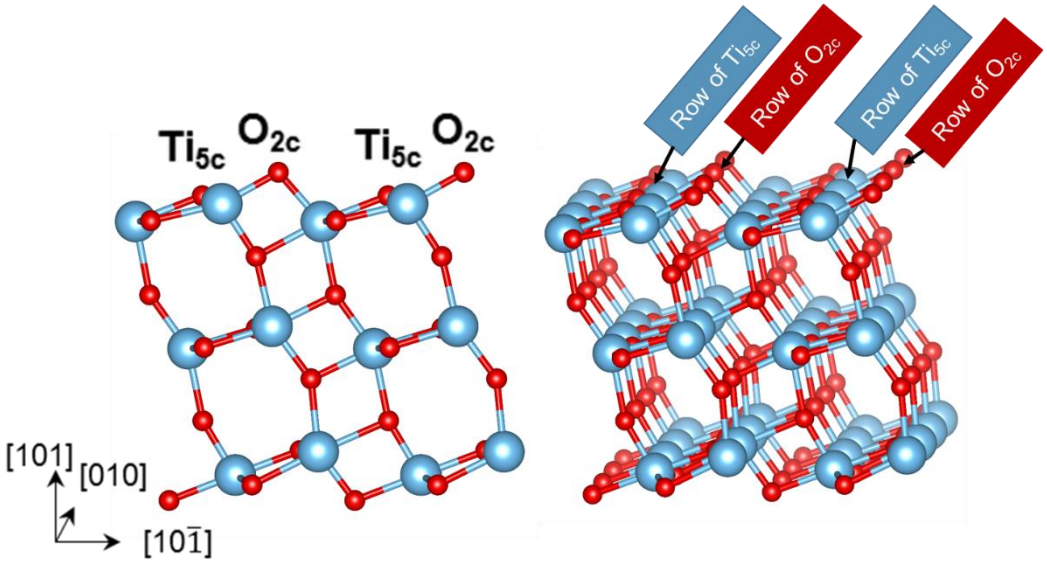

Figure 2.2. Slab model 1×4 for TiO_2 (101) anatase. Rows of Ti_{5c} and O_{2c} are highlighted in the picture.

2.6.2. TiO_2 curved nanoparticles

Curved surfaces present a major amount of undercoordinated sites with respect to the flat surface. This makes their reactivity towards adsorbed molecules, e.g. dopamine, peculiar with respect to the clean flat TiO_2 surface.

In this work, the curved surface is represented by a realistic spherical nanoparticle (NP) with a diameter of 2.2 nm, previously developed in our research group.[81] Unlike faceted anatase TiO_2 NPs, which have a well-defined structure, spherical nanoparticles are more structurally complex; first, they present many undercoordinated surface atoms. Therefore, intrinsic chemisorbed water is necessary to keep the chemical stability. The amount of water was kept as low as possible. Structural rearrangement of the surface is likely to happen. The spherical NP is centered on a Ti atom, with a D_{2d} point symmetry for the whole system. After the addition of intrinsic water, the final stoichiometry of the NP is $(TiO_2)_{223}•10H_2O$ and the symmetry is reduced to D_2. In fact, it is experimentally proved that a small quantity of strongly bound water on spherical NPs is present up to 600–700 K.[204] Thus, this can be considered as "intrinsic" water, being extremely hard to remove. These molecules are dissociated at very low-coordinated (3- or 4-fold) Ti sites at the surface, which are particularly reactive. Therefore, when modeling a spherical nanoparticle, some dissociated water molecules in the form of hydroxyl (OH) groups have to be added to achieve the overall chemical stability of the system. The distribution of OH groups resulting from the dissociation of the ten water molecules is

assessed according to the following criteria: the lowest coordination sites are filled (Ti_{3c}) first, followed by higher binding sites, and no defect states appear in the band gap. Therefore, the electronic structure of this nanoparticle does not present any peculiar feature, with a band gap of 4.1 eV.

Regarding the band gap, thought very large, NPs are still finite molecular systems, hence it is not fully correct to refer to band states. Indeed, it is possible to distinguish between very localized states (molecular orbitals, MOs), and states which are delocalized on several atoms of the NP and, thus, can be considered as (quasi-)band states. For the bare spherical NP, the highest occupied molecular orbital (HOMO) is a fully localized on a surface state, involving the protruding hydroxyl groups. Thus, rather than considering the HOMO-LUMO difference as the band gap of the NPs, a Kohn-Sham band gap, E_{gKS}, can be defined by selecting a lower energy occupied state, which is delocalized on oxygen atoms of the NP and can be truly considered a "band" state.[83]

This model has been fully optimized through a simulated annealing procedure, which allowed to locate the global minimum structure on the potential energy surface. It was then redefined through atomic relaxation by DFT (B3LYP level of theory). The resulting NP is reported in **Figure 2.3**.

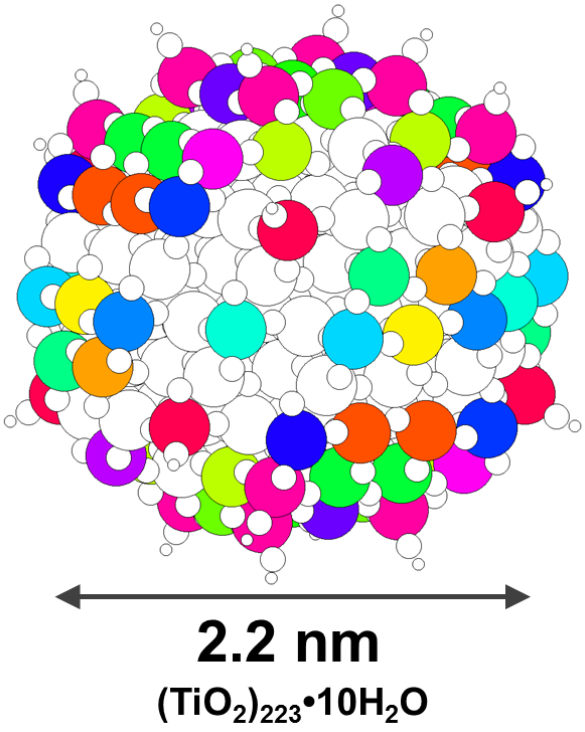

Figure 2.3. Optimized 2.2 nm NP used in this work. The (almost) symmetrically equivalent sites are identified by the color coding.

Due to the annealing procedure, the nanosphere is not perfectly symmetrical anymore, since no symmetry constraint was imposed. This means that the symmetry operations of the D_2 point group applied on an atom would move that atom onto an equivalent site, which would be roughly in that position (see color-code in **Figure 2.3**).

Several kinds of undercoordinated sites are present on the NP, including not only Ti_{5c} and O_{2c}, but also Ti_{4c} (4-fold coordinated), $Ti_{3c}OH$, $Ti_{4c}(OH)$ and OH sites. The location and the reactivity of these undercoordinated sites will be better assessed in **Chapter 4**, **Section 4.2**. The reactivity of all these surface sites towards the dissociation of the water molecule have been investigated by Fazio et al.[85] and used as a starting point to study the adsorption of dopamine. The titanium undercoodinated sites placed at the equator of the NP resulted to be the most stable ones (see **Chapter 4**, **Section 4.2**, **Figure 4.2**). The core of the NP, instead, is similar to the bulk material (see **Chapter 1**, **Section 1.2.3.1**).

3 From single molecule to full monolayer adsorption of dopamine on TiO_2 surface

Despite the many successful synthesis and applications of dopamine-functionalized TiO_2 nanohybrids, there is not yet an atomistic understanding of the interaction of this 1,2-dihydroxybenzene derivative ligand with the titanium dioxide surfaces. In this Chapter, based on a wide set of dispersion-corrected hybrid density functional theory (DFT) calculations and on density functional tight binding (DFTB) molecular dynamics simulations, we present a detailed study of the adsorption modes, patterns of growth and configurations of dopamine on the anatase (101) TiO_2 surface, with reference to the archetype of 1,2-dihydroxybenzene ligands, i.e. catechol. At low coverage, the isolated dopamine molecule prefers to bend towards the surface, coordinating the NH_2 group to a Ti_{5c} ion. At high coverage, the packed molecules succeed in bending towards the surface only in some monolayer configurations. When they do, we observe a proton transfer from the surface to the ethyl-amino group, forming terminal NH_3^+ species, which highly interact with the O atoms of a neighboring dopamine molecule. This strong coulombic interaction largely stabilizes the self-assembled monolayer. Based on these results, we predict that improving the probability of dopamine molecules being free to bend towards the surface through thermodynamic versus kinetic growth conditions will lead to a monolayer of fully protonated dopamine molecules.

3.1. Introduction

Surface modification of titanium dioxide with organic or organometallic molecules has been attracting the attention of the scientific community during the last two decades due to the variety of applications of this material, in particular in photocatalysis and photovoltaic solar cells.[74,205,206] In normal conditions, rutile is the most stable bulk TiO_2 polymorph, however when nanostructured (usually below 20nm) the anatase phase is preferred[40] with the (101) being the most stable and exposed surface.[53] Furthermore, the anatase allotrope is considered particularly photoactive[207] and, thus, a good candidate to be used in high surface area photocatalytic and photovoltaic devices. A major bottleneck, however, is that anatase TiO_2 only absorbs the ultraviolet light, due to its large band gap of 3.2 eV at room temperature.[208] Surface modification with appropriate organic ligands generally allows tuning the band gap of the bare metal oxide, through a red shift of the adsorption band from the UV to the visible range. Functionalization, for example with catechol, improves the adsorption of the solar spectrum, refining the performances of the material in photoactivated devices.[119–125] Due to its central role in the electron-transfer process, the adsorption of catechol, which is the archetype for all functionalized 1,2-dihydroxybenzene ligands, on the anatase (101) TiO_2 surface has been widely investigated, both experimentally[110, 111, 112, 113, 114] and theoretically, using cluster or surface models.[118,119,120,121] Some of the works present in literature indicate the bidentate adsorption mode as the most stable one.[110,112,117]

More recently, surface modification of TiO_2 has also found application in the modern field of nanomedicine.[1, 129] In particular, TiO_2 nanoparticles (NPs) are functionalized in order to build novel bioinorganic hybrid nanoconjugates. In general, these systems are prepared by connecting an inorganic component, such as a metal or metal oxide NP, to biomolecules (e.g. polymers, proteins, DNA fragments). They are used for several biomedical applications, including biocompatibility, multimodal imaging and targeting of specific cells.[108, 209,210,137] The use of TiO_2 nanoparticles makes the nanoconjugates perfect candidates for photocatalytic therapy or photoactivated drug release.

However, due to their peculiar surface chemistry, largely determined by the presence of undercoordinated Ti atoms, bare TiO_2 NPs are cytotoxic.[89,91] This problem can be overcame by exploiting the high reactivity exhibited by these undercoordinated sites towards oxygen-reach ligands, as they fill the octahedral coordination sites.[107] Once functionalized, the reactivity of the NPs with cellular proteins is minimized, reducing potential particle toxicity and eventually assuming site selectivity and functionality.[92]

The additional advantage deriving from functionalization with organic molecules is that they provide the NP with specific binding sites for biomolecules. A successful strategy for attaching biomolecules to the surface of TiO_2 is to exploit a linker with double functional moieties: one anchoring the surface of the metal oxide and the other binding the bioactive molecule. The linkers are organic molecules having oxygen-containing substituents, such as dopac or dopamine. [130,132,134,135,136] Dopamine exhibits a diolic group (two OH) in the catechol-like portion for surface anchoring and one ethyl-amino group ($-CH_2CH_2NH_2$), for the bioactive molecule binding. Moreover, it has been shown to facilitate the charge transfer between the inorganic and biological component.[144]

Dopamine-modified TiO_2 NPs were used to detect and repair DNA mutations or to activate specific oxidation processes, in analogy to endonucleases activity.[108,137] Rajh and coworkers also developed a method to control charge transfer from DNA to TiO_2/dopamine, exploiting the sequence dependent charge separation.[137] Similarly-built systems were used to specifically bind proteins, altering cell metabolism and inducing cell death.[135,138,139] Moreover, Kenneth et al. synthetized TiO_2/dopamine/DNA nanoconjugates to be used as gene knockout devices and tumor imaging agents at the same time.[145] Dopamine functionalized TiO_2 NPs can also bind proteins or peptides to build up electrochemical biosensors, relevant for drug discovery, diagnostics, environmental applications, as well as for food safety.[146,147]

Despite the long list of successful synthesis and applications of dopamine-functionalized TiO_2 nanohybrids, a complete atomistic understanding of the structure, function and mechanism of these nanodevices is still lacking. Differently from catechol, very little is known about dopamine adsorption on the anatase (101) TiO_2 surface, in particular with regards to the different binding configurations. Most of the works assume that dopamine adsorbs on the TiO_2 surface in a bidentate configuration similar to catechol,[149] while the possible role of the ethyl-amino functionality in the binding to the surface is generally neglected.[150,151] The adsorption of one single molecule of dopamine was studied theoretically by Vega-Arrojo et al. with a TiO_2 cluster model, who stated that the bidissociated bidentate adsorption mode is favored with respect to the monodentate or molecular ones.[150,151] Urdaneta et al. investigated the adsorption of dopamine in a low coverage regime, by considering uniquely a bidentate configuration on different low index anatase surfaces.[151]

From an experimental point of view, the surface of some spherical colloidal NPs was modified with different amounts of dopamine and optically characterized through adsorption and diffuse reflectance spectroscopy,[142] however the dopamine adsorption mode was not investigated nor discussed. On an anatase TiO_2 (101) single crystal, a photoemission study

addressing the adsorption of one monolayer of dopamine molecules suggested the bidentate configuration to be the most likely one, even if no assessment on the actual structure of the monolayer was reported.[144] Therefore, a complete and exhaustive understanding of the mechanism of dopamine adsorption on the anatase TiO_2 (101) surface and of the electronic properties of the resulting hybrid organic/ inorganic interface is still lacking.

The aim of this work is to investigate, by means of a wide set of hybrid density functional theory (DFT) calculations including dispersions correction, the details of the dopamine adsorption on a slab model of the anatase (101) surface of TiO_2 at increasing coverage, up to a full monolayer. The well-known case of catechol is used as a reference for the more complex case of dopamine, comparing various conceivable low coverage adsorption configurations and identifying the modifications caused by the anchoring molecule to the electronic structure of the material. We considered then increasing dopamine coverages in order to establish the molecular layer growth mechanism, both under kinetic and thermodynamic control. To this end, molecular dynamics simulations, based on the self-consistent charge density-functional tight-binding (SCC-DFTB) theory, have also been performed, screening several possible configurations for a full monolayer of dopamine molecules. Some unexpected proton transfers are observed.

The Chapter is organized as follows: in **Section 3.2.** we describe the computational details and models used in this work. Later, we present our results on the isolated molecule adsorption of catechol and dopamine (**Section 3.3.**), on the growth mechanism up to a full monolayer of catechol or dopamine under kinetic control (**Section 3.4.**), on the most stable dopamine monolayer structure (**Section 3.5**.) and on the possibility of a different thermodynamic growth mechanism (**Section 3.6**.). Finally, we present a summary and the relevant conclusions from this study.

3.2. Computational details

For all the density functional theory (DFT) electronic structure calculations and geometry optimizations we made use of the CRYSTAL14 simulation package,[203] where the Kohn-Sham orbitals are expanded in Gaussian-type orbitals. The all-electron basis sets are Ti 86-4111 (d41), O 8-4111 (d1) for TiO_2 and H 5-111 (p1), C 6-31111 (d1), O 8-41111 (d1), N 6-311 (d1) for the adsorbed catechol and dopamine molecules. We used the HSE06[211] screened hybrid density functional and we took into account long-range van der Waals interactions with the inclusion of the semiempirical dispersion correction proposed by Grimme (DFT-D2).[212] The cut-off limits in the evaluation of the Coulomb and exchange series/sums were set to 10^{-7} for Coulomb overlap tolerance, 10^{-7} for Coulomb penetration tolerance, 10^{-7} for exchange overlap tolerance, 10^{-7} for exchange pseudo-overlap in the direct space and 10^{-14} for exchange pseudo-overlap in the reciprocal space. For the geometry optimization, forces were relaxed to be less than 4.5×10^{-4} a.u. and displacements to be less than 1.8×10^{-3} a.u.

All the self-consistent-charge density functional tight-binding (SCC-DFTB)[213,214] electronic structure calculations, geometry optimizations and molecular dynamics simulations were performed with the DFTB+ simulation package.[215] We employed the MATORG parameterization set[216] for the pairwise interaction of the atoms of both TiO_2 and adsorbed molecules. The description of the hydrogen bonding has been further improved with the inclusion of the empirical HBD correction ($\zeta = 4$).[217]

Born-Oppenheimer molecular dynamics simulations were performed within the canonical ensemble (NVT). The Newton's equations of motion were integrated with the Velocity Verlet algorithm and a relative small time step of 0.5 fs was used to ensure reversibility. A Nosé-Hoover thermostat, with a time constant of 0.03 ps, kept the temperature to 300 K. After 10 ps of equilibration, the systems were allowed to evolve for other 40 ps. Statistical sampling has been enhanced running four separate simulations for each system, where different random seeds for velocity assignment were considered.

The full optimization of bulk TiO_2 anatase was carried out on the primitive cell using a Monkhorst-Pack k-point mesh of 12×12 ×12 to ensure the convergence on the electronic part. The values of the optimized lattice parameters for bulk anatase TiO_2 are 3.746 and 3.796 Å for a and 9.674 and 9.790 Å for c with HSE06-D2 and DFTB(MATORG), respectively. The bandgap (E_g) for bulk anatase (101) has been calculated to be 3.7 eV with HSE06-D2 and 3.3 eV with DFTB(MATORG). In **Table 3.1** these data have been compared with other hybrid DFT functionals[81,218] and experimental values.[52,219]

Table 3.1. Optimized cell parameters *a* and *c* (in Å) and electronic band gap E_g (in eV) of TiO_2 bulk anatase computed with DFT(HSE06) and DFTB(MATORG) and compared with other hybrid DFT functionals and experimental values.

METHOD	*a*	*c*	E_g
DFT(HSE06), this work	3.746	9.674	3.7
DFTB(MATORG), this work	3.796	9.790	3.3
DFT(B3LYP)[83]	3.789	9.777	3.8
DFT(PBE0)[218]	3.758	9.704	4.5
Exp.[52]	3.782	9.502	-
Exp.[54]	-	-	3.4

To model the (101) anatase surface a three tri-atomic layers of TiO_2 slab was considered. The bottom layer was kept fixed to the optimized bulk positions during the geometry optimization (no periodic boundary conditions were imposed in the direction perpendicular to the surface). To investigate binding energies and equilibrium geometries we used two supercell models: (i) the 1×4 supercell model (144 atoms,) has eight Ti_{5c} (five-fold coordinated) adsorption sites, thus it allows to model a coverage density of one monolayer, 1 ML (four molecules in the supercell), 0.5 ML (two molecules in the supercell) and 0.25 ML (one molecule in the supercell); (ii) the 2×4 supercell model (288 atoms) with sixteen Ti_{5c} adsorption sites has been used to model lower coverage densities of 0.125 ML (one molecule in the supercell). Preliminary geometry optimization were performed at Γ point, and then the most stable selected configurations have been further optimized using a k-point mesh of 2×2×1 to ensure the convergence of the electronic structure. The total adsorption energy per molecule has been defined as:

$$\Delta E_{ads}^{mol} = (E_{slab+nmol} - [E_{slab} + n_{mol}E_{mol}])/n_{mol} \quad (3.1)$$

where $E_{slab+nmol}$ is the total energy of the whole system, E_{slab} is the energy of the surface slab, E_{mol} is the energy of the molecule in the gas phase and n_{mol} is the number of molecules adsorbed on the surface.

The total density of states (DOS) and projected density of states (PDOS) were computed with a finer k-point mesh of 30×30×1. For 3D electron charge density plots of the localized states in the band gap, an isovalue of 0.003 au has been used.

The transition state structure for the protonation of the $-NH_2$ group of a single dopamine molecule to give $-NH_3^+$ on a fully covered 1×2 supercell model (72 atoms, 2 dopamine

molecules) has been evaluated with the NEB method,[219] as implemented in the Atomic Simulation Environment (ASE).[220] This toolkit is a driver, which we interfaced to the CRYSTAL14 code in order to use its internal NEB algorithm which, otherwise, it is not implemented in CRYSTAL14. The NEB procedure was carried out employing seven intermediate images. The reaction barrier for the dissociation process is defined as:

$$\Delta E_{diss}^{\ddagger} = E_{TS} - E_{slab+mol} \quad (3.2)$$

where, E_{TS} is the energy of the transition state geometry and $E_{slab+mol}$ is the total energy of the optimized geometry of the dopamine molecules adsorbed on the titania surface with unprotonated -NH_2 groups.

3.3. Low coverage: isolated molecule adsorption

In this section, we analyze the adsorption of an isolated molecule of catechol and then of an isolated molecule of dopamine on the anatase (101) TiO_2 surface. First, we define the nomenclature to label the various model structures obtained. Both catechol and dopamine may bind to the five-coordinated titanium (Ti_{5c}) on the anatase surface through one (monodentate, M) or two (bidentate, B) O atoms of the hydroxyl groups, in an undissociated (″U″), or dissociated (″D″) mode. Upon dissociation, one (″D_1″) or two (″D_2″) protons are transferred to neighboring surface two-fold coordinated O atoms (O_{2c}). Finally, dopamine may also bind through the N atom of the ammino group in a monodentate fashion (″M^{NH2}″).

We analyzed six different adsorption configurations of catechol, which differ both for the relative position of the molecule with respect to the surface orientation, and for the OH dissociation extent. The optimized geometries and the relative HSE06-D2 adsorption energies (ΔE_{ads}^{mol}) are shown in **Figure 3.1**. To enucleate the dispersion contribution to ΔE_{ads}^{mol}, we refer to some further data reported in **Table 3.2**. The six configurations are: 1) monodentate undissociated cathecol with the molecular plane parallel to the Ti_{5c} row ($MU_{//}$, **Figure 3.1a**); 2) monodentate undissociated cathecol with the molecular plane perpendicular to the Ti_{5c} row ($MU_{\perp}$, **Figure 3.1b**); 3) monodentate dissociated cathecol (MD, **Figure 3.1c**); 4) bidentate undissociated cathecol (BU, **Figure 3.1d**); 5) bidentate singly-dissociated (BD_1, **Figure 3.1e**) and 6) bidentate doubly-dissociated (BD_2, **Figure 3.1f**). The angle between the phenyl ring plane and the plane along the Ti_{5c} row (i.e. the [10-1] direction) is 18.76° and 72.29° for $MU_{//}$ and $MU_{\perp}$, respectively. In all the bidentate structures the phenyl ring tilts towards the nearest O_{2c} atoms, in agreement with previous studies.[110] For the monodentate geometries, the dispersion interactions between the molecule and the slab play a crucial role. As the distance between the average z coordinate of the phenyl ring and the slab decreases, the contribution of the dispersions interaction and, consequently, ΔE_{ads}^{mol} increases. Thus, the order of stability for the monodentate configurations is $MU_{//}$>MD> $MU_{\perp}$.

As an overall trend, the bidentate geometries of adsorption, already considered by Liu et al,[110] result to be more stable than the monodentate ones. In the doubly dissociated BD_2, the two dissociated protons are transferred on the nearest and on the farthest neighboring O_{2c} atoms, respectively (see **Figure 3.1f**). For BD_1 and BU, the undissociated hydroxyl groups preferentially form H-bonds with the farthest neighboring O_{2c} atoms of the surface (see **Figure 3.1d** and **Figure 3.1e**, respectively). We found that the BD_2 structure is approximately degenerate to BD_1 (-0.01 eV), therefore, in the low coverage regime, both configurations are

likely to exist, whereas the molecular adsorbed configuration BU is higher in energy. The contribution of the dispersion energies is nearly constant for the bidentate conformations (around -0.6/0.7 eV for HSE06-D2).

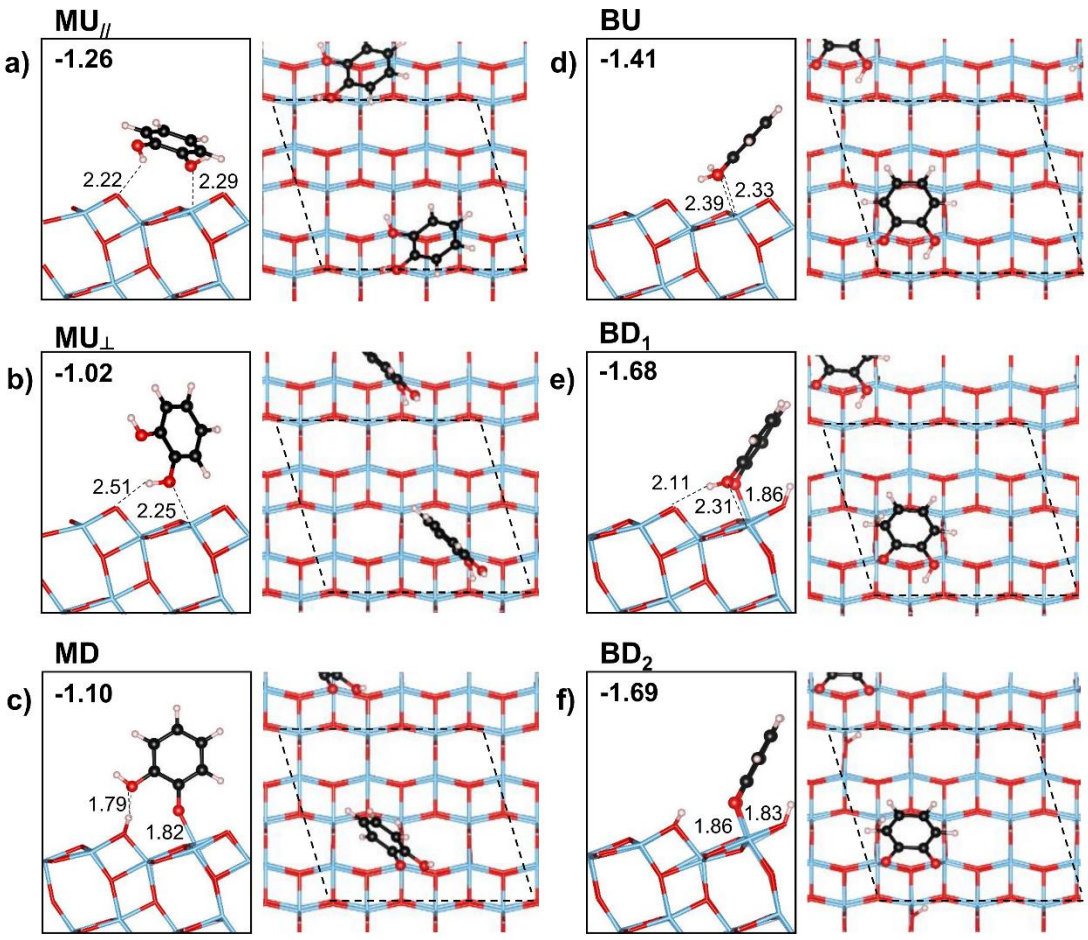

Figure 3.3. Adsorption modes (side and top views) and adsorption energies (in eV) for one molecule of catechol on the anatase (101) TiO_2 surface, as obtained by HSE06-D2.a) Monodentate undissociated parallel ($MU_{//}$) to the surface; b) Monodentate undissociated perpendicular ($MU_{\perp}$) to the surface; c) Monodentate dissociated (MD); d) Bidentate undissociated (BU); e) Bidentate singly-dissociated (BD_1); f) Bidentate doubly-bidissociated (BD_2). Significant distances are reported in Å.

Table 3.2. Adsorption energies (ΔE_{ads}^{mol}) in eV of the different configurations of one isolated molecule of catechol adsorbed on the anatase (101) surface TiO_2 surface, as calculated by HSE06-D2 and with HSE06 in the HSE06-D2 geometry (HSE06/HSE06-D2). For the labeling, refer to **Figure 3.1**.

ΔE_{ads}^{mol}	**HSE06-D2 (HSE06/HSE06-D2)**
MU$_{//}$	-1.26 (-0.58)
MU$^{\perp}$	-1.02 (-0.56)
MD	-1.10 (-0.68)
BU	-1.41 (-0.78)
BD$_1$	-1.68 (-1.03)
BD$_2$	-1.69 (-1.04)

Since we found that the bidentate (singly and doubly) dissociated adsorption modes are the most favored in the case of catechol, those are the ones we will consider for dopamine adsorption. Although dopamine presents many more configurational degrees of freedom than catechol, only few geometries of adsorption have been considered in the literature so far. [149,150,151] In **Figure 3.2** we report the six most interesting structures among those studied in the present work, with both the phenyl ring tilting towards the nearest surface O_{2c} (three on the left) and towards the nearest O_{3c} atoms (three on the right). The adsorption energies (ΔE_{ads}^{mol}) obtained by HSE06-D2 (and HSE06 on the HSE06-D2 optimized geometry) are summarized **Table 3.3**.

The configurations are: 1) bidentate and singly-dissociated dopamine with respect to the OH group and monodentate with respect to the NH_2 group binding to a surface Ti_{5c} atom ($B^OD_1M^{NH2}$, **Figure 3.2a**); 2) bidentate and doubly-dissociated dopamine with respect to the OH groups (B^OD_2 in **Figure 3.2b**); 3) bidentate and doubly-dissociated with respect to the OH groups and monodentate with respect to the NH_2 group binding a surface Ti_{5c} atom ($B^OD_2M^{NH2}$, **Figure 3.2c**). We always started the relaxation from the bidentate configuration, but in one case this evolved into a monodentate species ($M^OD_1M^{NH2}$, see **Figure 3.2a**). In the B^OD_2 adsorption mode, the amino-ethyl group ($-CH_2CH_2NH_2$) stands up toward the vacuum, while in $B^OD_2M^{NH2}$ the molecule bends towards the surface to allow the binding of the $-NH_2$ group to a Ti_{5c} and the formation of H-bonds with the surface O_{2c}. B^OD_2 is the dopamine corresponding structure for the BD_2 with catechol (**Figure 3.1f**) and it is the only bidentate configuration that was previously reported in the literature for dopamine. However, we find that it is the least stable among those considered in this work, by about 1 eV (**Table 3.3.**). Furthermore, since for B^OD_2

there is no additional interaction of the $–CH_2CH_2NH_2$ group with the surface, the molecule can be indifferently tilted towards the O_{2c} or towards the O_{3c} (the two structures are perfectly isoenergetic, ΔE_{ads}^{mol} = -1.64 eV). On the other hand, both for $B^OD_1M^{NH2}$ and $B^OD_2M^{NH2}$, the configurations bent towards the O_{3c} are slightly more favored, due to a larger interaction of the ring with the underlying surface. Since $B^OD_2M^{NH2}$ is the most stable adsorption mode (ΔE_{ads}^{mol} = -2.91 eV) and the relative stability with respect to $B^OD_1M^{NH2}$ is -0.24 eV, such structure is expected to be the predominant one in the low coverage regime. This conclusion is different from what found for catechol, where BD_2 and BD_1 structures are likely to co-exist, as discussed above.

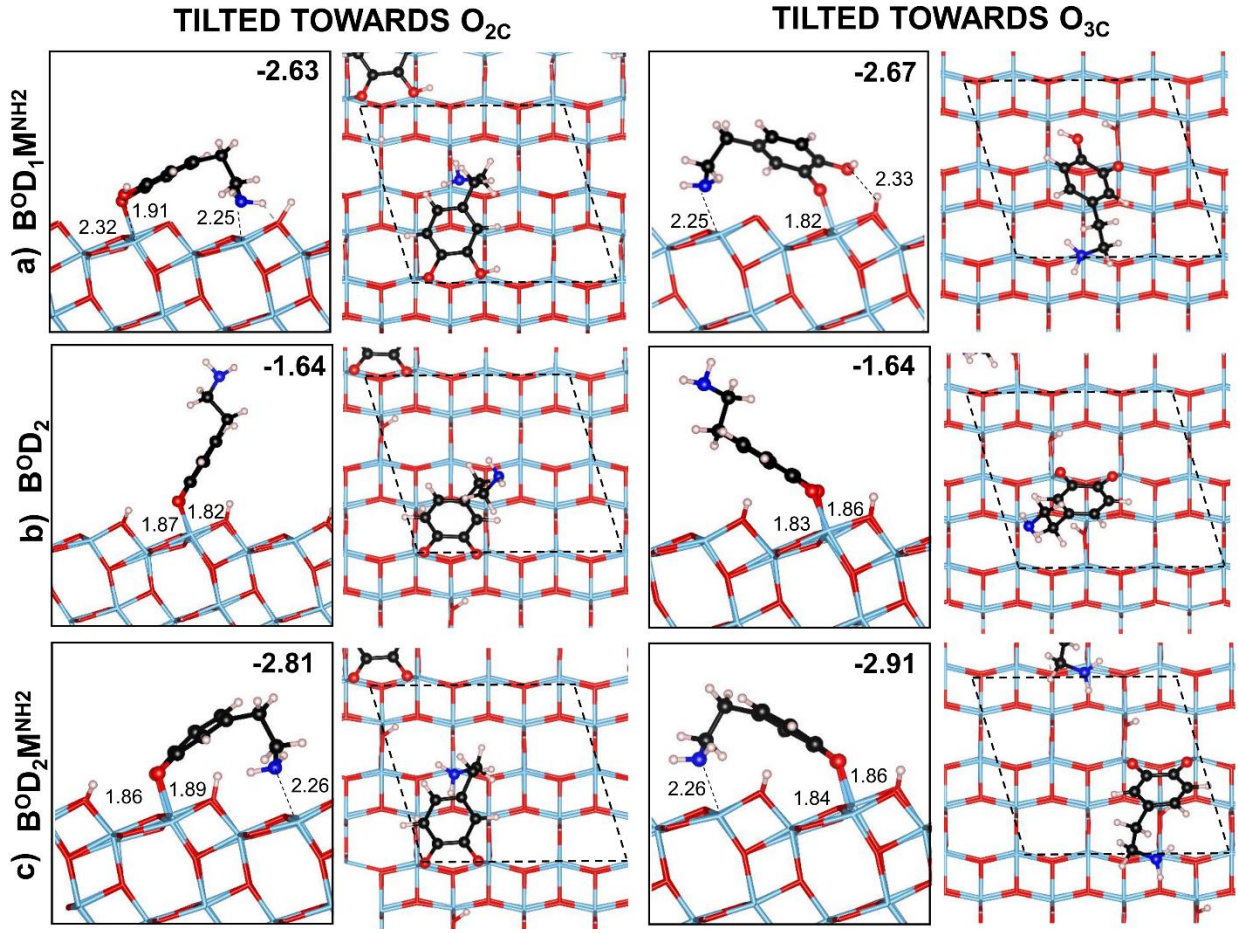

Figure 3.4. Adsorption modes (side and top views) and adsorption energies per molecule (ΔE_{ads}^{mol}, in eV) for one molecule of dopamine on the anatase (101) TiO_2 surface, as obtained by HSE06-D2. The molecules can be tilted both towards the O_{2c} atoms of the surface (left panel), and towards the O_{3c} (right panel). a) Singly-dissociated bidentate with respect to OH and monodentate with respect to NH_2 ($B^OD_1M^{NH2}$) when tilted towards O_{2c} an singly-dissociated monodentate ($M^OD_1M^{NH2}$) when tilted towards O_{3c}; b) Bidentate doubly-dissociated with respect to OH (B^OD_2); c) Bidentate doubly-dissociated with respect to OH and monodentate with respect to NH_2 ($B^OD_2M^{NH2}$). Significant distances are reported in Å.

Table 3.3. Adsorption energies **(ΔE_{ads}^{mol})** in eV of the different configurations of one isolated molecule of dopamine adsorbed on the anatase (101) surface TiO_2 surface, as calculated by HSE06-D2 and with HSE06 in the HSE06-D2 geometry (HSE06/HSE06-D2). For the labeling, refer to **Figure 3.2** and **Figure 3.3**.

Eads (eV)		**HSE06-D2 (HSE06/HSE06-D2)**	
		TILTED TOWARDS O_{2C}	**TILTED TOWARDS O_{3C}**
B^OD_2	-	-1.64 (-1.01)	-1.64 (-0.82)
$B^OD_2M^{NH2'}$	ab	-2.33 (-1.21)	-
	ae	-2.45 (-1.29)	-
	af	-2.33 (-1.12)	-
	be	**-2.66 (-1.54)**	**-2.65 (-1.54)**
	bf	-2.40 (-1.26)	-
	ef	-2.64 (-1.34)	-2.47 (-1.34)
$B^OD_2M^{NH2}$	be	-2.81 (-1.65)	-2.91 (-1.67)
$B^OD_2M^{NH3+}$	ae	-2.03 (-1.08)	-
	be	-2.09 (-1.17)	-
$B^OD_2M^{NH2'}$	-	-2.39 (-1.49)	-
$B^OD_1M^{NH2}$	-	-2.63 (-1.51)	-2.67 (-1.49)

For the most stable $B^OD_2M^{NH2}$ adsorption configuration of dopamine, both OH groups are dissociated and, consequently, two protons are transferred to surface O_{2c} atoms. We considered different H positions, as detailed in **Figure 3.3** and in **Table 3.3**, to define which is the lowest energy one, i.e.: one H on the O_{2c} just under the phenyl ring and the other H on a O_{2c} in the next parallel row (see **Figure 3.2c**).

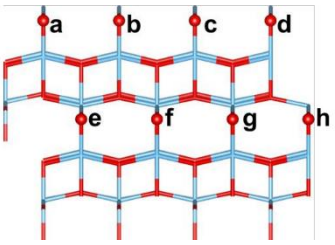

Figure 3.3. Labeling of the different possible positions for the dissociation of the H atoms of an isolated molecule of dopamine in a $B^OD_2M^{NH2}$ configuration.

Finally, we also evaluated the cell size effect on the absorption energy values by means of a larger surface model (2×4 supercell, with 16 Ti_{5c} sites). Only $B^{O}D_1M^{NH2}$ resulted to be slightly stabilized, with ΔE_{ads}^{mol} = -2.71 eV (vs -2.67 eV in the 1×4 supercell). This result further confirms that, at low coverage, this is the principal adsorption mode for dopamine molecules on the anatase (101) TiO_2 surface.

3.3.1. Electronic properties

In this section, we investigate and compare the electronic structure of the most stable configurations identified in the previous section both for catechol and dopamine. In **Table 3.4**, we report the values for the electronic band (E_g) and HOMO-LUMO ($\Delta_{HOMO\text{-}LUMO}$) gaps calculated for the anatase TiO_2 (101) slab, for the BD_2 (even if it is nearly isoenergetic with BD_1 at low coverage, it was found to be predominant at increasing coverage)[110] and $B^{O}D_2M^{NH2}$ structures for catechol and dopamine, respectively. The $\Delta_{HOMO\text{-}LUMO}$ gap is defined as the difference between the highest occupied state introduced by the adsorbed molecule and the bottom of the conduction band (CB). As it can be seen, the band gap (E_g) is essentially not affected by the adsorption of one single molecule of catechol BD_2 or dopamine $B^{O}D_2M^{NH2}$ (E_g=4.11 eV for the slab alone and E_g=4.12 eV with the molecules adsorbed). The $\Delta_{HOMO\text{-}LUMO}$ gap is evaluated to be 2.15 eV for BD_2 catechol and 2.26 eV for dopamine $B^{O}D_2M^{NH2}$, which indicates a sensible red-shift of the optical band gap of the TiO_2 surface resulting from the adsorption. In addition, for both systems, we have calculated the total (DOS) and projected density of states (PDOS) in the range between −5 and +5 eV, with reference to the Fermi energy of the system. The electronic structures (**Figure 3.4**) for catechol BD_2 and dopamine $B^{O}D_2M^{NH2}$ are shown in **Figure 3.4a** and **Figure 3.4b**, respectively and present several analogies. The 3D charge density plots for the mid-gap states arising in the presence of the adsorbed single molecule of catechol and dopamine are reported in **Figure 3.5**.

Table 3.4. Electronic (E_g) and HOMO-LUMO ($\Delta_{HOMO\text{-}LUMO}$) band gap in eV for one single molecule of catechol BD_2 and dopamine $B^{O}D_2M^{NH2}$ adsorbed on the anatase (101) TiO_2 surface, as calculated by HSE06-D2.

	E_g (eV)	$\Delta_{HOMO\text{-}CB}$ (eV)
BARE TiO_2 SURFACE	4.11	-
TiO_2 + CATECHOL(BD_2)	4.12	2.15
TiO_2 + DOPAMINE($B^{O}D_2M^{NH2}$)	4.12	2.26

The peak placed at lowest energy (HOMO-2) is mainly due to the *p* state of the O atoms of the molecule, while the other two states (HOMO-1 and HOMO) are related to the π and π^* orbitals of the C atoms of the phenyl ring. It is possible to see that, differently from HOMO and HOMO-1 states, which are totally localized on the molecule, the electronic density for HOMO-2 has a contribution also from the nearest surface O_{3c} atoms.

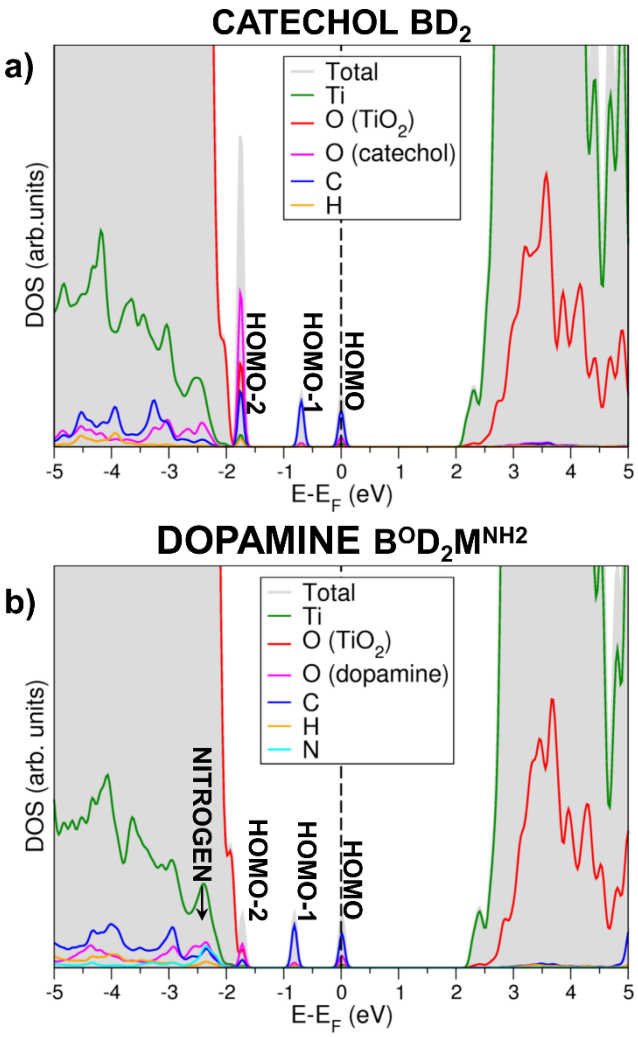

Figure 5.4. Total (DOS) and projected (PDOS) density of states for low coverage adsorption of a single molecule of a) catechol BD_2 and b) of dopamine $B^{O}D_2M^{NH2}$ on the anatase (101) TiO_2 surface. The zero energy reference is set at the Fermi energy of the system and highlighted by a dotted line.

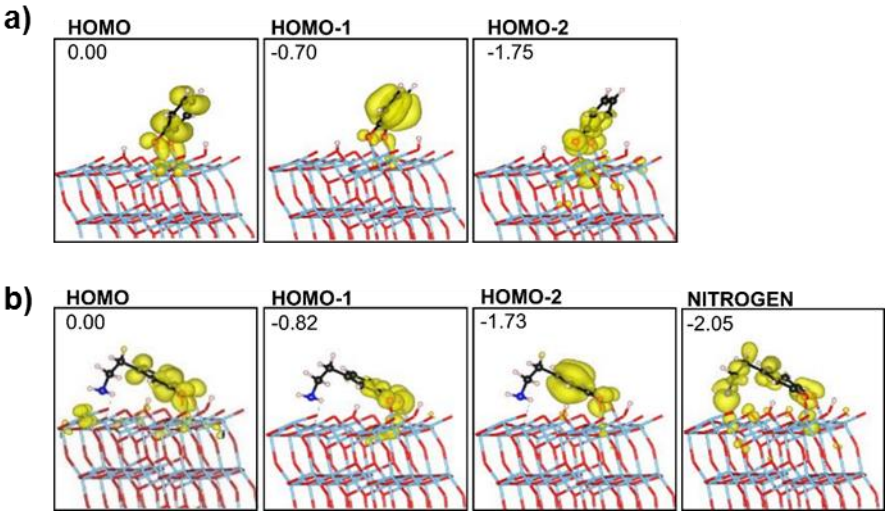

Figure 3.5. 3D charge density plot (isovalue 0.003 a.u.) of the mid-gap states for one isolated molecule of a) catechol BD_2 and b) dopamine $B^{O}D_2M^{NH2}$ adsorbed on anatase (101) TiO_2. For $B^{O}D_2M^{NH2}$ the state relative to nitrogen located inside the valence band is also reported.

For dopamine $B^{O}D_2M^{NH2}$, the peak relative to the *p* states of N is placed inside the valence band and the 3D charge density plot is reported in **Figure 3.5b**. This is due to the formation of a bond between N and the underneath Ti_{5c}, increasing the hybridization of the molecule with the surface.

3.4. Growth mechanism

In this section, we focus on the growth mechanism of one full monolayer of catechol and then of dopamine molecules on the TiO_2 anatase (101) surface. We assume that deposition takes place under kinetic control and, therefore, molecules quickly arrange on the surface one after the other, before the ethyl-amino functionality of dopamine has time to bend towards the surface. We will give more insights about the possible final and thermodynamically more stable configurations and adsorption patterns of the full monolayer of dopamine molecules in the next Section 3.3. The molecules are considered to grow in the bidentate adsorption mode: BD_2 for catechol (see **Figure 3.6** and image on left side, central row of **Figure 3.7),** which was found to be the most stable adsorption mode at increasing coverage,[110] and up_NH_2 for dopamine (see image on left side, bottom row of **Figure 3.7**).

The up_NH_2 adsorption mode is a doubly dissociated bidentate configuration only slightly different with respect to B^OD_2 (see **Section 3.3**, **Figure 3.2b**) due to the different orientation of the amino-ethyl functionality. In the up_NH_2 adsorption mode this points upwards, towards the vacuum, and does not interact with the surface (see **Figure 3.7**), as suggested by previous studies.[150,151,152] This is not the only possible adsorption mode for dopamine (neither the most stable, see **Section 3.3**), but it is the one we expect to observe in the initial phase of the self-assembling growth process.

In the bidentate modes above, molecules bind two of the eight Ti_{5c} sites present in the 1×4 supercell, therefore at full coverage four molecules adsorb. The adsorption energies at increasing coverage for catechol BD_2 are reported in **Table 3.5**, whereas the adsorption configurations for 0.5 and 1.0 ML coverage regimes are shown in **Figure 3.6** and **Figure 3.7** middle row), respectively. At 0.5 ML coverage, the second catechol molecule can bind either next to the first, thus on the same Ti_{5c} row ("0.5 ML[same row]" in **Table 3.5** and **Figure 3.7a**, or on the parallel Ti_{5c} row ("0.5 ML[diff. row]" in **Table 3** and **Figure 3.7b**), along the [11-1] direction and zigzag ("0.5 ML[zig-zag]" in **Table 3.5** and **Figure 3.7c**). The last two configurations are nearly isoenergetic and are favored by -0.34/-0.35 eV with respect to the first one.

Table 3.5. Adsorption energies per molecule (ΔE_{ads}^{mol}, in eV) for different growing patterns and coverages of catechol BD_2 adsorbed on the anatase (101) TiO_2 surface, as calculated by HSE06-D2. For the labeling, refer to **Figure 3.1**, **Figure 3.6** and **Figure 3.7**.

BD_2 Catechol Coverage	**N. Occ Ti_{5c}**	**N. molecules**	**ΔE_{ads}^{mol} (eV) HSE06-D2**
0.25 ML	2/8	1	-1.69
0.5 ML[same row]	4/8	2	-1.62
0.5 ML[diff. row]	4/8	2	-1.96
0.5 ML [zig-zag]	4/8	2	-1.97
1.0 ML [11-1] or [1-1-1]	8/8	4	-1.98
1.0 ML [zig-zag]	8/8	4	-1.99

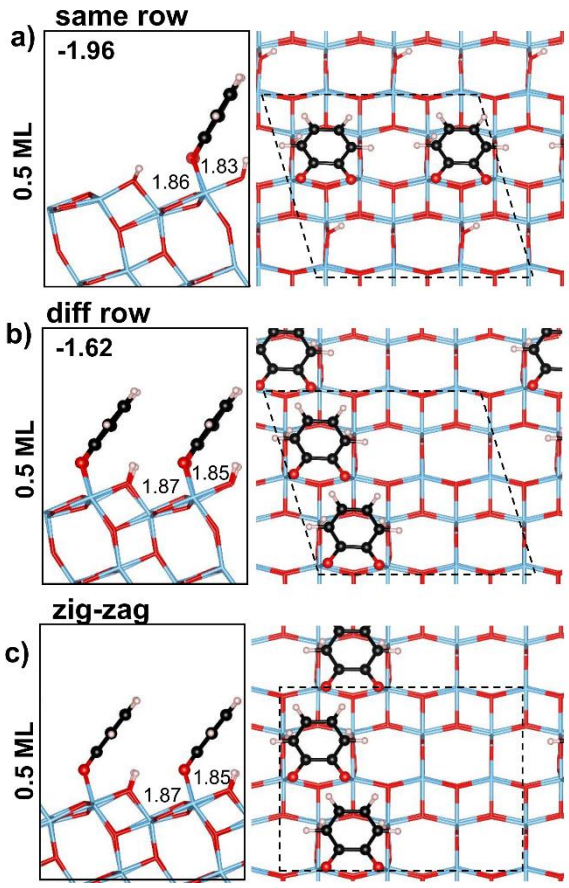

Figure 3.6. Adsorption modes (side and top view) and adsorption energies (ΔE_{ads}^{mol}) per molecule (in eV) for half coverage of catechol BD_2 on the anatase (101) TiO_2 surface, as obtained by HSE06-D2: a) half coverage (two molecules per supercell) on same row, and on b) different rows. Significant distances are reported in Å.

For the full coverage regime of bidentate molecules three different patterns are possible, as represented in **Figure 3.7**: the already mentioned growth along the [11-1] direction (**Figure**

3.7a), the symmetrically equivalent one along the [1-1-1] direction (**Figure 3.7b**) and the zig-zag growth (**Figure 3.7c**), modeled by means of an orthorhombic cell. According to our calculation, the zig-zag pattern is isoenergetic with those along the [11-1] and [1-1-1] direction in the case of catechol. Experimentally, however, Liu et al. observed by means of an STM (Scanning Tunneling Microscope) study that an adsorbed monolayer of catechol molecules on the anatase (101) TiO_2 surface forms elongated islands along the two symmetric directions [11-1] and [1-1-1].[110] Therefore, for some kinetic reasons that do not emerge from our static calculations, the zigzag pattern is not experimentally observed.

In the case of a just deposited dopamine monolayer (up_NH_2 configuration), we obtain again similar energies for the corresponding three possible growth directions ([11-1], [1-1-1] and zigzag, as shown in bottom row of **Figure 3.7**). Since in this case, no experimental STM image is reported in the literature, we cannot exclude the possibility of a zigzag type growth pattern, as discussed in the next **Section 3.5**.

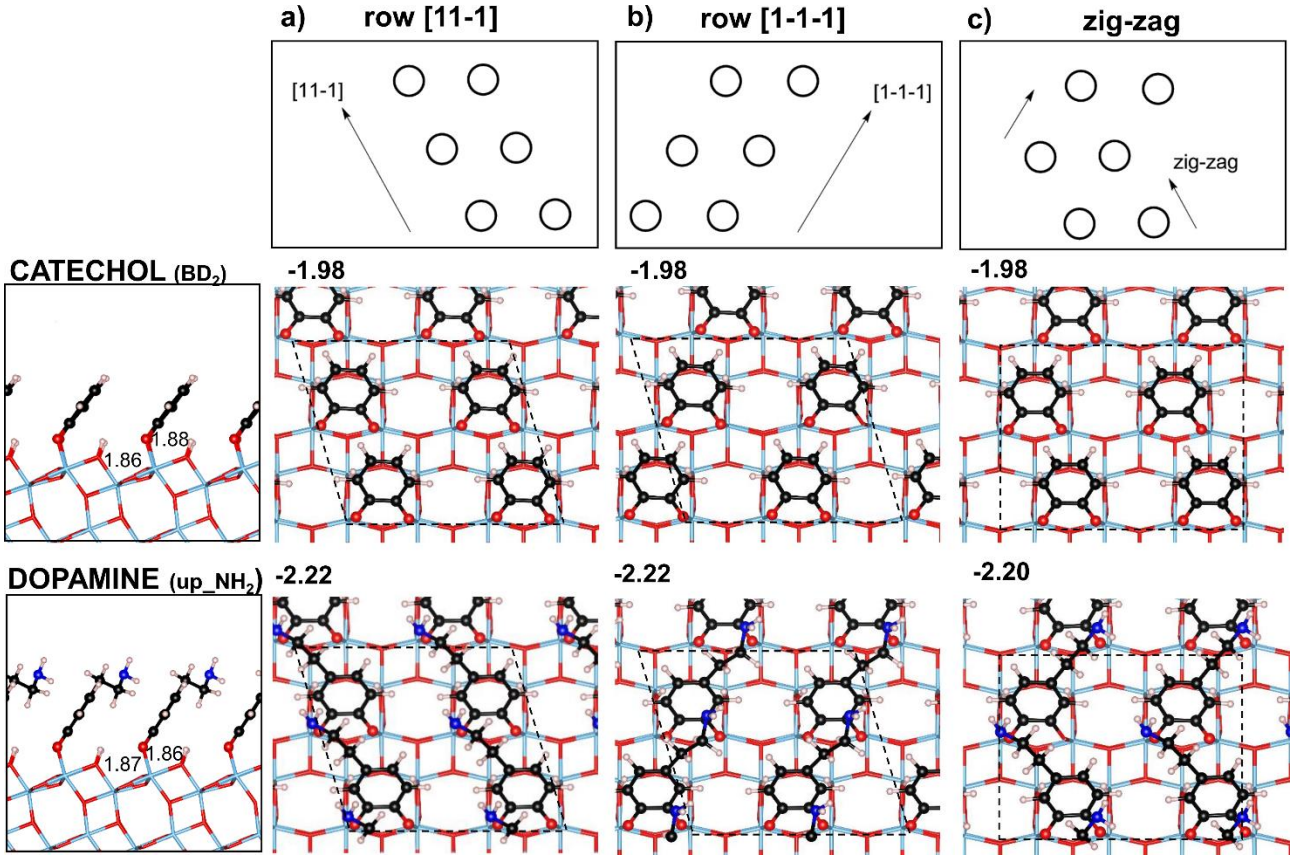

Figure 3.7. Adsorption modes (side and top view) for different growing patterns and adsorption energies per molecule (ΔE_{ads}^{mol}, in eV) for a full monolayer (1.0 ML) of bidentate BD_2 catechol (upper panel) or bidentate up_NH_2 dopamine molecules (lower panel) on the anatase (101) TiO_2 surface, as calculated by HSE06-D2. The growth of the full monolayer is schematically represented at the top: along the a) [11-1] row; b) [1-1-1] row; and with a c) zig-zag pattern.

3.5. Full coverage of dopamine

In this section, we discuss in detail the different possible minimum structures for a full monolayer of dopamine molecules. We will first focus on the [11-1] growth direction (see **Figure 3.7a**).

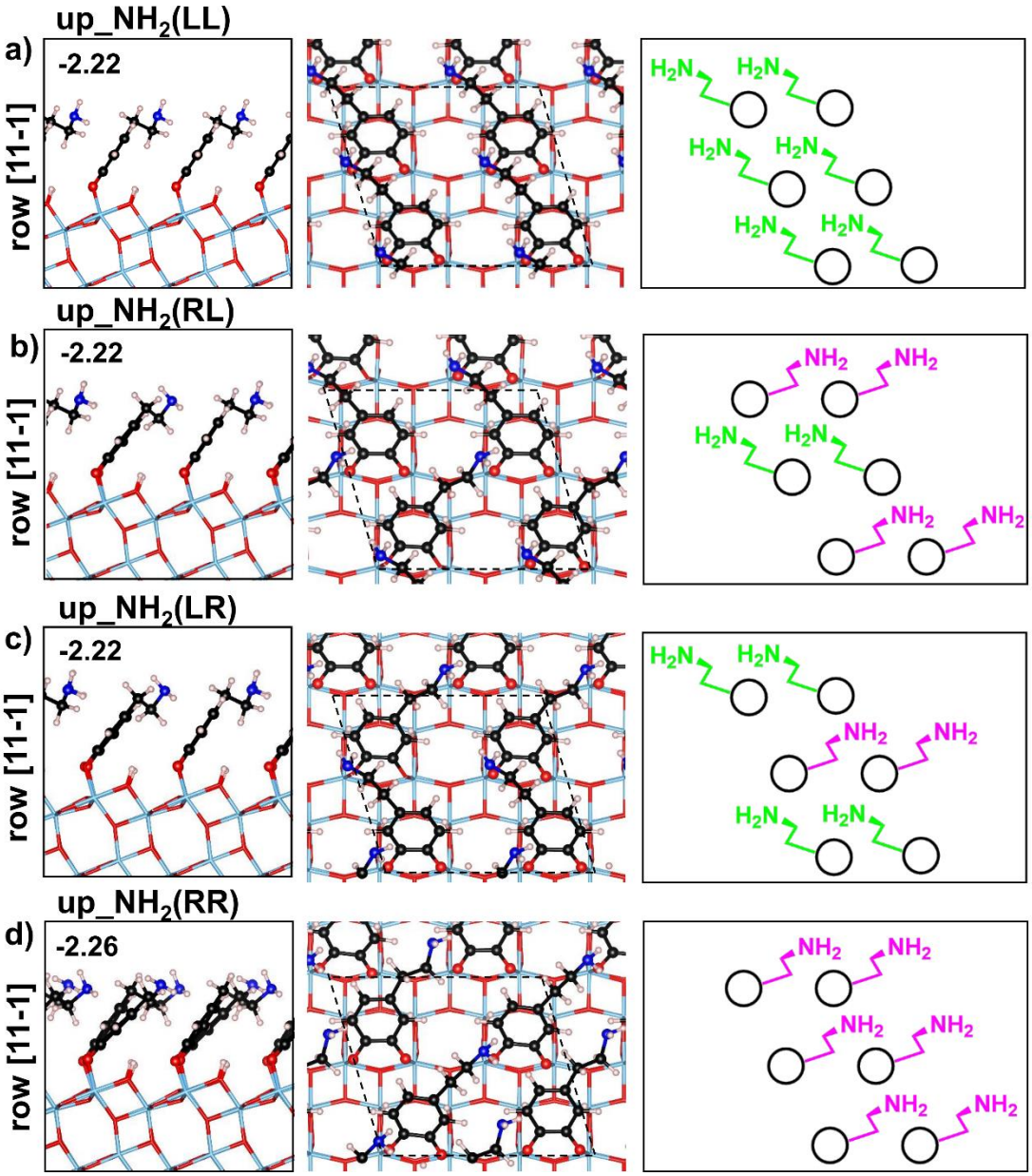

Figure 3.8. Adsorption modes (side and top view), adsorption energies per molecule (ΔE_{ads}^{mol}, in eV) and schematic top view sketch of the $–CH_2CH_2NH_2$ functionality for a full monolayer of dopamine molecules a) up_NH_2(LL), b) up_NH_2(RL), c) up_NH_2(LR), and d) up_NH_2(RR) adsorbed on the anatase (101) TiO_2 surface. LEFT-oriented and RIGHT-oriented functional groups are marked in green and purple, respectively.

More configurations for the monolayer of the up_NH_2 dopamine molecules are possible than the ones shown in **Figure 3.7a**, depending on the relative orientation of the $–CH_2CH_2NH_2$ group with respect to the [010] direction. The equilibrium structures, the schemes of adsorption patterns and the relative adsorption energies are reported in **Figure 3.8**. More specifically, the

$–CH_2CH_2NH_2$ functional group of the four dopamine molecules can be all LEFT-oriented (up_NH_2(LL), **Figure 3.8a**), mixed RIGHT/ LEFT (up_NH_2(RL), **Figure 3.8b**) or LEFT/RIGHT (up_NH_2(LR), **Figure 3.8c**), or all RIGHT-oriented (up_NH_2(RR), **Figure 3.8d**). These adsorption patterns are nearly isoenergetic and their appearance is consequently equally probable from a thermodynamic point of view. This fact has crucial consequences on the final adsorption structure of the dopamine molecules composing the monolayer on anatase (101) TiO_2, as we will extensively discuss in the following.

In order to investigate how the temperature will affect the rearrangement of the as-deposited up_NH_2 dopamine molecules in the three possible configurations, we performed three DFTB molecular dynamics runs at 1 atm and 300 K. To monitor the dynamical behavior of different configurations considered, we plotted the p(z) distributions of the vertical (z) component of the distance between the N atom of the dopamine molecules, and the Ti_{5c} atoms of the surface (see **Figure 3.9**). In the case of up_NH_2(RR) (black line in **Figure 3.9**), all the functional groups which initially are oriented towards the vacuum, rotate during the simulation allowing the N atoms of each dopamine molecule to bend down towards the slab (as shown going from **Figure 3.10a** to **Figure 3.10b**). This gives rise to a major peak of the p(z) at ~ 3.5 Å, thus having the N atom very close to the surface. In the case of up_NH_2(RL) (blue line in **Figure 3.9**), only for half of the dopamine molecules (the ones with the ethyl-amino functionalities RIGHT-oriented) is possible to rotate their functional groups and to bend towards the surface because of the steric hindrance of another dopamine molecule in front of them. Thus, the p(z) presents two peaks: one at ~ 3.5 Å, relative to the molecules that bent down, and one at ~ 6.5 Å relative to the molecule (LEFT-oriented) that cannot bend down. For the up_NH_2(LL) configuration (red line in **Figure 3.9**), all the N atoms remain at ~ 6.5 Å since none of functional groups has the space to bend down toward the surface. In this last case, we can notice the presence of a second small peak at around 4.5-5 Å in the p(z) distribution. This is due to a partial rotation of the $–CH_2CH_2NH_2$ group induced by the temperature, which does not result in the complete sloping towards the surface.

The result of the MD simulation starting from an up_NH_2(RR) configuration is schematically represented in the first part of **Figure 3.10** (**a** and **b**).

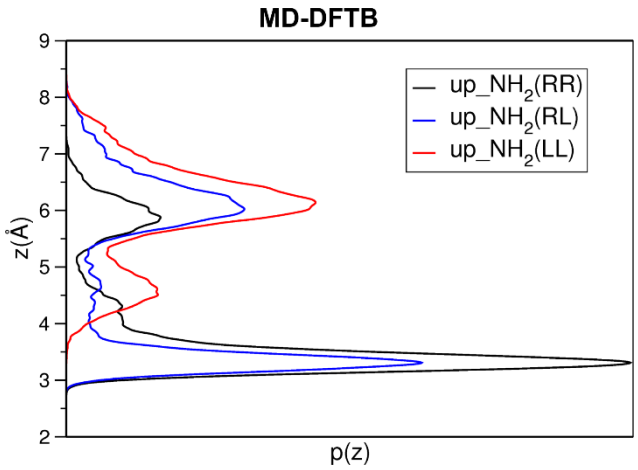

Figure 3.9. DFTB distribution p(z) of vertical z component of the distances between the N atoms of the ethyl-amino group of the dopamine monolayer and the (101) anatase TiO_2 surface (Ti_{5c} atoms). Colors refer to the different initial configurations, up_NH_2(RR) in black, up_NH_2(RL) in blue and up_NH_2(LL) in red.

As a result of a rotation, we observe a bidentate down_NH_2(RR) structure (**Figure 3.10b**), where all the amino-ethyl groups have sloped down and H-bonding with the anchoring O atoms of two neighboring dopamine molecules on the next parallel Ti_{5c} row (see the scheme in **Figure 3.10**). This down_NH_2(RR) structure is extremely stable (ΔE_{ads}^{mol} = -2.63 eV), almost -0.40 eV more stable than up_NH_2(RR) (see **Table 3.5**). We can estimate the barrier for the process of –$CH_2CH_2NH_2$ rotation/bending to be of the order of kT (25 meV), where k is the Boltzmann constant, since this process occurred within the first 10 ps of the MD at 300 K.

When the dopamine molecules bind the surface through a bidentate adsorption mode, the protons deriving from the dissociation of the OH groups saturate all the O_{2c} of the surface forming bridging $O_{2c}H$ groups. Therefore, since at the full coverage there is such a high density of bridging $O_{2c}H$ groups formed on the surface, we considered the possibility that some of the protons are transferred to the NH_2 moieties of the dopamine molecules, resulting in the formation of R-NH_3^+ groups. Indeed, we found that this is a thermodynamic favorable process for all the four molecules, leading to the formation of a very stable structure (ΔE_{ads}^{mol} = -3.12 eV) down_NH_3^+(RR) structure (**Figure 3.10c**). Each proton transfer is associated to an energy stabilization of nearly -0.15 eV. All adsorption energies are detailed in **Table 3.5**. Some other less stable optimized structures were examined throughout this work, but none of them resulted to be more stable than the down_NH_3^+(RR) structure (**Figure 3.10c**). Therefore, we did not show them in this thesis work.

To confirm that the protonation of the R–NH_2 groups of the dopamine molecules to form R-NH_3^+ is feasible from a kinetic point of view, we computed the activation barrier by means of nudged elastic band calculations (NEB). The process is found to be barrierless, so we can conclude that when and if the R–NH_2 group of a dopamine molecule gets close to the anatase

(101) TiO_2 surface, there will be a spontaneous proton transfer from the surface $O_{2c}H$ to the R–NH_2 group.

Differently from the low coverage regime, where all the configurations considered are most stable if the phenyl ring is tilted toward the O_{3c} atom of the surface (see **Figure 3.2** in **Section 3.3**), at full coverage a larger stability is observed when the phenyl ring is tilted toward the O_{2c}. For the most favorable down_NH_3^+, the difference is of -0.27 eV in favor of the tilting towards the O_{2c}.

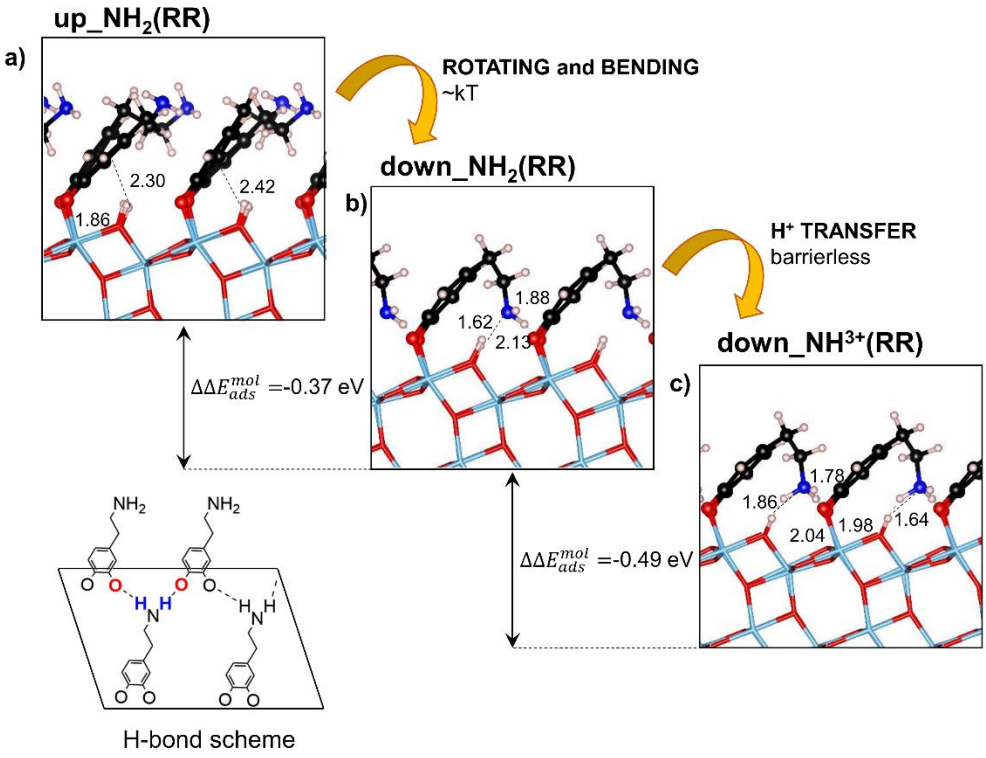

Figure 3.10. Process of rotation and protonation of the adsorbed dopamine molecules in the full coverage regime, starting from a) up_NH_2(RR) configuration, resulting in b) down_NH_2(RR) structure and followed by the protonation, which yields the c) down_NH_3^+(RR) structure. Adsorption energy per molecule (ΔE_{ads}^{mol}, in eV) and differences of adsorption energy between configurations ($\Delta\Delta E_{ads}^{mol}$) are reported. On the left bottom corner we show a scheme of H-bonding for the full monolayer of dopamine molecules in the down_NH_2(RR) configuration. Significant distances are reported in Å.

On the basis of the results obtained so far: i) all the up_NH_2 configurations in **Figure 3.8** are almost isoenergetic (see also **Table 3.5**), ii) the –$CH_2CH_2NH_2$ tend to rotate and slope down (as observed during the DFTB-MD simulations), iii) the proton transfer from $O_{2c}H$ to the R–NH_2 is barrierless, and iv) down_NH_3^+ is the thermodynamically most favorable adsorption mode, we may infer what are the possible scenarios for the different patterns of a full monolayer of dopamine molecules along the [11-1] row on anatase (101) TiO_2 surface. The configuration where all the molecules are RIGHT-oriented (up_NH_2(RR) in **Figure 3.8d**) result in a the structure where 100% of –$CH_2CH_2NH_2$ groups slope down and consequently accept a proton from the surface, leading to the formation of down_NH_3^+(RR) (see **Figure 3.10a**). On the other

hand, the configuration where all the molecules are LEFT-oriented (up_NH_2(LL)) along the [11-1] direction (see **Figure 3.8a**) remain 100% up, with the non-protonated NH_2 group, since there is no sufficient space for the $–CH_2CH_2NH_2$ groups to rotate and bend down towards the surface. Finally, the mixed 50% RIGHT/LEFT (up_NH_2(RL) in **Figure 3.8b**) or LEFT/RIGHT (up_NH_2(LR) in **Figure 3.8c**) configurations will result in 50% up_NH_2 and 50% down_NH_3^+ structure. Therefore, overall, the proportion between the dopamine molecules up_NH_2 and the protonated molecules down_NH_3^+present on the surface is 50:50. Our conclusions provide a solid rationalization of the experimental observations by Syres et al., based on photoemission spectra (XPS) of one monolayer of dopamine molecules on the anatase TiO_2 (101) surface.[144] The measurements detected the presence of NH_2 and of another N containing species, whose binding energy is consistent with that of the NH_3^+ group, with a proportion of nearly 50:50.

Table 3.5. Adsorption energy per molecule (ΔE_{ads}^{mol}, in eV) for the possible configurations reached during the formation of a full monolayer of dopamine, as calculated by HSE06-D2 and by HSE06 on the HSE06-D2 geometry (HSE06/HSE06-D2). For the labeling, refer to **Figure 3.7**, **Figure 3.8** and **Figure 3.10**.

ΔE_{ads}^{mol} **HSE06-D2 (HSE06/HSE06-D2)**	**row [11-1] TILTED TOWARDS O_{2c}**	**zig-zag**
up_NH_2(RR)	-2.26	-
up_NH_2(RL)	-2.22	-2.20
up_NH_2(LR)	-2.22	-
up_NH_2(LL)	-2.22	-
down_NH_2(RR)	-2.63	-
down_NH_3^+(RR)	-3.12	-3.06

This scenario does not only hold for the case of the dopamine molecules deposited along the [11-1] direction, but also along the [1-1-1] direction and with the zig-zag pattern (see Section 3.2 for definitions). For all these three cases, there is a proper orientation of the ethyl-amino groups, which allows the rotation, the sloping and the consequent protonation, forming the thermodynamic most stable down_NH_3^+structures (see **Figure 3.10**), but also an improper orientation, which prevents such motion of the ethyl-amino groups, leaving all the dopamine molecules in the up_NH_2 configuration, and finally a mixed configurations, where up_NH_2 and down_NH_3^+ are equally represented.

In particular, regarding the case of the growth along the [1-1-1] row, it results to be symmetrically equivalent to the [11-1]: when the molecules on the surface assemble with the

functional group RIGHT-oriented (**Figure 3b**), they assume an up_NH_2 adsorption configuration, since there is not enough space for the $–CH_2CH_2NH_2$ rotation. On the contrary, when they are LEFT-oriented, the dopamine molecules will arrange to reach the most stable down_NH_3^+ structure (**Figure 8b**). The case in which the molecules are half RIGHT- and half LEFT-oriented results in a mixed 50% up_NH_2 and 50% down_NH_3^+ structure for full coverage.

Even in a zigzag growth regime, there are configurations, with alternating LEFT- and RIGHT- oriented groups, where the molecules are prevented from sloping down, such as the one in **Figure 3.7c**, and configurations, with alternating RIGHT- and LEFT- oriented groups, where the molecules find enough space to slope down, producing the down_NH_3^+ pattern (see **Figure 8c**). If the functional groups are all RIGHT- or all LEFT-oriented, 50% of the molecules are expected to be up_NH_2 and 50% to be down_NH_3^+.

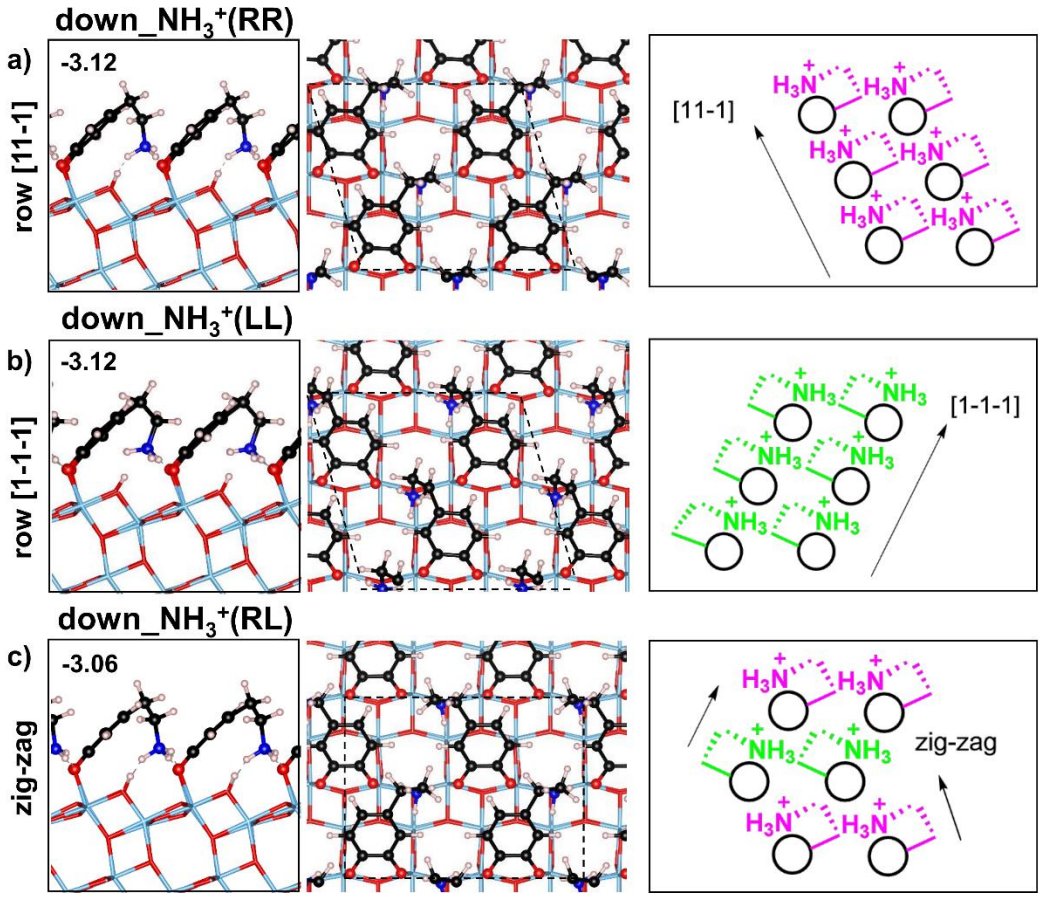

Figure 3.11. Possible growing patterns and related adsorption energies per molecule (ΔE_{ads}^{mol}, in eV) for a full monolayer of down_NH_3^+ dopamine molecules on the anatase (101) TiO_2 surface, as calculated by HSE06-D2. Growth of full monolayer is reported along the a) [11-1] row); b) [1-1-1] row; and with a c) zig-zag pattern.

Overall, independently from the deposition pattern considered, in a full monolayer of dopamine molecules on anatase (101) TiO_2 surface, we expect to observe an average of 50% of

dopamine molecules standing up and preserving the NH_2 group, and 50% of protonated molecules (NH_3^+), as a result of the rotation and sloping of the ethyl-amino functionality.

3.5.1. Electronic properties

In this section, we investigate and compare the electronic structure of one full monolayer of dopamine molecules in the up_NH_2(RR) and down_NH_3^+(RR) configurations adsorbed on anatase (101) TiO_2 in terms of the total (DOS) and projected density of states (PDOS) in the range between −5 and +5 eV with reference to the Fermi energy of the system. The electronic structures for the up_NH_2(RR) and down_NH_3^+(RR) configurations are shown in **Figure 3.12.** We report in **Table 3.7** the values for the electronic (E_g) and HOMO-LUMO ($\Delta_{HOMO-LUMO}$) band gap for the two structures.

The PDOS of up_NH_2(RR) (**Figure 3.12a**) presents five mid-gap states. The HOMO is predominantly constituted by one π state of the phenyl ring with a major contribution from the C atoms, whereas the HOMO-1 is localized on two equivalent N atoms of the dopamine molecule. Also the HOMO-2 state is mainly constituted by the *p* states of the nitrogen atoms while the HOMO-3 has a strong contribution of the bonding π orbital of the carbon atoms of the phenyl ring. The HOMO-4 is formed by the *p* states of the anchoring oxygen states of the dopamine molecules, hybridized with those from the O atoms of the TiO_2 surface.

Table 3.7. Electronic (E_g) and HOMO-LUMO ($\Delta_{HOMO-HOMO}$) band gaps in eV for one full monolayer of dopamine molecules adsorbed on the anatase (101) TiO_2 surface in the up_NH_2(RR) and down_NH_3^+ configurations, as calculated by HSE06-D2.

	E_g (eV)	**$\Delta_{HOMO-CB}$ (eV)**
up_allNH_2	4.16	2.20
down_NH_3^+	4.32	2.66

The PDOS of the down_NH_3^+(RR) full monolayer structure (**Figure 3.12b**) presents only three mid-gap states. The HOMO and HOMO-1 are essentially π orbitals of the C atoms of the phenyl ring. The HOMO-2 state has a major contribution from the O atoms states of the adsorbed dopamine molecules. Differently from up_NH_2(RR), there are no mid-gap states related to the N atom, which are deep inside the valence band, because of the large stabilization effect due to the positive charge. For the same reason, both the electronic (E_g=4.33 eV) and the optical ($\Delta_{HOMO-CB}$=2.66 eV) band gap are wider for down_NH_3^+ with respect to the

up_NH_2(RR) configuration (see **Table3.7**). The 3D charge density plots for the mid-gap states arising in the presence of the adsorbed dopamine molecules are reported in **Figure 3.13**.

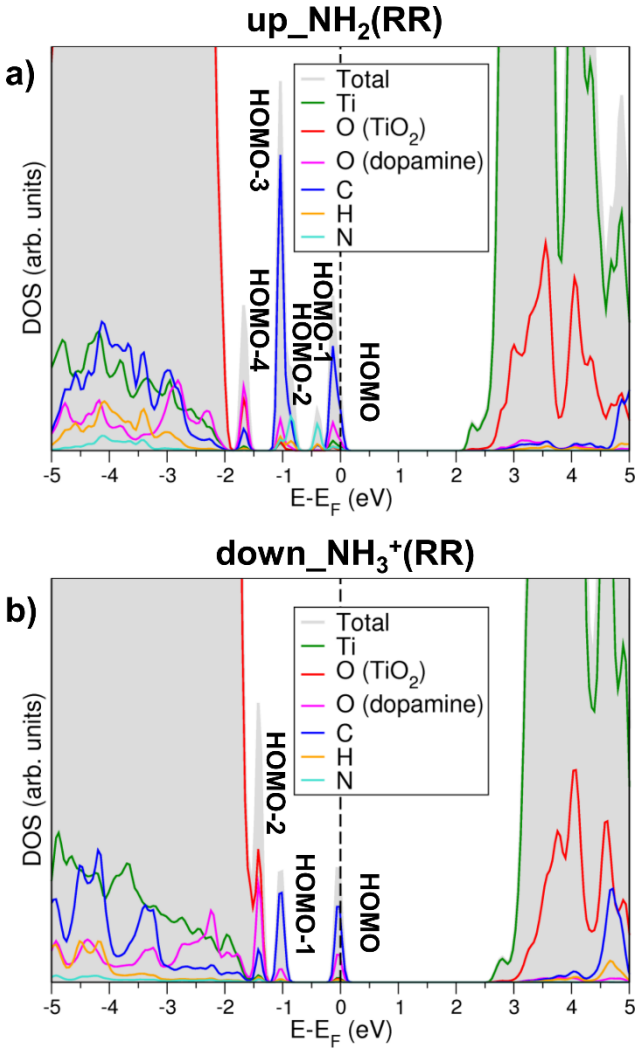

Figure 3.12. Total (DOS) and projected (PDOS) density of states for the adsorption of one full monolayer of dopamine molecules a) up_NH_2(RR) and b) down_NH_3^+(RR) on the anatase (101) TiO_2 surface. The zero energy reference is set at the Fermi energy of the system and highlighted by a dotted line.

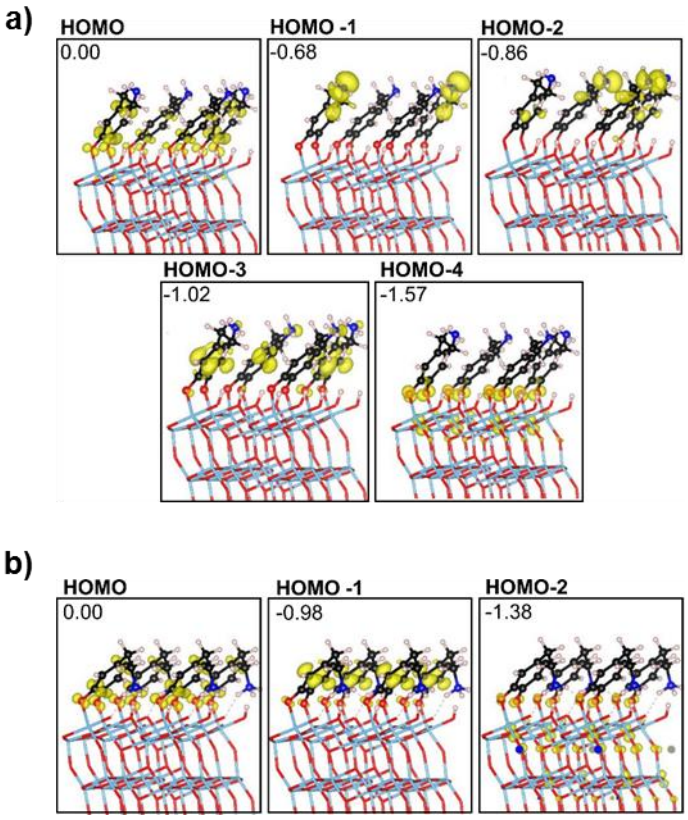

Figure 3.13. 3D charge density plot (isovalue 0.003 a.u.) of the mid-gap states for 1ML of dopamine a) up_NH_2(RR) and b) down_NH_3^+(RR) adsorbed on anatase (101) TiO_2.

3.6. Thermodynamic growth

As discussed at the beginning of **Section 3.4**, the patterns investigated so far are those expected under kinetic control. The paramount assumption is that the self-assembling process, namely the mechanism of adsorption of one dopamine molecule after the other on the surface of TiO_2, takes place before any added molecule has the time to bend down towards the surface. In this last section, we wish to discuss what would happen under thermodynamic control. In these conditions, we expect that 100% of dopamine molecules will bent down and receive a proton from the surface leading to the down_NH_3^+ adsorption mode, as we will describe in the following.

Under thermodynamic control, the self-assembling process to a full monolayer of dopamine molecules on anatase (101) occurs so slowly that there is sufficient time for the ethyl-amino group of the first adsorbed dopamine molecule to bend down towards the surface and/or eventually move to another adsorption site before a second molecule reaches the surface. Indeed, the dopamine molecules may have certain mobility on the surface, through the flipping from one Ti_{5c} atoms of the surface to another by rotation around one Ti-O bond. The thermodynamic growth is, therefore, completely different from the kinetic growth presented in **Section 3.4**.

We can consider the growth along the [11-1] row as a case study (see **Figure 3.14**) and analyze an initial situation where the first molecule is adsorbed with the ethyl-amino group as RIGHT-oriented. A second molecule will adsorb on the closest available position along the [11-1] direction, with the first dopamine molecule bending towards the surface. We considered the case where the ethyl-amino functionality of the second molecule is LEFT-oriented (note that RIGHT-orientation was already considered in down_NH_2(RR) in **Section 3.5**). Then, a third dopamine molecule binds the surface. If it anchors along the [11-1] row, there is not enough space for the bending of the second LEFT-oriented molecule. Therefore, the second molecule remains up_NH_2 (see side view in the bottom of **Figure 3.14a**), unless the third dopamine molecule flips, rotating around the Ti-O bond (**Figure 10b**).

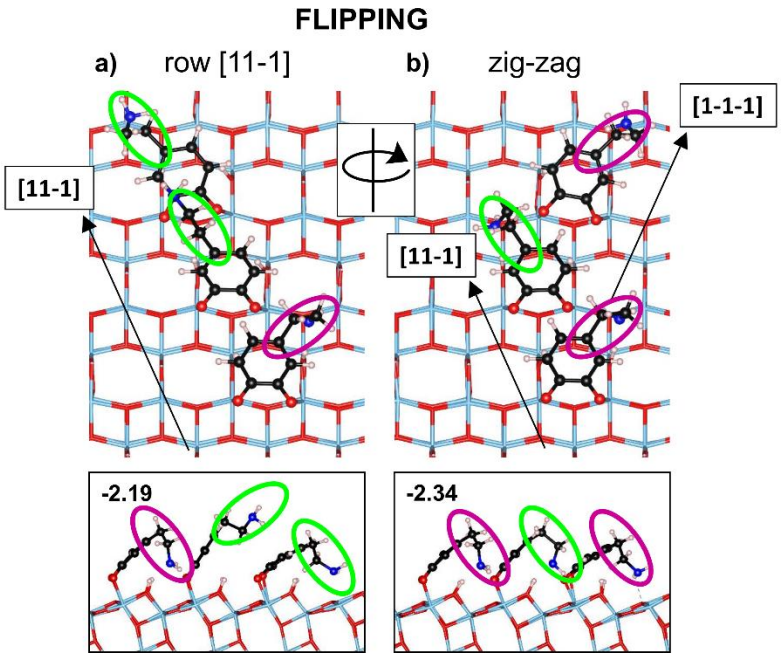

Figure 3.14. Scheme showing top and side (from [10-1] direction) views for two different growing mechanisms: a) growth along the [11-1] row and b) with a zig-zag pattern (after the flipping of the third dopamine molecule) and their relative adsorption energies per molecule (ΔE_{ads}^{mol}, in eV). LEFT-oriented and RIGHT-oriented functional groups are marked in green and purple, respectively.

After flipping, the third molecule would occupy a bonding position along the [1-1-1] row, allowing the second LEFT-oriented molecule to slope down (see side view in the bottom of **Figure 3.14b**). The adsorption energy per molecule for the zigzag pattern (**Figure 3.14b**) is -2.34 eV, which is -0.15 eV more favored than the one along the [11-1] row (-2.19 eV). This means that if the bending and the flipping are in the same time scale of the self-assembling (thermodynamic growth), the totality of the dopamine molecules will arrange in a way that their ethyl-amino functionality is allowed to bend towards the surface and accept a proton, resulting in 100% down_NH_3^+ configuration at the full coverage.

3.7. Conclusions

In summary, in this work we have first investigated, analyzed and compared the adsorption configurations and electronic structure of catechol and dopamine when adsorbed on the anatase (101) TiO_2 surface at low coverage. Isolated cathecol molecules preferentially bind in two bidentate modes (BD_1 and BD_2 in Figure 1), where either one or two protons are transferred to the surface. These two structures are essentially isoenergetic. Dopamine presents a larger number of degrees of freedom, given the added $–CH_2CH_2NH_2$ functional group. The most stable structure is bidentate ($B^OD_2M^{NH2}$ in **Figure 3.2**), tilting towards the O_{3c} side, coordinating the NH_2 group with a surface Ti_{5c} and with the two dissociated protons on different Ti_{5c} rows. The electronic structure analysis (**Figure 3.4**) for these stable adsorption structures of catechol and dopamine indicate similar features: three gap states are present, with those deriving from dopamine being slightly deeper.

Secondly, we investigated the growth mechanism of molecular monolayers under kinetic control, i.e. under fast molecular deposition time. In these conditions, molecules are expected to quickly arrange on the surface one after the other. In the case of dopamine, the consequence is that self-assembling takes place before the ethyl-amino group bends towards the surface (up_NH_2 models). We identified three isoenergetic growth paths: along the [11-1] and the [1-1-1] rows and zigzag (**Figure 3.7**). Note that in the case of catechol experimental STM images show only the first two.[110]

In the case of dopamine, we have further investigated all the possible configurations for the growth path along the [11-1] direction. The ethyl-amino group introduces the possibility of various configurations, as shown in **Figure 3.8**, for the up_NH_2 structures (RR, RL, LR and LL). Again, energy differences are negligible. However, starting from these structure and providing some temperature in a molecular dynamics simulation (with DFTB) we observe that the $–CH_2CH_2NH_2$ bents down (down_NH_2) when possible and receives a proton from the surface forming $–CH_2CH_2NH_3^+$ species (down_NH_3^+), see **Figure 3.10**. Kinetic barriers for these processes are found to be very low or null. However, not all configurations allow the ethyl-amino bending and the proton transfer due to steric hindrance. Therefore, we expect that 50% of the molecules will be bent and protonated, whereas 50% of them will be standing upward and not deprotonated. Analogous results are predicted for the [1-1-1] direction of growth and for the zigzag. Our analysis and conclusions provide a solid rationalization for the experimental observations by Syres et al. based on photoemission spectra of one monolayer of dopamine molecules on the anatase (101) TiO_2 surface.[144] The proton transfer from the surface to the dopamine moiety observed at full coverage affects the electronic structure of the hybrid

organic/inorganic system. At full coverage down_NH_3^+, the dopamine states are rather stabilized by the positive charge from the proton (**Figure 3.4b** vs **Figure 3.12b**).

Finally, we have considered what would differ if the growth took place under thermodynamic control. In these conditions molecules have time to diffuse, flip or bend on the surface, therefore, they all would be able to reach their thermodynamic minimum at full coverage, being all protonated and bent towards the surface (see **Figure 3.14** and related discussion).

To conclude, this study, based on a wide set of hybrid density functional theory calculations including dispersion forces, provides a clear scenario for the adsorption modes, patterns of growth and configurations of dopamine on the anatase (101) TiO_2 surface, with reference to the archetype of 1,2-dihydroxybenzene ligands, i.e. catechol. We concluded that at low coverage, the isolated dopamine molecule prefers to bend towards the surface, coordinating the NH_2 group to a Ti_{5c} ion. At high coverage, the packed molecules succeed in bending towards the surface only in some monolayer configurations. When they do, a proton is transferred from the surface to the ethyl-amino group forming terminal NH_3^+ species, which highly interact with the O atoms of a neighboring dopamine molecule. This strong coulombic interaction largely stabilizes the self-assembled layer. On the basis of these results, we predict that improving the probability of dopamine molecules being free to bend towards the surface through thermodynamic versus kinetic growth conditions will lead to a monolayer of fully protonated dopamine molecules.

4 Dynamical and light effects on dopamine-functionalized TiO_2 nanoparticles

In this Chapter, we provide an all-round investigation of the functionalization of realistic curved titanium dioxide nanoparticles (2.2 nm size) with dopamine. Similarly to what we did in **Chapter 3** for the adsorption of dopamine on the flat anatase surface, we consider both single-molecule adsorption and full coverage regime. For the low coverage, we achieve a detailed description of the mechanisms of molecular adsorption, and of the processes following visible light-irradiation, considering exciton formation, trapping and charge carriers diffusion or recombination. We then add molecules step by step on the NP and analyze the self-assembling mechanism of the growing molecular layer and the effects on the electronic properties of the complex. Finally, for the maximum coverage (46 molecules per NP) we perform molecular dynamics runs at 300 K, in order to account for thermal effects on the configuration and electronic properties of the NP-dopamine complex. The use of curved NP surfaces with respect to flat ones is found to be more effective for bioconjugation.

4.1. Introduction

Nanomedicine, i.e. the application of nanomaterials to medicine, could be the answer to the need for therapeutic agents with atom-size resolution, carrying out both therapeutic and diagnostic tasks at the same time. For example, nanoparticles (NPs) could be used to mediate targeted drug delivery or in vivo imaging, with the intent of overcoming many of the problems associated with the systemic administration of drugs and of contrast agents. NPs are characterized by a very high surface-to-volume ratios (i.e., at <2 nm >50%) and large surface areas. This allows for the display of multiple (possibly even different) molecules/biomolecules on their surfaces. NPs can act as carriers for insoluble materials (e.g. drugs or radioactive isotopes). As synthesized, many metal-, semiconductor-, and carbon-based NPs are hydrophobic and need to be made soluble and biocompatible by chemical modification of their surfaces, e.g. by polyethylene glycol (PEG) coating. The ligands may also provide the NP with additional chemical functionalities, useful to load biomolecules, giving birth to bioconjugates.

4.1.1. Bioinorganic nanohybrids

Various types of nano-bioconjugates can be designed,[221] which are able to perform multiple and simultaneous activities, such as tumor-targeting, active sensing, diagnostics, and delivery of drugs or imaging contrast agents.[222]

Bioinorganic nanoconjugates are composed of an inorganic part, such as a metal or metal oxide nanoparticle, and a biological active molecule, for example drugs, antibodies and DNA fragments.

TiO_2, which has outstanding photocatalytic properties, is a suitable material to be used as inorganic component of the nanoconjugates.

The strategy for attaching biomolecules to TiO_2 NPs is to exploit a linker, i.e. an oxygen containing organic molecule having double functionalities, anchoring the inorganic NP and tethering the biological molecule at the same time.

NPs bioconjugation should ideally be achieved with control over several aspects, such as: i) the number of binding sites on the NP; ii) the number of biomolecules that can be tethered; iii) the distance between the biomolecule and the NP; iv) the type of linkage (e.g. permanent or labile); v) the preservation of the function and the activity of both the NP and the biomolecule.

4.1.2. Pristine TiO_2 in nanomedicine

In recent years, TiO_2 has found application in the modern field of nanomedicine, due to its unique photocatalytic properties, excellent biocompatibility, high chemical stability and low toxicity. [1,223,129]

Recent advances in the biomedical applications of TiO_2 range from photodynamic therapy for cancer treatment,[224-227] drug delivery systems,[228] cell imaging,[145,229,230] biosensors, antimicrobial and bactericidal action and genetic engineering.[231,232]

Titanium dioxide NPs are typically prepared through sol-gel chemistry. Below 10-15 nm, anatase phase is preferred. The thermodynamically most stable anatase NP shape is a decahedron where the (101) and (001) stable surfaces are exposed. However, concentration and pH condition are growth-determining factors and in condition of high dilution, the faceted NPs partially dissolve and acquire a spherical shape.[1] This is more interesting for biomedical application since curved nanoparticles present a higher number of low-coordinated sites[81,86] that are better suited for the linker anchoring.

Pristine titanium dioxide NPs exhibit two different kinds of toxicity: toxicity in dark and phototoxicity. The former depends on the dimension of the NP and it becomes important for small NPs (below 25 nm), which could disrupt the barriers between the endothelial cells. Moreover, very small anatase NPs (10 and 20 nm) can induce hydrogen peroxide/ nitric oxide production, oxidative lipid peroxidation, DNA damage and micronuclei formation in a human epithelial cell line even in the absence of photoactivation.[233]

Phototoxicity, instead, is exhibited by all kinds of TiO_2 nanoparticles, independently on the size and shape, although it has been showed that TiO_2-induced cell death was inversely proportional to the NP size.[234] Photoexcitation of TiO_2 with an appropriate wavelength in aqueous solution results in the formation of various reactive oxygen species (ROS), such as hydroxyl ($OH^{\bullet}$), superoxide anions ($O_2^{-\bullet}$), hydroperoxyl ($HO_2^{\bullet}$) radicals, and hydrogen peroxide (H_2O_2).[235,236] These ROS cause oxidative stress, which is considered to be harmful to both normal and cancerous cells. However, increasing the oxidative stress using exogenous agents is more likely to be destructive in cancer cells than in normal cells due to the elevated levels of ROS registered in cancerous tissues.[237,238] Moreover, the response of TiO_2 NPs can be controlled locally by a light *stimulus*. Therefore, the photocatalytic properties of bare TiO_2 can be exploited in cancer therapy, i.e. through photodynamic therapy (PDT) (see **Chapter 1**).

As already mentioned, the employment of pristine TiO_2 in photoconversion applications is limited due to the wide band gap of this semiconducting material, triggering light absorption

into the ultraviolet range. On the other hand, water and fat tissues start absorbing at 1000 nm, leaving the optical window in the range of 600-1000 nm as the only feasible region where photoactive species can be efficiently activated for PDT by an external light source.

4.1.3. Functionalized TiO_2 NPs for nanomedicine

Functionalization of TiO_2 NPs may narrow the band gap, thus shifting light absorption towards longer wavelengths. Once functionalized, TiO_2 NPs could appropriately accomplish photocatalytic tasks, including not only PDT, but also other phototherapeutic applications, e.g. light-induced drug delivery.

Moreover, functionalization with a high density of molecules saturate the undercoordinated reactive site and prevent the undesired uncontrolled toxicity of the NP, making them biocompatible. Finally, providing new targeting functionalities to the NPs, could make the conjugates site-specific.

Therefore, the type of linkage of biomolecules to NPs together with the coverage density is a crucial factor, which is specifically dependent on the desired application. The conjugation could be based on non-covalent interactions (H-bonding, dispersion forces, electrostatic interactions) or on covalent or dative bonds.

Functionalization through bifunctional linkers provides an interesting bioconjugation strategy mostly because they behave as spacers between the NP and the biomolecules, which helps in maintaining their optimal respective functions and activities. Moreover, by the use of bifunctional linkers it is possible to control the binding strength between the NP and the biomolecule with the proper choice of the two functional groups used for anchoring the surface and for tethering the biomolecule. Additionally, it is possible to bridge the electronic properties of the NP material to those of the biomolecule (e.g. protein, oligonucleotides, DNA fragments, etc.). These linkers exploit the high reactivity of the undercoordinated surface sites of the nanoparticle, which are abundant especially in small spherical NPs. In particular, the undercoordinated Ti atoms are found to be reactive towards oxygen containing species.

4.1.3.1. Dopamine functionalized TiO_2 NPs

Catechol derivatives are an effective class of oxygen-containing bifunctional linkers for metal oxide NPs since they can firmly anchor the oxide surface by forming relative strong coordinative bonds with undercoordinated surface metal atoms.[153]

Among them, dopamine (4-(2-aminoethyl)benzene-1,2-diol), a catechol-like molecule having two hydroxyl portions in *ortho*- and one amino functional group on the opposite side of the ring, is a good candidate to be used for bioconjugation.

On one side of the benzene ring, the enediol portion binds the surface through coordination bonds, whereas on the other side, the primary amine remains exposed to the surrounding environment, imparting water dispersibility and acting as a potential handle for bio-active molecules (**Figure 4.1**).

Figure 4.6 Scheme of a bioincorganic nanoconjugate with dopamine working as a linker

The OH dissociative binding to metal atoms is preferred to carboxylic and phosphonic groups since a higher ligand-metal oxide electronic coupling results when only one O atom separates the two moieties.[239]

Catechol and catechol derivatives like dopamine can bidentate to surface fivefold coordinated Ti atoms or even chelate to fourfold coordinated Ti sites.[115,107] Interestingly, their presence on the surface is capable of shifting the absorption properties of TiO_2 from the UV to the visible region[1] because they introduce molecular states in the band gap. For the dopamine/TiO_2 NP system, an effective charge transfer mechanism was reported by surface-enhanced Raman spectroscopy (SER) measurements[240] with an unexpected dependence on coverage and shape. This effective charge transfer is at the basis of the instantaneous charge separation observed in DNA/dopamine/TiO_2 NPs triads.[108,129,137] Raman signal intensity was also found to depend on the number of surface binding sites, electron density of the ligands and dipole moment. Biofunctionalized TiO_2 nanomaterials through dopamine linkers are capable of bio-manipulation via altering intracellular biochemical pathways.[227] Dopamine linker was also successfully applied for labeling of TiO_2 with a fluorescent marker.[230] Despite of the different biomedical applications in which TiO_2 NPs modified by bifunctional linkers is exploited, still little is known of the atomistic details and electronic properties of these hybrid systems at the nanoscale level.

In this Chapter, a computational multiscale investigation of realistic size dopamine-TiO_2 NP (of ~700 atoms, 2.2 nm) composite systems is presented.[83,86] We investigate several aspects related to both structural and electronic properties. After presenting the spherical NP model, we consider the low coverage regime (**Section 4.2.**) and compare different adsorption modes of dopamine (**Section 4.2.2.**). Then, we analyze the electronic structure details (**Section 4.2.3.**) and the effect of light irradiation for the most stable configuration found for the composite: exciton formation, trapping, charge carriers diffusion and recombination processes (**Section 4.2.4.**). All the calculations for the low coverage regime are done at both hybrid density functional theory (DFT-B3LYP) and self-consistent-charge density functional tight-binding (SCC-DFTB) level of theory, which allows to assess the accuracy of DFTB in the description of both structural and electronic properties of these complex systems.

Next, we investigate increasing coverage regimes on the NP, up to full coverage (46 dopamine molecules anchored to the surface) (**Section 4.3.**). We modeled the self-assembling of the molecules on the surface and investigated the coverage effect on the adsorption energy (**Section 4.3.2.**) and on the electronic properties of the composite systems (**Section 4.3.3.**). The high coverage regime has been investigated by means of DFTB static and dynamic calculations, except for the electronic properties that were analyzed through single point DFT calculations on the DFTB geometries for a correct description of the TiO_2 band gap. In order to validate the method, we assessed the DFT/DFTB hybrid method by comparing the electronic structure obtained for the adsorption of dopamine at low and high coverage on the flat (101) anatase TiO_2 surface calculated by DFT, DFT/DFTB and DFTB (**Section 4.3.3.1.**).

For the fully covered NPs, we performed molecular dynamics runs and observe how the molecules rearrange on the surface and compare this with what reported in **Chapter 3** for dopamine full coverage on a flat (101) anatase TiO_2 surface (**Section 4.3.4**). Our computational results are discussed through a comparative analysis with all the available experimental observations and data. The size of the real TiO_2 nanoparticles used in the experiments is similar to that of the simulated systems. The experimental findings are mainly based on spectrophotometric measurements, electron paramagnetic resonance (EPR), nuclear magnetic resonance (NMR), X-ray absorption measurements (XANES and EXAFS), infrared (IR) and surface -enhanced Raman spectroscopy (SER).[1,107,108,115,132,241,242,243,244]

4.2. Computational details

In this work, we used two levels of theory: density functional theory (DFT) and self-consistent charge density functional tight-binding (SCC-DFTB).[213,214] Both methods have been employed for geometry optimization and electronic structure calculations, while the molecular dynamics simulations have been performed only by using the SCC-DFTB approach.

All the DFT calculations have been carried out with the CRYSTAL14 simulation code,[203] where the Kohn-Sham orbitals are expanded in Gaussian-type orbitals. The all-electron basis sets are Ti 86-4111(d41), O 8-4111(d1) for the oxygens of TiO_2; H 5-111(p1), C 6-31111 (d1), O 8-41111 (d1) and N 6-311(d1) have been employed for hydrogen, carbon, oxygen and nitrogen of the adsorbed molecules (dopamine or DOPAC). We used the B3LYP functional, [169,170] corrected by Grimme's D* to include dispersion forces.[245] The cut-off limits in the evaluation of Coulomb and exchange series/sums appearing in the SCF equation were set to 10^{-7} for Coulomb overlap tolerance, 10^{-7} for Coulomb penetration tolerance, 10^{-7} for exchange overlap tolerance, 10^{-7} for exchange pseudo-overlap in the direct space, and 10^{-14} for exchange pseudo-overlap in the reciprocal space. The condition for the SCF convergence was set to 10^{-6} a.u. on the total energy difference between two subsequence cycles. The equilibrium structure is determined by using a quasi-Newton algorithm with a BFGS Hessian updating scheme.[246] Geometry optimizations were performed without any symmetry constraint, forces were relaxed to be less than 4.5×10^{-4} au and displacements to be less than 1.8×10^{-3} au.

For all the SCC-DFTB calculations we used the DFTB+ open source package.[215] We employed the MATORG parameterization set[216] for the pairwise interaction of the atoms of both TiO_2 and adsorbed molecules. The description of the hydrogen bonding has been further improved with the inclusion of the empirical HBD correction ($\zeta = 4$).[217,247] For geometry relaxations, the threshold for the convergence of the self-consistent charge (SCC) procedure was set to 10^{-6} charge au and forces were relaxed to less than 10^{-4} au.

The anatase TiO_2 spherical nanoparticle (NP) model used throughout this work has been designed through global optimization with a simulated annealing process at the SCC-DFTB level of theory in a previous work by our group.[86] The stoichiometry of the model is $(TiO_2)223 \cdot 10H_2O$ and it is characterized by an equivalent diameter of 2.2 nm. The nanoparticle has been treated as a large isolated molecule in the vacuum without any periodic boundary condition.

For the slab calculation (**Section 4.4.2.1.**), we modeled the TiO_2 (101) anatase surface by the same slab composed of three tri-atomic layers that we used in **Chapter 3**. The bottom layer was

kept fixed to the optimized bulk positions during the geometry optimization. Periodicity was considered only along the $(10\bar{1})$ and (010) directions, while no periodic boundary conditions were imposed in the direction perpendicular to the surface. The 1×4 supercell model that we employed contains overall 144 atoms. Configurations have been optimized using a k-point mesh of 2×2×1 to ensure the convergence of the electronic structure.

The total adsorption energy per molecule, dopamine or DOPAC, on the spherical nanoparticle has been defined as:

$$\Delta E_{ads}^{mol} = (E_{(NP/slab)+\,n_{mol}} - [E_{(NP/slab)} + n_{mol}\,E_{mol}])/n_{mol} \quad (4.1)$$

where "$E_{(NP/slab)+\,n_{mol}}$is the total energy of the whole system, "$E_{(NP/slab)}$ is the energy of the NP/slab models, E_{mol} is the energy of the molecule in the gas phase and n_{mol} is the number of molecules adsorbed on the NP/slab.

Vertical and adiabatic ionization potentials (IP) are computed by removing one electron from the model of functionalized nanoparticle in its original geometry and by performing full atomic relaxation, respectively. Vertical and adiabatic electron affinities (EA) are computed by adding one electron to the model of functionalized nanoparticle in its original geometry and by performing full atomic relaxation, respectively.

Trapping energies (ΔE_{trap}) are computed as the energy difference between the isolated charges or electron-hole pairs in the trapping geometry and the delocalized solution in the neutral ground state geometry. Distortion energies (ΔE_{dist}) are obtained as the difference between the energy of the neutral system in the trapping geometry and the same system in the optimized geometry.

Simulated total densities of states (DOS) of the nanoparticles have been obtained through the convolution of Gaussian peaks (σ = 0.005 eV for DFT calculations, σ = 0.05 eV for DFTB) centered at the Kohn-Sham energy eigenvalue of each orbital. Projected densities of states (PDOS) have been obtained by using the coefficients in the linear combination of atomic orbitals (LCAO) of each molecular orbital: summing the squares of the coefficients of all the atomic orbitals centered on a certain atom type results, after normalization, in the relative contribution of each atom type to a specific eigenstate. Then, the various projections are obtained from the convolution of Gaussian peaks with heights that are proportional to the relative contribution. For spin polarized systems, (projected) densities of states are calculated using the Kohn-Sham eigenvalues of alpha or beta population separately. The zero energy for all the DOS is set to the vacuum level, corresponding to an electron at an infinite distance from the surface.

Born−Oppenheimer molecular dynamics simulations were performed on the high coveraged functionalized nanoparticle models within the canonical ensemble (NVT). The Newton equations of motion were integrated with the velocity Verlet algorithm, and a relative small time step of 0.5 fs was used to ensure reversibility. During the molecular dynamic simulation, the temperature has been kept constant to 300 K by using the Nosé − Hoover thermostat (time constant of 0.04 ps) and the system has been let evolve for 10 ps.

4.3. Single dopamine absorption on the spherical NP

In this section, the single linker dopamine molecule adsorption on a realistic model of spherical anatase TiO_2 nanoparticle (**Figure 4.2**) is examined. Different adsorption modes are considered. For few selected configurations, we also investigated electronic properties by means of the total (DOS) and projected density of states (PDOS). For the most stable adsorption configuration, we analyzed the effect of light irradiation, considering, as a first step, a vertical excitation (exciton formation), followed by atomic relaxation in the excited state (exciton self-trapping) and charge carriers dynamic evolution through charge hopping.

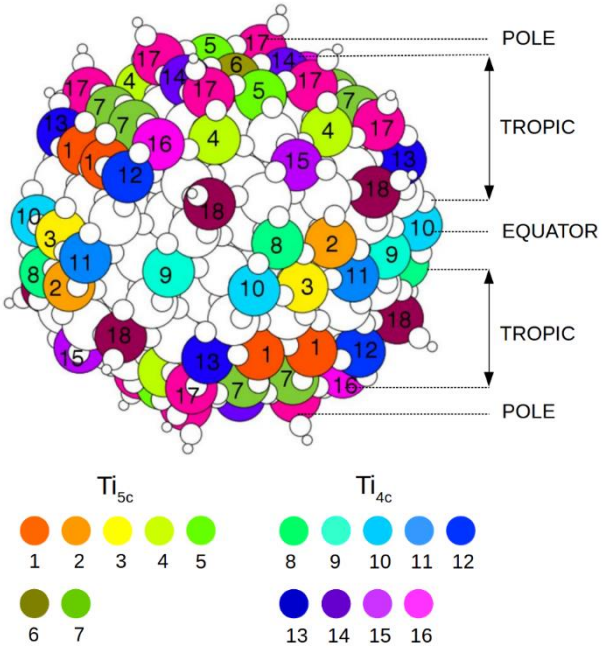

Figure 4.2. Map of the Ti atoms of the spherical anatase TiO_2 nanoparticle with different coordination environment, visually shown by the color-coding and numbering. Different areas of the sphere are identified: pole, tropic and equator.

The spherical NPs present a diameter of 2.2 nm, similar to those used in several experimental works of NP+linker (dopamine or DOPAC) complexation.[107,132,135,137,224,227,243,248,249] Experimental characterization of this type of NPs was obtained by XANES spectroscopy.[242] Four-, five- and six-fold coordinated Ti atoms were identified according to the position and the intensity of the pre-edge peaks. As the size of the NP decreases, the number of low coordinated sites increases. In several experimental studies, the fraction of surface TiO_2 in these NPs was estimated based on the number density of Ti on different lattice planes and on an assumed equal probability of exposure for different lattice planes.[241] According to this approach, the superficial

Ti atoms are proportional to $\frac{12.5}{d}$, where d is the diameter of the NP in Å. For a NP with diameter of 2.2 nm, the fraction of surface TiO_2 is expected to be 56%. We have applied the formula $[Ti_{surf}] = [TiO_2] \times \frac{12.5}{d}$ to evaluate the number of surface Ti site per particle, considering a perfect spherical volume ($\frac{4}{3}\pi r^3$) and the anatase density of 3.78 g/cm^3 (see page S2 in the Supporting Information for the details of the calculations). We obtain 90 surface Ti sites that rather nicely compares with the true number of Ti surface sites in the NP model (Ti_{4c}+Ti_{5c} in **Figure 4.2**), which is 106 (44+62, respectively). This confirms that our model satisfactorily resembles experimental NPs.

4.3.1. Adsorption modes

Dopamine is a bifunctional linker molecule (**Figure 4.3**). It is an enediol species, a derivative of catechol, with an additional ethylamino group attached to C4 of the ring. Diols bind quite strongly to metal oxide surfaces and have been successfully utilized in a range of conjugation protocols. Among diols, catechol is particularly strongly binding. Among catechol derivatives, dopamine is probably one of the most extensively studied linker for conjugation. While the bidentate catechol portion of dopamine binds to the oxide surface through coordination bonds, the primary amine could remain exposed to the surrounding environment, improving the water dispersibility of the nanoparticle and providing a hook to tether biomolecules or drugs.

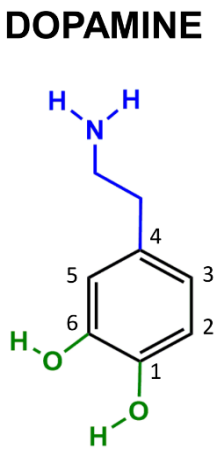

Figure 4.3 The structure of the dopamine [4-(2-aminoethyl)benzene-1,2-diol] with the enediol group in green and the ethylamino in blue.

However, we will show in the following that, especially at very low coverage (as it is the case on a single dopamine molecule on the nanoparticle's surface), the molecule could bend towards the surface and further bind through hydrogen bonding to surface O atoms or coordinating

surface Ti atoms, in analogy to what observed for dopamine adsorption on the flat (101) anatase TiO_2 surface in **Chapter 3**.

In **Figure 4.4** we present the configurations that have been considered. We compare bond lengths and adsorption energies per molecule (ΔE_{ads}^{mol}), as obtained after full geometry relaxation at DFT (B3LYP-D*) and DFTB level of theory. The dopamine molecules favorably adsorb through dissociation of the two OH groups. This is in line with infrared studies suggesting that the dopamine molecule binds via the two adjacent phenolic groups, causing a stretching of the C—C bonds in the aromatic ring.[243] The two dissociated protons are transferred to O_{2c} atoms. The binding may take place either in a bidentate ("B") or in a chelated ("C") fashion in agreement with experimental observations.[107,115] **Errore. Il segnalibro non è definito.** For completeness and for comparison, we also considered binding to a surface Ti atom through the N atom of the amino group in a monodentate fashion, but this resulted to be less favorable (by 1.36 eV). As mentioned above, the adsorbed dopamine molecule can bend down toward the surface ("D" for down). The map of the under-coordinated Ti atoms present on the nanoparticle's surface is shown in **Figure 4.2**. Later on, for the tag labeling of the binding Ti atoms, we will refer to the numbering in this map.

We now further analysed the six different adsorption configurations of dopamine on the surface of the NP, which differ both for the complexation mode and for the type of interaction of the amino group with the surface. The six configurations are: (1) bidentate on Ti [11] and [9] and bent towards the surface to establish a H-bond between the N of the NH_2 group with a surface OH ($B^{11,9}D^{H\text{-}bond}$, **Figure 4.4a**); (2) bidentate on Ti [11] and [9] and bent towards the surface to establish a coordination bond between the amino N atom and Ti [12] ($B^{11,9}D^{12}$, **Figure 4.4b**); (3) bidentate on Ti [3] and [11] and bent towards the surface to establish a coordination bond between the amino N atom and Ti [1] ($B^{3,11}D^{1}$, **Figure 4.4c**); (4) chelated on Ti [9] (C^{9}, **Figure 4.4d**); (5) chelated on Ti [9] and bent towards the surface to establish a coordination bond between the amino N atom and Ti [12] ($C^{9}D^{12}$, **Figure 4.4e**) ; (6) chelated on Ti [11] and bent towards the surface to establish a coordination bond between the amino N atom and Ti [12] ($C^{11}D^{12}$, **Figure 4.4f**).

The most favored structure is $B^{11,9}D^{12}$ (see **Figure 4.4b**) with a calculated adsorption energy of -5.17 eV in DFT and of -4.69 eV in DFTB. This adsorption mode is expected to be predominant at a very low coverage regime. The large stability comes from the bending of the molecule toward the surface and formation of an additional bond between the N of the ethyl-amino ($-CH_2CH_2NH_2$) group and a strongly binding four-fold coordinated Ti atom (Ti_{4c}) at the

nanoparticle surface. We also note that the Ti [9] and [11] are the most reactive sites, with reference to a previous work on water adsorption.[85]

In the $B^{3,11}D^{1}$ configuration, we observe formation of two H-bonds: the first one is between one H of the -NH_2 group and the O of a surface OH, whereas the second one is between one H of the -NH_2 group and a bridging O (O_{2c}) surface atom. There is also a coordination bond between the N atom of the ethyl-amino group and a five-fold coordinated Ti (Ti_{5c}) (see **Figure 4.4c**). But, adsorption energy is still lower (by 2.24 eV) compared to the $B^{11,9}D^{12}$ configuration on the grounds that the Ti [3] and [1] are five-fold coordinated in the bare NP and greatly less reactive compare to the four-fold coordinated Ti [9], [11] and [12].

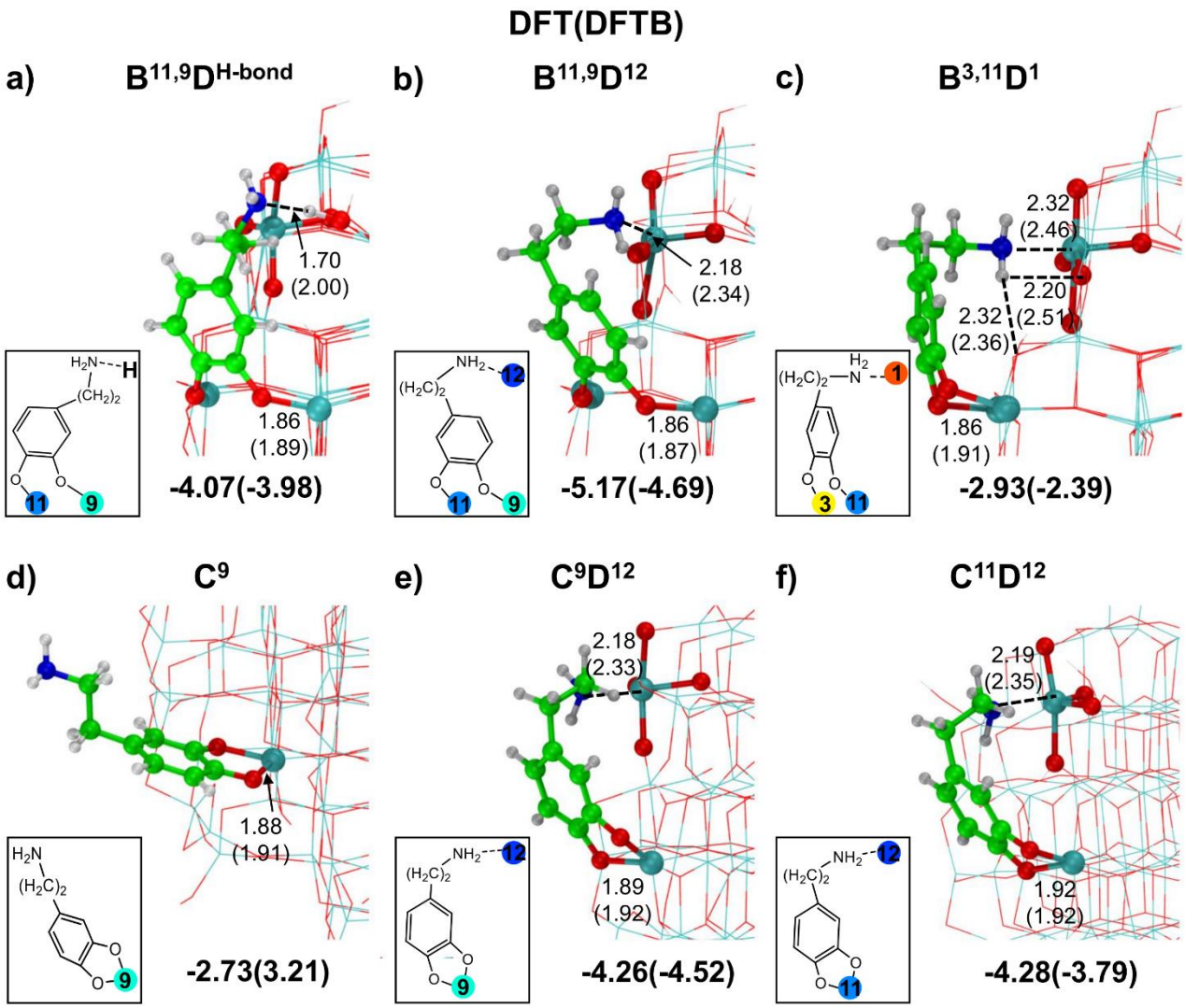

Figure 4.4 Adsorption configurations (side views) and energies per molecule in eV $\left(\Delta E_{ads}^{mol}\right)$ for one dopamine molecule on the surface of the spherical NP, as obtained by DFT(DFTB) calculations. (a) Bidentate and bent towards the surface making a H-bond ($B^{11,9}D^{H\text{-}bond}$); (b) bidentate and bent towards the surface making a covalent bond ($B^{11,9}D^{12}$); (c) bidentate and bent towards the surface making a covalent bond ($B^{3,11}D^{1}$); (d) chelated (C^{9}); (e) chelated and bent towards the surface making a covalent bond ($C^{9}D^{12}$); (f) chelated and bent towards the surface making a covalent bond ($C^{11}D^{12}$). Relevant distances are reported in Å.

Regarding the chelated adsorption mode, C^9D^{12} is the most stable configuration as a result of the molecule bending toward the surface, forming a covalent bond between the ethyl-amino N atom and the Ti_{4c} [12] (see **Figure 4.4e**). In contrast, C^9 is the least stable configuration since the dopamine molecule stands up toward the vacuum. Therefore, there is no interaction between the dopamine and the surface of the NP (see **Figure 4.4d**).

As a concluding remark on this section, we may note that details of the DFTB geometry somewhat differ from DFT, however, the general features of the different adsorption configurations and the relative adsorption energies are consistent with DFT.

4.3.2. Electronic properties of the nanoconjugate

For the dopamine-TiO_2 NP complex at low coverage (5%), experimental observations indicate a shift of the absorption onset to the visible range from 380 nm (bare NP) to 700-800 nm, due to charge transfer excitations.[132]

In order to rationalize this large shift, we analyzed the electronic structure of the most stable dopamine-TiO_2 NP complex configuration ($B^{11,9}D^{12}$) by means of the total (TDOS) and projected density of states (PDOS). The calculations were performed at three different levels of theory: i) DFTB, ii) single-point DFT calculation on the DFTB optimized geometry (DFT/DFTB) and iii) DFT (see **Figure 4.5**). Through the comparative analysis, we can assess whether DFTB is sufficiently robust to describe both structural and electronic properties. Note that the band gap value for the bare NP in DFTB and DFT is 3.11 and 4.13 eV, respectively.

The DOS by DFTB (**Figure 4.5a**) is characterized by the presence of one mid-gap state while those by DFT/DFTB (**Figure 4.5b**) and DFT calculations (**Figure 4.5c**) present two mid-gap states. HOMO is mainly related to the C and O atoms of the dopamine and HOMO-1 peak is ascribable to the C atoms. In the DFTB calculations, the HOMO-1 state is inside the valence band due to the underestimated band gap value.

To provide additional evidence of the legitimacy of the DFT/DFTB approach, we have performed similar comparative analysis for several other systems, including the bare (101) anatase TiO_2 surface, for a low and full coverage regime of dopamine on the same surface (see **Section 4.2.3.1.**). Also in those cases some of the mid gap states in DFT are not present in the DFTB DOS. However, DFT/DFTB and DFT electronic structure are very similar.

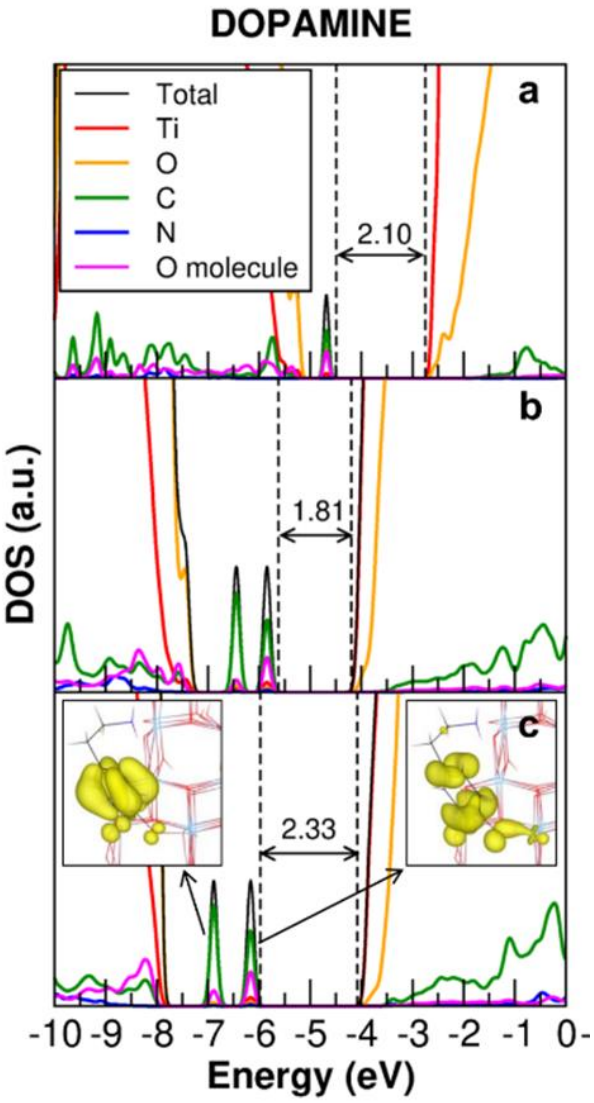

Figure 4.5. Total (DOS) and projected (PDOS) density of states for the $B^{11,9}D^{12}$ configuration of single dopamine molecule adsorption on the TiO_2 anatase nanoparticle as calculated by DFTB (a), DFT/DFTB (b) and DFT (c). The HOMO-LUMO gap is reported for each plot by dashed lines. The zero energy is set to the vacuum level. Electronic density plot for the HOMO and HOMO-1 of $B^{11,9}D^{12}$ and $B^{11,9}C^{12}$ configuration respectively. Iso-value=0.005 e/Å^3.

On this basis, we can infer that DFTB is generally not accurate enough for such delicate functionalized metal oxide systems. However, by performing DFT single point calculations on DFTB optimized geometries we obtain an improved description of the electronic structure, providing results in close agreement with DFT. Therefore, one can safely recourse to this cheap approach when studying high coverage densities or, in general, when performing a full DFT optimization is too expensive and time consuming.

4.3.2.1. Further validation of the method

In order to further assess the hybrid DFT/DFTB method, we anayzed the electronic structure of dopamine adsorbed on the flat anatase TiO_2 (101) surface, employing the small slab model presented in **Chapter 3**.

The 1×4 supercell model (144 atoms) of the anatase (101) TiO_2 surface used for the periodic calculations, presents eight Ti_{5c} (five-fold coordinated) adsorption sites. Since we bound the dopamine molecules in a bidentate adsorption mode, two T_{i5c} are occupied by each molecule, and there is a total of four molecules on the surface at the full coverage. The electronic structure of the bare surface of TiO_2 anatase (101), of the system TiO_2-dopamine at low and high coverage has been calculated with DFTB, performing a single-point DFT calculation on the DFTB geometry (DFT/DFTB) and with DFT on DFT optimized geometries (**Figure 4.6**). In the DFTB density of states (DOS) for one and four dopamine molecules on TiO_2, we identify only two peaks in the mid-gap zones (**Figure 4.6a**), while in the DFT/DFTB plot there are four mid-gap states (**Figure 4.6b**). Thus, this description of the electronic structure is much more similar to the one given by our reference DFT (B3LYP-D*), which also presents four mid-gap states (**Figure 4.6c**). In both cases, the HOMO and the HOMO-2 are mainly related to the C atoms of the phenyl ring, while the HOMO-1 peak is ascribable to the N atom. The HOMO-3 has its major contribution from the O atoms of the dopamine molecules. In the DFTB description, two out of the four mid-gap peaks became part of the valence band and the assignment of the states to the single atoms is more difficult, due to a larger hybridization. Moreover, the band gap for the bare material calculated by DFT/DFTB is closer to the one reported for DFT, even if the value of the HOMO-LUMO gap for the TiO_2-dopamine system at low and high coverage is generally undestimated (by ~ 0.4 eV).

Therefore, we can conclude that performing DFT/DFTB calculations of the surface does effectively improve the description of the electronic structure of the dopamine-TiO_2 surface model by a qualitative point of view.

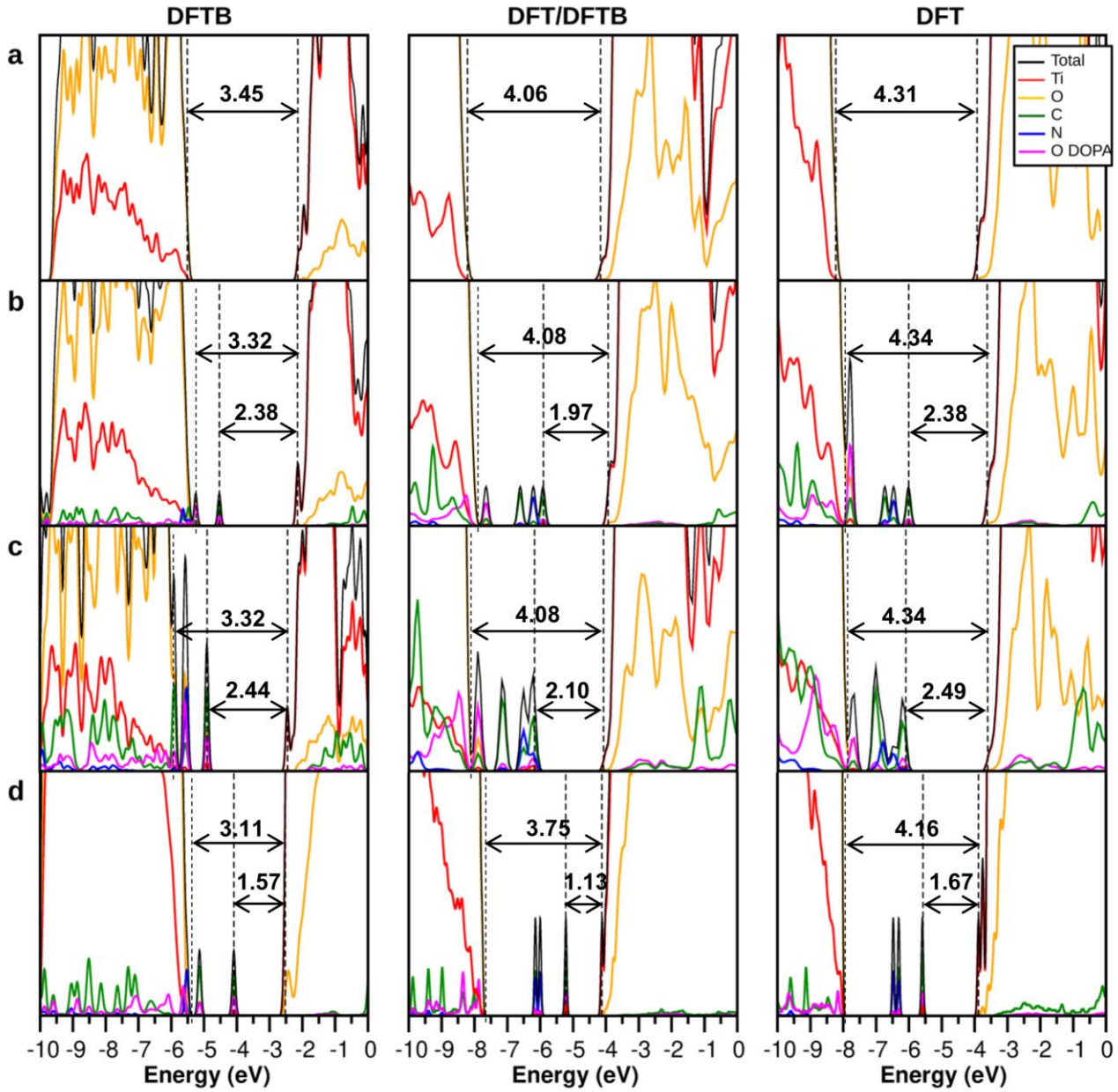

Figure 4.6 Total (DOS) and projected (PDOS) for the bare TiO_2 (101) surface (a), for one (b) and four (c) molecules of bidentate dopamine adsorbed on TiO_2 (101) surface and one molecule of dopamine on spherical TiO_2 NP (d) in the C^9 configuration calculated by DFTB, DFT/DFTB and DFT. Ti is represented in red, O is orange for the TiO_2 surface/NP, while O of the dopamine is marked in violet. C is green and N is reported with a blue line. The HOMO-LUMO gap and top of the valence band and the bottom of conduction band in the TiO_2 surface/NP is reported for each plot by dashed lines. The zero energy is set to the vacuum level.

4.3.3. Effect of light irradiation of the nanoconjugate

4.3.3.1. DFT approach to the study of excitations

Two different kinds of excitations exist and are commonly observed experimentally, as shown in the scheme in **Figure 4.7**. On the one hand, we may be interested in charged excitations, in which the system change is status from neutral to positively or negatively charged. This phenomena are experimentally measured through photoemission spectroscopy.[250] On the other

hand, the system could undergo a neutral excitation, which is observed through absorption spectroscopy or electron energy loss spectroscopy (EELS).[251]

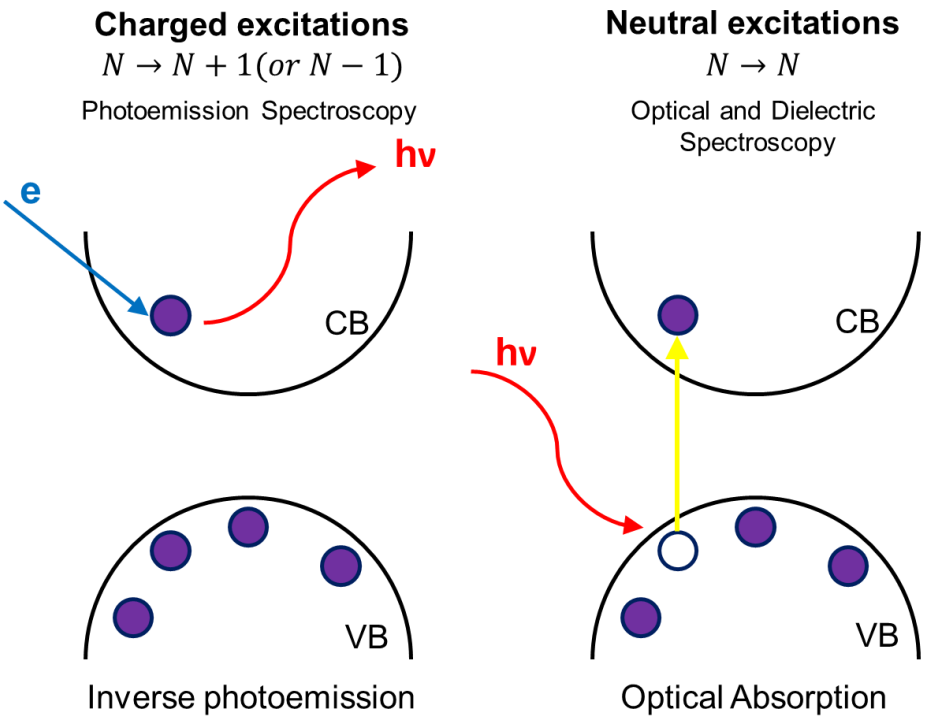

Figure 4.7 Schematic representation of charged (left) and neutral (right) excitations.

Charged excitations are usually calculated by means of the GW approach,[187] which belongs to the many body perturbation theory (MBPT). Through the GW approach, it is possible to get accurate energy levels only for the non-interacting electron and hole. Nevertheless, the GW approximation does not include the electron-hole interaction effects (e.g. the formation of an exciton), for which a more sophisticated Green's function approximation is required, i.e. the *Bethe-Salpeter* (BS) equation.[186] Unfortunately, the computational cost of the BS equation and of the GW approximation is extremely high and their employment for big-size systems is not feasible.

A viable, though not always applicable, solution for large systems is to use ΔSCF-DFT methods, that allow to compute excited states energy and forces at the same cost of a standard DFT calculation, employing *non-Aufbau* electronic configurations to converge the Kohn-Sham SCF equations to an excited state. If the excited state is the lowest-energy state with that symmetry, the SCF will converge to the right solution, or otherwise it may collapse to lower-energy state.

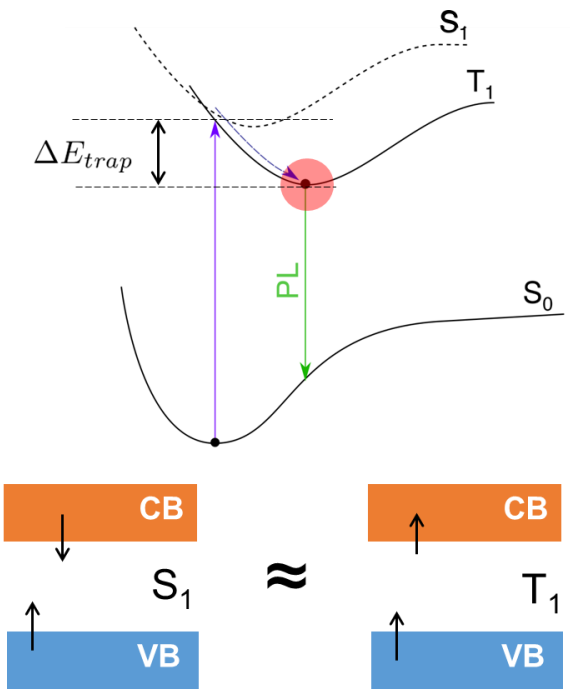

Figure 4.8 Scheme of the ΔSCF approach for the calculation of the charged excitations

In our case, the excited state is calculated as a simple ground state triplet T_1, for which we suppose that the energy is only slightly lower than the one of the singlet excited state S_1 (**Figure 4.8.).** We are aware of the fact that this is a spin forbidden excitation, however after atomic relaxation, it will be possible to localize the self-trapped triplet exciton, which is what could be observed in photoluminescence experiments, due to its longer lifetime with respect to the singlet one.

4.3.3.2. Charge carriers separation and recombination study

We investigate the light irradiation effect by computing first the vertically excited state (v), in the Franck-Condon approximation, from the S_0 to the T_1 state by means of a spin-constrained calculation (see **Figure 4.9** and **Figure 4.10**).

We compute a trapping energy of -0.89 eV for the self-trapped exciton and an emission energy (for $T_1 \rightarrow S_0$) of -0.51 eV. In the triplet self-trapped exciton $\left[B^{11,9}D^{12}\right]_a^{T_1}$, the hole is fully localized on the π orbital of the aromatic ring in dopamine (see **Figure 4.10**), in agreement with EPR experiments,[107] whereas the electron is fully trapped at a subsurface Ti_{6c} site. If, as a further step along the post-irradiation processes, we suppose that electron hopping is faster than radiative recombination, which agrees with some experimental findings of charge recombination suppression in dopamine/TiO_2 NP charge transfer complexes,[138] then the electron could localize on a different Ti atom (electron hopping barrier in anatase was

estimated to be about +0.09 eV).[57] Clearly, the nearby positions are the first to be reached and there is one where the electron is found to be particularly stable and still in close contact with the hole: configuration **b** (see **Figure 4.9** and **Figure 4.10**). The total trapping energy (ΔE_{trap}) in this case is much larger (-1.40 eV, with respect to the energy of the v configuration).

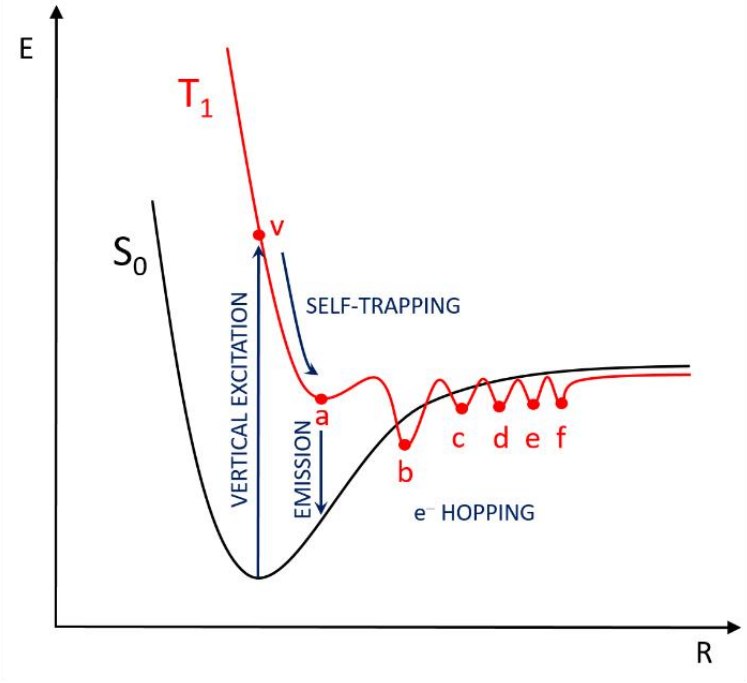

Figure 4.9 Schematic representation of the process involving e^-/h^+ pair: the vertical excitation $S_0 \rightarrow T_1$ (v), the self-trapping relaxation (a), the $T_1 \rightarrow S_0$ emission and the electron hopping follow by the non-radiative emission (b, c, d, e, f).

The hole is still localized in the dopamine molecule, whereas the electron is now trapped at the surface Ti atom that is bound to the amino residue of the dopamine molecule. The S_0 state curve lies above this T_1 minimum structure b (confirmed by a single point calculation in the closed-shell configuration) by +0.35 eV. Therefore, decay to the S_0 ground state geometry can only take place through a non-radiative process through the conical intersection on the left of b, shown in **Figure 4.9**.

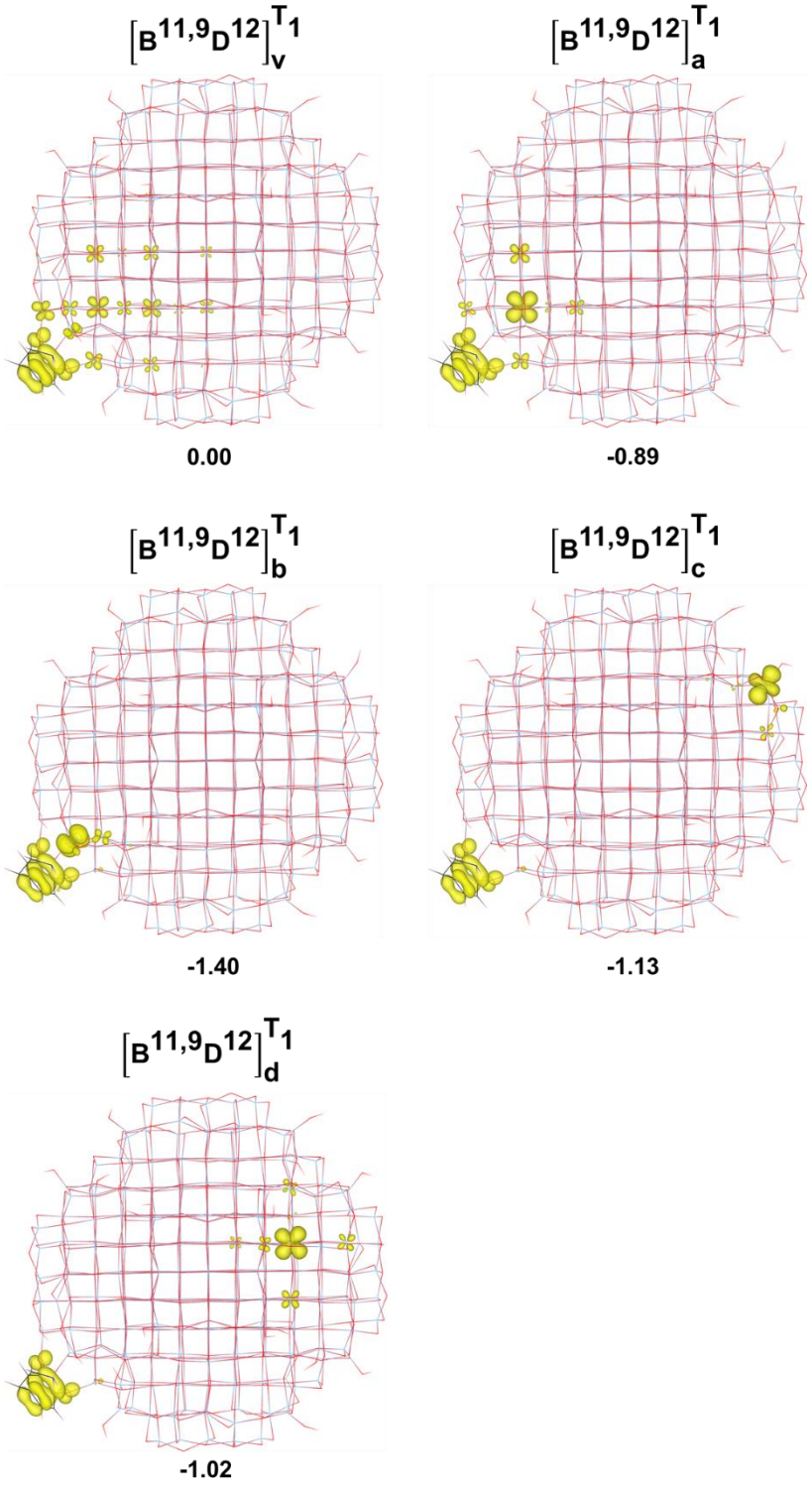

Figure 4.10 Top views of the spin density plots of the $B^{11,9}D^{12}$ configuration (see **Figure 4.4b**) for the v) vertical triplet state, a) self-trapped triplet exciton, b) triplet exciton involving the Ti atom bound to the NH_2 residue and c) separated charges with the hole on the dopamine molecule and the electron on a distant Ti atom, d) separated charges with the hole on the dopamine molecule and the electron on a distant subsurface Ti atom. Below each structure, the energy gain in eV with respect to $\left[B^{11,9}D^{12}\right]^{T_1}_{v}$ (ΔE_{trap}) is reported. Iso-value=0.005 e/Å^3.

We have considered other possible positions resulting from electron hopping (c and d in **Figure 4.9** and in **Figure 4.10**). However, none of them is lower in energy than configuration **b** (see

ΔE_{trap} values in **Table 4.1**). Therefore, it is highly improbable that the electron will have the chance to reach the nanoparticle's surface far apart from the adsorbed molecule. The hole is formed in a π state of dopamine, where it is very stable due to large structural deformation involving the elongation of C_1–C_2 and Ti–O bonds by ~0.09 and ~0.14 Å, respectively. It is relevant to note (see **Table 4.1**) that the smallest distortion energy value ($\Delta E_{dist} = [T_1 - S_0]$) is registered for the self-trapped exciton (1.31 eV), whereas for all the other electron/hole configurations we observe rather larger distortion energies from 1.66 to 2.24 eV.

Table 4.1. Trapping energy (ΔE_{trap}) in eV of photoexcited charge carriers at different sites for the adsorbed dopamine configuration $B^{11,9}D^{12}$ on the spherical TiO_2 nanoparticle in the T_1 excited state, with respect to $\left[B^{11,9}D^{12}\right]_v^{T_1}$, degree of localization (%electron or %hole), structural distortion energy with respect to the ground state ($\Delta E_{dist} = [T_1 - S_0]$) and $[S_0(T_1) - T_1]$ energy difference in eV. No symmetry constrains are imposed in all the calculations. The binding site numbering is defined graphically in **Figure 4.2**, whereas the charge carrier localization configuration is defined in **Figure 4.9.**

	ΔE_{trap} (eV)	%electron	%hole	ΔE_{dist} (eV)	$S_0(T_1) - T_1$ (eV)
DOPAMINE					
$\left[B^{11,9}D^{12}\right]_v^{T_1}$	0.00	12%	97%	0.00	-
$\left[B^{11,9}D^{12}\right]_a^{T_1}$	-0.89	76%	97%	1.31	-0.51
$\left[B^{11,9}D^{12}\right]_b^{T_1}$	-1.40	99%	98%	1.66	+0.35
$\left[B^{11,9}D^{12}\right]_c^{T_1}$	-1.13	93%	97%	2.24	+0.67
$\left[B^{11,9}D^{12}\right]_d^{T_1}$	-1.02	77%	97%	1.78	+0.09

To rationalize the reason why the **b** configuration of $B^{11,9}D^{12}$ in the T_1 state is so stable with respect to **a** configuration and even lower in energy than the corresponding S_0 state in those atomic distorted positions, we must analyze the DOS in detail and compare results for configurations **a** and **b** (see **Figure 4.10**). The critical feature is the position of the highest occupied state (HOMO) for the α or up component. For $\left[B^{11,9}D^{12}\right]_a^{T_1}$, this peak is very high in energy (at -4.56 eV), just below the bottom of the conduction band, whereas for $\left[B^{11,9}D^{12}\right]_b^{T_1}$ it is deeper in the gap (at -5.28 eV) by about -1.2 eV. This HOMOα state is the one hosting the excited electron, whereas the LUMOβ is the state associated to the hole. The recombination process is essentially the transfer of the electron from the HOMOα state to the LUMOβ one, leading to the electronic structure shown in c and d panels of **Figure 4.11**. Therefore, whereas in $\left[B^{11,9}D^{12}\right]_a^{T_1}$ the recombination process is favored since the LUMOβ is below the HOMOα

state, in $[B^{11,9}D^{12}]_b^{T_1}$ the recombination is not an energetically favorable process since LUMOβ is just slightly above the HOMOα state in the T_1 and, consequently, the resulting HOMO for $S_0(T_1)$ in panel d is higher in energy than the HOMOα in panel b for T_1. In this geometry T_1 is preferable than S_0, as schematically shown in **Figure 4.9**.

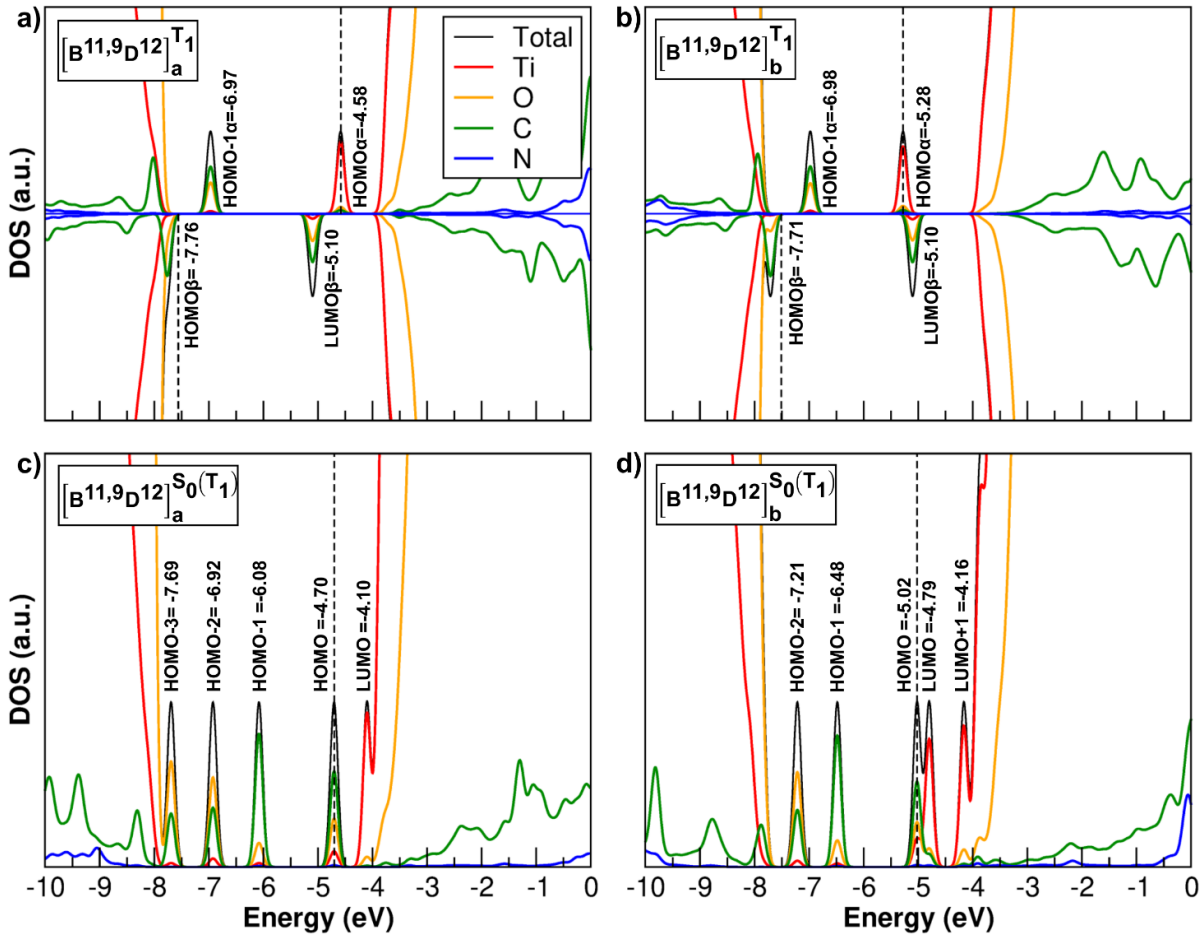

Figure 4.11 Total (DOS) and projected (PDOS) density of states for a) $[B^{11,9}D^{12}]_a^{T_1}$, b) $[B^{11,9}D^{12}]_b^{T_1}$, the recombined singlet in the T_1 optimized geometry for c) a and d) b configurations. Ti is represented in red, O is orange, C is green and N is reported with a blue line. The zero energy is set to the vacuum level. The energy in eV of all the mid-gap states are reported on each plot.

Based on the results presented in this section, we may conclude that in the photoexcited dopamine/TiO_2 anatase NP complex there is an intrinsic and effective charge separation, since the hole is localized on the dopamine and is not coupled with phonons of the TiO_2 lattice, whereas the electron sits on Ti ions of the NP in line with the experimental findings.[108,137,129,241] The hole localization on the dopamine has the beneficial effect of lowering the oxidative power of TiO_2 NP under light irradiation. We can prove this by computing the vertical and adiabatic ionization potentials (IP) for the bare NP and comparing them to the values for the dopamine/TiO_2 NP complex in the lowest energy $B^{11,9}D^{12}$ configuration (see **Table 4.2**). The reduction in the adiabatic IP value is of about 1.3 eV, in line with previous works.[252]

Table 4.2 Trapping energy (ΔE_{trap}) in eV for an excess electron and hole at the different sites with the charge localization (%electron or %hole) in the $B^{11,9}D^{12}$ and $B^{11,9}C^{12}$ configurations. The references zero for the ΔE_{trap} is obtained by adding one electron in the former case and removing one electron in the latter with no atomic relaxation. The charge localizations (%electron or %hole) are also given. Electron affinity (EA) of one extra electron coming from the vacuum and ionization potential (IP) of the most external, less bound, electron to the vacuum level are reported, together with a comparison with the values for the EA and IP of the bare NP. The binding site numbering is defined graphically in **Figure 4.2** whereas the charge carrier localization configuration is defined in **Figure 4.8**. Spin plots are shown in **Figure 4.9**.

Excess electron	ΔE_{trap} (eV)	**%electron**	**EA**	**EA BARE NS**
$\left[B^{11,9}D^{12}\right]^-_v$	0.00	5%	3.23	3.27[1]
$\left[B^{11,9}D^{12}\right]^-_a$	-0.12	17 %	3.35	3.40[1]
$\left[B^{11,9}D^{12}\right]^-_b$	-0.46	92%	3.69	3.67[1]
$\left[B^{11,9}D^{12}\right]^-_c$	-0.39	92%	3.62	-
$\left[B^{11,9}D^{12}\right]^-_d$	-0.27	77%	3.50	3.51[1]
Excess hole	ΔE_{trap} (eV)	**%hole**	**IP**	**IP BARE NS**
$\left[B^{11,9}D^{12}\right]^+_r$	-0.99	97%	6.23	7.50[2]

[1] Values calculated for the annealed NP used throughout this work.

[2] Values reported in ref.[83]

We have also estimated the electron affinity (EA) of the dopamine/TiO_2 NP complex in the lowest energy $B^{11,9}D^{12}$ configuration. In this case, we do not expect large differences from the bare TiO_2 NP because the electron is delocalized/localized on Ti atoms. This is confirmed by the data since, when comparing EA for corresponding electron position on the dopamine/TiO_2 NP complex and bare NP, the observed differences are tiny. Unexpectedly, this observation is true also for $\left[B^{11,9}D^{12}\right]^-_b$, where the electron is trapped at the Ti atom that is directly coordinated with the -NH_2 moiety of dopamine. The Ti---NH_2-dopamine interaction does not seem to have any effect on the electron trapping ability of that Ti site.

4.4. Increasing linker coverage on TiO_2 spherical NP

4.4.1. Adsorption modes and packing

In this section, we discuss the effect of binding an increasing number of dopamine molecules on the adsorption energy and on the electronic properties of the dopamine/TiO_2 NP composite system. To obtain the full coverage, the dopamine molecules were adsorbed in a mixture of bidentate and chelated fashion and with the ethyl-amino groups pointing up towards the vacuum. The dopamine molecules were added to the surface of the NP step by step. Due to the quasi-symmetry (D_{2d}) of the nanoparticle, in each step we filled the four symmetrically equivalent positions, relaxed the structure and then added the next four molecules. Based on this step-wise approach, we were able to build two different full coverage configurations. In the first model 46 (32 chelated and 14 bidentate, $TiO_2^{46\text{-dopamine}}$) and in the second one 42 (24 chelated and 18 bidentate, $TiO_2^{42\text{-dopamine}}$) dopamine molecules were anchored to the surface of the nanoparticle, as shown in a) and b) of **Figure 4.12**.

The main difference between the two models is in the number of molecules and type of binding on the Ti sites at the spherical NP equator (see **Figure 1**). In $TiO_2^{42\text{-dopamine}}$ (**Figure 12b**), there are four dopamine molecules adsorbed in bidentate fashion on Ti_{4c} [9] and [11] sites and four molecules bonded in chelated fashion on Ti_{4c} [10] sites. Therefore, the dopamine adsorption configurations at the NP equator are $\mathbf{B^{9,11}}$ and $\mathbf{C^{10}}$ (see Section 3.1.a). On the other hand, for $TiO_2^{46\text{-dopamine}}$, all the twelve Ti_{4c} sites at the NP equator are chelated to dopamine molecules ($\mathbf{C^9}$, $\mathbf{C^{10}}$, $\mathbf{C^{11}}$). For both configurations, we were not able to adsorb molecules on all the Ti_{5c} and Ti_{4c} undercoordinated sites on the NP due to steric hindrance and to geometrical arrangement of Ti sites on the surface, but we were able to reach up to ~61% of coverage (calculated as the ratio between the number of adsorbed molecules and the total number of binding sites on the NP model). Molecules on the tropic and pole regions (see **Figure 4.2** and **Figure 4.12**) are assembled similarly in the two models. After relaxation, only the molecules at the tropics are slightly affected by the different configurations at the equator, while those at the poles are identical for both models. We also observed the formation of four H-bonds between the ethyl-amino portions of dopamine molecules. These weak interactions are absent in $TiO_2^{42\text{-dopamine}}$, where the equator is less crowded compare to $TiO_2^{46\text{-dopamine}}$, due to the presence of bidentate molecules.

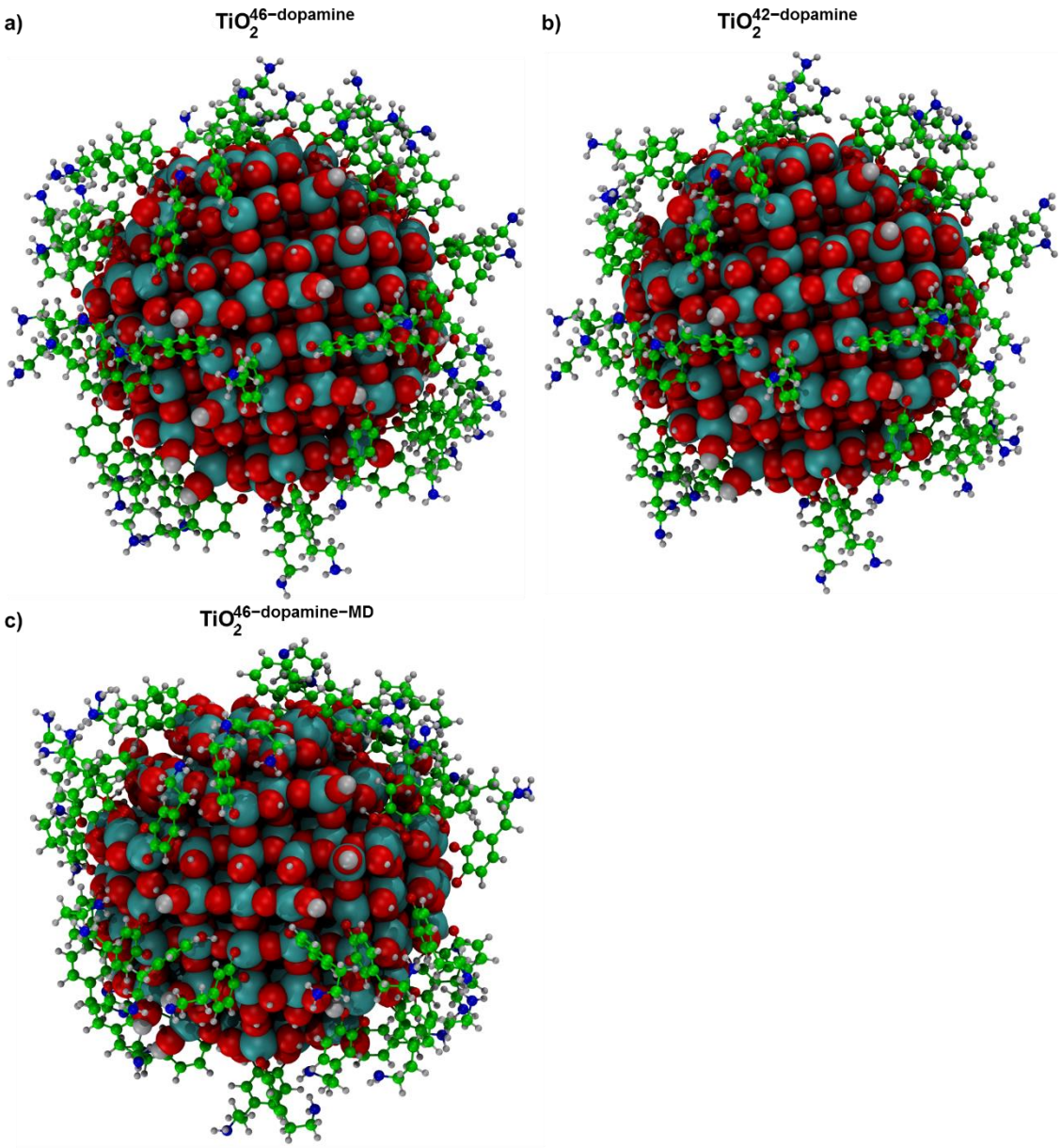

Figure 4.12 3D structure for the high coverage models: a) $TiO_2^{46\text{-}dopamine}$, b) $TiO_2^{42\text{-}dopamine}$ and c) $TiO_2^{46\text{-}dopamine\text{-}MD}$
.

As mentioned above, the dopamine molecules were added gradually in the equivalent positions on the NP, therefore, we were able to investigate the effect of increasing density coverage on the stability of the systems. In addition, we could also analyze the intermediate coverage structures for both models. In **Table 4.3** the adsorption energies per molecule (ΔE_{ads}^{mol}) are reported.

Table 4.3 Adsorption energies per molecule (ΔE_{ads}^{mol}) in eV for increasing coverage of dopamine according to the filling in $TiO_2^{42\text{-dopamine}}$ and $TiO_2^{46\text{-dopamine}}$ model, as calculated by DFTB.

DFTB-D3	$TiO_2^{46\text{-dopamine}}$ **C^{11}**, **C^{9}**, **C^{10}** equator	$TiO_2^{42\text{-dopamine}}$ **B^{11,9}**, **C^{10}** equator
Nr.	ΔE_{ads}^{mol}	ΔE_{ads}^{mol}
1	-3.21	-3.98
2	-3.22	-4.01
4	-3.17	-3.95
8	-3.10	-3.19
12	-2.92	-
16	-2.95	-
24	-2.80	-
High*	-2.46	-2.39

* The highest coverage for **B^{11,9}, C^{10}** equator growth is 42 dopamine molecules, while for **C^{11}**, **C^{9}**, **C^{10}** is 46 dopamine molecules.

Up to four bound molecules, the adsorption energy per molecule changed only slightly. Beyond that, we observe a distinguishable decrease of the adsorption energy value: for $TiO_2^{46\text{-dopamine}}$, the difference between ΔE_{ads}^{mol} at the lowest and highest coverage is 0.75 eV, whereas for $TiO_2^{42\text{-dopamine}}$, it is 1.59 eV. Therefore, the addition of dopamine molecules up to full coverage is an energetically favorable process, even though the energy gain at each step decreases. We also note that this is not a linear process particularly for $TiO_2^{42\text{-dopamine}}$ (blue line in **Figure 4.13**). Here the adsorption energy per molecule for 1, 2 and 4 adsorbed dopamine(s) remains nearly constant since the molecules are adsorbed on the quasi-equivalent positions far from each other. By adding the next four molecules we observed a sudden change of ~0.76 eV for the adsorption energy per molecule. At the highest coverage, $TiO_2^{46\text{-dopamine}}$ is more stable compared to $TiO_2^{42\text{-dopamine}}$, whereas at low coverage, when only few molecules are originally adsorbed the opposite is true. This inversion comes from the fact that at low coverage the bidentate adsorption is energetically favored over the chelated. On the other hand, at full coverage, due to the high packing of the dopamine molecules at the equator in $TiO_2^{46\text{-dopamine}}$, we observe the formation of H-bonds and π-π stacking interactions that are not present in $TiO_2^{42\text{-dopamine}}$.

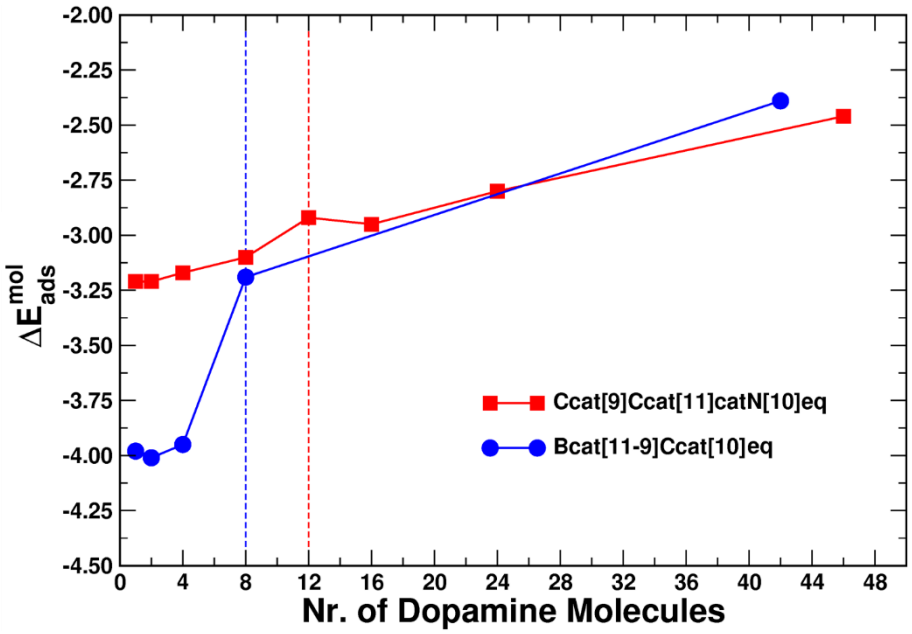

Figure 4.13 Adsorption energy per molecule in eV (ΔE_{ads}^{mol}) as a function of the number of dopamine molecules dissociated on the NS. The blue line represents the increasing coverage for the 42-dopamine model, while the red line represents the increasing coverage for the 46-dopamine model. The dashed lines indicate the number of molecules for which the equator is completely full in the two different configurations.

4.4.2. Electronic properties at increasing coverage

Absorption properties of dopamine/TiO_2 NP complex at increasing surface coverage (up to 80-90%)[107] have been investigated experimentally. The wavelength of the absorption onset is found to largely shift up to 800 nm with an increasing absorbance at all wavelengths with the coverage.[107] Based on measurements for increasing concentrations of linker and on the Job's method,[246] it was possible to determine both the constant of complexation (1400 M^{-1}) and the stoichiometric ratio between dopamine and Ti surface sites of 2:1, which is very close to the 2.3:1 ratio in the $TiO_2^{46\text{-dopamine}}$ model of the present study.

For this reason, the investigation of the effect of increasing dopamine coverage on the electronic properties of the complex was performed on the $TiO_2^{46\text{-dopamine}}$ model (by considering a progressively increasing number of molecules up to 46). At the full coverage the system has 1711 atoms. Due to the large size of these structures, a full geometry optimization at the hybrid DFT level of theory is prohibitive. On the other hand, as we discussed in **Section 4.2.3.1**, the electronic structure obtained using DFT/DFTB approach is qualitatively accurate enough to describe the electronic properties as compared to hybrid DFT calculations. Therefore, in the following we will discuss the results obtained by performing single point calculations at the hybrid DFT (B3LYP level of theory) on the DFTB optimized geometries (labeled as DFT/DFTB).

In **Figure 4.14** we show the electronic structure for the bare TiO_2 spherical nanoparticle, and for the dopamine/TiO_2 NP systems with 1, 2, 4, 8, 12, 16, 24, 46 dopamine molecules. The values for the HOMO-LUMO gap, calculated as the difference between the last occupied state (HOMO) and the lowest-energy empty state (LUMO) are reported on every plot. We also report the values for the band gap (E_g), calculated as the difference between the last occupied state related mainly to the oxygen atoms of TiO_2 and the first TiO_2 empty state.

The HOMO-LUMO gap clearly shrinks by increasing the coverage. This trend is present not only in the DFT/DFTB density of states (DOS), but also in the DFTB calculations, which are not reported for the sake of simplicity.

At low coverage, there are three localized mid-gap peaks for 1, 2, and 4 molecules adsorbed and all of them are related to the molecule: the HOMO and HOMO-1 are attributed to carbon atoms (even if highly hybridized with nitrogen), and the HOMO-2 is mainly composed ofì N atoms *p* states. Since up to four bound molecules, only the symmetrically equivalent positions are covered, the mid-gap states are located at the same energy, but the intensity of the peaks changes accordingly. By adsorbing more molecules on the surface, new localized peaks appear both inside the band gap and at the top of the valence band, causing a shrinking of the band gap value.

Going to higher coverages (above four molecules), the electronic structures become more complicated. Due to the increasing density coverage, the molecules interact both with each other and with the NP surface. Therefore, the peaks are highly hybridized and assigning them to a specific atom is not trivial. Nevertheless, we can still notice the predominant contribution of both C and N. Notably, we can observe that the HOMO-LUMO gap continues to narrow. At the highest possible coverage, the HOMO-LUMO energy difference is only 0.42 eV. Here, the localized peaks inside the gap and at the top of the valance band merge to create a continuous large band.

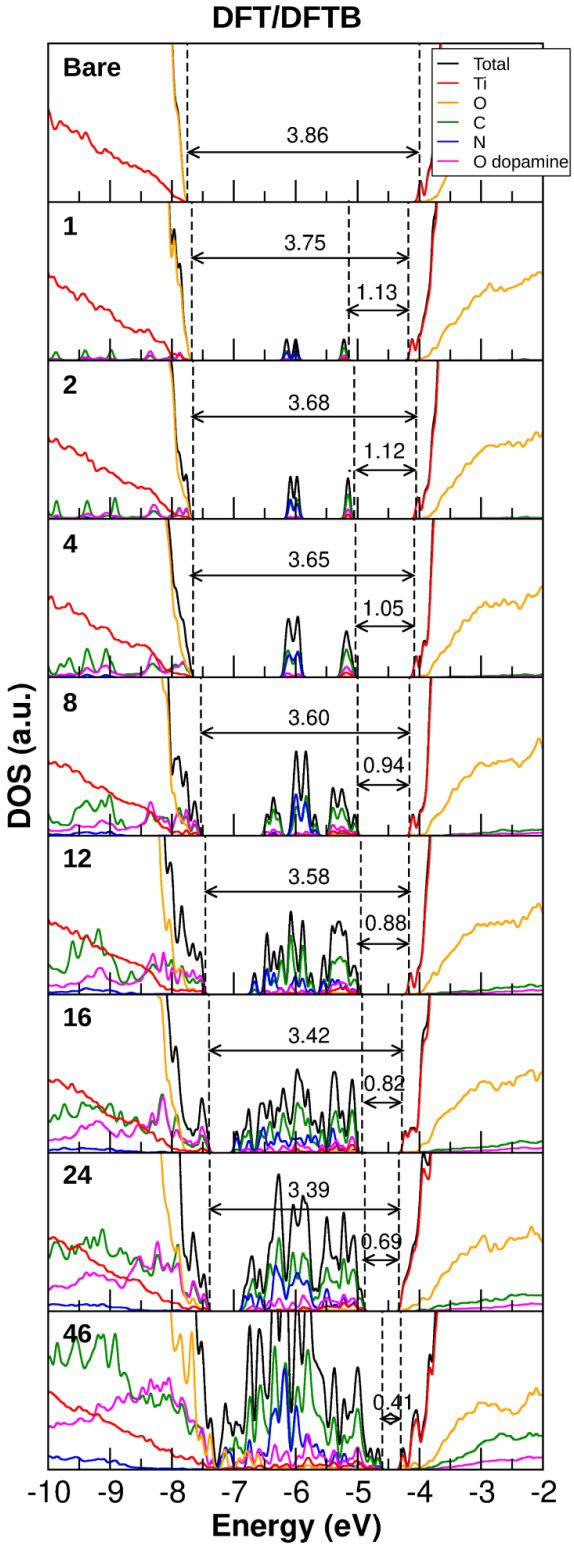

Figure 4.14. Total (DOS) and projected (PDOS) density of states for the bare TiO_2 2.2nm NP, and for 1, 2, 4, 8, 12, 16, 24 chelated dopamine molecules and for the 46-dopamine high coverage model on the TiO2 NP calculated by DFT/DFTB. Ti is represented in red, O of the TiO2 NP is orange, while O of the dopamine is marked in violet. C is green, and N is reported with a blue line. The zero-energy reference is set at the Fermi energy of the system and highlighted by a dotted line. The values for the HOMO-LUMO gap and the band gap are (Eg) are reported together with double-head arrows in on each plot.

4.4.3. Dynamics at full coverage of dopamine on TiO_2 NP

To investigate the effect of temperature on the rearrangement of the as-deposited dopamine molecules in the $TiO_2^{46\text{-dopamine}}$ model, we performed DFTB molecular dynamics runs at 300 K for 10 ps.

In the optimized $TiO_2^{46\text{-dopamine}}$ model shown in **Figure 4.12a**, before the MD at 300 K, there is no direct interaction between the -$CH_2CH_2NH_2$ functional groups and the surface of the nanoparticle. However, few H-bonds are established between the -NH_2 groups of spatially close dopamine pairs of molecules (eight H-bonds in the length range of 2.02-2.23 Å). In the optimized $TiO_2^{46\text{-dopamine}}$ model after MD at 300 K, shown in **Figure 4.12c**, ~24 % of -$CH_2CH_2NH_2$ functional groups have bent toward the surface (11 molecules out of 46), making a H-bond with the NP surface hydroxyl groups. The length of these H-bonds is in the range of 1.98-2.12 Å. The –NH_2-NH_2 bonds stabilizing the $TiO_2^{46\text{-dopamine}}$ model shown in **Figure 4.12a** are now seven.

The remaining molecules (~76 %) stay in an up configuration toward the vacuum. We also observed some partial rotation of the -$CH_2CH_2NH_2$ functional group, but, due to the lack of space between the molecules at the high coverage, the 7. functional groups do not reach the surface. In general, we observe that, during the dynamics, the molecules rearrange and try to get closer to the surface. To provide a quantitative measure of this effect, we calculated the average distance of the N dopamine atoms from the barycenter of the NP, before and after the MD run, and we observe a ~5% reduction is observed. This is a small effect. Differently, for a dopamine full monolayer adsorbed on a (101) surface model of anatase TiO_2, as we discussed in **Chapter 3**, 50% of the adsorbed molecules bent towards the surface, undergoing proton transfer processes from the surface bridging OH groups to the –NH_2 dopamine moiety. Also for the case of the $TiO_2^{46\text{-dopamine}}$ NP model, we considered the possibility that some of the fnctional groups could rotate in order to create hydrogen bonds with the anchoring oxygens of other adsorbed dopamine molecules, acquiring a proton from one O_{3c} of the surface. We were able to localize stable –NH_3^+ species only in the case of two out of 46 molecules. This configuration is 0.28 eV higher in energy per dopamine molecule (DFTB level of theory). Similarly, for the (101) slab the corresponding DFTB result was 0.33 eV. However, in DFT the relative stability was found to reverse for the (101) surface (see **Chapter 3**, **Section 3.5**). Thus, we might expect that only a very low percentage of dopamine molecules on curved NPs becomes protonated.

Nevertheless, it is important to remember that all these calculations were carried out in vacuum and the presence of an embedding solution like water could change the local polarization at the interface and therefore impact on the competition between molecule/surface and molecule/molecule interactions. The behavior of the $TiO_2^{46\text{-dopamine}}$ in water through a QM/MM (quantum mechanics/molecular mechanics) is now a work in progress in our group.

The electronic structure for the optimized $TiO_2^{46\text{-dopamine}}$ configuration after 10 ps MD at 300 K is shown in **Figure 4.14** and can be directly compared with that of the optimized configuration before MD at the bottom of **Figure 4.12**. The molecular rearrangement following the MD causes a different resulting dipole of the molecular layer on the NP surface that affects the position of the NP valence and conduction bands with respect to the vacuum. We register a rigid shift of 0.36 eV. On the contrary, the dopamine states are stabilized after MD because of a more favorable disposition by -0.23 eV. The net result is a widening of the HOMO-LUMO gap from 0.41 eV (for the configuration before MD at the bottom of **Figure 4.12**) to 1.0 eV (for the configuration after MD of **Figure 4.15**).

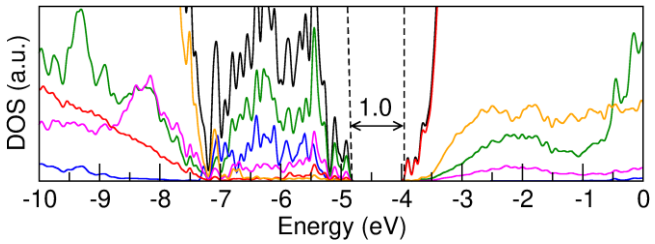

Figure 4.15 Total (DOS) and projected (PDOS) density of states for the 46-dopamine high coverage model on the TiO_2 NP calculated by DFT/DFTB after molecular dynamics simulation. Ti is represented in red, O of the TiO_2 NP is orange, while O of the dopamine is marked in violet. C is green, and N is reported with a blue line. The HOMO-LUMO gap is reported for each plot by dashed lines. The zero energy is set to the vacuum level.

4.5. Conclusions

In this Chapter, we presented a DFT- and DFTB-based study on the structural, electronic, and self-assembling properties of dopamine adsorption on curved TiO_2 NPs of realistic size (2−3 nm size with ~700 atoms). The investigation spanned from single molecule adsorption to a full coverage regime.

For the low coverage, we have determined the favorable molecular adsorption modes and analyzed the electronic charge-transfer effects, identifying the new molecular states in the band gap introduced by the adsorbed linker species.

On top of that, we have investigated the processes following visible-light photoexcitation of the charge transfer complex: exciton formation, trapping, charge carrier diffusion, or recombination. We have learned that the photoexcited hole is trapped in the π-states of the aromatic ring, whereas the photoexcited electron can hop on different Ti sites, leading to an effective charge transfer separation. Interestingly, the one that provides the strongest electron binding is the surface Ti atom already involved in the bonding with the $-NH_2$. The hole trapping has a beneficial effect of lowering the oxidative power of TiO_2 NPs under light irradiation.

As a further step, we then consider a growing molecular layer on the NP and analyze the self-assembling mechanism and the effects on the electronic properties of the complex. To achieve a very high coverage regime, most of the molecules have been chelated to four-fold coordinated Ti atoms and bind in bidentate mode to pairs of five-fold coordinated ones. All the molecules are positioned in an upward configuration to reduce the steric hindrance and maximize the dispersion interactions between them.

Molecular states in the gap increase progressively, until they form a continuous band from the top of the valence band of the TiO_2 NP to about 0.4 eV from the bottom of its conduction band. At the maximum coverage (46 molecules per NP), we perform molecular dynamics runs at 300 K to compare the molecular configuration and electronic properties of the NP/ linker complex before and after thermal treatment to better account for the competition between molecule/surface and molecule/molecule interactions.

Considering that on the flat anatase (101) surface 50% of dopamine molecules were found to bent toward the surface and undergo proton transfer (see **Chapter 3**), on curved NPs only a small fraction of them bends toward the surface, because of the lack of space and steric hindrance. Since nearly all the functionalities are not involved in any bond with the surface, they are disposable for further interactions with the external environment, e.g. with the solvent

or with a bio-active molecule. This highlights how curved NP surfaces are better substrates for bioconjugation through the bifunctional linker approach than flat ones. Our system composed of the spherical NP functionalized with dopamine molecules, is suitable to be used to build hybrid bioinorganic nanocomposites, which are the final aim of this project.

5 Optical and electronic properties of dopamine-functionalized TiO_2 surface through TDDFT

In this chapter, the optical properties of the dopamine-modified anatase TiO_2 (101) surface presented in **Chapter 3** are obtained through a time-dependent density functional theory (TDDFT) study. Firstly, the TDDFT method used for this work is assessed through a comparison of the optical spectra of a dopamine molecule in vacuum and of bulk TiO_2 anatase with experimental and computational data available in literature.[2,3] Secondly, the electronic absorption spectra for different geometrical configurations of dopamine on anatase TiO_2 (101) surface at low and full coverage regimes are reported.[1]

[1] This work was conducted in collaboration with Professor Silvana Botti's group, Institut für Festkörpertheorie und –optikin, Friedrich-Schiller Universität, Jena.

5.1 Introduction

5.1.1. Surface-modified TiO_2 for photoexcitation

As already discussed in the previous chapters, titanium dioxide is characterized by outstanding photoabsorption properties.[253,254,74] Therefore, TiO_2 is extensively used in photoenergy conversion applications, such as photocatalysis[35,60,255] and solar cells.[88,256,257,258,259] More recently, the possibility to exploit the photocatalytic properties of TiO_2 in nanomedicine has emerged,[1] since the photoexcited hole and electron are capable of generating reactive oxygen species (ROS), inducing cell death.[260] The fact that the TiO_2–NPs are cytotoxic only once they are light-activated is crucial for the purpose of selectively kill only the targeted sick cells, limiting the side effects on the rest of the body, and making them good candidates for cancer treatment.[37]

Between the three possible crystal phases of TiO_2, we focus on anatase, which is characterized by an indirect band gap, experimentally measured to be 3.2 eV at environmental temperature,[52] and 3.4 eV at 4 K[52], that is larger compared to the direct band gap of rutile, measured to be 3.0 eV[42], making the recombination of charge carriers slower.[254] As previously discussed in detail in **Chapter 1**, anatase is usually considered to be more suitable for light-energy conversion applications.

The major drawback in the use of anatase in photo-applications is that, due to its wide band gap, it only absorbs light in the ultraviolet energy region, which represents only a small portion (< 5%) of the solar spectrum. Since the light absorption process determines the amount of excited charges, more charge carriers are likely to be accumulated on the surface if more light can be absorbed by the photocatalyst. The wide band gap limits the use of bare TiO_2 in photovoltaic and photocatalytic applications, due to the low efficiency of absorption of the solar spectrum frequencies. Even more so, the use of TiO_2 is very much restricted in photodynamic therapies, since the UV-light required to excite TiO_2 does not match the optical window of the biological tissues (**Figure 5.1**), at 600-1000 nm (visible and near-IR).

Among the possible strategies available for the band gap engineering of anatase, surface modification is particularly interesting for biomedical applications, which are of interest for this thesis. In fact, one can functionalize the surface with organic ligands presenting a spare functional group, that can further link biological molecules.

Surface functionalization of semiconducting oxides and, in particular, of TiO_2 is a wide and active area of research due to the variety of applications, including photocatalysis, photoelectrochemistry and photovoltaic cells, and in particular dye-sensitized solar cells

(DSSCs). [258,259,257,258,259] In the case of TiO_2, surface functionalization aims at narrowing the band gap of the semiconductor in order to modify its range of absorption. Moreover, the linking of organic molecules to the undercoordinated sites of the surface has significant impact on charge separation, transport, and recombination processes. Once functionalized, TiO_2 surfaces or nanostructures develop the ability to harvest a major portion of the solar spectrum, becoming suitable for photon energy conversion, both for environmental and nanomedical applications.

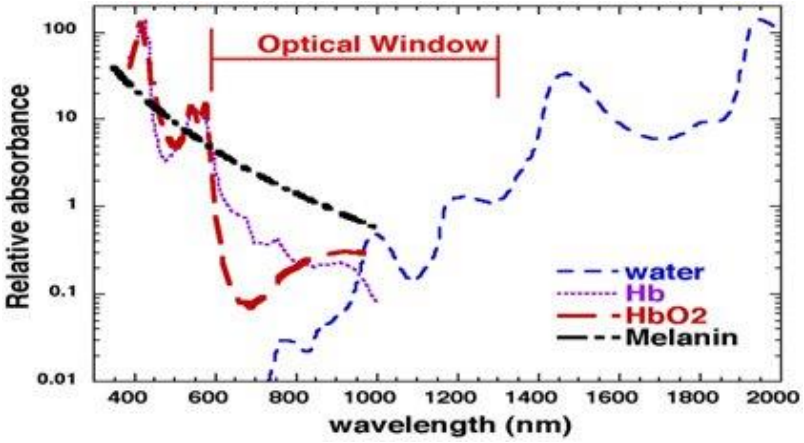

Figure 5.1 Optical therapeutic window in the optical spectral range of red and near infrared, wherein the efficiency of light penetration in the tissue is maximum. Hb: Hemoglobin. HbO2: Oxygenated hemoglobin. [261]

5.1.2. Ligand to metal charge transfer (LMCT)

Two main types of electronic transitions are observed in transition metal complexes: the *d-d* transitions between the orbitals split in the crystal field and the charge transfer transitions. As the term implies, these transitions involve electron transfer from one part of a complex to another.

Let us consider a generic coordination complex, consisting of a central metal atom or ion surrounded by bound molecules or ions, which are usually referred as ligands. These ligands are characterized σ, σ^*, π, π^*, and nonbonding (n) molecular orbitals. If the ligand molecular orbitals are full, charge transfer may occur from the ligand molecular orbitals to the empty or partially filled metal *d*-orbitals (**Figure 5.2**). The absorptions that arise from the transfer of one electron from an orbital that is mainly ligand in character, to one that is mainly metal in character are called ligand-to-metal charge-transfer (LMCT) and they result in intense bands. When these absorptions fall in the visible region, i.e. the energy required for the LMCT transition is not too high, they often produce rich colors. In a primitive sense, a charge transfer transition may be regarded as an internal redox process.[262] In fact, ligand to metal charge transfer results in the reduction of the metal and the oxidation of the ligands.

This makes it possible to use familiar ideas, such as ionization energy and electron affinities, to predict the conditions that will favor this transition. In order to have a favorable LMCT, we would want a metal with a relatively high ionization energy so that it would have empty orbitals at fairly low energies. Therefore, transition metals are good candidates to be used as acceptor metals. An ideal ligand would be a non-metal with a relatively low electron affinity, which would imply filled orbitals of fairly high energy and would be readily oxidizable. The net result of such a metal-ligand combination would be that the orbitals involved in the LMCT process would be close enough in energy, so that the transition could be induced by a photon in the visible ore in the near-ultraviolet region.

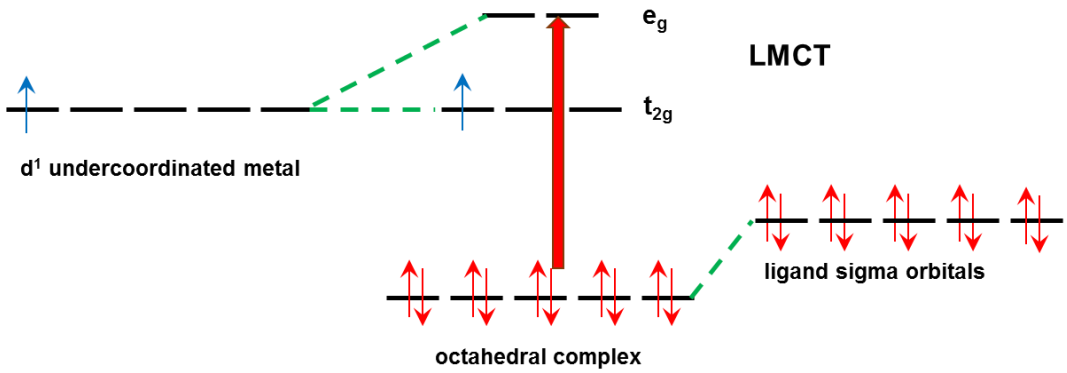

Figure 5.2 Scheme for a generic ligand-to-metal transition in a charge transfer complex

When one or two molecules associate and a fraction of electronic charge is transferred between the molecular entities, a charge-transfer complex (CT complex) is formed. The eventual creation of a new absorption band in the visible range enables us to develop TiO_2-based photocatalytic systems for energy conversion. Titanium atom are in a high oxidation state (Ti^{4+}) in titanium dioxide, therefore they are extremely inclined to be reduced. The HOMO of dopamine, on the other side, is constituted by the π state of the phenyl ring.

5.1.3. Two models for the charge transfer

When the modified TiO_2 system is properly irradiated, an electron is excited from the molecular moiety, which works as an electron donor or reductant, to the semiconductor, which is the electron acceptor or oxidant. The electron transfer from the HOMO of an adsorbed molecule to the CB of a semiconductor has been modeled in literature through two different limit mechanisms, depending on the nature of the electron coupling between the different components of the system (**Figure 5.3**).

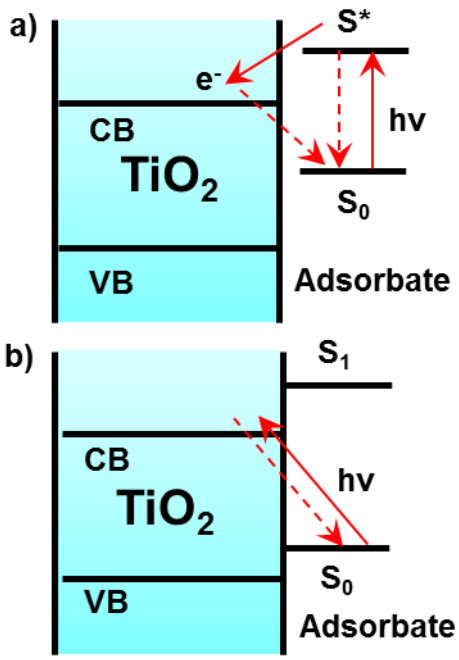

Figure 5.3 Scheme of the a) indirect b) direct mechanism of electronic injection from an adsorbed molecule to the semiconductor TiO_2.

On one hand, for weakly coupled systems, usually described by the Sakata-Himamoto-Hashimoto model,[263] one electron is initially promoted to the LUMO of the dye molecule and later transferred to the solid. On the other hand, strongly-coupled systems are better represented through a direct mechanism by the Creutz-Brunschwig-Sutin model, [264,265] which means that an electron from the HOMO of the molecule is injected in the CB of the semiconductor in one step, giving birth to a LMCT transition. This mechanism of charge transfer is often referred to as ultra-fast direct injection, since it does not involve any intermediate excited state and the related time-scale has been estimated to be in the 10-25 fs range.[266,267] According to the latter model, the dipole transition moment for a generic semiconductor-molecule system, which indicates the probability to observe an electronic transition between the two components of the system, is directly proportional to their coupling:

$$\mu_{12} = \frac{H_{12} er}{v_{max}} \tag{5.1}$$

where μ_{12} is the transition dipole moment from state 1, localized on the molecule, and state 2, localized on the semiconductor, H_{12} is the electronic coupling between the two states, r is the distance over which electron transfer occurs and v_{max} is the maximum frequency irradiating the system. This means that the LMCT does not necessarily involve the first empty levels at the bottom of the CB because the selection rule for this charge transfer requires the existence of an electronic coupling between ligand and semiconductor. Understanding in practice the

mechanism of this coupling is one of the aims of this work and it is crucial for the building of efficient devices through surface-modified systems.

Both limit mechanisms can take place in the same system. In particular, the appearance of direct charge transfer bands at low energy in the spectrum does not exclude that a HOMO-LUMO molecular transition could also take place at higher energy values.

5.1.4. State-of-the-art of theoretical calculations

In order to investigate if the system undergoes a direct or indirect injection mechanism, theoretical investigation can be a useful tool. From a theoretical point of view, density functional theory (DFT) is a ground state theory and, therefore, it cannot be used to simulate UV-visible spectra and investigate optical properties, which are related to excited states. In the earliest publications, excitations of TiO_2-modified systems with catechol or benzoic acid have been studied by semiempirical methods, as INDO/S-CI (Intermediate Neglect of Differential Overlap/Singles-Configuration Interaction) calculations.[268] The INDO methods use zero differential overlap for two-electron integrals and, therefore, is still a rough approximation.

In more recent computational works, TDDFT has been used to describe the optical properties of TiO_2-modified systems.[96,100-106,128] TDDFT,[188] which extends density functional theory into the time domain, is capable to describe excited states.

Since TDDFT is computationally costly compared to semiempirical methods, up to now it has been mainly used to investigate molecular systems or small clusters, by selecting only a narrow range of energy, which means a small number of excitations in the spectrum to be computed. Large system size and broad spectral region (from IR to UV through the whole visible region) bring linear response TDDFT computation quickly to its limit.

System composed of TiO_2 modified by organic dyes were modeled through small clusters, $(TiO_2)_9$, by Sánchez-de-Armas et al.[128] By the comparison of the spectrum for the free dyes and for the dyes adsorbed on TiO_2, together with the analysis of the molecular orbitals of these complexes, they could distinguish between direct or indirect mechanism for electron injection. The authors even suggested the existence of intermediate possible mechanisms, depending on the energy difference between the HOMO and the LUMO of the molecule.

A much bigger cluster, $(TiO_2)_{38}$, was extensively used by De Angelis et al. with Ru dyes,[96,100] with perylene,[101] with $[Fe(CN)_6]^{4-}$,[101] and by Zhao et al. with a metal-free C217 dye.[103]

De Angelis et al. also managed to simulate the absorption spectrum of squaraine molecules adsorbed on the anatase TiO_2 surface through time-dependent DFT calculations applied to periodic models.[104] Moreover, they interfaced the system with water, considered different geometries and calculated the optical spectrum of several snap-shots from a Car-Parrinello molecular dynamics in order to investigate the effect of the temperature on the properties of the system.[105,106] In order to perform TDDFT on big periodic systems, they employed a recursive scheme, where instead of individual excitation energies, the complete dipole response function is computed using a Lanczos algorithm.[269]

5.1.5. Dopamine-TiO_2 systems

Although there has been an advance in the dimensions of the TiO_2 systems considered and in the modeling of the charge transfer mechanism through quantum chemical calculations, we believe that a systematic description of the role of the coupling is still lacking. Moreover, the sensitization by surface adsorbates (or complexes) that do not absorb visible light by themselves and, in particular, the optical properties of the TiO_2 surface modified by the dopamine molecule, which is the object of this thesis, have not yet been theoretically investigated so far.

Catechol derivatives bind extremely strong to the TiO_2 surface and show a high stabilization through the bidentate binding.[107, 108] Between these catechol-like molecules, dopamine is one interesting case, because it has double functionality: two hydroxyl groups on one side and one ethyl-amino functionality ($CH_2CH_2NH_2$) on the other side, which could interact either with the surface of the semiconductor or with other molecules, such as with the solvent or with active molecules.[137,138,139,270]

The experimental UV-Vis absorption spectrum of dopamine bound to commercial spherical TiO_2 nanoparticles has been previously reported in literature.[153,154] Once the nanoparticle is modified by dopamine, a redshift of the light absorption with respect to the bare system is recorded, which can be attributed to the formation of a charge transfer complex. In a recent work, dopamine has been used as a representative *N*-containing catechol compound for the generation of visible-light-driven hybrid *N*-doped carbon/TiO_2 (C_N-TiO_2) photocatalysts.[35] The

charge transfer complex is prepared through the binding of dopamine to TiO_2 10 nm nanoparticles (NPs), which are later subjected to carbonization. From the analysis of the experimental UV-Vis spectra, the dopamine-NP system exhibits a redshift of 0.35 eV with respect to the bare TiO_2 and an additional 0.41 eV shift is recorded for the carbonized system, enabling this way the efficient visible-light driven photocatalytic degradation of the environmental pollutant rhodamine B.

Moreover, at low coverage, free dopamine is known to be an efficient antioxidant and it has been shown to protect neurocytes from oxidative stress by scavenging free radicals,[271] on the other hand, at higher dopamine concentrations, the generation of superoxide (O_2^-) and H_2O_2 can be increased. [272] Therefore, it is important to consider the effect of different coverage densities of dopamine.

In this work, we investigate the optical and electronic properties of a TiO_2 anatase (101) periodic surface modified with dopamine at different coverage densities by real-time Time-Dependent DFT and by DFT, respectively.

In the next sections, after discussing the methods and the convergence tests (**5.2**), we show the features of the spectrum of dopamine in vacuum (**5.3**), and then we move to the bulk and the bare TiO_2 surface (**5.4**). Later, we present the dopamine modified-TiO_2 (101) surface spectrum at low (**5.5**) and high coverage (**5.6**) in different geometries of adsorption, assessing the mechanism of the charge transfer through the analysis of the density of states.

5.2. Computational details

5.2.1. Ground state calculations

All DFT calculations were performed using the CRYSTAL14 package[203], where the Kohn-Sham orbitals are expanded in Gaussian-type orbitals, with the PBE exchange-correlation functional.[168] The all-electron basis sets are Ti 86-4111(d41), O 8-4111(d1) for the oxygen atoms of TiO_2; H 5-111(p1), C 6-31111 (d1), O 8-41111 (d1) and N 6-311(d1) have been employed for hydrogen, carbon, oxygen and nitrogen of the adsorbed molecules.The cut-off limits in the evaluation of Coulomb and exchange series/sums appearing in the SCF equation were set to 10^{-7} for Coulomb overlap tolerance, 10^{-7} for Coulomb penetration tolerance, 10^{-7} for exchange overlap tolerance, 10^{-7} for exchange pseudo-overlap in the direct space, and 10^{-14} for exchange pseudo-overlap.

The TiO_2 anatase bulk parameters optimized by CRYSTAL are a=b= 3.8030 Å anc c= 9.7672 Å.

We modeled the (101) anatase surface with a slab made of three tri-atomic layers of TiO_2. The bottom layer was kept fixed to the optimized bulk positions during the geometry optimizations by CRYSTAL/PBE (no periodic boundary conditions were imposed in the direction perpendicular to the surface). We used mainly the 1×4 supercell model (144 atoms), already described in **Chapter 3**. After cutting the slab along the (101) surface, we obtained the following optimized parameters: a=15.2119 Å, b= 6.6785 Å. The vacuum size along the z direction, necessary to avoid the spurious interaction with the slab replicas, was set to 500 Å.

All configurations were optimized using a k-point mesh of 2×2×1 to ensure the convergence of the electronic structure. The total density of states (DOS) and projected density of states (PDOS) were computed with a finer k-point mesh of 30×30×1.

The use of the 1×4 supercell allows us to differentiate between a low coverage regime (0.25 monolayer (ML)), in which two out of eight Ti_{5c} of the surface are saturated by the dopamine molecule, and a full coverage regime (1 ML), with four dopamine molecules binding eight different Ti sites. Moreover, we can take in account possible interactions between the molecules forming the ML.

The total adsorption energy per molecule has been defined as:

$$\Delta E_{ads}^{mol} = (E_{slab+nmol} - [E_{slab} + n_{mol}E_{mol}])/n_{mol} \quad (5.2)$$

where $E_{slab+nmol}$ is the total energy of the whole system, E_{slab} is the energy of the surface slab, E_{mol} is the energy of the molecule in the gas phase and n_{mol} is the number of molecules adsorbed on the surface.

As it is well accepted in literature,[53] TiO_2 is an indirect band-gap semiconductor, with the top of the valence band (VB) placed very close to the X point and the bottom of the conduction band (CB) lying at Γ. The indirect band gap (E_g^{ind}), calculated to be 2.16 eV according to the present PBE calculations, is underestimated with respect to the experimental value of 3.4 eV at the liquid helium temperature.[54] This underestimation of the gap by GGA functionals is a well known drawback of these methods that can be solved either improving the description of the exchange-correlation functional (v_{xc}), for example by employing hybrid functionals,[201] or by calculating the one-particle excitations from the self-energy operator with Green's function based methods (GW).

Nevertheless, the aim of this work is not the perfect reproduction of the gap, but the analysis of the differences between the spectrum of the isolated systems and the one of the TiO_2-dopamine complex, unraveling the nature of the charge transfer mechanism. Therefore, the PBE functional, which is much less computationally expensive, can be safely used for the comparative analysis.

5.2.2. Excited state calculations

When light interacts with a material, an applied time-dependent external perturbation polarizes the system such that the electrons screen the system from the applied perturbation. The response to the external perturbation can be calculated through *time-dependent* density-functional theory (TDDFT). All time-dependent calculations in this Chapter were carried out using the Octopus code,[157] which is a pseudopotential planewaves-based real-space package.

In the following section we provide a focus on the two response functions, i.e. the polarizability α and the imaginary part of the dielectric function ε''. Moreover, we describe the real-time propagation implemented in the Octopus code to describe the time evolution of the electronic systems and obtain the response functions. In particular, we specify the parameters set for the calculations in this Chapter. A more general overview and further details about the approximations of the TDDFT method were already given in **Chapter 2**, **Section 2.5**.

The program is based on TDDFT in the Kohn-Sham scheme. In the TDDFT framework, the evolution of the system is defined by a set of auxiliary non-interacting on particle Kohn-Sham

orbitals, which satisfy the time dependent Khon-Sham (TD-KS) equations. Therefore, N Kohn-Sham orbitals $\phi_1(\boldsymbol{r}_1 t_1)\phi_2(\boldsymbol{r}_2 t_2) \ldots \phi_2(\boldsymbol{r}_N t_N)$ are propagated in time.

The TD-KS potential v_s is a functional of the time-dependent density and it is defined as:

$$v_s(\boldsymbol{r}, t) = \int \frac{\rho(\boldsymbol{r}', t)}{|\boldsymbol{r} - \boldsymbol{r}'|} dr' + v_{xc}[\rho](\boldsymbol{r}, t) + v_{ne}(\boldsymbol{r}) + v_{ext}(\boldsymbol{r}, t) \quad (5.3)$$

where v_{xc} is the exchange correlation potential accounting for all many-body effects, for which we used the PBE functional.[168] $v_{ne}(r)$ represents the interaction between valence electrons and the ionic core, and is modeled by the sg15 set of optimized norm-conserving Vanderbilt PBE pseudopotentials.[159] $v_{ext}(r, t)$ is the external potential.

Through the application of an external potential in the adiabatic approximation, it is possible to obtain the linear optical response for the investigated system. For the time-dependent propagation of the KS equantions in the case of finite systems, we follow the scheme proposed by Yabana and Bertsch,[199] and excite all the frequencies by giving a small momentum (K) to the electrons. This external kick has to be small enough to keep the response linear, but should be sufficiently large to avoid numerical problems. For dopamine, we used a value of K 0.01 $Å^{-1}$ and repeated the propagation along the three indipendent polarization directions: x, y and z, after centering the geometry. This is achieved by transforming the ground-state wavefunctions according to:

$$\phi_i(\boldsymbol{r}, dt) = e^{iKz}\phi_i(\boldsymbol{r}, 0) \quad (5.4)$$

and then propagating these wavefunctions for some finite time. The spectrum is then obtained by the expression for the dipole strength function $S(\omega)$:

$$S(\omega) = \frac{2\omega}{\pi} Im[\alpha(\omega)] \quad (5.5)$$

where the dynamical polarizability, $\alpha(\omega)$, is essentially the Fourier transform of the dipole moment of the system $d(t)$:

$$\alpha(\omega) = -\frac{1}{K}\int d^3\boldsymbol{r}\chi d\varrho(\boldsymbol{r}', \omega) \quad (5.55)$$

The polarizability per unit volume in a solid is the constant of proportionality relating the local electric field $\boldsymbol{E}$ to the induced dipole moment $\boldsymbol{d}$:

$$\boldsymbol{d} = \varepsilon_0 \alpha \boldsymbol{E} \quad (5.7)$$

The total spectrum is calculated as an average of the the strength function $S(\omega)$ in the three directions.

For a cluster system, the dielectric function ε and the polarizability α are equivalent.

$$\varepsilon \propto \frac{\alpha}{V} \; for \; \varepsilon \; dimensionles \tag{5.8}$$

Since we are dealing with periodic systems, ε and α do not coincide. Through the Clausius-Mossotti relation, it is possible to express the dielectric constant of a material in terms of the atomic polarizability α of its molecular constituents:

$$\frac{\varepsilon_r - 1}{\varepsilon_r + 2} = \sum_i \frac{N_i \alpha_i}{3\varepsilon_0} \tag{5.9}$$

where $\varepsilon_r = \frac{\varepsilon}{\varepsilon_0}$ is the dielectric constant of the material, ε_0 is the vacuum permittivity, N is the number density of the molecules (number per cubic meter) and α_i is the molecular polarizability of the component i.

The dielectric function is a complex quantity:

$$\varepsilon_r = \varepsilon' + \varepsilon'' \tag{5.10}$$

and the imaginary dielectric function, ε'' is directly related to the experimental linear optical spectrum and ε is directly correlated to the induced dipole moment $\boldsymbol{d}$:

$$\boldsymbol{d} = \varepsilon_0 \chi \boldsymbol{E} \tag{5.11}$$

where the susceptibility χ is the linear response function of the system (which we called α for the finite system)

$$\chi = \varepsilon_r - 1 \tag{5.12}$$

Octopus follows a real-space, real-time method for the calculation of the dielectric function, implemented by Bertsch et al.[201]

For the calculation of the linear optical spectrum of periodic systems, which are three-dimensional, the external potential $v_{ext}(r, t)$ is modeled by a vector field, representing a spatially uniform (but time-dependent) external electrical potential. In te current implementation of Octopus, the Gauge Vector Field can be applied uniquely along the *x* direction.

In order to propagate the KS-TD equations, the Octopus code employs a propagator, which refers to the algorithm used to approximate the time evolution operator $U(t + dt, t)$. Both for the finite and periodic calculations, we employed the ETRS (Enforced Time Reversal Symmetry) propagator. For the calculations of the exponential of the Hamiltonian, we used the Lanczos method,[269] which allows us to avoid the calculation of the empty KS states, evaluating directly the polarizability of the system, through an explicit representation of the density matrices.[273]

We define two parameters for the time propagation, i.e. the time step and the length of the propagation. A smaller tie step and a longer propagation would result in an accurate optical spectrum.

Seeking for a compromise between computational cost and a high definition spectrum, we used a time step of 0.01 a.u. and we extended the TD propagations for ~5 fs (200 $\hbar\,/Hartree$).

All quantities are expanded in a regular mesh in real space, and the simulations are performed in real-time. Real-space implementations are not variational, so we may find a total energy lower than the real one, even if we refine the parameters, which determine the quality of the calculation, as the value of the grid-spacing. The optimization of this and other parameters is described in detail in **Section 5.2.1**.

5.2.3. Total energy convergence

Since the Octopus code exploits a real-space grid, once the shape of the box in which the simulation is executed is defined, there are only two parameters that need to be brought to convergence: the spacing between the points of the mesh and the box radius. The default option in Octopus is to use a Cartesian grid, which is a regular grid where the spacing along each Cartesian direction is the same.

The spacing controls the quality of the discretization: smaller spacing gives more precise results, but increased computational cost. The total energy at the different spacing values depends on the pseudopotentials used for the calculations, in the present case SGE set.[159]

The shape of the box defines the three-dimensional area in which the calculation is performed. For periodic solids like TiO_2, the spacing is the only parameter to converge, since the box shape and size are defined by the lattice vectors. The simulation box we employed in our two-dimension periodic slab calculations has the shape of a parallelepiped having the same lengths of the cell parameters of our systems, as obtained by the PBE/CRYSTAL optimization. In real-space calculations, it is possible to set a mixed periodicity for the system (see **Section 5.2.2.**). For a slab calculation, only the *x* and *y* direction are periodic. For the *z* non-periodic out-of-plane dimension, we set a vacuum value of 42.3342 Å (80 bohr).

We used a cut-off of for the Coulomb interactions equals to half of the *c* non-periodic direction ~21 Å.

For the isolated dopamine, we must define a shape of the box. We chose a spherical box and we completed the convergence study of the total energy by varying the radius of the sphere.

The convergence studies have been repeated for the ground state and for the time-dependent calculations. We report the convergence test on the spacing both for bulk TiO_2 (**Figure 5.2a**) and for the dopamine molecule in vacuum (**Figure 5.2b**) and on the radius of the sphere for the dopamine molecule in vacuum (**Figure 5.2c**).

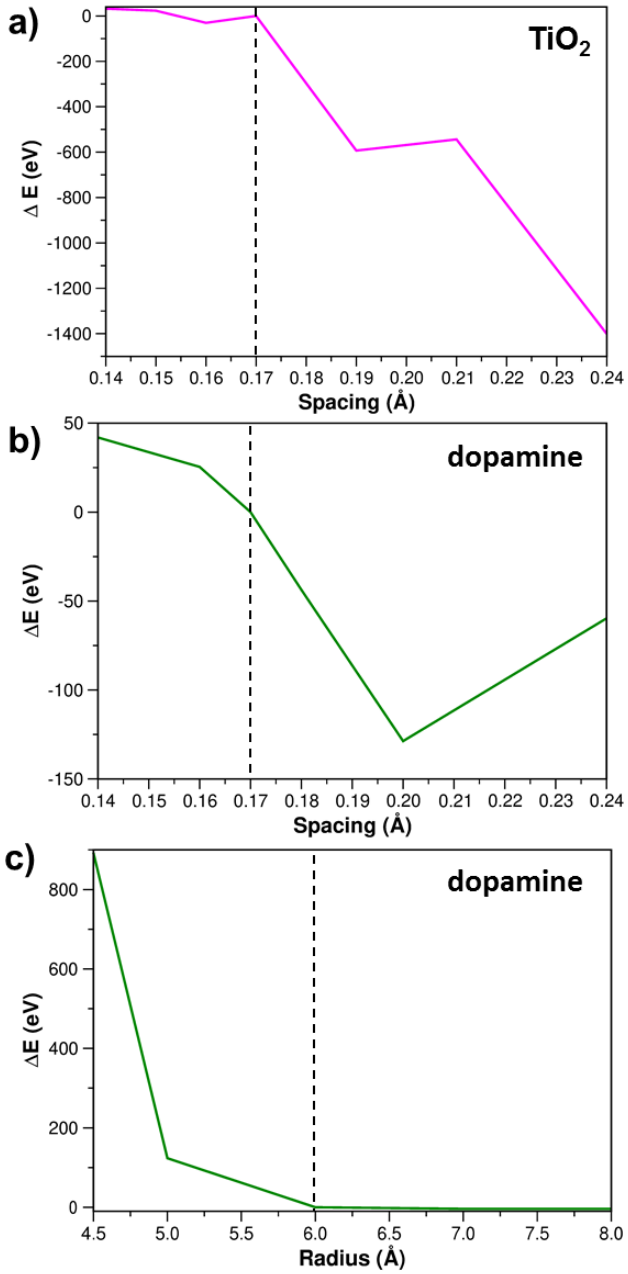

Figure 5.4 Convergence test for the total energy a) of bulk TiO_2 with respect to the spacing of the mesh in Å, b) of dopamine with respect to the spacing in Å, c) of dopamine with respect to the radius of the sphere in Å.

From the analysis of the graph (**Figure 5.4a**), we acknowledged that a spacing of 0.17 Å is enough to correctly compute the total energy of bulk TiO_2. For dopamine, the total energy converges at a spacing of 0.16 Å, but in the view of performing computationally expensive time-dependent propagations of periodic slab systems with dopamine adsorbed on TiO_2, we select a spacing of 0.17 Å, which is still acceptable for our comparative purposes (**Figure 5.4b**).

A radius of 6.0 Å for the sphere containing a dopamine molecule correctly describes the total energy of the molecule (**Figure 5.4c**).

5.3. Dopamine absorption spectrum

As a preliminary study, we calculated the PBE/Octopus optical spectrum of dopamine in vacuum (**Figure 5.5**) through a TD propagation and we compared it to experimental data.

When we calculate a linear optical absorption spectrum through TD propagation, the code performs the time-propagation of the electronic orbitals, following an external perturbation represented by a small momentum as described in **Section 5.5.2**. The linear response of a molecule to an electric field is the polarizabilty, the relative tendency of a charge distribution to be distorted from its normal shape, already defined in Equation (5.7).

The spectrum obtained for dopamine is reported in **Figure 5.5a**, together with the three components of the strength function along *x*, *y* and *z* (**Figure 5.5b**). The strength function is directly related to the polarizabilty as reported in equation (5.5).

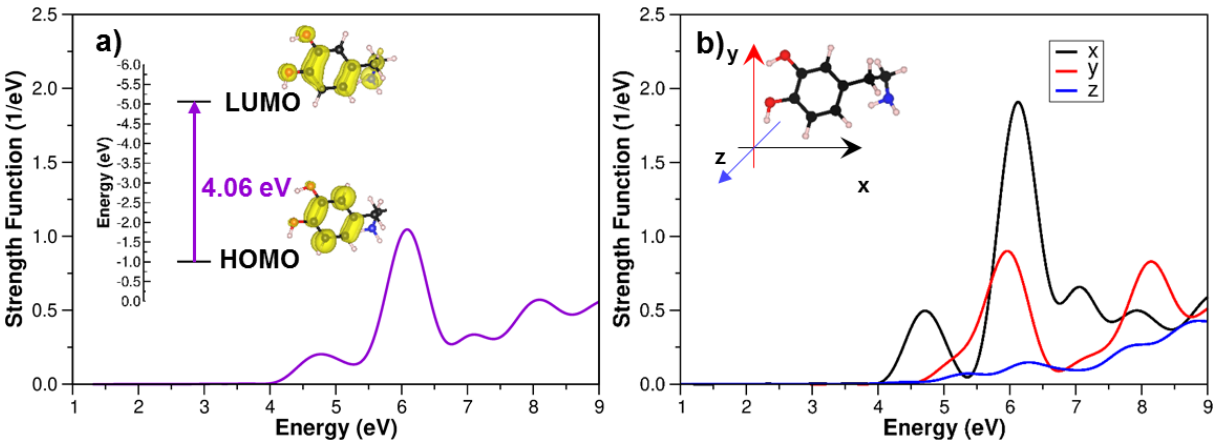

Figure 5.5 Absorption spectrum for the dopamine molecule in vacuum calculated with the PBE functional a) averaged strength function and comparison with the HOMO-LUMO energy difference in eV (inset with 3D density plots) and b) three separate directions of the strength function *x*,*y*, and *z*, according to the orientation of the centered molecule (inset).

There are two main peak of absorption for dopamine: the first one, less intense, is centered at 4.7 eV (263.8 nm), while the second at 6.1 eV eV (203.2 nm). In the experimental spectrum, the two peaks are respectively at 281 and 220 nm.[2] This means that, with the GGA/PBE functional, the calculated optical spectrum is in good agreement with the experimental one. The onset of the absorption is found at 4.02 eV, which is consistent with the optical HOMO-LUMO gap value of 4.06 eV calculated at the same level of theory (PBE) by means of the localized basis set code CRYSTAL14 for the HOMO-LUMO gap of dopamine (inset in **Figure 5.5a**).

5.4. Bulk TiO_2 anatase and (101) surface electronic spectrum

In the following section, we calculate optical and electronic properties of TiO_2 anatase bulk and of the (101) surface with the PBE functional, using two different codes: the Octopus code is employed for the calculation of time-dependent optical properties, and the localized basis set program CRYSTAL for the calculation of the electronic properties of the ground state.

Firstly, we test the quality of the dielectric function spectrum calculated by PBE/Octopus in comparison with data present in literature[3] and with the widely used and tested VASP code. [274,275,276,277] Later, we calculate the PBE/Octopus spectrum for the anatase (101) slab model and we compare it with the one obtained for the bulk.

Firstly, we test the quality of the dielectric function spectrum calculated by PBE/Octopus in comparison with data present in literature[3] and with the widely used and tested VASP code. [278,279,280,281] Later, we calculate the PBE/Octopus spectrum for the anatase (101) slab model and we compare it with the one obtained for the bulk.

The optical response function of a solid subjected to an external perturbation constituted by a vector field is represented by the imaginary part of the dielectric function ε'' (see **Section 5.2.2.**)

The band structure for bulk anatase calculated according to PBE/CRYSTAL is reported in **Figure 5.6**. The indirect band gap (E_g^{ind}) is calculated to be 2.16 eV, which is underestimated with respect to the experimental one, i.e. 3.2 eV, but it can be used for a comparative analysis, as discussed in **Section 5.2.1**. Consistently, according to PBE/Octopus, the indirect gap E_g^{ind} is 2.20 eV, while the direct band gap (E_g^{dir}), which will be used below for comparison with the absorption onset (A_{ons}) obtained by TDDFT/PBE, is 2.62 eV.

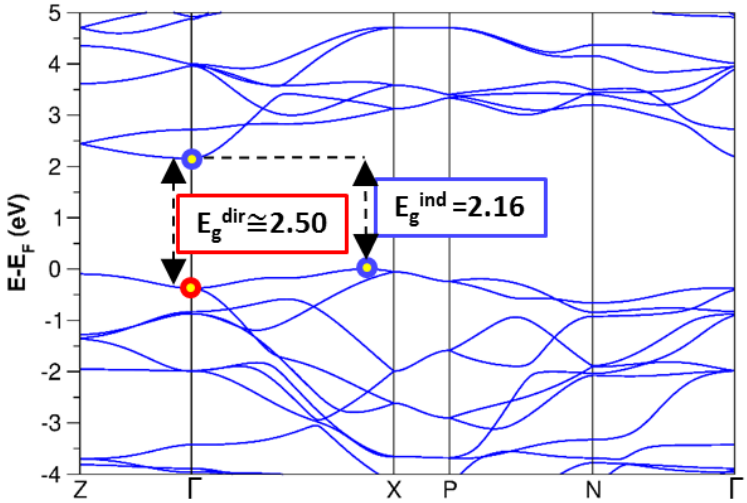

Figure 5.6 Electronic band structure of the bulk anatase TiO_2. The indirect (E_g^{ind}) and direct (E_g^{dir}) band gap in eV calculated according to PBE/CRYSTAL are reported.

In **Figure 5.7** we compare the dielectric function spectra obtained by PBE/Octopus for anatase along the a=b and the c crystallographic direction (**Figure 5.7a)** with those obtained by PBE/VASP (**Figure 5.7b)**.

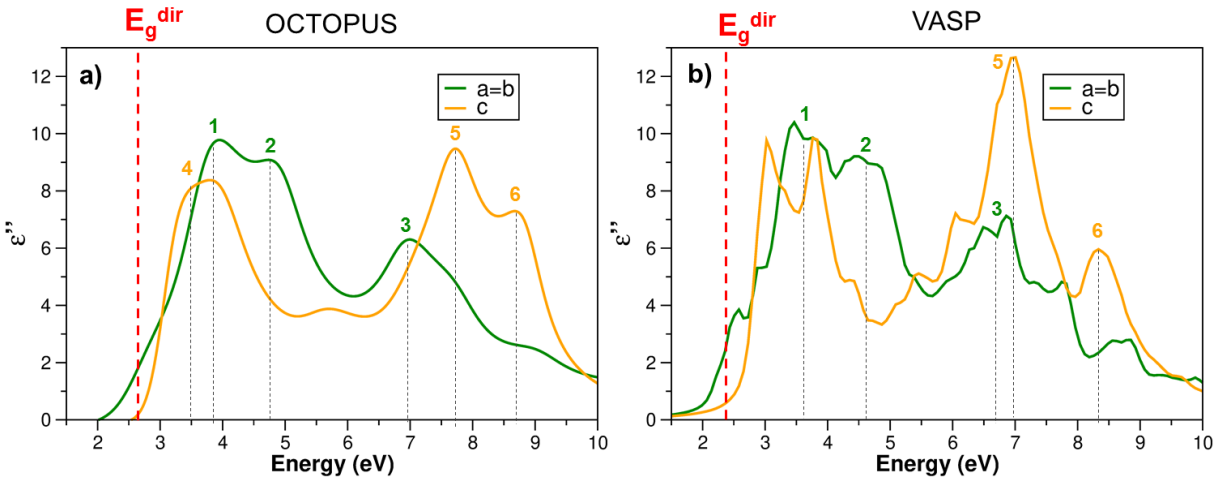

Figure 5.7 Imaginary part of the dielectric function of a single crystal of bulk anatase TiO_2 for light polarized along the a=b (green) and the c (yellow) crystallographic directions calculated with a) PBE/Octopus and b) PBE/VASP. The peaks are identified by numbers and color-coded according to the direction of the lattice. The Kohn-Sham the direct gap, E_g^{dir} =2.62 eV and E_g^{dir}=2.43 eV according to PBE/Octopus and PBE/VASP respectively, are indicated by a dashed red line.

The calculation performed with the VASP code applies the Fermi Golden Rule is applied and the probability of each transition is calculated according to:

$$P \sim \sum_{v,c} |\langle c|D|v\rangle|^2 \delta(\varepsilon_c - \varepsilon_v - \omega) \tag{5.56}$$

where v and c are the occupied and the unoccupied states, respectively.

The calculations through which we obtained the spectra in **Figure 5.7** are not done in the same approximation (Fermi Golden Rule and TDPBE) and this explains the slight differences in the intensity of the peaks.

The detailed positions of the peaks in **Figure 5.7** are reported in **Table 5.1** in comparison for the two codes.

	Peak energy (eV)	
Label	**OCTOPUS**	**VASP**
1	3.9	3.6
2	4.8	4.6

3	7.0	6.8
4	3.6	3.0 (**4**) / 3.8 (**4'**)
5	7.7	7.0
6	8.8	8.4

Table 5.1 Energy values (eV) calculated at the center of the absorption peaks of bulk anatase TiO_2 calculated according PBE/Octopus and PBE/VASP.

In the following, we will comment mainly the results obtained by PBE/Octopus. Along the *a=b* direction, we can observe that the semiconductor starts to absorb at around 2.0 eV, which is red-shifted by about 0.6 eV with respect to E_g^{dir} obtained by PBE/Octopus (2.62 eV). This shift could be due to an excessive broadening value used to obtain the simulated spectrum, which in Octopus is inversely proportional to the length of the time-dependent propagation (~5 fs, 200 h/Hartree). By increasing the propagation time, we should observe a value for the A_{ons} closer to E_g^{dir}. We are planning to work on this issue in the next future. Nevertheless, the spectrum by VASP (**Figure 5.7b**) has a very similar profile and the position of the peaks is in good agreement with that obtained by Octopus (**Table 5.1**).

We now compare our data with BSE-GW calculations and the experimental spectrum measured at 20 K, reported by Baldini et al. for a more narrow range along the *a=b* (**Figure 5.8a**) and the *c* directions (**Figure 5.8b**).3 According to GW results, the direct band gap is 3.92 eV, which is 1.30 eV larger than the one calculated by PBE/Octopus (2.62 eV), as one could expect. Therefore, the absorption onsets along *a=b* and *c* crystallographic directions in the simulated BSE-GW spectra are red-shifted with respect to the GW calculated direct band gap (E_g^{dir}), in analogy with what observed with TDDFT/PBE with respect to PBE/Octopus direct band gap, as just discussed above.

However, a clear difference between BSE-GW in **Figure 5.8** and TDDFT/PBE in **Figure 5.7** is the absence of the first excitonic peak that cannot be revealed by TDDFT/PBE periodic calculations due the approximated exchange-correlation kernel.

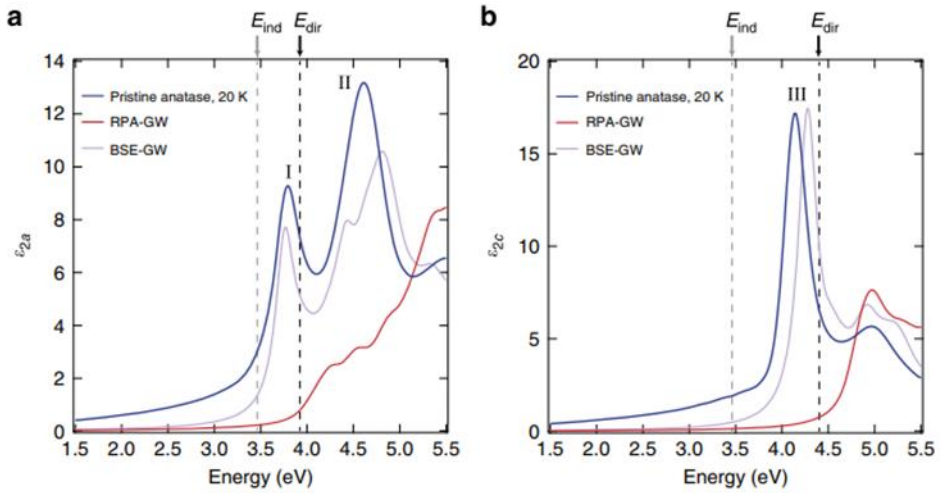

Figure 5.8 Imaginary part of the dielectric function of pristine anatase TiO_2 along the a) *a*=*b* and b) *c* crystallographic directions. Comparison between the spectra measured at 20 K on the pristine anatase TiO_2 single crystal and those obtained from frozen-lattice *ab initio* calculations for pristine anatase TiO_2. The experimental data are reported in blue, the calculated spectra in the RPA-GW approximation in red and the calculated spectra in the BSE-GW scheme in violet. The quasiparticle indirect gap E_{ind} = 3.46 eV is indicated by a dashed grey vertical line; the direct optical gaps E_{dir} = 3.92 eV (at the Γ point) for E ⊥ *c* and E_{dir} = 4.40 eV (coincident with the onset of the RPA-GW) for E ∥ c are indicated by dashed black vertical lines.[3]

In the following, we show a comparison between the imaginary part of the dielectric functions, ε'' (see **Section 5.2.2.**), of the three model candidates for TiO_2: a 6-layer 1×1 slab, a 3-layer 1×1 slab and a 3-layer 1×4 slab (**Figure 5.9**). In the Octopus code, the Gauge Vector Field acting as an external perturbation for the calculation of the dielectric function spectrum can be oriented along a unique direction, which in our case corresponds to the *a* one. The three spectra have the same profile and in all of them, we can identify two peaks, placed at around 4.3 eV and 7.0 eV, respectively. For the 1×4 case, the peaks are slightly blue-shifted and they are centered at 4.6 eV and 7.2 eV, respectively. The absorption starts at ∼2.0 eV for the 1×1 6-layer model and at ∼2.5 eV for both the 1×1 and 1×4 3-layer models as it is also confirmed by the calculated band gap value of the three models, which is 1.95 eV, 2.53 and 2.54 eV according to PBE/CRYSTAL, respectively.

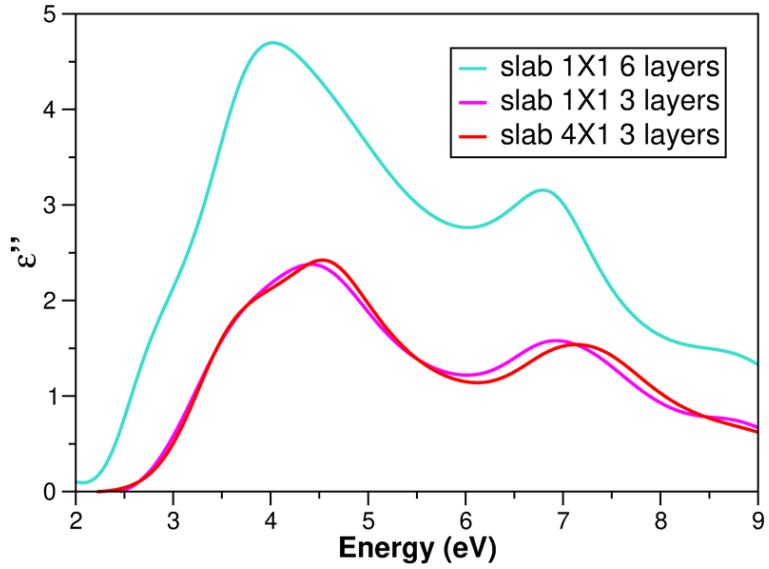

Figure 5.9 Imaginary part of the dielectric function ε'' for the TiO_2 anatase (101) surface along the *a* crystallographic direction calculated with OCTOPUS/PBE for the 6 layers slab 1×1 (turquoise), the 3 layers slab 1×1 (violet) and the 3 layers slab 1×4.

Since the results seem to be only slightly affected by the choice of the thickness of the slab, we decided to focus on the 3-layer model.

Even if the bare 3-layer surface spectra are very similar to each other, the smaller 1×1 cell, which is computationally less expensive, does not allow us to describe the low coverage regime. In the 1×1 cell there are only two Ti_{5c} atoms on the surface and we would obtain a full monolayer (1 ML) by adding only one bidentate dopamine molecule (see **Section 5.5** and **Section 5.6**). On the other side, by binding one dopamine molecule to the 1×4 cell, two out of eight Ti5c of the surface are covered (0.25 ML), correctly reproducing the low density regime. In addition, the 1×1 slab is not able to describe properly the geometry of the full monolayer, since only one bidentate dopamine molecule is present in the cell and, therefore, all the molecules are in the same exact position. As we have shown in **Chapter 3**, in some configurations for the full coverage the adsorbed molecules interact with each other and the configuration of each single dopamine is not exactly identical to the others (see **Figure 3.8d**). Therefore, for the dopamine-TiO_2 systems, we will show only the results for the 1×4 cell.

5.5. Low coverage of dopamine: optical and electronic properties

In order to simulate a low coverage (one molecule per supercell) density of dopamine molecules adsorbed on anatase (101) TiO_2 surface, we used the 1×4 supercell, which results in the formation of a 0.25 ML.

The possible configurations for dopamine adsorbed on anatase at low coverage are already shown and discussed in **Chapter 3** (**Section 3.3**). From the configurational analysis, we have learnt that dopamine binds to the anatase TiO_2 (101) surface preferentially in a bidentate fashion. The two most interesting bidentate binding modes are reported in **Figure 5.10**. In the B^OD_2 structure (**Figure 5.10a**) the dopamine molecule is standing up towards the vacuum, while in the $B^OD_2M^{NH2}$ configuration (**Figure 5.10b**), which is more stable than the former one by 0.48 eV, the molecule bends in order to allow the nitrogen atom of the ethyl-amino functionality to coordinate the Ti_{5c} underneath.

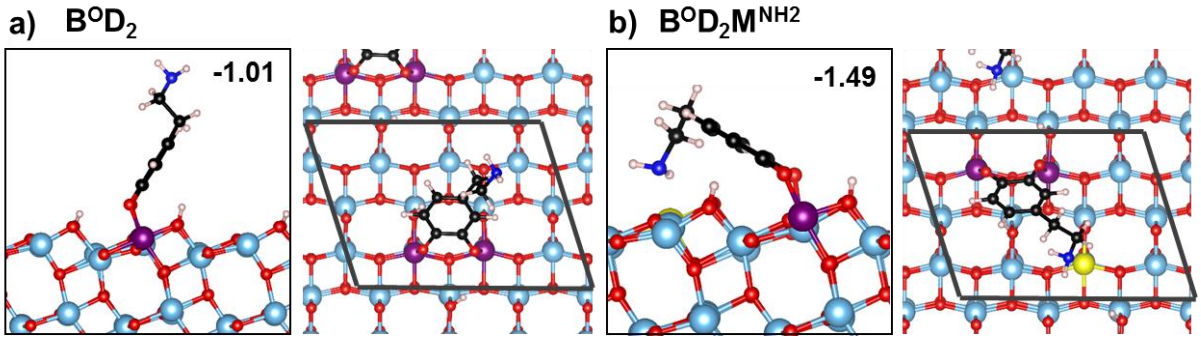

Figure 5.10 Adsorption modes (side and top views) and adsorption energies per molecule (ΔE_{ads}^{mol}, in eV) for one molecule of dopamine on the TiO_2 anatase (101)surface as obtained by CRYSTAL/PBE in the **a)** B^OD_2 and in the **b)** $B^OD_2M^{NH2}$ configurations. The Ti_{5c} atoms of the surface bound to the anchoring oxygen of the molecule are highlighted in violet, the Ti_{5c} coordinated to nitrogen is yellow.

We report the imaginary dielectric function spectra obtained using the Octopus code for low coverage adsorption of a single molecule of dopamine in the B^OD_2 and the $B^OD_2M^{NH2}$ configurations, in comparison with reference to the bare 1×4 anatase slab (**Figure 5.11)**.

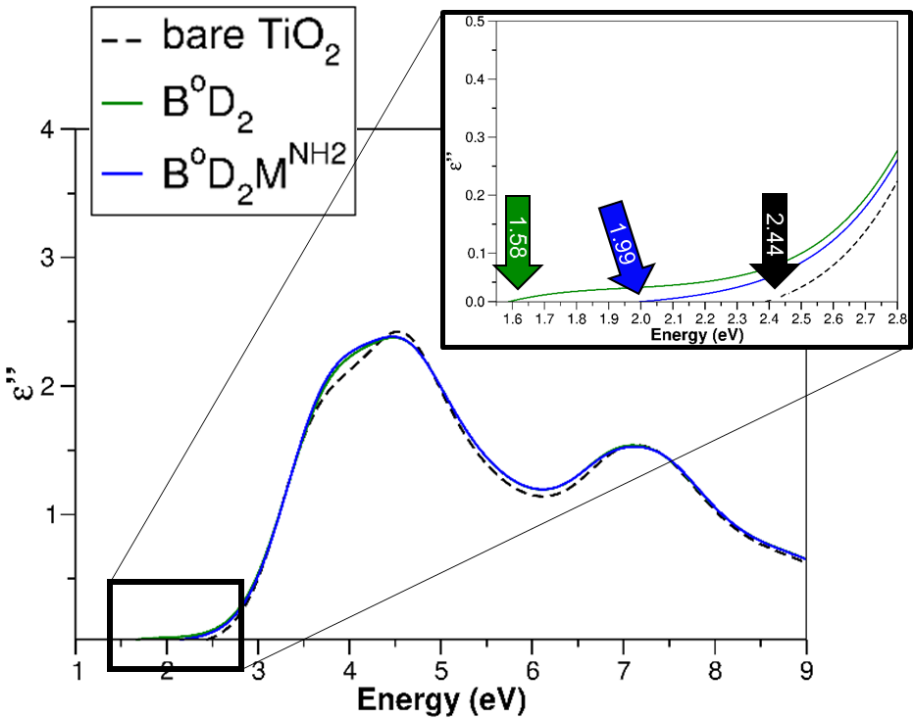

Figure 5.11 Imaginary part of the dielectric function (ε'') calculated along the *a* crystallographic direction for one dopamine adsorbed on TiO_2 in the B^oD_2 (green solid line) and in the $B^oD_2M^{NH2}$ configuration (blue solid line) with reference to the bare 1×4 TiO_2 anatase surface (black dashed line). In the inset, zoom of the absorption onset region.

At a first sight, it is clear that the profile of the spectra for the two different configurations of one single dopamine adsorbed on the TiO_2 surface are extremely similar to the one of the bare surface (black dashed line in **Figure 5.11**). In the case of a purely indirect injection mechanism for the charge transfer, we would not expect to observe any absorption at energy values lower than the HOMO-LUMO difference for the isolated molecule, which for dopamine is equal to 4.06 eV. Moreover, the shape of the spectrum for the adsorbed molecule should resemble that of the isolated one, since the first peak should correspond to the first allowed excitation, i.e. the HOMO-LUMO excitation for the molecule. In our case, the onset of the local bands was at 4.02 eV for the isolated dopamine molecule and at 2.44 eV for the TiO_2 surface. Therefore, the new absorption bands appearing at 1.58 and 1.99 eV for the B^OD_2 and the $B^OD_2M^{NH2}$ dopamine-TiO_2 complexes, respectively, are both red-shifted with respect to the ones of the isolated components. This means that they derive from a direct mechanism of injection, where the electron is excited in one-step from the molecular HOMO to the semiconductor empty states, i.e. they are LMCT excitations.

In order to better understand the observed absorption peaks, we also analyze the electronic structure for the B^OD_2 and the $B^OD_2M^{NH2}$ configurations (**Figure 5.12**), as calculated by the PBE/CRYSTAL. The values for the gap calculated between the last occupied state and the first empty one (HOMO-CB) in comparison with the absorption onset (A_{ons}) in eV are

reported in **Table 5.2**. We plotted the total (brown area) and projected density of states on TiO_2 (blue line), on the dopamine molecule (green area) and on the Ti_{5c} atoms of the surface directly involved in the formation of the bonds with the anchoring oxygen atoms (violet area) or with the nitrogen atom of the molecule (yellow area). In the case of the bare TiO_2 surface, the HOMO-CB gap corresponds to the band gap (E_g), calculated between the valence band maximum (VBM) and the conduction band minimum (CBM). Differently, when the dopamine molecule is adsorbed on TiO_2, the HOMO is constituted by a mid-gap molecular state related to the carbon atoms of the π system, while the first empty state of the system is the CBM, as already discussed in **Chapter 3**.

Table 5.2 Band gap calculated between the molecular HOMO and the bottom of the CB (E_g), absorption onset (A_{ons}) and energy difference between the empty states of Ti bound to dopamine (Ti_{bound}) and the HOMO localized on the molecule (ΔTi_{bound}-HOMO) for the bare TiO_2 surface and for the the B^OD_2 and the $B^OD_2M^{NH2}$ configuration.

	HOMO-CB (eV)	A_{ons} **(eV)**	**ΔTi_{bound}-HOMO (eV)**
Bare TiO_2	2.54	2.44	-
B^OD_2	1.14	1.58	1.56
$B^OD_2M^{NH2}$	1.27	1.99	1.89

Since we are suggesting that the charge transfer between the two components of the system takes place mainly through a direct mechanism from the HOMO of the molecule to the CBM, we would expect to observe a correspondence between the HOMO-CB gap calculated by DFT and the absorption onset (A_{ons}) derived by TDDFT calculations. Surprisingly, we notice that there is a discrepancy between the A_{ons} and the HOMO-CB, both for the B^OD_2 and the $B^OD_2M^{NH2}$ configurations. In fact, the system starts to absorb at energy values larger than the HOMO-CB gap, with an energy difference of 0.44 eV and 0.72 eV, respectively for the two configurations, while such difference was only 0.10 eV for the bare TiO_2 surface.

For the correct attribution of the transitions involved in the formation of the charge transfer band from dopamine to TiO_2, an advanced analysis of the optical transitions, such as a Casida-like decomposition or a transition charge analysis would be necessary. This kind of analysis requires extensive computational resources and it is a work in progress.

With a crude justification, based on one-electron orbitals, it is possible to rationalize the mismatching between the A_{ons} and the HOMO-CB values. By analyzing the PDOS, we observe that some of the states in the CB are mixed with the molecular ones, in particular the states projected on the titanium atoms directly involved in the formation of the bonds with dopamine.

We expect these states to have a major role in the transition, due to their mixing with the molecular states, which is directly proportional to the dipole transition moment according to **Equation 5.1**. When there is a covalent bond between the atoms at the surface of the semiconductor and the dopamine molecule, there is an efficient coupling between the states of the two components of the complex and the transition is allowed. The states related to those specific Ti atoms are not located exactly at the bottom of the CB but at higher energy values inside the CB, namely 0.43 and 0.62 eV higher for $B^{O}D_2$ and $B^{O}D_2M^{NH2}$, respectively.

The difference between the energy levels of the Ti atoms bound to the anchoring O atoms of dopamine inside the CB and the HOMO localized on the molecule (ΔTi_{bound}-HOMO) for the $B^{O}D_2$ and the $B^{O}D_2M^{NH2}$ configurations are reported in **Table 5.2**. These energy differences (1.56 eV and 1.89 eV for $B^{O}D_2$ and $B^{O}D_2M^{NH2}$, respectively) are in line with the shift between the A_{ons} values for the two systems (1.58 eV and 1.99 eV).

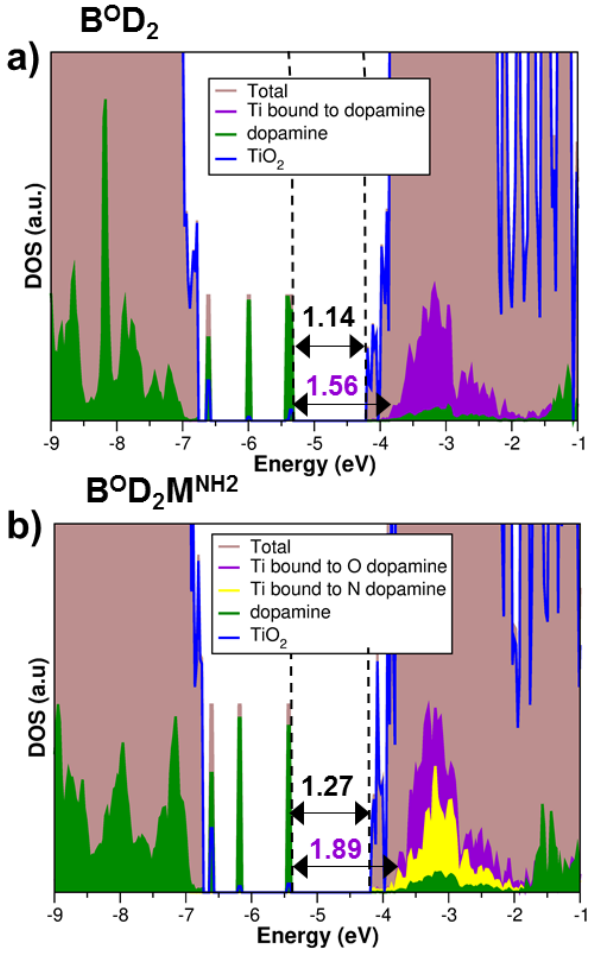

Figure 5.12 Total (DOS) and projected (PDOS) density of states for a single molecule of dopamine adsorbed on the anatase (101) TiO_2 surface in a **a)** $B^{O}D_2$ and **b)** $B^{O}D_2M^{NH2}$ configuration. The zero energy reference is set at the vacuum level. The HOMO-CB gap in eV is reported in black, while the energy difference between the states of Ti directly connected to O of the molecule and the HOMO (ΔTi_{bound}-HOMO) is violet.

This further validates our hypothesis according to which a ligand-to-metal charge transfer is taking place through a direct mechanism at the interface between dopamine and TiO_2, as we initially deduced by the analysis of the optical spectra. This CT would mainly involve the HOMO of the molecule and the Ti atoms which are directly bound to the dopamine molecule and not all the Ti of the surface. Nevertheless, we cannot exclude that an intramolecular HOMO-LUMO transition, as described by an indirect charge transfer mechanism, is taking place at higher energy values. However, this HOMO-LUMO transition is not responsible of the red-shift observed in the spectrum, moving the absorption towards the visible range. This last feature is instead due to a direct CT between dopamine and TiO_2. Tae et al. reported the UV-Vis spectrum of dopamine adsorbed on TiO_2 nanocrystalline nanoparticles (~20 nm of diameter) confirming our observations: the local bands for the two isolated components of the system, i.e. dopamine and TiO_2, do not overlap with the new CT absorption bands of the dopamine-TiO_2 complex in the visible region.[282]

5.6. Full coverage of dopamine: optical and electronic properties

By binding four bidentate dopamine molecules to the eight undercoordinated Ti of the 1×4 model, one monolayer (1 ML) of adsorbed molecules is formed. In **Chapter 3**, we studied the formation of a full ML of dopamine molecules and we found out that, under kinetic growth conditions, two configurations are present on the surface (**Figure 5.13**) with a proportion of ~50:50: the up_NH_2 (**Figure 5.13a**), in which the ethyl-amino functional groups of the dopamine molecules stand up towards the vacuum, and the down_NH_3^+ (**Figure 5.13b**), in which the functionalities rotate and acquire one proton from the O_{2c}-H from the slab. The down_NH_3^+ configuration is the thermodynamic minimum and it is favored by 0.59 eV over the up_NH_2 structure calculated with the CRYSTAL code.

In the up_NH_2 configuration, not all the ethyl-amino functionalities are standing parallel to each other, but two of them rotate during the optimization (**Figure 5.13a**). This feature can be reproduced only with a big enough model, such as the 1×4 slab employed for these calculations.

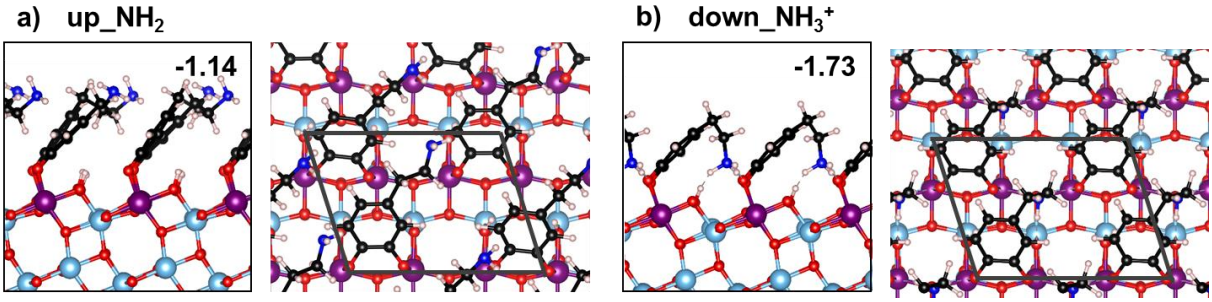

Figure 5.13 Adsorption modes (side and top views) and adsorption energies per molecule (ΔE_{ads}^{mol}, in eV) for 1 ML of dopamine molecules on the anatase (101) TiO_2 surface as obtained by CRYSTAL/PBE in the **a)** up_NH_2 and in the **b)** down_NH_3^+ configuration. The Ti_{5c} atoms of the surface bound to the anchoring oxygen of the molecule are highlighted in violet.

We calculated the imaginary part of the dielectric function ε'' with the Octopus code both for the up_NH_2 and the up_NH_3^+ configurations at full coverage, and we compared them to the bare 1×4 anatase slab system (**Figure 5.14)**.

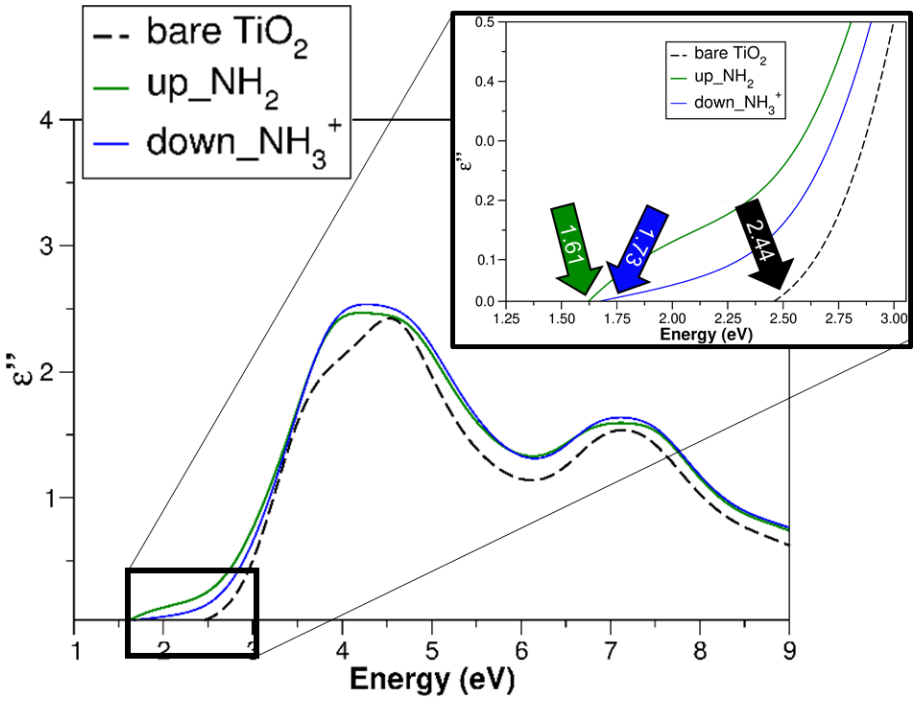

Figure 5.14 Imaginary dielectric function (ε'') calculated along the *a* crystallographic for 1 ML of dopamine molecules adsorbed on TiO_2 in the up_NH_2 (green solid line) and in the down_NH_3^+ (blue solid line) configurations with reference to the bare 1×4 TiO_2 anatase surface (black dashed line). In the inset, zoom of the absorption onset region.

Also in this case, the profile of the spectra for the two different configurations of 1ML of dopamine molecules adsorbed on the TiO_2 surface are extremely similar to the one of the bare semiconductor. The absorption onset (A_{ons}) is 1.61 eV and 1.73 eV for the up_NH_2 and the down_NH_3^+ configuration, respectively (**Figure 5.14** and **Table 5.3**). Once again, a transition analysis would be necessary for the correct attribution of the transition giving birth to the red-shift, observed as a consequence of the binding of dopamine to the semiconductor. The up_NH_2 configuration presents a major red-shift with respect to down_NH_3^+. In order to rationalize this, we suppose that the Ti states inside the CB of TiO_2, involved in the formation of the bonds with the anchoring oxygens of the dopamine molecules, are the first final states accessible in the CT transition. In fact, similarly to the low coverage case, the values for the E_g do not match the A_{ons} of the dopamine-TiO_2 system. This means that the transition from the HOMO to the first Ti states at the bottom of the CB is not allowed, since the coupling between the molecule and the semiconductor is essential in order to observe a transition.

Table 5.3 Band gap calculated between the molecular HOMO and the bottom of the CB (E_g), absorption onset (A_{ons}) and energy difference between the empty states of Ti bound to dopamine (Ti_{bound}) and the HOMO localized on the molecule (ΔTi_{bound}-HOMO) for the bare TiO_2 surface and for the up_NH_2 and the down_NH_3^+ configuration.

	HOMO-CB (eV)	A_{ons} (eV)	ΔTi_{bound}-HOMO (eV)
Bare TiO_2	2.54	2.44	-
up_NH_2	1.29	1.61	1.67
down_NH_3^+	1.60	1.73	1.85

Looking at the electronic structures for the two systems (**Figure 5.15**), we find that the empty bands in the CB related to the Ti atoms of the surface anchored by the O atoms of the molecule (violet area), are localized 0.38 and 0.25 eV higher inside the CB for up_NH_2 and down_NH_3^+, respectively. The energy difference between the bands of Ti bound to the O anchoring atoms of dopamine and the HOMO localized on the molecule (ΔTi_{bound}-HOMO) reflects the A_{ons} trend calculated by the Octopus code more accurately (**Table 5.2**).

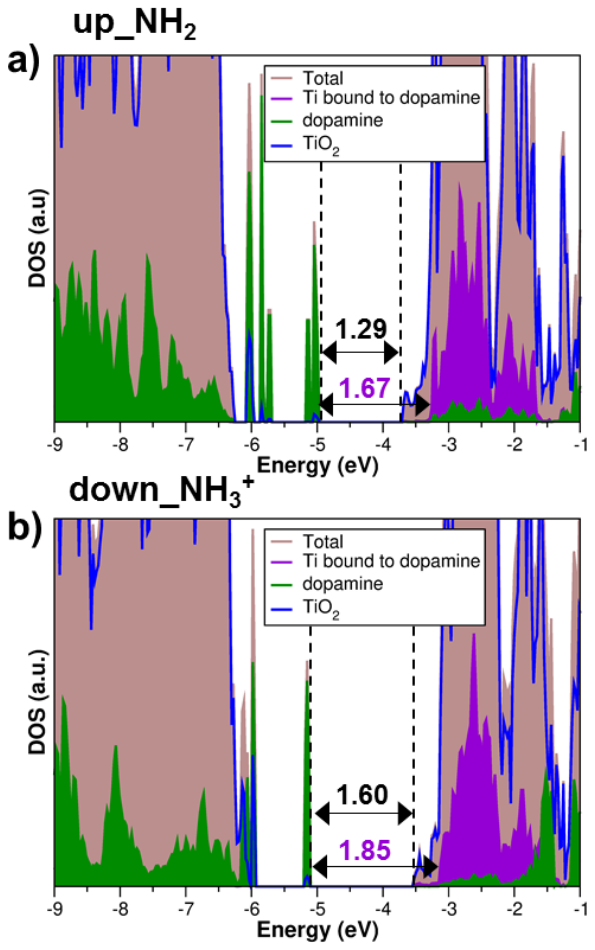

Figure 5.15 Total (DOS) and projected (PDOS) density of states for low coverage adsorption of 1 ML of dopamine on the anatase (101) TiO_2 surface in a **a)** up_NH_2 and **b)** down_NH_3^+ configuration. The zero energy reference is

set at the vacuum level. The HOMO-CB gap in eV is reported in black, while the energy difference between the states of Ti directly connected to O of the molecule and the HOMO (ΔTi_{bound}-HOMO) is violet.

In the case of the full coverage, the difference between the A_{ons} calculated for the up_NH_2 and down_NH_3^+ geometries, is very low (0.12 eV), because the binding takes place through the dissociation of the two –OH groups for both configurations, which are differentiated by the position of the ethyl-amino group, which is creating a net of hydrogen bonds stabilizing the monolayer in down_NH_3^+. In the low coverage regime, instead, the difference between the A_{ons} of B^OD_2 and $B^OD_2M^{NH2}$ is higher (0.41 eV), because there is more difference between the two binding modes with respect to the full coverage. In the $B^OD_2M^{NH2}$ configuration, the additional N-Ti bond moves the HOMO of the system at lower energy values and, consequently, the gap is enlarged with respect to B^OD_2.

Through a comparison with the results reported in **Section 5.3**, we see that the HOMO-CB values at high coverage of dopamine are slightly higher than the ones calculated at low coverage. This is probably due to the major mixing of the adsorbed dopamine molecules with the surface and to the low energy position of the HOMO. The A_{ons} values, instead, are not much affected by the major gap between the HOMO and the CB. At the full coverage, the Ti states bound to the molecules, which are involved in the charge transfer process, are located closer to the bottom of the CB (up_NH_2 and down_NH_3^+ are 0.38 eV and 0.25 eV higher in energy, respectively), than what they are at the low coverage (0.43 and 0.62 eV for B^OD_2 and $B^OD_2M^{NH2}$). Therefore, for the A_{ons} there is no much difference between a single dopamine molecule and a full monolayer of molecules adsorbed on the TiO_2 surface, suggesting that a transition analysis would be necessary to furnish a complete rationalization of the observed absorption red-shifts.

5.7. Conclusions

In this Chapter, we calculated through time dependent DFT, the absorption spectra for dopamine in vacuum, for the bare TiO_2 anatase (101) surface and for dopamine adsorbed on TiO_2 at low and high coverage densities. We performed all the TD calculations with the Octopus package, which directly calculates the polarizability or the dielectric function of the system, with no need to include empty states in the calculation. This allowed us to perform periodic slab calculations in real-time on systems reaching dimensions up to 232 atoms and to consider a very wide energy range, since all the frequencies are excited according to the Yabana and Bertsch scheme[199] adopted by Octopus code, at a reasonable computational cost.

For the dopamine molecule in vacuum, we found two main peaks in the absorption spectrum at 4.7 eV (263.8 nm) and 6.1 eV (203.2 nm), which are comparable with the experimental data. The absorption onset is calculated to be equal at 4.02 eV, and it coincides nearly perfectly with the HOMO-LUMO gap of the molecule (4.06 eV as calculated by the PBE functional), responsible for the first transition.

The imaginary dielectric function for TiO_2 bulk has been compared in detail to the experimental spectra and to the ones calculated by GW.

From **Chapter 3**, we already know that dopamine anchors the (101) surface of TiO_2 anatase through the dissociation of the two OH groups on two Ti_{5c} undercoordinated sites, followed by the transfer of the proton to the O_{2c} of the surface.

At low coverage, we considered two different bidentate configurations at low coverage: the $B^{O}D_2$, in which the ethyl-amino moiety of the molecule stands up towards the vacuum, and the $B^{O}D_2M^{NH2}$, which is more stable due to the formation of an additional bond between the nitrogen of the molecule and the underneath Ti_{5c}. For both of them, the calculated absorption spectrum is red-shifted with respect to the one of bare and the shape of the spectrum is very similar to the one of the unmodified surface. Through a detailed analysis of the electronic structure of the two systems, we located the excitation, which may be responsible for the onset of the absorption, involving the molecular HOMO and the Ti states directly connected to dopamine, placed inside the conduction band. The red-shift effect due to the surface modification with $B^{O}D_2M^{NH2}$ is slightly lower. One of the possible reasons for this is that in the mid-gap there are not states related to the nitrogen atom, since for this configuration these states are hybridized with the valence band thanks to the additional N-Ti bond. Therefore, the HOMO is placed at lower energy values with respect to $B^{O}D_2$ and, consequently, the calculated value of the A_{ons} is higher.

At full coverage, we examined the optical response and the electronic properties of the up_NH_2 configuration, in which all the molecules have their functionalities pointing up towards the vacuum, and the down_NH_3^+, where the functional groups rotate and bend toward the next line of adsorbed molecules in order to create additional stabilizing hydrogen bonds, with four protons of the surface transferring to the NH_2 moieties. The red-shift of the absorption with respect to the bare surface is encountered also for the full coverage, but it is not enhanced by the increased amount of adsorbed molecules, nor is the gap observed in the density of states narrowed. On the contrary, the E_g is slightly enlarged because the mid-gap molecular states are more stable than at low coverage thanks to the hybridization with the surface. The A_{ons} is not really affected by this hybridization of the molecular states, maybe because, together with the molecular HOMO, even the Ti states to which we presume the electron to be excited are stabilized and, consequently, they are found at lower energy values in the CB with respect to the low coverage case.

To conclude, it is important to highlight the fact that this is the first time that a TDDFT analysis of a periodic surface modified by molecules is carried out with the real-time, real-space method employed by the Octopus code. By studying the dopamine-TiO_2 system, we delineate a method to rationalize the charge transfer, employing the comparative analysis of the absorption spectra and the projected density of states. For the TiO_2 anatase (101) surface modified by dopamine, we observed a red-shift of the absorption edge with respect to the bare semiconductor. The excitations, responsible for the absorption onset shift, are located at lower energy values with respect to the ones of the isolated dopamine molecule and the isolated TiO_2 surface. Therefore, we supposed that these low energy excitations in the spectrum of the dopamine-TiO_2 complexes are due mainly to a transition going from the HOMO located on the molecule, to the empty states in the CB, which are related to the Ti atoms of the surface connected to dopamine and mixed with the states of the molecule.

This suggests the presence of a one-step direct mechanism for the charge transfer. Therefore, we expect the direct charge injection to happen in a very short time-scale for this system, through an ultra-fast direct mechanism. This observation does not exclude that an intramolecular transition could also take place at higher energy values, close to the HOMO-LUMO gap of the isolated dopamine molecule (~4.06 eV). Our results clarify the LMCT mechanism not only for the dopamine-TiO_2 complex, but they also shed light on the functioning of the direct charge transfer mechanism in general, proposing a way to qualitatively identify the states involved in the coupling and, therefore, in the observed electronic transition.

6 Summary and Conclusions

In order to use titanium dioxide for photon energy conversion applications, the wide band gap of this material has to be modified, shifting light absorption from the ultraviolet towards higher wavelengths. In particular, for light-involving therapies in nanomedicine, the absorption edge of TiO_2 should be shifted to the near infrared region of the spectrum, matching the optical window of the body tissues (600-1000 nm).

Among the possible approaches to modify the range of absorption of TiO_2, functionalization with organic molecules, such as dopamine, presents the additional advantage of introducing functionalities on the surface, which are available for further reactivity with chemical species present in the environment. Dopamine, a bifunctional organic molecule with two hydroxyl functionalities on one side of the benzene ring and one ethyl-amino group on the opposite side, could work as a linker between TiO_2 nanoparticles and bioactive molecules, for example DNA fragments or drugs, contributing to the building of bioinorganic hybrid nanoconjugates, which find application in nanomedicine.

In this work, we studied ground and excited state properties of TiO_2 flat and curved surfaces functionalized with dopamine. The dopamine-TiO_2 system has been investigated in its diverse aspects with different methods: the structural and electronic properties were assessed by hybrid density functional theory (DFT) and approximate-DFT, namely density functional tight binding (DFTB), temperature effects were studied with DFTB molecular dynamics (DFTB-MD), while time-dependent DFT (TDDFT) was used to calculate the optical properties. The combined employment of these different methods allows to reach the boundaries of the state-of-the-art of calculations on TiO_2, in particular with regard to the spherical nanoparticle model of realistic size (2.2 nm, ~1700 atoms).

The first part of this work of thesis, based on a wide set of hybrid density functional theory calculations including dispersion forces, provides a clear scenario of the adsorption modes, patterns of growth and configurations of dopamine on the anatase (101) TiO_2 surface,

with reference to the archetype of 1,2-dihydroxybenzene ligands, i.e. catechol. We concluded that at low coverage, the isolated dopamine molecule prefers to bend towards the surface, coordinating the -NH_2 group to a Ti_{5c} ion. At high coverage, the packed molecules succeed in bending towards the surface only in some monolayer configurations, as we demonstrated by MD-DFTB simulations. When they bend, a proton is transferred from the surface OH to the ethyl-amino group forming terminal NH_3^+ species, which highly interact with the O atoms of a neighboring adsorbed dopamine molecule. This strong coulombic interaction largely stabilizes the self-assembled layer. On the basis of these results, we predict that if the dopamine molecules free bending towards the surface is facilitated through thermodynamic versus kinetic growth conditions to a full monolayer of protonated dopamine molecules.

In the second part of this thesis, we moved to the study of the structural, electronic, and self-assembling properties of dopamine adsorption on curved TiO_2 nanoparticles of realistic size (2.2 nm). The DFT- and DFTB-based investigation spanned from single molecule adsorption to a full coverage regime. For the low coverage, we have determined the favorable molecular adsorption modes and analyzed the electronic charge-transfer effects, identifying the new molecular states in the band gap introduced by the adsorbed linker species. On top of that, we investigated the interaction of the charge transfer complex with light, learning that the photoexcited hole is trapped in the π-states of the aromatic ring, whereas the photoexcited electron can hop on different Ti sites, leading to an effective charge transfer separation. The hole trapping has a beneficial effect of lowering the oxidative power of TiO_2 NPs under light irradiation. As a further step, we considered a growing molecular layer on the NP and analyzed the self-assembling mechanism and the effects on the electronic properties of the complex. In the high-coverage model that we have built, all the molecules are positioned in an upward configuration. The number of molecular states in the gap increases progressively, until they form a continuous band from the top of the valence band of the TiO_2 nanoparticle to about 0.4 eV from the bottom of its conduction band. For the maximum coverage model, we performed molecular dynamics runs at 300 K, to better account for the competition between molecule/surface and molecule/molecule interactions. Considering that on the flat anatase (101) surface 50% of dopamine molecules were found to bend toward the surface and undergo proton transfer, on curved nanoparticles only a small fraction of them succeeds in bending toward the surface, because of the lack of space and steric hindrance.

Since nearly all the functionalities are not involved in any bond with the surface, they are available for further interactions with molecules from the external environment, e.g. with the solvent or with a bioactive molecule. This highlights how curved nanoparticle surfaces are

better substrates for bioconjugation through the bifunctional linker approach with respect to the flat ones. Therefore, the modeling of a spherical surface can provide precious insights about the possibility of using functionalized TiO_2-based systems to build efficient hybrid bioconjugates.

In the third part of this work, we studied through real-time TDDFT the optical properties of dopamine adsorbed on the flat anatase (101) TiO_2 surface in different configurations at the low and full coverage regimes. By studying the dopamine-TiO_2 system, we rationalized the charge transfer, employing the comparative analysis of the absorption spectra and the projected density of states. We found that the absorption spectrum of the dopamine-TiO_2 complexes is red-shifted compared to the bare surface, as expected by the analysis of the electronic structure, exhibiting mid-gap molecular states. For the TiO_2 anatase (101) surface modified by dopamine, we demonstrated that the charge transfer takes place in one step. The excitation goes from the HOMO located on the molecule, to the empty states in the conduction band, which are mixed with the d states of the Ti atoms of the surface bound to dopamine. Therefore, we expect the charge injection to happen in a very short time-scale, through an ultra-fast direct mechanism. This analysis revealed a LMCT mechanism for the dopamine-TiO_2 specific case. More generally, we can conclude that by individuating the specific states involved in the excitation process inside the electronic structure of a system, it is possible to get insights about the direct or indirect nature of the mechanism of CT.

In conclusion, throughout this work of thesis we provided an atomistic understanding of the phenomena involving the dopamine-TiO_2 interface. This work furnished deep insights about the mechanism of self-assembling of a full monolayer of dopamine molecules on TiO_2. Moreover, by the comparison between the results obtained for flat and curved TiO_2 surfaces, we found out that the use of spherical model is paramount for the correct quantum mechanical modeling of TiO_2-based nanohybrid systems. In fact, from the molecular dynamics DFTB analysis, most of the functionalities of the dopamine molecules result still available for further reactivity with bioactive molecules. Finally, TDDFT calculations revealed a red-shift in the optical spectrum when dopamine is adsorbed on the TiO_2 surface, which moves light absorption of the system closer to the therapeutic window of body tissues. Overall, dopamine constitutes an appropriate linker for bioconjugation, acting on one side as an efficient hook for bioactive molecules and improving, on the other side, the performance of TiO_2 nanoparticles in photoinduced therapy applications.

REFERENCES

[1] Rajh, T.; Dimitrijevic, N. M.; Bissonnette, M.; Koritarov, T.; Konda, V. Titanium Dioxide in the Service of the Biomedical Revolution. *Chem. Rev.* **2014**, *114* (19), 10177–10216.

[2] Barreto, W. J.; Ponzoni, S.; Sassi, P. A Raman and UV-Vis Study of Catecholamines Oxidixed with Mn(III). *Spectrochimica Acta Part A* **1999**, *55*, 65–72.

[3] Baldini, E.; Chiodo, L.; Dominguez, A.; Palummo, M.; Moser, S.; Yazdi-Rizi, M.; Auböck, G.; Mallett, B.P.P.; Berger, H.; Magrez, A.; Bernhard, C.; Grioni, M.; Rubio, A., Chergui, M. Strongly Bound Excitons in Anatase TiO_2 Single Crystals and Nanoparticles. *Nature Communications* **2017**, *8*, 1–10.

[4] Beatriz, M.; Lopes, S. The 2017 World Health Organization classification of tumors of the pituitary gland: a summary. *Acta Neuropathol*. **2017**, *134*, 521–535.

[5] Nguyen, J. Targeted Nanoparticles for Cancer Therapy: Promises and Challenges. *Nanomedic Nanotechnol* **2011**, *2*, 1–2.

[6] Frangioni, J.V. New Technologies for Human Cancer Imaging. *J. Clin. Oncol.* **2008**, *26*, 4012–4021.

[7] Fornaguera, C.; Solans, C. Methods for the In Vitro Characterization of Nanomedicines—Biological Component Interaction. *J. Pers. Med.* **2017**, *7*, 1–16.

[8] Feynman, R. P. There's Plenty of Room at the Bottom. *Eng Sci* **1960**, *23*, 22–36.

[9] McNaught, A. D.; Wilkinson, A.; Andrew, R. (1997). *Compendium of Chemical Terminology (IUPAC Chemical Data*. 2nd Edition. Blackwell Science.

[10] Lombardo, D.; Kiselev, M. A.; Caccamo, M. T. Smart Nanoparticles for Drug Delivery Application: Development of Versatile Nanocarrier Platforms in Biotechnology and Nanomedicine. *Journ. Nanomat.* **2019**, 1-26.

[11] Subbiah, R.; Veerapandian, M.; Yun. K. S. Nanoparticles: Functionalization and Multifunctional Applications in Biomedical Sciences. *Curr. Med. Chem.* **2010**, *17*, 4559–4557.

[12] Gu, F.; Langer, R.; Farokhzad, O. C. Formulation/Preparation of Functionalized Nanoparticles For In Vivo Targeted Drug Delivery. *Methods Mol Biol.* **2009**, *544*, 589–598.

[13] Xia, Y.; Xu, T.; Wang, C.; Li, Y.; Lin, Z.; Zhao, M.; Zhu, B. Novel Functionalized Nanoparticles for Tumor-Targeting Co-Delivery of Doxorubicin and Sirna to Enhance Cancer Therapy. *Int J Nanomedicine*. **2018**, *13*, 143–159.

[14] Sun, L.; Huang, C.; Gong, T,: Zhou, S. A Biocompatible Approach To Surface Modification: Biodegradable Polymer Functionalized Super-Paramagnetic Iron Oxide Nanoparticles. Materials Science and Engineering: C **2010**, *30*, 583–589.

[15] Hsiao, I.-L.; Fritsch-Decker, S.; Leidner, A.; Al-Rawi, M.; Hug, V.; Diabaté, S.; Grage, S. L.; Meffert, M.; Stoeger, T.; Gerthsen, D.; Ulrich, A.S.; Niemeyer, C. M.; Weiss, C. Biocompatibility of Amine-Functionalized Silica Nanoparticles: The Role of Surface Coverage. *Small* **2019**, *15*, 1805400.

[16] You, C. C.; Miranda, O. R; Gider, B.; Ghosh, P. S.; Kim, I. B.; Erdogan, B.; Krovi, S.A.; Bunz, U. H., Rotello V. M. Detection And Identification Of Proteins Using Nanoparticle-Fluorescent Polymer 'Chemical Nose' Sensors. *Nat Nanotechnol*. **2007**, 2, 318–23.

[17] Jiang, Y.; Zhao, H.; Lin, Y.; Zhu, N.; Ma, Y.; Mao, L. Colorimetric Detection of Glucose in Rat Brain using Gold Nanoparticles. *Angew Chem Int Ed Engl.* **2010**, *49*, 4800–4804.

[18] Bajaj, A.; Miranda, O. R.; Kim, I. B.; Phillips, R. L.; Jerry, D. J.; Bunz, U. H.; Rotello, V. M. Detection and Differentiation of Normal, Cancerous, and Metastatic Cells Using Nanoparticle-Polymer Sensor Arrays. *Proc Natl Acad Sci USA* **2009**, *106*, 10912–10926.

[19] Bajaj, A.; Rana, S.; Miranda, O.R.; Yawe, J. C.; Jerry, D. J., Bunz, U. H. F., Rotello, V. M. Cell Surface-Based Differentiation of Cell Types and Cancer States Using a Gold Nanoparticle-GFP Based Sensing Array. *Chem Sci.* **2010**; *1*, 134–138.

[20] El-Boubbou, K.; Zhu, D. C.; Vasileiou, C.; Borhan, B.; Prosperi, D.; Li, W.; Huang, X. Magnetic Glyco-Nanoparticles: a Tool to Detect, Differentiate, and Unlock the Glyco-Codes of Cancer via Magnetic Resonance Imaging. *J. Am. Chem. Soc.* **2010**, *132*, 4490–4499.

[21] Couleaud, P.; Bechet, D.; Vanderesse, R.; Barberi-Heyob, M.; Faure, A. C.; Roux, S.; Tillement, O.; Porhel, S.; Guillemin, F.; Frochot, C. Functionalized Silica-Based Nanoparticles for Photodynamic Therapy. *Nanomedicine* **2011**, *6*. 995–1009.

[22] Eun, J.; Dae, G.; Min, S. Targeted and Effective Photodynamic Therapy for Cancer Using Functionalized Nanomaterials. *Acta Pharmac. Sinica B* **2016**, *6*, 297–307.

[23] Mout, R.; Moyano, D. F.; Rana, S.; Rotello, V. M. Surface Functionalization of Nanoparticles for Nanomedicine. *Chem Soc Rev*. **2012** , *41*, 2539–2544.

[24] Duncan, R.; Sat, Y.-N. Tumour targeting by enhanced permeability and retention (EPR) effect. *Ann. Oncol.* **1998**, *9*, 39–39.

[25] Matsumura, Y.; Maeda; H. A New Concept for Macromolecular Therapeutics in Cancer Chemotherapy: Mechanism of Tumoritropic Accumulation of Proteins and the Antitumor Agent Smancs. *Cancer Res.* **1986**, *46*, 6387-6392.

[26] Petros, R. A.; DeSimone, J. M. Strategies in the Design of Nanoparticles for Therapeutic Applications. *Nat Rev Drug Discov.* **2010**, *9*, 615−627.

[27] Kumari, P.; Ghosh, B.; Biswas, S. Nanocarriers for Cancer-Targeted Drug Delivery. *J Drug Target.*, **2016**, *24*, 179–191.

[28] Yatvin, M. B.; Weinstein, J. N.; Dennis, W. H.; Blumenthal, R. Design of Liposomes for Enhanced Local Release of Drugs by Hyperthermia. *Science* **1978**, *202*, 1290–1293.

[29] Raza, A.; Hayat, U.; Rasheed, T.; Bilal, M.; Iqbal, H. M. N. "Smart" Materials-Based Near-Infrared Light-Responsive Drug Delivery Systems for Cancer Treatment: A Review. *Journ. of Mat. Res. and Tech.* **2019**, *8*, 1497–1509.

[30] Faustino, M.; Nicole, L.; Ruiz-Hitzky, E.; Sanchez, C. History of Organic-Inorganic Hybrid Materials: Prehistory, Art, Science and Advanced Applications. *Adv. Funct. Mat.* **2018**, 1–78

[31] Drisko, G. L.; Sanchez, C. Hybridization in Materials Science–Evolution, Current State, and Future Aspirations. *Eur. J. Inorg. Chem.* **2012**, 5097–5105.

[32] Nicole, L.; Rozes, L.; Sanchez, C. Integrative Approaches to Hybrid Multifunctional Materials: From Multidisciplinary Research to Applied Technologies. *Adv. Mater.* **2010**, *22*, 3208–3214.

[33] Varshni, Y. P. Temperature Dependence of the Energy Gap in Semiconductors. *Physica* **1967**, *34* (1), 149–154.

[34] Mao, J.; Lia, K.; Peng, T. Recent Advances in the Photocatalytic CO_2 Reduction over Semiconductors. *Catal. Sci. Technol.* **2013**, *3*, 2481−2498.

[35] Fujishima, A.; Honda, K. Electrochemical Photolysis of Water at a Semiconductor Electrode. *Nature* **1972**, *238*, 37–38.

[36] Yin, Z. F.; Wu, L.; Yang, H. G.; Sua, Y. H. Recent Progresses in Biomedical Applications of Titanium Dioxide. *Phys Chem. Phys.* **2013**, *15*, 4844–4858.

[37] Doane, T.; Burda, C. The Unique Role of Nanoparticles in Nanomedicine: Imaging, Drug Delivery and Therapy. *Chem. Soc. Rev.* **2012**, *41*, 2885–2911.

[38] Shannon, R.D.; Pask; J.A. Kinetics of the Anatase-Rutile Transformation. *J Am Ceram Soc*, **1965**, *48*, 391–398.

[39] Lazzeri, M.; Vittadini, A.; Selloni, A. Structure and Energetics of Stoichiometric TiO_2 Anatase Surfaces. *Phys Rev B*, **2001**, *63*, 155409.

[40] Zhang, H.; Banfield, J. F. Thermodynamic Analysis of Phase Stability of Nanocrystalline Titania. *J. Mater. Chem.* **1998**, *8*, 2073−2076.

[41] Leary, R.; Westwood, A. Carbonaceous Nanomaterials for the Enhancement of TiO_2 Photocatalysis. *Carbon* **2011** *49*, 741–772.

[42] Amtout, A.; Leonelli; R. Optical Properties of Rutile Near its Fundamental Band Gap. *Phys. Rev. B* **1995** *51*, 6842–6851.

[43] Nakaoka, Y.; Nosaka; Y. ESR Investigation into the Effects of Heat Treatment and Crystal Structure on Radicals Produced over Irradiated TiO_2 Powder. *Journ. of Photochem. and Photobiol. A: Chemistry* **1997**, *110*, 299–305.

[44] Nosaka, Y.; Kishimoto, M.; Nishino, J. Factors Governing the Initial Process of TiO_2 Photocatalysis Studied by Means of in-Situ Electron Spin Resonance Measurements. *J. Phys. Chem. B* **1998**, *102*, 10279–10283.

[45] Tang, H.; Berger, H.; Schmid, P. E.; Levy, F. Optical Properties of Anatase (TiO2*). Solid State Commun*. **1994**, *92*, 267–271.

[46] Preclíkova, J.; Galar, P.; Trojanek, F.; Danis, S.; Rezek, B.; Gregora, I.; Nemcova, Y.; Maly, P. Nanocrystalline Titanium Dioxide Films: Influence of Ambient Conditions on Surface- and Volume-Related Photoluminescence. *J. Appl. Phys.* **2010**, *108*, 113502–1135029.

[47] Lu, G.; Linsebigler, A.; Yates, J. T. J. The Adsorption and Photodesorption Of Oxygen on The TiO_2(110) Surface. *J. Chem. Phys.* **1995**, 102, 4657−4662.

[48] Di Valentin, C.; Selloni, A. Bulk and Surface Polarons in Photoexcited Anatase TiO_2. *J. Phys. Chem. Lett*. **2011**, *2*, 2223−2228.

[49] Chen, X.; Mao, S. Titanium Dioxide Nanomaterials: Synthesis, Properties, Modifications, and Applications. *Chem. Rev*. **2007** *107*, 2891–2959.

[50] Wanga, T.; Jiang, H.; Wan, L.; Zhao, Q.; Jiang, T.; Wang, B.; Wang, S. Potential Application of Functional Porous TiO_2 Nanoparticles in Light-Controlled Drug Release and Targeted Drug Delivery. *Acta Biomater.* **2015** *13*, 354-363.

[51] Xu, M.; Gao, Y.; Moreno, E.; Kunst, M.; Muhler, M.; Wang, Y.; Idriss, H.; Wöll; C. Photocatalytic Activity of Bulk TiO_2 Anatase and Rutile Single Crystals Using Infrared Absorption Spectroscopy. *Phys. Rev. Lett.* **2011**, *106*, 138302−138304.

[52] Burdett, J. K.; Hughbanks, T.; Miller, G. J.; Richardson, J. W.; Smith, J. V. Structural-Electronic Relationships in Inorganic Solids: Powder Neutron Diffraction Studies of the Rutile and Anatase Polymorphs of Titanium Dioxide at 15 and 295 K. *J. Am. Chem. Soc.* **1987**, *109*, 3639–3646.

[53] De Angelis, F.; Di Valentin, C.; Fantacci, S.; Vittadini, A.; Selloni, A. Theoretical Studies on Anatase and Less Common TiO_2 Phases: Bulk, Surfaces, and Nanomaterials. *Chem. Rev.* **2014**, *114*, 9708−9753.

[54] Tang, H.; Lévy, F.; Berger, H.; Schmid, P. E. Urbach Tail of Anatase TiO_2. *Phys. Rev. B* **1995**, *52*, 7771–7774.

[55] Zhang, Y.-F.; Lin, W.; Li, Y.; Ding, K.-N.; Li, J.-Q. A Theoretical Study on the Electronic Structures of TiO_2: Effect of Hartree−Fock Exchange. *J. Phys. Chem. B* **2005**, *109*, 19270–19277.

[56] Chiodo, L.; García-Lastra, J. M., Iacomino, A., Ossicini, S., Zhao, J., Petek, H., Rubio, A. Self-Energy and Excitonic Effects in The Electronic and Optical Properties Of TiO_2 Crystalline Phases. *Phys. Rev. B* **2010**, *82*, 045207.

[57] Deskins, N. A.; Dupuis, M. Electron Transport Via Polaron Hopping in Bulk TiO_2: A Density Functional Theory Characterization. *Phys. Rev. B* **2007**, *75*, 195212.

[58] Morgan, B. J.; Watson, G. W. Polaronic Trapping of Electrons and Holes by Native Defects in Anatase TiO_2. *Phys. Rev. B* **2009**, *80*, 233102.

[59] Micic, O. I.; Zhang, Y.; Cromack, K. R.; Trifunac, A. D.; Thurnauer, M. C. Trapped Holes on Titania Colloids Studied by Electron Paramagnetic Resonance. *J. Phys. Chem.* **1993**, *97*, 7277−7283.

[60] Kang, X.; Liu, S.; Dai, Z.; He, Y.; Song, X.; Tan, Z. Titanium Dioxide: From Engineering to Applications. *Catalysts* **2019**, *9*, 191.

[61] Bai, J.; Zhou, B. Titanium Dioxide Nanomaterials for Sensor Applications. *Chem. Rev.* **2014**, *114*, 10131−10176.

[62] Cargnello, M.; Gordon, T. R.; Murray, C. B. Solution-Phase Synthesis of Titanium Dioxide Nanoparticles and Nanocrystals. *Chem. Rev.* **2014**, *114*, 9319–9345.

[63] Barnard, A. S.; Zapol, P. Effects of Particle Morphology and Surface Hydrogenation on the Phase Stability of TiO_2. *Phys. Rev. B: Condens. Matter Mater. Phys*. **2004**, *70*, 235403.

[64] Dai, Y.; Cobley, C. M.; Zeng, J.; Sun, Y.; Xia, Y. Synthesis of Anatase TiO_2 Nanocrystals with Exposed {001} Facets. *Nano Lett.* **2009**, *9*, 2455–2459.

[65] Chu, L.; Qin, Z.; Yang, J.; Li, X. Anatase TiO_2 Nanoparticles with Exposed {001} Facets for Efficient Dye-Sensitized Solar Cells. *Scientific Rep.* **2015**, *5*, 12143.

[66] Pan, J.; Liu, G.; Lu, G. Q.; Cheng, H. On the True Photoreactivity Order of {001}, {010}, and {101} Facets of Anatase TiO_2 Crystals. *Angew. Chem. Int. Ed.* **2011**, *50*, 2133–2137.

[67] D'Arienzo, M.; Carbajo, J.; Bahamonde, A.; Crippa, M.; Polizzi, S.; Scotti, R.; Wahba, L.; Morazzoni, F. Photogenerated Defects in Shape-Controlled TiO_2 Anatase Nanocrystals: A Probe To Evaluate the Role of Crystal Facets in Photocatalytic Processes. *J. Am. Chem. Soc.* **2011**, *133*, 17652–17661.

[68] Hymmer, D. R.; Kubicki, J. D.; Kent, P. R. C.; Post, J. E.; Heaney, P. J. Origin of Nanoscale Phase Stability Reversals in Titanium Oxide Polymorphs *J. Phys. Chem. C* **2009**, *113*, 4240−4245.

[69] Li, Y.-F.; Liu, Z.-P. Particle Size, Shape and Activity for Photocatalysis on Titania Anatase Nanoparticles in Aqueous Surroundings. *J. Am. Chem. Soc.* **2011**, *133*, 15743–15752.

[70] Nunzi, F.; Storchi, L.; Manca, M.; Giannuzzi, R.; Gigli, G.; De Angelis, F. Shape and Morphology Effects on the Electronic Structure of TiO_2 Nanostructures: from Nanocrystals to Nanorods. *ACS Appl. Mater. Interfaces* **2014**, *6*, 2471– 2478.

[71] Wallace, S. K.; Mckenna, K. P. Facet-Dependent Electron Trapping in TiO_2 Nanocrystals. *J. Phys. Chem. C* **2015**, *119*, 1913–1920.

[72] Sugimoto, T.; Zhou, X.; Muramatsu, A. A. Synthesis of Uniform Anatase TiO_2 Nanoparticles by Gel–Sol Method: 1. Solution Chemistry of $Ti(OH)n(4–n)^+$ Complexes. *J. Colloid Interface Sci.* **2002**, *252*, 33−346.

[73] Gordon, T. R.; Cargnello, M.; Paik, T., Mangolini, F., Weber, R. T., Fornasiero, P., Murray, C. B. Nonaqueous Synthesis of TiO_2 Nanocrystals Using TiF_4 to Engineer Morphology, Oxygen Vacancy Concentration, and Photocatalytic Activity. *J. Am. Chem. Soc.* **2012**, *134*, 6751−6761.

[74] Diebold, U. The Surface Science of Titanium Dioxide. *Surf. Sci. Rep.* **2003**, *48*, 53−229.

[75] Barnard, A. S., Zapol, P. Effects of Particle Morphology and Surface Hydrogenation on The Phase Stability of TiO_2. *Phys Rev B* **2004**, *70*, 235403.

[76] Vittadini, A.; Casarin, M.; Selloni, A. Chemistry of and on TiO_2-Anatase Surfaces by DFT Calculations: A Partial Review. *Theor Chem Acc* **2007**, *117*, 663−671.

[77] Arrouvel, C.; Digne, M.; Breysse, M.; Toulhoat, H.; Raybaud, P. Effects of Morphology on Surface Hydroxyl Concentration: a DFT Comparison of Anatase–TiO_2 and γ-Alumina Catalytic Supports. *Journ. of Catal.* **2004**, *222*, 152−166.

[78] Zhao, Z.; Li, Z.; Zou, Z. Surface properties and electronic structure of low-index stoichiometric anatase TiO_2 surfaces. *J. Phys. Condens. Matter* **2010**, *22*, 175008.

[79] Hardman, P. J.; Raikar, G. N.; Muryn, C. A.; Vanderlaan. G.; Wincott, P. L.; Thornton, G.; Bullet, D. W.; Dale, P. Valence-Band Structure of TiO_2 Along the Γ-Δ-X and Γ-Σ-M Directions. *Phys. Rev. B* **1994**, *49*, 7170−7176.

[80] Chen, L.X.; Rajh, T.; Jager, W.; Nedeljkovic, J.; Thurnauer, M. C. X-Ray Absorption Reveals Surface Structure of Titanium Dioxide Nanoparticles. *J. Synchrotron Radiat*. **1999**, *6*, 445−447.

[81] Fazio, G.; Ferrighi, L.; Di Valentin, C. Spherical versus Faceted Anatase TiO_2 Nanoparticles: A Model Study of Structural and Electronic Properties. *J. Phys. Chem. C*, **2015**, *119*, 20735−20746.

[82] Naicker, P. K.; Cummings, P. T.; Zhang, H.; Banfield, J. F. Characterization of Titanium Dioxide Nanoparticles Using Molecular Dynamics Simulations. *J. Phys. Chem. B* **2005**, *109*, 15243–15249.

[83] Fazio, G.; Ferrighi, L.; Di Valentin, C. Photoexcited Carriers Recombination and Trapping in Spherical vs Faceted TiO_2 nanoparticles. *Nano Energy* **2016**, *27*, 673–689.

[84] Selli, D.; Fazio, G.; Di Valentin, C. Using Density Functional Theory to Model Realistic TiO_2 Nanoparticles, Their Photoactivation and Interaction with Water. *Catalysts*, **2017**, *7*, 357.

[85] Fazio, G.; Selli, D.; Ferraro, L., Seifert, G.; Di Valentin, C. Curved TiO_2 Nanoparticles in Water: Short (Chemical) and Long (Physical) Range Interfacial Effects. *Acs. Appl. Mater. Interfaces*, **2018**, *10*, 22943–22953.

[86] Selli, D.; Fazio, G.; Di Valentin, C. Modelling realistic TiO_2 nanospheres: A benchmark study of SCC-DFTB against hybrid DFT. *J. Chem. Phys* **2017**, *147* (16), 164701–164701.

[87] Tachikawa, T.; Asanoi, Y.; Kawai, K.; Tojo, S.; Sugimoto, A.; Fujitsuka, M.; Majima, T. Photocatalytic Cleavage of Single TiO_2/DNA Nanoconjugates. *Chem. Eur. J.* **2008**, *14*, 1492–1498.

[88] O'Regan, B.; Grätzel, M. A Low-Cost, High-Efficiency Solar Cell Based on Dye-Sensitized Colloidal TiO_2 Films. *Nature* **1991**, *353*, 737−740.

[89] Trouiller, B.; Reliene, R.; Westbrook, A.; Solaimani, P.; Schiestl, R. H. Titanium Dioxide Nanoparticles Induce DNA Damage and Genetic Instability in Vivo in Mice. *Cancer Res.* **2009**, *69*, 8784–8789.

[90] Oberdorster, G.; Ferin, J.; Gelein, R.; Soderholm, S. C.; Finkelstein, J. Role of the Alveolar Macrophage in Lung Injury: Studies with Ultrafine Particles. *Environ. Health Perspect.* **1992**, *97*, 193−199.

[91] Hamzeh, M.; Sunahara, G. I. In Vitro Cytotoxicity and Genotoxicity Studies of Titanium Dioxide (TiO_2) Nanoparticles in Chinese Hamster Lung Fibroblast Cells. *Toxicol. In Vitro* **2013**, *27*, 864−873.

[92] Ray, P. C.; Yu, H; Fu, P. P. Toxicity and Environmental Risks of Nanomaterials: Challenges and Future Needs. *J Environ Sci Health C Environ Carcinog Ecotoxicol Rev.* **2009**, *27*, 1–35.

[93] Desilvestro, J.; Graetzel, M.; Kavan, L.; Moser, J.; Augustynski, J. Highly Efficient Sensitization of Titanium Dioxide. *J. Am. Chem. Soc.* **1985**, *107*, 2988–2990.

[94] Bossmann, S. H.; Turro, C.; Schnabel, C.; Pokhrel, M. R.; Payawan, L. M.; Baumeister, B.; Wörner, M. $Ru(bpy)_3^{2+}$/TiO_2-Codoped Zeolites: Synthesis, Characterization, and the Role of TiO_2 in Electron Transfer Photocatalysis. *J. Phys. Chem. B* **2001**, *105*, 5374–5382.

[95] Leandri, V.; Liu, P.; Sadollahkhani, A.; Safdari, M.; Kloo, L.; Gardner, J. M. Excited-State Dynamics of $[Ru(bpy)_3]^{2+}$ Thin Films on Sensitized TiO_2 and ZrO_2. *ChemPhysChem* **2019**, *20*, 618–626.

[96] De Angelis, F.; Fantacci, S.; Selloni, A.; Nazeeruddin, M. K.; Grätzel, M. Time-Dependent Density Functional Theory Investigations on the Excited states of Ru(II)-Dye Sensitized TiO_2 Nanoparticles: the Role of Sensitizer Protonation. *J. Am. Chem. Soc.* **2007**, *129*, 14156–14157.

[97] Jana, A.K. Solar Cells Based on Dyes. *J Photochem Photobiol A: Chem* **2000**, *132*, 1–17.

[98] Argazzi, R.; Iha, N.Y.M.; Zabri, H.; Odobel, F.; Bignozzi, C.A. Design of Molecular Dyes For Application in Photoelectrochemical and Electrochromic Devices Based on Nanocrystalline Metal Oxide Semiconductors. *Coord. Chem. Rev.* **2004**, *248*, 1299–1316.

[99] Polo, A. S.; Itokazu, M. K.; Iha, N. Y. M. Metal Complex Sensitizers in Dye-Sensitized Solar Cells. *Coord. Chem. Rev.* **2004**, *248*, 1343–1361.

[100] De Angelis, F.; Fantacci, S.; Mosconi, E.; Nazeeruddin, M. K., Grätzel, M. Absorption Spectra and Excited State Energy Levels of the N719 Dye on TiO_2 in Dye-Sensitized Solar Cell Models. *J. Phys. Chem. C* **2011**, *115*, 8825–8831.

[101] De Angelis, F.; Tilocca, A., Selloni, A. Time-Dependent DFT Study of $[Fe(CN)_6]^{4-}$ Sensitization of TiO_2 Nanoparticles. *J. Am. Chem. Soc.* **2004**, *126*, 15024–15025.

[102] De Angelis, F. Direct vs. Indirect Injection Mechanisms in Perylene Dye-Sensitized Solar Cells: A DFT/TDDFT Investigation. *Chem. Phys. Lett.* **2010**, *493*, 323–327.

[103] Zhao, C.; Jin, L.; Ge, H.; Wang, Z.; Zhang, Q.; Wang, W. Improvement of Photovoltaic Performances by Optimizing π-Conjugated Bridge for the C217-Based Dyes: A Theoretical Perspective. *Journ. of Photochem. & Photobiol. A: Chemistry* **2018**, *360*, 137–144.

[104] Rocca, D.; Gebauer, R.; De Angelis, F.; Nazeeruddin, M. K.; Baroni, S. Time-Dependent Density Functional Theory Study of Squaraine Dye-Sensitized Solar Cells. *Chem. Phys. Lett.* **2009**, *475*, 49–53.

[105] De Angelis, F.; Fantacci, S.; Gebauer, R. Simulating Dye-Sensitized TiO_2 Heterointerfaces in Explicit Solvent: Absorption Spectra, Energy Levels, and Dye Desorption. *J. Phys. Chem. Lett.* **2011**, *2*, 813–817.

[106] Gebauer, R.; De Angelis, F. A. Combined Molecular Dynamics and Computational Spectroscopy Study of a Dye-Sensitized Solar Cell. *New Journ. Of Phys.* **2011**, *13*, 085013.

[107] Rajh, T.; Chen, L.X.; Lukas, K.; Liu, T.; Thurnauer, M. C.; Tiede, D. M. Surface Restructuring of Nanoparticles: An Efficient Route for Ligand−Metal Oxide Crosstalk. *J Phys. Chem. B*, **2002**, *106*, 10543–10552.

[108] Rajh, T.; Saponjic, Z.; Liu, J.; Dimitrijevic, N. M.; Scherer, N. F.; Vega-Arroyo, M.; Zapol, P.; Curtiss, L. A.; Thurnauer, M. C. Charge Transfer Across the Nanocrystalline-DNA Interface: Probing DNA Recognition. *Nano Lett.* **2004**, *46*, 1017–1023.

[109] Ye, Q.; Zhou, F.; Liu, W. Bioinspired Catecholic Chemistry for Surface Modification. *Chem. Soc. Rev.*, **2011**, *40*, 4244–4258.

[110] Liu, L. M.; Li, S. C.; Cheng; H.; Diebold, U; Selloni, A. Growth and Organization of an Organic Molecular Monolayer on TiO_2: Catechol on Anatase (101). *J. Am. Chem. Soc.* **2011**, *133*, 7816–7823.

[111] Nawrocka, A.; Zdyb, A.; Krawczyk, S. Stark Spectroscopy of Charge-Transfer Transitions in Catechol-Sensitized TiO_2 Nanoparticles. *Chem. Phys. Lett.* **2009**, *475*, 272–276.

[112] Syres, K. L.; Thomas, A. G.; Flavell, W. R.; Spencer, B. F.; Bondino, F.; Malvestuto, M.; Preobrajenski, A.; Grätzel, M. Adsorbate-Induced Modification of Surface Electronic Structure: Pyrocatechol Adsorption on the Anatase TiO_2 (101) and Rutile TiO_2 (110) Surfaces. *J. Phys. Chem. C* **2012**, *116*, 23515–23525.

[113] Li, S.-C.; Losovyj, Y.; Diebold, U. Adsorption-Site-Dependent Electronic Structure of Catechol on the Anatase TiO_2 (101) Surface. *Langmuir* **2011**, *27*, 8600–8604.

[114] Creutz, C.; Chou, M. H. Binding of Catechols to Mononuclear Titanium(IV) and to 1- and 5-nm TiO_2 Nanoparticles. *Inorg. Chem.* **2008**, *47*, 3509–3514.

[115] Finkelstein-Shapiro, D; Davidowski, S. K.; Lee, P.B.; Guo, C.; Holland, G. P.; Rajh, T.; Gray, K. A.; Yarger, J. L.; Calatayud, M. Direct Evidence of Chelated Geometry of Catechol on TiO_2 by a Combined Solid-State NMR and DFT Study. *J. Phys.Chem. C* **2016**, *120*, 23625−23630.

[116] Lana-Villarreal, T.; Rodes, A.; Pérez J. M.; Gomez R. A Spectroscopic and Electrochemical Approach to the Study of the Interactions and Photoinduced Electron Transfer between Catechol and Anatase Nanoparticles in Aqueous Solution. *J. Am. Chem. Soc.* **2005**, *127*, 12601−12611.

[117] Moser, J.; Punchihewa, S.; Infelta, P. P.; Grätzel, M. Surface Complexation of Colloidal Semiconductors Strongly Enhances Interfacial Electron-Transfer Rates. *Langmuir* **1991**, *7*, 3012−3018.

[118] Sánchez-de-Armas, R.; San-Miguel, M.; Oviedo, J.; Márquez, A. Sanz, J. F. Electronic Structure and Optical Spectra of Catechol on TiO_2 Nanoparticles from Real Time TD-DFT Simulations. *Phys. Chem. Chem. Phys.* **2011**, *13*, 1506–1514.

[119] Rego, L. G. C.; Batista, V. S. Quantum Dynamics Simulations of Interfacial Electron Transfer in Sensitized TiO_2 Semiconductors. *J. Am. Chem. Soc.* **2003**, *125*, 7989–7997.

[120] Lin, H.; Fratesi; G.; Selçuk, S.; Brivio, G. P.; Selloni, A. Effects of Thermal Fluctuations on the Structure, Level Alignment, and Absorption Spectrum of Dye-Sensitized TiO_2: A Comparative Study of Catechol and Isonicotinic Acid on the Anatase (101) and Rutile (110) Surfaces. *J. Phys. Chem. C* **2016**, *120*, 3899–3905.

[121] Xu, Y.; Chen, W.-K.; Liu; S. H.; Cao M. J.; Li, J. Q. Interaction of Photoactive Catechol with TiO_2 Anatase (101) Surface: A Periodic Density Functional Theory Study. *Chem. Phys.* **2007**, *331*, 275–282.

[122] Redfern, P. C.; Zapol, P.; Curtiss, L. A.; Rajh, T.; Thurnauer, M. C. Computational Studies of Catechol and Water Interactions with Titanium Oxide Nanoparticles. *J. Phys. Chem.* B **2003**, *107*, 11419–11427.

[123] Di Valentin, C.; Fittipaldi, D. Hole Scavenging by Organic Adsorbates on the TiO_2 Surface: A DFT Model Study. J. *Phys. Chem. Lett.* **2013**, *4*, 1901−1906.

[124] Neouze, M.; Schubert; U. Surface Modification and Functionalization of Metal and Metal Oxide nanoparticles by Organic Ligands. *Monatsh. Chem* **2008**, *139*, 183–195.

[125] Faure, B.; Salazar-Alvarez, G.; Ahniyaz, A.; Villaluenga, I.; Berriozabal, G.; De Miguel, Y. R.; Bergström, L. Dispersion and Surface Functionalization of Oxide Nanoparticles for Transparent Photocatalytic and UV-Protecting Coatings and Sunscreens. *Sci. Technol. Adv. Mater.* **2013**, *14*, 023001.

[126] Abuabara, S. G.; Rego, L. G. C.; Batista; V. S. Influence of Thermal Fluctuations on Interfacial Electron Transfer in Functionalized TiO_2 Semiconductors. *J. Am. Chem. Soc.* **2005**, *127*, 18234–18242.

[127] Rajh, T.; Nedeljkovic, J. M.; Chen, L. X.; Poluektov, O.; Thurnauer, M. C. Improving Optical and Charge Separation Properties of Nanocrystalline TiO_2 by Surface Modification with Vitamin C. *J. Phys. Chem. B*, **1999**, *103*, 3515–3519.

[128] Sánchez-de-Armas, R.; Oviedo, J.; Ángel San Miguel, M.; Fdez, J. Sanz. Direct vs Indirect Mechanisms for Electron Injection in Dye-Sensitized Solar Cells. *J. Phys. Chem. C* **2011**, *115*, 11293–11301.

[129] Paunesku, T.; Rajh, T.; Wiederrecht, G.; Maser, J.; Vogt, S.; Stojićević, N.; Protić, M.; Lai, B.; Oryhon, J.; Thurnauer, M.; Woloschak, G. Biology of TiO_2–Oligonucleotide Nanocomposites. *Nat. Mater.* **2003**, *2*, 343–346.

[130] Weng, Y.-X.; Li, L.; Liu, Y.; Wang, L.; Yang, G.-Z. Surface-Binding Forms of Carboxylic Groups on Nanoparticulate TiO_2 Surface Studied by the Interface-Sensitive Transient Triplet-State Molecular Probe. *J. Phys. Chem. B* **2003,** *107*, 4356–4363.

[131] Vittadini, A.; Selloni, A.; Rotzinger, F. P.; Grätzel, M. Formic Acid Adsorption on Dry and Hydrated TiO_2 Anatase (101) Surfaces by DFT Calculations. *J. Phys. Chem. B* **2000**, *104*, 1300–1306.

[132] de la Garza, L.; Saponjic, Z. V.; Dimitrijevic, N. M.; Thurnauer, M. C.; Rajh, T. Surface States of Titanium Dioxide Nanoparticles Modified with Enediol Ligands. *J. Phys. Chem. B* **2006**, *110*, 680–686.

[133] Di Valentin, C.; Costa, D. Anatase TiO_2 Surface Functionalization by Alkylphosphonic Acid: A DFT+D Study. *J. Phys. Chem. C* **2012**, *116*, 2819–2828.

[*134*] Luschtinetz, R.; Frenzel, J.; Milek, T.; Seifert, G. Adsorption of Phosphonic Acid at the TiO_2 Anatase (101) and Rutile (110) Surfaces. *J. Phys. Chem. C* **2009,** *113*, 5730–5740.

[135] Rozhkova, E. A.; Ulasov, I.; Lai, B.; Dimitrijevic, N. M.; Lesniak, M. S., Rajh, T. A High-Performance Nanobiophotocatalyst for Targeted Brain Cancer Therapy. *Nano Lett.* **2009**, *9*, 2005–2008.

[136] Duan, D.; Liu, H.; Xu, Y.; Han, Y.; Xu, M.; Zhang, Z.; Liu, Z. Activating TiO_2 Nanoparticles: Gallium-68 Serves as a High-Yield Photon Emitter for Cerenkov-Induced Photodynamic Therapy. *ACS Appl. Mater. Interfaces* **2018**, *10*, 5278–5286.

[137] Liu, J.; de la Garza, L.; Zhang, L.; Dimitrijevic, N. M.; Zuo, X. Tiede, D. M.; Rajh, T. Photocatalytic Probing of DNA Sequence by Using TiO_2/Dopamine-DNA Triads. *Chemical Physics* **2007**, *339*, 154–163.

[138] Dimitrijevic, N. M.; Rozhkova, E.; Rajh, T. Dynamics of Localized Charges in Dopamine-Modified TiO_2 and Their Effect on the Formation of Reactive Oxygen Species. *J. Am. Chem. Soc.* **2009**, *131*, 2893–2899.

[139] Xu, J.; Sun, Y.; Huang, J.; Chen, C.; Liu, G.; Jiang, Y.; Zhao, Y.; Jiang, Z. Photokilling Cancer Cells Using Highly Cell-Specific Antibody-TiO_2 Bioconjugates and Electroporation. *Bioelectrochemistry* **2007**, *71*, 217–222.

[140] Mehrotra, R. C.; Singh, A. Chemistry of Oxo-Alkoxides of Metals. *Chem. Soc. Rev.* **1996**, *25*, 1–13.

[141] Zhang, W.; Zhu, Z.; Cheng, C. Y. A Literature Review of Titanium Metallurgical Processes. *Hydrometallurgy*, **2011**, *108*, 177–188.

[142] Dugandžić, I. M.; Jovanović, D. J.; Mančić, L. T.; Milošević, O. B.; Ahrenkiel, S. P.; Šaponjić, Z. V.; Nedeljković, J. M. Ultrasonic Spray Pyrolysis of Surface Modified TiO_2 Nanoparticles with Dopamine. *Mater. Chem. Phys.* **2013**, *143*, 233–239.

[143] Kaviani, M., Di Valentin, C. Rational Design of Nanosystems For Simultaneous Drug Delivery and Photodynamic Therapy by Quantum Mechanical Modeling. *Nanoscale*, **2019**, *11*, 15576–15588.

[144] Syres, K. L.; Thomas, A. G.; Bondino, F.; Malvestuto, M.; Gratzel, M. Dopamine Adsorption on Anatase TiO_2(101): A Photoemission and NEXAFS Spectroscopy Study. *Langmuir* **2010**, *26*, 14548–14555.

[145] Thurn, K. T.; Paunesku, T.; Wu, A.; Brown, E. M.; Lai, B.; Vogt, S.; Maser, J.; Aslam, M.; Dravid, D.; Bergan, R.; Woloschak, G. E. Labeling TiO_2 Nanoparticles with Dyes for Optical Fluorescence Microscopy and Determination of TiO_2–DNA Nanoconjugate Stability. *Small* **2009**, *5*, 1318–1325.

[146] Wang, G. L.; Xu, J. J.; Chen, H. Y. Dopamine Sensitized Nanoporous TiO_2 Film on Electrodes: Photoelectrochemical Sensing of NADH Under Visible Irradiation. *Biosens. Bioelectron.* **2009**, *24*, 2494–2498.

[147] Lin, C.-C.; Chu, Y.-M.; Chang, H. C. In Situ Encapsulation of Antibody on TiO_2 Nanowire Immunosensor Via Electro-Polymerization of Polypyrrole Propylic Acid. *Sensors Actuators, B Chem.* **2013**, *187*, 533–539.

[148] Deng, F.; Guan, Y.; Shi, Z.; Wang, F.; Che, X.; Liu, Y.; Wan, Y. The Effect of Dopamine Modified Titanium Dioxide Nanoparticles on the Performance of Poly(Vinyl Alcohol)/Titanium Dioxide Composites. *Compos. Sci. and Technol.* **2017**, *150*, 120–127.

[149] Luppi, E.; Urdaneta, I.; Calatayud, M. Photoactivity of Molecule-TiO_2 Clusters with Time-Dependent Density-Functional Theory. *J. Phys. Chem. A* **2016**, *120*, 5115−5124.

[150] Vega-Arroyo, M.; LeBreton, P. R.; Zapol, P., Curtiss L. A.; Rajh, T. Quantum Chemical Study of TiO_2/Dopamine-DNA Triads. *Chem. Phys.* **2007**, *339*, 164–172.

[151] Vega-Arroyo, M.; Lebreton, P. R.; Rajh, T., Zapol, P.; Curtiss, L. A. Density Functional Study of the TiO_2-Dopamine Complex. *Chem. Phys. Lett.* **2005**, *406*, 306–311

[152] Urdaneta, I.; Keller, A.; Atabek, O.; Palma, J. L.; Finkelstein-Shapiro, D.; Tarakeshwar, P.; Mujica, V.; Calatayud, M. Dopamine Adsorption on TiO_2 Anatase Surfaces. *J. Phys. Chem. C* **2014**, *118*, 20688–20693.

[153] Geiseler, B.; Fruk, L. Bifunctional Catechol Based Linkers for Modification of TiO_2 Surfaces. *J. Mater. Chem.* **2012**, *22*, 735–741.

[154] Geiseler, B.; Miljevic, M.; Müller, P.; Fruk, L. Phototriggered Production of Reactive Oxygen Species by TiO_2 Nanospheres and Rods. *Journ. of Nanomat.* **2012**, *2012*, 708519.

[155] Monkhorst, H. J.; Pack, J. D. Special Points for Brillouin-Zone Integrations. *Phys. Rev. B* **1976**, *13*, 5188−5192.

[156] Singh, D. J., Nordstrom, L. (2006) *Planewaves, Pseudopotentials and the LAPW Method*. II Edition, Springer.

[157] Andrade, X.; Alberdi-Rodriguez, J.; Strubbe, D. A.; Oliveira, M. J. T.; Nogueira, F.; Castro, A.; Muguerza, J.; Arruabarrena, A.; Louie, S. G.; Aspuru-Guzik, A.; Rubio, A.; Marques, M. A. L. Time-Dependent Density-Functional Theory in Massively Parallel Computer Architectures: the Octopus Project, J. *Phys. Cond. Matt*. **2012,** *24*, 233202.

[158] Hamann, D. R.; Schlüter, M.; Chiang, C. Norm-Conserving Pseudopotentials. *Phys. Rev. Lett.* **1979**, *43*, 1494−1497.

[159] Schlipf, M.; Gygi, F. Optimization Algorithm for the Generation of ONCV Pseudopotentials. *Comp. Phys. Commun.* **2015**, *196*, 36–44.

[160] Jensen, F. (2006) *Introduction to Computational Chemistry*, John Wiley & Sons, West Sussex.

[161] Jørgensen, M. R. V.; Hathwar, V. R.; Bindzus, N.; Wahlberg, N.; Chen, Y.-S.; Overgaarda, J.; Iversena, B. B. Contemporary X-ray Electron-Density Studies Using Synchrotron Radiation. *IUCrJ*, **2014**, *1*, 267−280.

[162] Hohenberg, P.; Kohn, W. Inhomogeneous Electron Gas. *Phys. Rev. B*, **1964**, *136*, B864−B871.

[163] Dirac, P. A. M. Note on Exchange Phenomena in the Thomas Atom. *Proc. Camb. Phil. Soc*., **1930**, *26*, 376−385.

[164] Ceperley, D. M.; Alder, B. J. Ground State of the Electron Gas by a Stochastic Method. *Phys. Rev. Lett.* **1980**, *45*, 566–569.

[165] Vosko, S. H.; Wilk, L.; Nusair, M. Accurate Spin-Dependent Electron Liquid Correlation Energies for Local Spin Density Calculations: A Critical Analysis. *Can. J. Phys*., **1980**, 58, 1200 −1211.

[166] Staroverov, V. N.; Scuseria, G. E.; Tao, J.; Perdew, J. P. Energy Band Gaps and Lattice Parameters Evaluated with the Heyd-Scuseria-Ernzerhof Screened Hybrid Functional. *J. Chem. Phys.* **2005**, *123*, 174101.

[167] Boese, A. D.; Martin, M. L. The Role of the Basis Set: Assessing Density Functional Theory. *J. Chem. Phys.* **2003**, *119*, 3005−3014.

[168] Perdew, J. P.; Burke, K.; Ernzerhof, M. Generalized Gradient Approximation Made Simple. *Phys. Rev. Lett.* **1996**, *77*, 3865−3868.

[169] Lee, C.; Yang, W.; Parr, R. G. Development of the Colle-Salvetti Correlation-Energy Formula into a Functional of the Electron Density. *Phys. Rev. B* **1988**, *37*, 785−789.

[170] Becke, A. D. Density-Functional Thermochemistry. III. The Role of Exact Exchange. *J. Chem. Phys.* **1993**, *98*, 5648−5652.

[171] Muscat, J.; Wander, A.; Harrison, N. M. On The Prediction of Band Gaps from Hybrid Functional Theory. *Chem. Phys. Lett.* **2001**, *342*, 397−401.

[172] Labat, F.; Baranek, P.; Adamo, C. Structural and Electronic Properties of Selected Rutile and Anatase TiO_2 Surfaces: An ab Initio Investigation. *J. Chem. Theory Comput.* **2008**, *4*, 341−352.

[173] Heyd, J.; Scuseria, G. E. Efficient Hybrid Density Functional Calculations in Solids: Assessment of the Heyd–Scuseria–Ernzerhof Screened Coulomb Hybrid Functional. *J. Chem. Phys.* **2004**, *121*, 1187−1192.

[174] Adamo, C.; Barone, V. Toward Reliable Density Functional Methods Without Adjustable Parameters: The PBE0 Model. *Jour. Chem. Phys.* **1999**, *110*, 6158−6170.

[175] Perdew, J. P.; Levy, M. Physical Content of the Exact Kohn-Sham Orbital Energies: Band Gaps and Derivative Discontinuities. *Phys. Rev. Lett.* **1983**, *51*, 1884−1987.

[176] Perdew, J. P.; Levy, M. Comment on "Significance of the Highest Occupied Kohn-Sham Eigenvalue". *Phys. Rev. B* **1997**, *56*, 16021−16028.

[177] Di Valentin, C.; Botti, S.; Coccioni, M. (2014) *First Principles Approaches to Spectroscopic Properties of Complex Materials.* Springer.

[178] Kümmel S.; Kronik, L. Orbital-Dependent Density Functionals: Theory and Applications. *Rev. Mod. Phys.* **2008**, *80*, 3−60.

[179] Paier, J.; Marsman, M; Hummer, K.; Kresse, G. Screened Hybrid Density Functionals Applied to Solids. *J. Chem. Phys.* **2006**, *124*, 154709.

[180] Seifert, G.; Joswig, J.-O. Density-Functional Tight Binding—An Approximate Density-Functional Theory Method. *Wiley Interdiscip. Rev. Comput. Mol. Sci.* **2012**, *2*, 456−466.

[181] Verlet, L. Computer "Experiments" on Classical Fluids. I. Thermodynamical Properties of Lennard-Jones Molecules. *Phys. Rev.* **1967**, *159*, 98−103.

[182] Li, X.; Millam, J. M.; Schlegel, H. B. Ab Initio Molecular Dynamics Studies of the Photodissociation of Formaldehyde, $H_2CO \rightarrow H_2+CO$: Direct Classical Trajectory Calculations by MP2 and Density Functional Theory. *J. Chem. Phys.* **2000**, *113*, 10062−10067.

[183] Car, R.; Parrinello, M. Unified Approach for Molecular Dynamics and Density-Functional Theory. *Phys. Rev. Lett.* **1985**, *55*, 2471−2474.

[184] Hoover, W. G. Canonical Dynamics: Equilibrium Phase-Space Distributions. *Phys. Rev. A* **1985**, *31*, 1695−

[185] Martyna, G. J.; Klein, M. L. Nosé–Hoover Chains: The Canonical Ensemble via Continuous Dynamics. J. Chem. Phys. 97, 2635 (1992)

[186] Salpeter, E. E.; Bethe, H. A. A Relativistic Equation for Bound-State Problems. *Phys. Rev*. **1951**, *84*, 1232−1242.

[187] Hedin, L. New Method for Calculating the One-Particle Green's Function with Application to the Electron-Gas Problem. *Phys. Rev.* **1965**, *139*, A796−A823.

[188] Runge, E.; Gross, E.K. U. Density-Functional Theory for Time-Dependent Systems. *Phys. Rev. Lett.* **1984**, *52*, 997−1000.

[189] Zangwill, A.; Soven, P. Resonant Photoemission in Barium and Cerium. *Phys. Rev. Lett.* **1980**, *45*, 204−207.

[190] Gross, E. K. U.; Kohn, W. Local Density-Functional Theory of Frequency-Dependent Linear Response. *Phys. Rev. Lett.* **1985**, *55*, 2850−2852.

[191] van Leeuwen, R. Key Concepts in Time-Dependent Density-Functional Theory. *Int. J. Mod. Phys. B* **2001**, *15*, 1969−2003.

[192] Leeuwen, R. Causality and Symmetry in Time-Dependent Density-Functional Theory. *Phys. Rev. Lett.* **1988**, *80*, 1280−1283.

[193] Petersilka, M., Gossmann, U. J., Gross, E. K. U. Excitation Energies from Time-Dependent Density-Functional Theory. *Phys. Rev. Lett.*, **1996**, *76*, 1212−1215.

[194] Bertsch, G. F., Iwata J. I., Rubio, A., Yabana, K. Excitation Energies from Time-Dependent Density Functional Theory for Linear Polyene Oligomers: Butadiene to Decapentaene. *Phys. Rev. B* **2001**, *105*, 451−458.

[195] Castro, A.; Marques, M. A. L.; Alonso, J. A.; Rubio, A. Optical Properties of Nanostructures from Time-Dependent Density Functional Theory. *J Comp Theoret Nanoscience*, **2004**, *1*, 231−255.

[196] Ehrenreich, H.; Cohen, M. Self-Consistent Field Approach to the Many-Electron Problem. *Phys Rev* **1959**, *115*, 786−790.

[197] Wiser, N. Dielectric Constant with Local Field Effects Included. *Phys Rev*, **1963**, *129*, 62−69.

[198] Maddocks, N. E.; Godby, R. W.; Needs, R. J. Bandstructure Effects in the Dynamic Response of Aluminium. *Europhys Lett*, **1994**, *27*, 681–686.

[199] K. Yabana, T. Nakatsukasa, J.-I. Iwata, G. F. Bertsch. Time-Dependent Local-Density Approximation in Real Time. *Phys. Rev. B* **1996**, *54*, 4484–4487.

[200] Castro, A.; Marques, M.A.L.; Varsano, D.; Sottile, F.; Rubio, A. The Challenge of Predicting Optical Properties of Biomolecules: What Can We Learn from Time-Dependent Density-Functional Theory. Comptes Rendus Physique 10, 469 - 490 (2009)

[201] G. F. Bertsch, J.-I. Iwata, Angel Rubio, K. Yabana. Real-Space, Real-Time Method for the Dielectric Function. *Phys. Rev. B* **2000**, *62*, 7998–8002.

[202] Castro, A.; Marques, M.A.L.; Alonso, J. A.; Bertsch, G. F.; Rubio; A. Excited States Dynamics in Time-Dependent Density Functional Theory. High-field Molecular Dissociation and Harmonic Generation. *Eur. Phys. J. D* **2004**, *28*, 211–218.

[203] Dovesi, R.; Saunders, V. R.; Roetti, C.; Orlando, R.; ZicovichWilson, C. M.; Pascale, F.; Civalleri, B.; Doll, K.; Harrison, N. M.; Bush, I. J.; et al. *CRYSTAL14 User's Manual*; University of Torino: Torino, Italy, **2014**.

[204] Shirai, K.; Sugimoto, T.; Watanabe, K.; Haruta, M.; Kurata, H.; Matsumoto, Y. Effect of Water Adsorption on Carrier Trapping Dynamics at the Surface of Anatase TiO_2 Nanoparticles. *Nano Lett.* **2016**, *16*, 1323–1327.

[205] Grätzel, M. Photoelectrochemical Cells. *Nature*, **2001**, *414*, 338–344.

[206] Henderson, M. A. A. Surface Science Perspective on TiO_2 Photocatalysis. *Surf. Sci. Rep.* **2011**, *66*, 185–297.

[207] Kavan, L.; Grätzel, M.; Gilbert, S. E.; Klemenz, C.; Scheel, H. J. Electrochemical and Photoelectrochemical Investigation of Single-Crystal Anatase. *J. Am. Chem. Soc.* **1996**, *118*, 6716–6723.

[208] Hanaor, D. A. H.; Sorrell, C. C. Review of the Anatase to Rutile Phase Transformation. *J. Mater. Sci.* **2011**, *46*, 855–874.

[209] Mano, S. S.; Kanehira, K.; Sonezaki, S.; Taniguchi, A. Effect of Polyethylene Glycol Modification of TiO_2 Nanoparticles on Cytotoxicity and Gene Expressions in Human Cell Lines. *Int. J. Mol. Sci.* **2012**, *13*, 3703−3717.

[210] Lopez, T.; Ortiz, E.; Alvarez, M.; Navarrete, J.; Odriozola, J. A.; Martinez-Ortega, F.; Paez-Mozo, E. A.; Escobar, P.; Espinoza, K. A.; Rivero, I. A. Study of the Stabilization of Zinc Phthalocyanine in Sol-Gel TiO_2 for Photodynamic Therapy Applications. *Nanomed. Nanotechnol.* **2010**, *6*, 777−785.

[211] Heyd, J.; Scuseria, G. E.; Ernzerhof, M. Hybrid functionals based on a screened Coulomb potential. *J. Chem. Phys.* **2003**, *118***,** 8207–8215.

[212] Grimme, S. Semiempirical GGA-Type Density Functional Constructed with a Long-Range Dispersion Correction. *J. Comput. Chem.* **2006**, *27***,** 1787–1799.

[213] Elstner, M.; Porezag, D.; Jungnickel, G.; Elsner, J.; Haugk, M.; Frauenheim, T.; Suhai, S.; Seifert, G. Self-Consistent-Charge Density Functional Tight-Binding Method for Simulations of Complex Materials Properties. *Phys. Rev. B: Condens. Matter Mater. Phys.* **1998**, *58*, 7260–7268.

[214] Elstner, M.; Seifert, G. Density Functional Tight Binding. *Philos. Trans. R. Soc. A* **2014**, *372*, 20120483.

[215] Aradi, B.; Hourahine, B.; Frauenheim, T. DFTB+, A Sparse Matrix-Based Implementation of the DFTB Method. *J. Phys. Chem. A* **2007**, *111*, 5678–5684.

[216] Selli, D.; Fazio, G.; Seifert, G.; Di Valentin, C. Water Multilayers on TiO_2 (101) Anatase Surface: Assessment of a DFTB-Based Method.; *J. Chem. Theory Comput.* **2017**, *13*, 3862–3873.

[217] Hu, H.; Lu, Z.; Elstner, M.; Hermans, J.; Yang, W. Simulating Water with the Self-Consistent-Charge Density Functional Tight Binding Method: From Molecular Clusters to the Liquid State. *J. Phys. Chem. A* **2007**, *111*, 5685–5691.

[218] Labat, F;, Baranek, Ph.; Domain, C.; Minot, C.; Adamo, C. Density Functional Theory Analysis of the Structural and Electronic Properties of TiO_2 Rutile and Anatase Polytypes: Performances of Different Exchange-Correlation Functionals. *J. Chem. Phys.* **2007**, *126*, 154703.

[219] Henkelman, G.; Uberuaga, B. P.; Jonsson, H. A Climbing Image Nudged Elastic Band Method for Finding Saddle Points and Minimum Energy Paths. *J. Chem. Phys.* **2000**, *113*, 9901−9904.

[220] Bahn, S. R.; Jacobsen, K. W. An Object-Oriented Scripting Interface to a Legacy Electronic Structure Code. *Comput. Sci. Eng.* **2002**, *4*, 56−66.

[221] Sapsford, K. E.; Algar, W. R.; Berti, L.; Gemmill, K. B.; Casey, B. J.; Oh, E.; Stewart, M. H.; Medintz, I. L. Functionalizing Nanoparticles with Biological Molecules: Developing Chemistries that Facilitate Nanotechnology. *Chem. Rev.* **2013**, *113*, 1904–2074.

[222] Erathodiyil, N.; Ying, J. Y. Functionalization of Inorganic Nanoparticles for Bioimaging Application. *Acc. Chem. Res*. **2011**, *44*, 925–935.

[223] Shi, H.; Magaye, R.; Castranova, V.; Zhao, J. Titanium Dioxide Nanoparticles: a Review of Current Toxicological Data. *Part Fibre Toxicol*. **2013**, *10*, 1–33.

[224] Rozhkova, E. A.; Ulasov, I. V.; Lai, B.; Dimitrijevic, N. M.; Lesniak, M. S.; Rajh, T. A High-Performance Nanobio Photocatalyst for Targeted Brain Cancer Therapy. *Nano Lett.* **2009**, *9*, 3337–3342.

[225] Kotagiri, N.; Sudlow, G. P.; Akers, J. W.; Achilefu, S. Breaking the Depth Dependency of Phototherapy with Cerenkov Radiation and Low Radiance Responsive Nanophotosensitizers. *Nat Nanotechnol*. **2015**, *10*, 370–379.

[226] Duan, D.; Liu, H.; Xu, Y.; Han, Y.; Xu, M.; Zhang, Z.; Liu, Z. Activating TiO_2 Nanoparticles: Gallium-68 Serves as a High-Yield Photon Emitter for Cerenkov-Induced Photodynamic Therapy. *ACS Appl. Mater. Interfaces* **2018**, *10*, 5278–5286.

[227] Rozhkova, E. A.; Ulasov, I. V.; Kim, D. H.; Dimitrijevic, N. M.; Bader, S. D.; Lesniak, M. S.; Rajh, T. Multifunctional Nano-Bio Materials within Cellular Machinery. *Int. J. Nanosci.* **2011**, *10*, 899–908.

[228] Shrestha, N.K.; Macak, J. M.; Schmidt-Stein, F.; Hahn, R.; Mierke, C. T.; Fabry, B.; Schmuki, P. Magnetically Guided Titania Nanotubes for Site-Selective Photocatalysis and Drug Release. *Angew. Chem., Int. Ed.* **2009**, *48*, 969–972.

[229] Endres, P. J.; Paunesku, T.; Vogt, S.; Meade, T. J.; Woloschak, G. E. DNA−TiO_2 Nanoconjugates Labeled with Magnetic Resonance Contrast Agents. *J. Am. Chem. Soc.* **2007**, *129*, 15760–15761.

[230] Brown, T.; Thurn, T.; Xin, L.; Liu, W.; Bazak, R.; Chen, S.; Lai, B.; Vogt, S.; Jacobsen, C.; Paunesku, T.; Woloschak, G. E. Intracellular in Situ Labeling of TiO_2 Nanoparticles for Fluorescence Microscopy Detection. *Nano Res.* **2018**, *11*, 464–476.

[231] Yin, Z. F.; Wu, L.; Yang, H. G.; Su, Y. H. Recent Progress in Biomedical Applications of Titanium Dioxide. *Phys. Chem. Chem. Phys.* **2013**, *15*, 4844–4858.

[232] Katz, E.; Willner,I. Integrated Nanoparticle-Biomolecule Hybrid Systems: Synthesis, Properties, and Applications. *Angew Chem Int Ed Engl*. **2004**, *43*, 6042–6108.

[233] Gurr, J.R.; Wang, A. S.; Chen, C. H.; Jan, K.Y. Ultrafine Titanium Dioxide Particles in The Absence of Photoactivation Can Induce Oxidative Damage to Human Bronchial Epithelial Cells. *Toxicology* **2005**, *213*, 66−73.

[234] Yin, J. J.; Liu, J.; Ehrenshaft, M.; Roberts, J. E.; Fu, P. P.; Mason, R. P.; Zhao, B. Phototoxicity of Nano Titanium Dioxides in HaCaT Keratinocytes--Generation of Reactive Oxygen Species and Cell Damage. *Toxicol Appl Pharmacol.* **2012**, *263*, 81−88.

[235] Hoffmann, M. R.; Martin, S. T.; Choi, W.; Bahnemann, D. W. Environmental Applications of Semiconductor Photocatalysis. *Chem. Rev.* **1995**, *95*, 69−96.

[236] Mills, A.; Le Hunte, S. An Overview of Semiconductor Photocatalysis. *J. Photochem. Photobiol.* A **1997**, *108*, 1−35.

[237] Fruehauf, J.P; Meyskens, F. L. Reactive Oxygen Species: A Breath of Life or Death? *Clin. Cancer Res.* **2007**, *13*, 789−794.

[238] Trachootham, D.; Alexandre, J.; Huang, P. Targeting Cancer Cells by ROS-Mediated Mechanisms: A Radical Therapeutic Approach? *Nat Rev Drug Discov.* **2009**, *8*, 579–591.

[239] Duncan, W.; Prezhdo, O.V. Theoretical Studies of Photoinduced Electron Transfer in Dye-Sensitized TiO_2. *Annu. Rev. Phys. Chem.* **2007**, *58*, 143–184.

[240] Finkelstein-Shapiro, D.; Tarakeshwar, P.; Rajh, T.; Mujica, V. Photoinduced Kinetics of SERS in Bioinorganic Hybrid Systems. A Case Study: Dopamine−TiO_2. *J. Phys. Chem. B* **2010**, *114*, 14642–14645.

[241] Chen, L. X.; Rajh, T.; Wang, Z.; Thurnauer, M. C. XAFS Studies of Surface Structures of TiO_2 Nanoparticles and Photocatalytic Reduction of Metal Ions. *J. Phys. Chem. B* **1997**, *101*, 10668-10697.

[242] Yeung K. L.; Maira, A. J.; Stolz, J.; Hung, E; Ho, N. K-C.; Wei, A. C.; Soria, J.; Chao, K-J.; Yue, P. L. Ensemble Effects in Nanostructured TiO_2 Used in the Gas-Phase Photooxidation of Trichloroethylene. *J. Phys. Chem. B* **2002**, *106*, 4608–4616.

[243] Radoičić, M. B.; Janković, I. A.; Despotović, V. N.; Šojić, D. V.; Savić, T. D.; Šaponjića Z. V.; Abramović, B. F.; Čomora, M. I. The Role of Surface Defect Sites of Titania Nanoparticles in the Photocatalysis: Aging and Modification. *Appl. Catal. B: Environ.* **2013**, *138*(139), 122–127.

[244] Hurst, S. J.; Christopher Fry, H. C.; Gosztola, D. J.; Finkelstein-Shapiro, D.; Vladimiro Mujica, V.; Rajh, T. Mechanistic Studies into the Raman Enhancement of Enediol-Semiconducting Nanoparticle Conjugates and their Use in Biological Applications. *Proc. SPIE* **2010**, *7758*, 77580E.

[245] Civalleri, B.; Zicovich-Wilson, C. M.; Valenzano, L.; Ugliengo,P. B3LYP Augmented with an Empirical Dispersion Term (B3LYP- D*) as Applied to Molecular Crystals. *CrystEngComm* **2008**, *10*, 405−410.

[246] Civalleri, B.; D'Arco, Ph.; Orlando, R.; Saunders, V. R.; Dovesi, R. Hartree–Fock Geometry Optimisation of Periodic Systems with the Crystal code. *Chem. Phys. Lett.* **2001**, *348*, 131−138.

[247] Elstner, M. The SCC-DFTB Method and its Application to Biological Systems. Theor Chem Acc, **2006**, *116*, 316–325.

[248] Hurst, J. S.; Fry, H. C.; Gosztola, D. J.; Rajh, T. Utilizing Chemical Raman Enhancement: A Route for Metal Oxide Support-Based Biodetection. *J. Phys. Chem. C* **2011**, *115*, 620–630.

[249] Niederberger, M.; Garnweitner, G.; Krumeichm F.; Nesper, R.; Cölfen, H.; Antonietti, M. Tailoring the Surface and Solubility Properties of Nanocrystalline Titania by Nonaqueous in Situ Functionalization Process. *Chem. Mater.* **2004**, *16*, 1202–1208.

[250] Turner, D. W.; Al Jobory, M. I. Determination of Ionization Potentials by Photoelectron Energy Measurement". J. Chem. Phys. **1962**, *37*, 3007–3008.

[251] Ramasse, Q. M.; Seabourne, C. R.; Kepaptsoglou, D.-M.; Zan, R.; Bangert, U.; Scott, A. J. Probing the Bonding and Electronic Structure of Single Atom Dopants in Graphene with Electron Energy Loss Spectroscopy. *Nano Lett.* **2013**, *13*, 4989–4995.

[252] Dimitrijevic, N. M.; De la Garza, L; Rajh, T. Light-Induced Charge Separation across Bio-Inorganic Interface. *Int. J. Mod. Phys. B* **2009**, *23*, 473 473–491.

[253] Linsebigler, A. L.; Lu, G.; Yates, J. T. Photocatalysis on TiO_2 Surfaces: Principles, Mechanisms, and Selected Results. *Jr. Chem. Rev.* **1995**, *95*, 735–758.

[254]Carp, O.; Huisman, C. L.; Reller, A. Photoinduced Reactivity of Titanium Dioxide. *Prog. Solid State Chem.*, **2004**, *32*, 33–177.

[255] Gao, M.; Zhu, L.; Ong, W. L.; Wang, J.; Ho, G. W. Structural Design of TiO_2-Based Photocatalyst for H_2 Production and Degradation Applications. *Catal. Sci. Technol.* **2015**, *5*, 4703–4726.

[256] Grätzel, M. Synthesis and Characterization of TiO_2 Thin Films for DSSC Prototype. J. *Photochem. Photobiol. A* **2004**, *164*, 2052–2061.

[257] Bisquert, J.; Cahen, D.; Hodes, G.; Rühle, S.; Zaban, A. Physical Chemical Principles of Photovoltaic Conversion with Nanoparticulate, Mesoporous Dye-Sensitized Solar Cells. *J. Phys. Chem. B* **2004**, 108, 8106–8118.

[258] Quintana, M.; Edvinsson, T.; Hagfeldt, A.; Boschloo, G. Comparison of Dye-Sensitized ZnO and TiO_2 Solar Cells: Studies of Charge Transport and Carrier Lifetime. *J. Phys. Chem. C* **2007**, *111*, 1035–1041.

[259] Baxter, B.; Aydil, E.S. Nanowire-Based Dye-Sensitized Solar Cells. *Appl. Phys. Lett.* **2005**, *86*, 053114.

[260] Maness, P.; Smolinski, S.; Blake, D. M.; Huang, Z.; Wolfrum, E. J.; Jacoby, W. A. Bactericidal Activity of Photocatalytic TiO_2 Reaction: toward an Understanding of Its Killing Mechanism. *Appl Environ Microbiol*. **1999**, *65*, 4094–4098.

[261] de Abreu Chaves, M. E.; de Araújo, A. R.; Cruz Piancastelli, A. C.; Pinotti, M. Effects of Low-Power Light Therapy on Wound Healing: LASER x LED. *An. Bras. Dermatol*. **2014**, *89*, 616–623.

[262] Huheey, J. E.; Keiter, E. A., Keiter, R. L. (1993) *Inorganic Chemistry: Principles of Structure and Reactivity.* Fourth Edition. HarperCollinsCollegePublisher.

[263] Sakata, T.; Hashimoto, K.; Hiramoto, M. New Aspects of Electron Transfer on Semiconductor Surface: Dye-Sensitization System. *J. Phys. Chem.* **1990**, *94*, 3040–3045.

[264] Creutz, C.; Brunschwig, B.; Sutin, N. Interfacial Charge-Transfer Absorption: Semiclassical Treatment. *J. Phys. Chem. B* **2005**, *109*, 10251–10260.

[265] Creutz, C.; Brunschwig, B.; Sutin, N. Interfacial Charge-Transfer Absorption: 3. Application to Semiconductor–Molecule Assemblies. *J. Phys. Chem. B* **2006**, *110*, 25181–25190.

[266] Benkö, G.; Kallioinen, J.; Korppi-Tommola, J. E. I.; Yartsev, A. P.; Sundström, V. Photoinduced Ultrafast Dye-to-Semiconductor Electron Injection from Nonthermalized and Thermalized Donor States. *J. Am. Chem. Soc.* **2002**, *124*, 489–493.

[267] Wenger, B.; Grätzel, M.; Moser, J. Rationale for Kinetic Heterogeneity of Ultrafast Light-Induced Electron Transfer from Ru(II) Complex Sensitizers to Nanocrystalline TiO_2. *J. Am. Chem. Soc.* **2005**, *127*, 12150–12151.

[268] Persson, P.; Bergström, R.; Lunel, S. Quantum Chemical Study of Photoinjection Processes in Dye-Sensitized TiO_2 Nanoparticles. *J. Phys. Chem. B* **2000**, *104*, 10348–10351.

[269] Malcıoğlu, O. B.; Gebauer, R.; Rocca, D.; Baroni, S. TurboTDDFT – A Code for the Simulation of Molecular Spectra using the Liouville–Lanczos Approach to Time-Dependent Density-Functional Perturbation Theory. *Comput.Phys. Commun.* **2011**, *182*, 1744.

[270] Chae, A.; Jo, S.; Choi, Y.; Min, B.; Park, S. Y.; In, I. Visible-Light-Driven Photocatalysis with Dopamine Derivatized Titanium Dioxide/N-Doped Carbon Core/Shell Nanoparticles. *J. Mater. Sci.* **2017**, *52*, 5582–5588.

[271] Luga, C.; Alvarez-Idaboy, J. R.; Vivier-Bunge, A. ROS Initiated Oxidation of Dopamine under Oxidative Stress Conditions in Aqueous and Lipidic Environments. *J. Phys. Chem. B* **2011**, *115*, 12234–12246.

[272] Yang, Z.; Asico, L. D.; Yu, P.; Wang, Z.; Jones, J. E.; Escano, C. S.; Wang, X.; Quinn, M. T.; Sibley, D. R.; Romero, G. G.; Felder, R. A.; Jose, P.A. D5 Dopamine Receptor Regulation of Reactive Oxygen Species Production, NADPH Oxidase, and Blood Pressure. *Am J Physiol Regul Integr Comp Physiol.* **2006**, *290*, 96–104.

[273] Saad, Y. (2003) *Iterative Methods for Sparse Linear Systems*. 2nd edition, SIAM, Philadelphia.

[274] G. Kresse, J. Hafner. Ab Initio Molecular Dynamics for Liquid Metals. *Phys. Rev. B* **1993**, *47*, 558.

[275] G. Kresse, J. Hafner. Ab Initio Molecular Dynamics Simulation of the Liquid-Metal-Amorphous-Semiconductor Transition in Germanium. *Phys. Rev. B* **1994**, *49*, 14251.

[276] G. Kresse, J. Furthmüller. Efficiency of Ab-Initio Total Energy Calculations for Metals and Semiconductors Using a Plane-Wave Basis Set. *Comput. Mat. Sci*. **1996**, *6*, 15.

[277] G. Kresse, J. Furthmüller. Efficient Iterative Schemes for Ab Initio Total-Energy Calculations Using a Plane-Wave Basis Set. *Phys. Rev. B* **1996**, *54*, 11169.

[278] G. Kresse, J. Hafner. Ab Initio Molecular Dynamics for Liquid Metals. *Phys. Rev. B* **1993**, *47*, 558.

[279] G. Kresse, J. Hafner. Ab Initio Molecular Dynamics Simulation of the Liquid-Metal-Amorphous-Semiconductor Transition in Germanium. *Phys. Rev. B* **1994**, *49*, 14251.

[280] G. Kresse, J. Furthmüller. Efficiency of Ab-Initio Total Energy Calculations for Metals and Semiconductors Using a Plane-Wave Basis Set. *Comput. Mat. Sci*. **1996**, *6*, 15.

[281] G. Kresse, J. Furthmüller. Efficient Iterative Schemes for Ab Initio Total-Energy Calculations Using a Plane-Wave Basis Set. *Phys. Rev. B* **1996**, *54*, 11169.

[282] Tae, E. L.; Lee, S. H.; Lee, J. K.; Yoo, S. S.; Kang, E. J.; Yoon, K. B. A Strategy To Increase the Efficiency of the Dye-Sensitized TiO_2 Solar Cells Operated by Photoexcitation of Dye-to-TiO_2 Charge-Transfer Bands. *J. Phys. Chem. B* **2005**, *109*, 22513–22522.

LIST OF PUBLICATIONS:

- Ronchi, C.; Datteo, M.; Perilli, D.; Ferrighi, L.; Fazio, G.; Selli, D.; Di Valentin, C. π Magnetism of Carbon Monovacancy in Graphene by Hybrid Density Functional Calculations. *J. Phys. Chem. C*, **2017**, *121*, 8653–8661.
- Ronchi, C.; Selli, D.; Pipornpong, W.; Di Valentin, C. Proton Transfers at a Dopamine-Functionalized TiO_2 Interface. *J. Phys. Chem. C*, **2018**, *123*, 7682–7695.
- Ronchi, C.; Datteo, M.; Kaviani, M.; Selli, D.; Di Valentin, C. Unraveling Dynamical and Light Effects on Functionalized Titanium Dioxide Nanoparticles for Bioconjugation. *J. Phys. Chem. C*, **2019**, *123*, 10130–10144.